Experimental study of the fundamental phenomena involved in pool boiling at low pressure

Sandra Michaïe

N°d'ordre NNT : 2018LYSEI040

THÈSE de DOCTORAT DE L'UNIVERSITÉ DE LYON
opérée au sein de
INSA Lyon

Ecole Doctorale N° 162
Mécanique, Énergétique, Génie Civil et Acoustique

Spécialité de doctorat : Thermique et Énergétique

Soutenue publiquement le 04/05/2018, par :
Sandra MICHAÏE

Experimental study of the fundamental phenomena involved in pool boiling at low pressure

(Étude expérimentale des phénomènes fondamentaux de l'ébullition en vase à basse pression)

Devant le jury composé de :

DI MARCO Paolo	Professeur (Università di Pisa)	Président
ROBINSON Anthony J.	Professeur (Trinity College, Dublin)	Rapporteur
TADRIST Lounès	Professeur (Aix-Marseille Université)	Rapporteur
BARTHÈS Magali	Maître de Conférences (Univ. de Franche-Comté)	Examinateur
BONJOUR Jocelyn	Professeur (INSA Lyon)	Directeur de thèse
RULLIÈRE Romuald	Maître de Conférences (INSA Lyon)	Co-encadrant
ZAJACZKOWSKI Bartosz	Docteur (Politechnika Wroclawska)	Invité

Département FEDORA – INSA Lyon - Ecoles Doctorales – Quinquennal 2016-2020

SIGLE	ECOLE DOCTORALE	NOM ET COORDONNEES DU RESPONSABLE
CHIMIE	**CHIMIE DE LYON** **http://www.edchimie-lyon.fr** Sec. : Renée EL MELHEM Bât. Blaise PASCAL, 3e étage **secretariat@edchimie-lyon.fr** INSA : R. GOURDON	M. Stéphane DANIELE Institut de recherches sur la catalyse et l'environnement de Lyon IRCELYON-UMR 5256 Équipe CDFA 2 Avenue Albert EINSTEIN 69 626 Villeurbanne CEDEX **directeur@edchimie-lyon.fr**
E.E.A.	**ÉLECTRONIQUE, ÉLECTROTECHNIQUE, AUTOMATIQUE** **http://edeea.ec-lyon.fr** Sec. : M.C. HAVGOUDOUKIAN **ecole-doctorale.eea@ec-lyon.fr**	M. Gérard SCORLETTI École Centrale de Lyon 36 Avenue Guy DE COLLONGUE 69 134 Écully Tél : 04.72.18.60.97 Fax 04.78.43.37.17 **gerard.scorletti@ec-lyon.fr**
E2M2	**ÉVOLUTION, ÉCOSYSTÈME, MICROBIOLOGIE, MODÉLISATION** **http://e2m2.universite-lyon.fr** Sec. : Sylvie ROBERJOT Bât. Atrium, UCB Lyon 1 Tél : 04.72.44.83.62 INSA : H. CHARLES **secretariat.e2m2@univ-lyon1.fr**	M. Philippe NORMAND UMR 5557 Lab. d'Ecologie Microbienne Université Claude Bernard Lyon 1 Bâtiment Mendel 43, boulevard du 11 Novembre 1918 69 622 Villeurbanne CEDEX **philippe.normand@univ-lyon1.fr**
EDISS	**INTERDISCIPLINAIRE SCIENCES-SANTÉ** **http://www.ediss-lyon.fr** Sec. : Sylvie ROBERJOT Bât. Atrium, UCB Lyon 1 Tél : 04.72.44.83.62 INSA : M. LAGARDE **secretariat.ediss@univ-lyon1.fr**	Mme Emmanuelle CANET-SOULAS INSERM U1060, CarMeN lab, Univ. Lyon 1 Bâtiment IMBL 11 Avenue Jean CAPELLE INSA de Lyon 69 621 Villeurbanne Tél : 04.72.68.49.09 Fax : 04.72.68.49.16 **emmanuelle.canet@univ-lyon1.fr**
INFOMATHS	**INFORMATIQUE ET MATHÉMATIQUES** **http://edinfomaths.universite-lyon.fr** Sec. : Renée EL MELHEM Bât. Blaise PASCAL, 3e étage Tél : 04.72.43.80.46 Fax : 04.72.43.16.87 **infomaths@univ-lyon1.fr**	M. Luca ZAMBONI Bât. Braconnier 43 Boulevard du 11 novembre 1918 69 622 Villeurbanne CEDEX Tél : 04.26.23.45.52 **zamboni@maths.univ-lyon1.fr**
Matériaux	**MATÉRIAUX DE LYON** **http://ed34.universite-lyon.fr** Sec. : Marion COMBE Tél : 04.72.43.71.70 Fax : 04.72.43.87.12 Bât. Direction **ed.materiaux@insa-lyon.fr**	M. Jean-Yves BUFFIÈRE INSA de Lyon MATEIS - Bât. Saint-Exupéry 7 Avenue Jean CAPELLE 69 621 Villeurbanne CEDEX Tél : 04.72.43.71.70 Fax : 04.72.43.85.28 **jean-yves.buffiere@insa-lyon.fr**
MEGA	**MÉCANIQUE, ÉNERGÉTIQUE, GÉNIE CIVIL, ACOUSTIQUE** **http://edmega.universite-lyon.fr** Sec. : Marion COMBE Tél : 04.72.43.71.70 Fax : 04.72.43.87.12 Bât. Direction **mega@insa-lyon.fr**	M. Jocelyn BONJOUR INSA de Lyon Laboratoire CETHIL Bâtiment Sadi-Carnot 9, rue de la Physique 69 621 Villeurbanne CEDEX **jocelyn.bonjour@insa-lyon.fr**
ScSo	**ScSo*** **http://ed483.univ-lyon2.fr** Sec. : Viviane POLSINELLI Brigitte DUBOIS INSA : J.Y. TOUSSAINT Tél : 04.78.69.72.76 **viviane.polsinelli@univ-lyon2.fr**	M. Christian MONTES Université Lyon 2 86 Rue Pasteur 69 365 Lyon CEDEX 07 **christian.montes@univ-lyon2.fr**

*ScSo : Histoire, Géographie, Aménagement, Urbanisme, Archéologie, Science politique, Sociologie, Anthropologie

« La connaissance s'acquiert par l'expérience,
tout le reste n'est que de l'information. »

Albert Einstein

Acknowledgments/Remerciements

Une thèse de doctorat a beau être l'aboutissement d'un travail personnel, l'implication et le soutien sans faille de nombreuses personnes sont indispensables au succès du doctorant. C'est pourquoi je tiens maintenant à exprimer ma profonde gratitude à tous ceux qui – de près ou de loin – ont contribué à ce que ces trois années (et même un peu plus) passées à observer des bulles débouchent sur ce manuscrit.

Cette étude a été réalisée au Centre d'Énergétique et de Thermique de Lyon (CETHIL UMR5008) sous la direction du Professeur Jocelyn Bonjour et du Docteur Romuald Rullière. Elle a été financée par une bourse du Ministère de l'Enseignement Supérieur et de la Recherche (MESR) pour l'attribution de laquelle je remercie vivement l'École Doctorale n° 162 (Mécanique, Énergétique, Génie Civil et Acoustique – MEGA).

Je tiens tout d'abord à remercier les membres du jury pour le fort intérêt qu'ils ont manifesté pour ce travail de thèse (certains se souviendront qu'il leur a fallu braver les grèves des transports ferroviaires et/ou aériens pour pouvoir assister à la soutenance !). Merci donc au Professeur Paolo Di Marco d'avoir assuré la présidence de ce jury ainsi qu'aux Professeurs Anthony J. Robinson et Lounès Tadrist d'en avoir été les rapporteurs. Merci également au Docteur Magali Barthès d'avoir évalué mon travail notamment à travers son regard d'expérimentatrice.

Pour leurs conseils avisés et le soutien qu'ils m'ont apportés tout au long de ces années de doctorat, je remercie chaleureusement mes encadrants. J'ai apprécié la confiance et l'autonomie que vous m'avez accordées au cours de ce projet, elles m'ont permis de développer ma confiance en moi.

Jocelyn, merci de m'avoir conseillée et guidée dans cette découverte du monde de la recherche académique. Ta rigueur, ton optimisme à toute épreuve (même lorsque rien ne fonctionne comme prévu pour la manip' !) et ta grande réactivité (notamment en phase de rédaction) ont été des éléments clefs pour la réussite de ce travail et la qualité de ce manuscrit.

Romuald, merci d'avoir su te rendre disponible au quotidien (quitte à te mettre en retard pour tes cours/réunions...). Nos fréquents échanges (toujours avec le sourire !) vis-à-vis de questions pratiques de tout ordre (expérimental, rédactionnel et même administratif) ont été indispensables à l'avancée de cette thèse. Un grand merci aussi pour tes nombreux coups de main sur le banc d'essais : le changement de bain thermostaté, la fabrication maison d'un super passage étanche et surtout la tentative de sauvetage du fluxmètre resteront mémorables !

Mes remerciements s'adressent ensuite au Docteur Bartosz Zajaczkowski grâce à l'initiative duquel – à l'issue d'une rencontre avec Jocelyn lors d'une conférence au Japon – un partenariat entre le CETHIL et la Wrocław University of Science and Technology (WUST, Pologne) est né. Ce partenariat international s'est très vite concrétisé au cours de cette thèse avec les séjours de Tomasz Hałon (devenu Docteur depuis !) et de Karolina Wojtasik au CETHIL. Je remercie

donc Bartosz à la fois pour nos discussions et pour avoir accepté notre invitation à relire ce mémoire et à assister à la soutenance. Je remercie évidemment Tomasz et Karolina pour leur contribution tant scientifique qu'humaine à ce projet. Karolina reprenant la suite de ce travail, je lui souhaite de plus une bonne continuation.

Il me faut maintenant remercier l'ensemble du personnel administratif et technique du laboratoire à qui la réussite de ce projet doit beaucoup.

Indispensable au bon fonctionnement du CETHIL, je remercie en premier lieu toute l'équipe (ancienne et actuelle) du secrétariat. Je pense plus particulièrement à Florence (ex-responsable administrative), Nazaré (responsable administrative), Marilyne, Christine et Silas (secrétaires-gestionnaires).

Un grand merci également à l'atelier (notamment à Christophe, Nicolas, Joël et Xavier) pour la conception et la réalisation de pièces destinées au dispositif expérimental.

Enfin, comment remercier Serge et Anthony pour l'intérêt qu'ils ont porté (et portent d'ailleurs encore) aux problématiques expérimentales de ce travail de recherche ? Merci pour votre patience, le temps que vous avez consacré au développement et à la mise en œuvre du nouveau système d'acquisition et votre soutien. Je n'y serai probablement pas arrivée sans vous. Merci également pour tous vos précieux conseils, qu'ils soient scientifiques/techniques ou non, ainsi que pour les moments plus légers partagés dans la bonne humeur lors de pauses.

Je souhaite bien sûr remercier nombre de collègues doctorants et post-doctorants grâce à qui l'ambiance de travail est particulièrement agréable et les journées souvent joviales au CETHIL. Merci aux plus anciens dont Ali A., Damien G., Kévin T., Christophe K., Florine (Ton manuscrit aura eu une place de choix sur mon bureau jusqu'au bout ! Merci d'être passée pour la soutenance.) Aurélia et Quentin pour leur accueil. Merci à eux et à tous les autres (Thibaut, Adrien, Chi-Kien, Loïc R., Rémi, Kévin R. D., Nicolas C., Nicolas B., Damien Gl., Roberto, Samuel, Martin, Éloïse, Loïc F., Philémon, Élise, Hazem et... tous ceux que j'ai le malheur d'oublier) pour le bout de chemin parcouru ensemble, les parties de coinches, les échanges de volants et/ou de balles jaunes ou encore – pour certains – les bons moments partagés à l'occasion de conférences.

Je tiens enfin à adresser quelques mots à mes proches, à ma famille et à mes amis.

Je remercie évidemment mes amis ensmatiques, en particulier Armande (même si, retenue par une audition à l'autre bout de la France, tu n'as pas pu venir le jour J) et Pierre (cordialement !) pour être venu assister à ma soutenance et fêter la fin de cette aventure.

Que dire du soutien indéfectible que Guillaume, mon cher et tendre (encore un ensmatique !), a su me procurer tout au long de cette thèse ? Malgré la distance, tu as toujours su être là pour moi (même quand, n'ayant plus que mon manuscrit et ma rédaction en tête, je devais être particulièrement insupportable !). Simplement, merci ! C'est maintenant à mon tour de t'encourager dans la finalisation de ton doctorat, sache que j'essaie de faire au moins aussi bien que toi !

Merci à ma sœur et à toute sa petite famille pour leur soutien mais aussi pour les moments de détente (souvent accompagnés de fous rires) que nous partageons régulièrement. Vivement les prochains !

Un grand merci à mes parents dont l'amour et les encouragements quotidiens m'ont permis d'en arriver là. Je vous suis reconnaissante de toujours me suivre dans mes choix (quitte à voir du pays d'un déménagement à l'autre...).

Je conclurai ces remerciements en dédiant ce manuscrit à mes grands-parents et par une pensée émue à mon grand-père, parti avant la fin de la rédaction. J'aurais tellement aimé l'entendre s'exclamer : *« C'est quand même quelque chose... »* à l'annonce de mon nouveau titre de "Docteur"...

Abstracts

Abstract

Boiling is an efficient heat transfer mode used in a number of thermal or energy systems. In some systems – such as evaporators for sorption chillers or some thermosyphons – boiling takes place under low pressure conditions. In such a case, the static head induced by the liquid column over the wall where bubbles nucleate is not negligible with respect to the saturation pressure prevailing at the level of the free surface. The local pressure in the liquid is thus equal to the sum of the saturation pressure and of the static head. The pressure and the subcooling degree induced by the static head therefore cannot be considered as homogeneous around growing bubbles, which results in non-homogeneous thermophysical properties in the fluid. Consequently, the relative influence of the forces acting on a growing bubble differs from what is encountered under normal or higher pressure conditions, which leads to specific bubble dynamics features, *e.g.* different size, shape or bubble frequency. These particular conditions also affect the heat transfer.

In order to analyze the effect of the pressure on pool boiling from a fundamental point of view, an experimental study of boiling from a single activated nucleation site during the isolated bubbles regime was carried out. From a practical point of view, this regime was set – in horizontal upward orientation – on a mirror-polished copper surface at the center of which a conical cavity was created. Once this artificial nucleation site activated, the imposed heat flux was decreased until only this site remained active. Experiments were first conducted with water at constant imposed heat flux and liquid level for a range of pressure starting from the atmospheric pressure (P_v = 101.4 kPa (T_v = 100 °C)) down to P_v = 4.2 kPa (T_v = 30 °C)). Four distinct bubble dynamics behaviors were identified through high-speed camera visualizations. The bubble shape is thus changing as the imposed pressure decreases: near-spherical close to the atmospheric pressure, then mushroom and column shaped, mushroom shaped and finally oblate spheroid shaped at the lowest investigated pressure levels. For some of these regimes, a home-made image processing tool (developed under MATLAB environment) applied on the recordings enabled the measurement of several bubble dynamics characteristics (growth time, departure frequency, instantaneous volume, *etc.*). The dependence of these parameters on the working pressure (evaluated at the level of the heated wall in order to take into consideration the effect of the static head induced by the liquid column) was then analyzed. In order to generalize the concept of pool boiling at "low pressure" and to get a better understanding of the related fundamental phenomena, new experiments were performed with a second fluid, namely cyclohexane, that was chosen from original thermodynamic similarity criteria with reference to water boiling at pressures lower than atmospheric pressure. The operating conditions used during the cyclohexane test campaign were determined according to both the thermodynamic similarity criteria previously mentioned and the limits of the experimental facility. Some behaviors already noticed with water were then also observed in cyclohexane. The comparative analysis of fluids' behaviors made afterwards possible the identification of some of parameters

governing the specific phenomena that occur during boiling at low pressure.

Beyond these results, the experimental facility was improved to provide it new functionalities. In particular, two new test samples were used as heaters. The first one, provided with a multizone heat flux sensor employed as the heated surface, enables to perform – synchronously with the high-speed video recording – the measurement of the local heat flux transferred under any growing bubble. The triple line motion occurring during a bubble growth can therefore be monitored both visually and thermally. The second test sample enables the study of boiling on enhanced surfaces. Several geometries of enhanced surfaces such as narrow perforated tunnel structures were then studied. These are indeed supposed to be closer to real systems' heated walls than the mirror-polished surface provided with a unique artificial cavity that was previously tested. An analysis of the influence of those geometries on the low pressure boiling phenomenology was then performed. All these results display promising perspectives for a better understanding of the specific behaviors of boiling at low pressure and for a future exploitation of them in practical applications.

Keywords: *Pool boiling, low pressure, experiments, visualization, bubble dynamics, comparison of fluids, thermodynamic similarity.*

Résumé

L'ébullition est un mode de transfert de chaleur intervenant dans de nombreux systèmes thermiques ou énergétiques en raison de son efficacité. Dans certains systèmes – par exemple les évaporateurs des machines frigorifiques à sorption ou certains thermosiphons – l'ébullition se produit sous de faibles pressions. Dans ces conditions, la pression statique induite par la colonne de liquide au-dessus de la surface où les bulles de vapeur se forment n'est pas négligeable devant la pression de saturation prévalant au niveau de la surface libre, la pression locale dans le liquide étant alors la somme de la pression de saturation et de la pression statique. Dès lors, la pression et le sous-refroidissement induit par la pression ne peuvent plus être considérés comme homogènes autour des bulles, ce qui conduit à des inhomogénéités des propriétés thermophysiques dans le fluide. En conséquence, les influences relatives des différentes forces s'exerçant sur une bulle lors de sa croissance ne sont plus les mêmes que dans des conditions de pressions normales ou hautes, ce qui implique une dynamique de bulles différente : la taille, la forme ou encore la fréquence des bulles sont modifiées. Les transferts thermiques sont également affectés par ces conditions particulières.

Afin d'observer l'influence de la pression sur l'ébullition en vase d'un point de vue fondamental, ce travail s'est restreint à l'étude expérimentale de l'ébullition en site unique en régime de bulles isolées. D'un point de vue pratique, ce régime est atteint – en orientation horizontale vers le haut – sur une surface en cuivre polie miroir au centre de laquelle une cavité conique a été créée. Une fois ce site de nucléation artificiel activé, le flux imposé est ajusté de sorte à ce que seul ce site reste actif. L'eau a d'abord été testée à flux imposé et hauteur de liquide constants pour une gamme de pression s'étendant de la pression atmosphérique (P_v = 101,4 kPa (T_v = 100 °C)) jusqu'à P_v = 4,2 kPa (T_v = 30 °C). En termes de dynamique de bulles, quatre comportements ont pu être identifiés grâce à la visualisation par caméra rapide. Ainsi, selon la pression imposée, la forme des bulles change : quasi-sphériques à proximité de la pression atmosphérique, elles prennent la forme de champignon et/ou de colonne de vapeur puis uniquement de champignon et enfin de sphéroïde aplati au fur et à mesure que la pression décroît. Pour certains de ces régimes, l'emploi d'un outil de traitement d'images adapté – développé sous l'environnement MATLAB dans le cadre de cette thèse – a alors permis la quantification de plusieurs paramètres de la dynamique (temps de croissance, fréquence de détachement, volume instantané, *etc.*) à partir de l'exploitation des séquences vidéo enregistrées. Les évolutions de ces paramètres en fonction de la pression de travail (évaluée au niveau de la surface chauffée pour tenir compte de la pression induite par la colonne de liquide) ont donc pu être étudiées. Afin de généraliser le concept d'ébullition en vase à « basse pression » et de mieux en appréhender les phénomènes fondamentaux, de nouveaux essais ont été ensuite réalisés avec un second fluide, le cyclohexane, choisi en respectant des critères de similitude thermodynamique vis-à-vis de l'eau bouillant à des pressions inférieures à la pression atmosphérique. Les conditions opératoires des tests en cyclohexane ont été déterminées en considérant à la fois les critères de similitude thermodynamique mentionnés précédemment et les limites expérimentales du banc d'essais. Certains comportements déjà observés avec l'eau ont été retrouvés avec le cyclohexane. Par la suite, l'étude comparative des

comportements des deux fluides a permis d'identifier un certain nombre de paramètres responsables des phénomènes spécifiques de l'ébullition à basse pression.

Au-delà de ces résultats, le dispositif expérimental a été amélioré afin de lui conférer de nouvelles fonctionnalités. En particulier, deux nouveaux échantillons ont été utilisés comme éléments chauffants. Le premier, muni d'un fluxmètre thermique multizone utilisé comme surface d'ébullition, permet la mesure – synchrone avec l'acquisition par caméra rapide – de la densité de flux transférée localement sous une bulle au cours de sa croissance. Le déplacement de la ligne triple lors de la croissance d'une bulle a alors pu être suivi tant visuellement que thermiquement. Le second échantillon permet quant à lui l'étude de surfaces structurées. Ainsi, plusieurs géométries de surface chauffée telles que des agencements de tunnels perforés ont été étudiées. Ces géométries sont en effet supposées plus proches de celles rencontrées dans les systèmes réels que la surface plane polie avec site artificiel précédemment testée. L'influence de ces structurations de surface sur la phénoménologie de l'ébullition à basse pression a alors pu être analysée. Les résultats obtenus ouvrent des perspectives encourageantes pour mieux analyser les comportements spécifiques de l'ébullition à basse pression afin de pouvoir les exploiter dans des applications pratiques.

Mots-clefs : *Ébullition en vase, basse pression, essais expérimentaux, visualisation, dynamique de bulles, comparaison de fluides, similitude thermodynamique.*

Contents

Nomenclature

Latin

A	Area of the cross section of the heater	m^2
A_n	Area of the n^{th} zone of the heat flux sensor	m^2
C	A constant	
c_p	Constant-pressure specific heat capacity	$\mathrm{J} \cdot \mathrm{kg}^{-1} \cdot \mathrm{K}^{-1}$
D	Bubble diameter	m
d	Distance between two thermocouples	m
f	Bubble departure frequency	Hz
g	Gravitational acceleration	$\mathrm{m} \cdot \mathrm{s}^{-2}$
H	Height	m
h	Heat transfer coefficient	$\mathrm{W} \cdot \mathrm{m}^{-2} \cdot \mathrm{K}^{-1}$
$\mathcal{H}$	Hypothesis	
HF_n	Heat flux measured for the n^{th} zone of the heat flux sensor	$\mathrm{W} \cdot \mathrm{m}^{-2}$
HP	Heating power	W
I	Intensity of a pixel	
i	Electrical current	A
L	Length	m
m	Mass	kg
$M_{\tilde{x}}$	Number of points for which the altitude is measured along the $\tilde{x}$-axis	
$M_{\tilde{y}}$	Number of points for which the altitude is measured along the $\tilde{y}$-axis	
N	Number of recorded bubbles on a video	
n	An exponent	
P	Pressure	Pa
p	Spatial step of the confocal microscope	m
R	Bubble radius	m
r	Cavity radius	m
$\tilde{r}$	Radius of the dry area	m
s_n	Sensitivity of the n^{th} zone of the heat flux sensor	$\mathrm{V} \cdot (\mathrm{W} \cdot \mathrm{m}^{-2})^{-1}$
S_q	Root mean square roughness	m
$s_{\Delta T}$	Sensitivity of the temperature difference ΔT of the heat flux sensor	$\mathrm{V} \cdot \mathrm{K}^{-1}$
T	Temperature	°C
t	Time	s
u	Voltage	V
U	Velocity	$\mathrm{m} \cdot \mathrm{s}^{-1}$
V	Instantaneous volume of a bubble	m^3
$\mathcal{V}$	Volume of liquid	m^3

v	Volume of the system	m^3
x	Horizontal distance from the border of the ROI	pixel
$\tilde{x}$	First direction of the horizontal plane of the microscope	m
$\tilde{y}$	Second direction of the horizontal plane of the microscope	m
Z	Vertical distance to the heated surface (upwardly oriented axis)	m
z	Vertical distance to the free surface (downwardly oriented axis)	m
$\tilde{z}$	Surface altitude measured with the confocal microscope	m

Greek

α	Thermal diffusivity	$m^2 \cdot s^{-1}$
β	Cavity angle	rad
Δh_{lv}	Latent heat of vaporization	$J \cdot kg^{-1}$
ΔP	Pressure difference	Pa
ΔT	Temperature difference	K
Δt	Time step between two successive measurements	s
Δt_i	Non dimensional characteristic time of the conduction problem	
ε	Small variation of time	s
λ	Thermal conductivity	$W \cdot m^{-1} \cdot K^{-1}$
μ	Dynamic viscosity	$Pa \cdot s$
$\tilde{\mu}$	Mean value of the altitude $\tilde{z}$ on a given area	m
ν	Specific volume	$m^3 \cdot kg^{-1}$
φ	Heat flux	$W \cdot m^{-2}$
Ψ	A function	
ρ	Density	$kg \cdot m^{-3}$
σ	Surface tension	$N \cdot m^{-1}$
τ	Duration	s
θ	Contact angle	rad
ξ	A function	
ζ	A function	

Subscripts

atm	Atmospheric
automatic	From automatic treatment
BL	Boundary layer
bubble	Bubble
bulk	Bulk
cav	Artificial nucleation site
center	Center of the heat flux sensor and/or of the heated surface
co	Connection ribbon cable of the heat flux sensor
cond	Conduction
Cu	Copper
departure	Bubble detachment
eff	Effective
eq	Equivalent
growth	Growth
input	Imposed
l	Liquid
left	Left hand side

LH	Latent heat
localized	Automatically found interface
manual	From manual treatment
max	Maximum
meas	Measured
min	Minimum
nucleation	Bubble nucleation
right	Right hand side
sat	Saturation
sub	Subcooling
t	Triple point
v	Vapor
wait	Waiting
wall	Heated surface

Superscripts

*	Dimensionless value
crit	Critical
delay	Delay
exp	Experimental
relative	Relative value
static	Static head
sys	System

Dimensionless numbers

I_R	Robinson and Judd criterion $I_R = \left(\frac{4}{27}\right)\left(\frac{\sigma}{\rho_l \alpha_l^2}\right)\frac{R^{crit}}{Ja^2}$
Ja	Jacob number $Ja = \frac{\rho_l c_{p_l} \Delta T}{\rho_v \Delta h_{lv}}$
Pe	Péclet number $Pe = RePr$
Pr	Prandtl number $Pr = \frac{\mu c_p}{\lambda}$
Re	Reynolds number $Re = \frac{\rho U L}{\mu}$

Acronyms and abbreviations

EC	Empirical Criterion
IMG_n	n^{th} picture of the sequence
NI	National Instruments
NTS	Narrow Tunnel Structure
PC	Personal Computer
PDF	Probability Density Function
PFV	Photron Fastcam Viewer
RMSE	Root Mean Square Error
ROI	Region Of Interest
TS	Tunnel Structure

List of Figures

List of Tables

Introduction

Boiling is an efficient heat transfer mode involved in various practical applications. To cite a few examples, this phenomenon is used in steam turbine power plants, refrigeration units, heat pumps or microelectronics cooling systems. Whatever the scale, all the concerned applications require either high heat transfer rates, homogeneous temperature fields or a high compactness of thermal components. In all these technologies, a proper design should ensure the effectiveness, the reliability and the efficiency but also the safety of use of the systems. Boiling heat transfer must thus be sufficiently understood to become predictable. Boiling has therefore been extensively studied (experimentally, analytically and – more recently – numerically) in numerous configurations by thermal scientists for several decades. However, the complexity of the various and multiscaled fundamental phenomena taking part in boiling heat transfer makes its understanding still challenging. This is particularly true under unconventional conditions. In such a case, the boiling phenomenon may indeed be even more complex than under more usual conditions while relevant data tend to remain scarce in the literature.

In the 1960's and 1970's, the first few experimental studies interested in pool boiling at low imposed pressure – which constitutes such an unusual condition for boiling – reported some specific characteristics. It was thus demonstrated that pool boiling exhibits very different behaviors at low pressure than at normal or higher pressure levels. Yet, no further investigation was performed on this topic until recently. A renewal of interest for analyzing and understanding low pressure pool boiling has indeed arisen in the last ten years as a consequence of both the increased need of efficient low temperature systems for electronics cooling and the implementation of new environmental regulations for refrigeration units and air-conditioning applications. In this context, passive thermal management systems and environmentally friendly fluids have to be promoted, so that in some systems – such as evaporators for sorption chillers or some thermosyphons – boiling takes place under low pressure conditions. The design of such systems is however strongly limited by the poor knowledge and understanding of the fundamental phenomena involved in boiling under this particular condition. As a result, the optimization of the design of these systems requires new pieces of information about low pressure pool boiling that can be obtained only through new and various experimental studies.

The present thesis is therefore aimed at bringing a new contribution to knowledge on the fundamentals of low pressure pool boiling. Experimental test campaigns were thus carried out to analyze the influence of the pressure on both the bubble dynamics and the heat transfer at the bubble scale. In that goal, the experiments focused on the growth of bubbles formed from a smooth copper heated surface provided with a unique artificial nucleation site during the isolated bubbles regime. In addition, as it appears from the comparative review of the existing literature that the definition of what is "low pressure" in boiling still remains to be extended properly to other working fluids than water (for which low pressure boiling commonly means boiling at a subatmospheric pressure), a new specification of this particular operating condition was attempted through the development of the concept of "mock-up fluids".

This thesis is divided into five chapters (with several appendixes) as follows:

Chapter 1: This chapter constitutes an introduction to both the fundamental concepts of boiling from a general point of view and the main characteristics of low pressure pool boiling that are already reported in the literature. The limits of the existing literature dealing with low pressure pool boiling are also discussed.

Chapter 2: This chapter is aimed at describing the experimental facility used in this study. The experimental procedures as well as the measurement and post-processing methods and the related uncertainties are also detailed.

Chapter 3: Results obtained during a test session performed with water boiling in a wide range of subatmospheric pressures are presented and discussed.

Chapter 4: A generalization of the "low pressure" boiling concept to other fluids than water was attempted according to a mocking up method. A mock-up fluid, namely the cyclohexane, was indeed selected for a new series of experiments whose results are presented in this chapter. Finally, the behaviors of the two fluids are compared to make possible the identification of some of parameters governing the specific phenomena that occur during boiling at low pressure.

Chapter 5: An original improvement of the experimental facility – aiming at getting a better understanding of the correlation that exists between the heat transfer and the bubble dynamics – was designed and implemented. This chapter demonstrates how the associated results display promising perspectives for further investigations.

Chapter 1

Literature review: boiling at low pressure

Boiling enables the dissipation of high heat fluxes with low driving temperature differences, which makes it a highly efficient heat transfer mode. It is therefore implemented in many technologies or industries where either high heat transfer rates, homogeneous temperature fields or high compactness of thermal components are critical features. Boiling is thus involved in various fields at different scales: from power plants to refrigeration units or microelectronics cooling.

Boiling has therefore been a major topic of research in thermal sciences for several decades. However, the complexity of the various fundamental phenomena involved in boiling heat transfer makes its understanding still challenging. This is especially the case under unusual conditions such as low imposed pressure, which is precisely the subject of this work. As a complete state-of-the-art of boiling heat transfer is not possible here while numerous books have already been written on the topic, this chapter only aims at giving the necessary background to understand the results presented in this manuscript and their relevance. Some fundamental concepts of boiling are first described in Section 1.1 before some of the already-reported characteristics of low pressure pool boiling are introduced in Section 1.2. Additional pieces of literature will be provided later on along the document, each time the specific subjects investigated will make it necessary.

1.1 Introduction to fundamental concepts of boiling

Fundamental concepts of boiling will be succinctly presented hereafter at once from a macroscopic point of view (Section 1.1.1), at the scale of the nucleation phenomenon (Section 1.1.2) and at the growing bubble scale (Section 1.1.3).

1.1.1 Pool boiling curve

Pool boiling corresponds to the boiling process taking place from a heated surface immersed in a large bulk of stagnant liquid. It is named "saturated pool boiling" when the bulk liquid is at the saturation temperature ($T_{l,\,bulk} = T_{sat}$) or "subcooled pool boiling" if the liquid is cooler ($T_{l,\,bulk} < T_{sat}$). From a macroscopic point of view, the heat transfer occurring during this phenomenon is usually described according to "boiling curves" plotting the instantaneous wall heat flux φ_{wall} as a function of the instantaneous wall superheat $T_{wall} - T_{sat}$. Such a representation was first proposed by Nukiyama in 1934 [85, 86], who observed that – in steady state boiling – two boiling curves shapes can be obtained depending on whether the temperature or the heat flux is imposed at the heated surface. These curves are schematically sketched on Fig. 1.1. A short description of each of the specific boiling regime associated with every part of these curves is hereafter given.

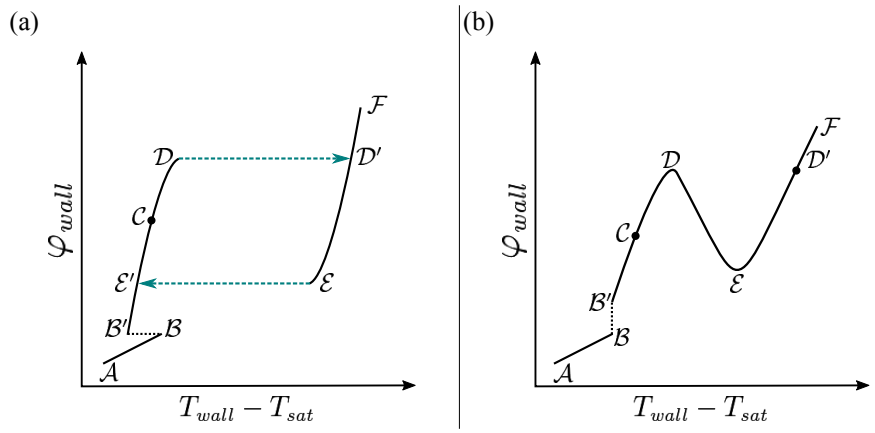

Figure 1.1 – Saturated boiling curves at (a) imposed heat flux; (b) imposed temperature.

Natural convection ($\mathcal{AB}$): The heated surface is heating the surrounding liquid: a thermal boundary layer is thus formed above the wall. Heat is transferred by natural convection in the bulk liquid while vaporization occurs at the free surface.

Onset of boiling ($\mathcal{BB}'$): The wall superheat is then high enough to enable the generation of vapor bubbles. A part of the heat being dissipated by phase change, the heat transfer is enhanced. At imposed heat flux, this results in a wall superheat drop whereas at imposed temperature, this results is a sudden increase of the wall heat flux.

Isolated bubble regime ($\mathcal{B}'\mathcal{C}$): Bubbles are nucleating from isolated sites of the heated surface. The wall temperature increases slowly with the heat flux, which results in a very efficient heat transfer. More and more nucleation sites become active on the heated surface so that the dissipation of heat raises both by phase change (increasing number of bubbles) and by convection (enhanced through the liquid agitation induced by the growth and departure of bubbles).

Fully developed nucleate boiling regime ($\mathcal{CD}$): Active nucleation sites are numerous and sufficiently close to each other to make possible the coalescence of bubbles growing from neighboring cavities ("lateral coalescence"). The heat flux being increased, the bubble frequency becomes higher as well. As a consequence, successive bubbles from the same site can also merge ("vertical coalescence"). There may come a situation at which the large masses of vapor limit the liquid motion close to the wall yielding a slight decrease of the heat transfer coefficient.

Critical heat flux ($\mathcal{DD}'$): At this point, the heat flux reaches a critical value because of the vapor masses which prevent a sufficient re-wetting of the surface by the liquid. A film of vapor of high thermal resistance is then formed on the wall leading to a sudden rise of the wall temperature that can damage the system ("burn out" phenomenon).

Film boiling regime ($\mathcal{EF}$): The vapor film created on the surface becomes stable. The heat is transferred from the surface to the vapor layer by conduction and convection while phase change takes place at the liquid-vapor interface. The vapor detaches periodically from the wall with regularly spaced bubble columns shape. The temperature increasing with the heat flux, radiative heat transfer through the vapor film can become a predominant process. Once the stable film boiling regime established, it remains observable even if the heat flux (and consequently the temperature) is decreased below the critical heat flux value (and temperature). In this regime, the burn out phenomenon can still be a strong limitation which can damage the heated surface if an excessive surface temperature is reached.

Leidenfrost point ($\mathcal{EE}'$): The heat flux is then low enough to make the vapor film broken. Liquid is again able to re-wet the heated wall: heat transfer is enhanced (a sudden temperature drop occurs) and the isolated bubble regime is back. This point corresponds thus to the minimum heat flux reachable in the film boiling regime.

The analysis of such pool boiling curves clearly demonstrates which regimes are interesting for thermal management systems. Isolated bubble and fully developed boiling regimes (gathered together under the name of "nucleate boiling regime") are indeed of major interest through their ability to release high heat fluxes to the fluid with relatively low wall superheats. This representation of the boiling phenomenon is yet not sufficient to understand its lower scale phenomenology. The fundamental phenomena involved in boiling are indeed numerous and are related to many parameters such as the fluid nature, the working pressure and temperature or the geometry of the heated surface and its roughness. The different mechanisms governing the boiling process have therefore to be studied at the microscopic scale as well.

1.1.2 Bubble nucleation

1.1.2.1 Thermodynamic considerations

From the thermodynamic point of view, liquid-vapor phase change can occur only under certain conditions. The Clapeyron diagram of a pure substance (schematically represented on Fig. 1.2) shows indeed domains where such a substance can be in a liquid or vapor state or where these two phases can coexist. The binodal curve (black line on Fig. 1.2) delimits the liquid-vapor region.

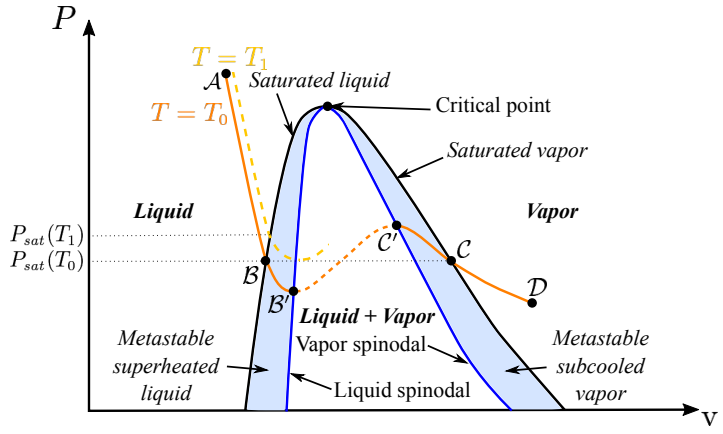

Figure 1.2 – Schematic Clapeyron diagram of a pure substance.

Along the isotherm curve $T = T_0$, the fluid is in a stable liquid state (subcooled liquid) from $\mathcal{A}$ to $\mathcal{B}$ and in a stable vapor state (superheated vapor) between $\mathcal{C}$ and $\mathcal{D}$. Along the segment $\mathcal{BC}$, liquid and vapor phases coexist in a stable thermodynamic equilibrium at a uniform pressure with a flat interface.

Liquid and vapor phases can also exist in other states, namely the "metastable states", in which they are not in a stable thermodynamic equilibrium. For instance, while keeping the same temperature T_0, the saturated liquid phase can have its volume increased from $\mathcal{B}$ to $\mathcal{B}'$ (inducing a pressure reduction) without the occurrence of any phase change. The same phenomenon appears for the vapor phase[1] between $\mathcal{C}$ and $\mathcal{C}'$. These metastable states are bordered by the spinodal curve (blue line on Fig. 1.2). Spinodal points correspond actually the local minimum and maximum of each isotherm. They represent the ultimate limits where single liquid phase and single vapor phase (at the left hand side and at the right hand side respectively) can exist at a given temperature. $\frac{\partial P}{\partial \mathrm{v}} > 0$ (with v representing here the volume of the system) between $\mathcal{B}'$ and $\mathcal{C}'$ which is indeed not representative of any physical reality.

At a constant bulk pressure $P = P_{sat}(T_0)$, liquid can be heated up to the saturation temperature T_0 and above in the superheated liquid domain. At a moment, a vapor nucleus will appear

[1] No phase change takes place as the volume of the saturated vapor is decreased from $\mathcal{C}$ to $\mathcal{C}'$ (leading to an increase of the pressure).

and the two phases will then coexist at a same temperature $T_1 > T_0$. They will yet be at different pressures since the liquid will be at $P_{sat}(T_0)$ while the vapor will be at the saturation pressure corresponding to its temperature that is $P_{sat}(T_1)$. This pressure difference between the two phases will induce mechanical forces acting on the liquid-vapor interface whose balance will make this interface curved towards the nucleus.

Let a spherical bubble of radius R at a given temperature $T_{v,\,bubble}$ and pressure $P_{v,\,bubble}$ being immersed in an extended liquid bulk uniformly superheated whose temperature $T_{l,\,bulk}$ and pressure $P_{l,\,bulk}$ are imposed by external means. Such a bubble can be in equilibrium with its environment only if the variation of the Helmholtz free energy of formation of the bubble is equal to zero. This requires thus the system to be, at once:

- In a chemical equilibrium (equality of the vapor and liquid chemical potentials);
- In a thermal equilibrium (equality of the temperatures of liquid $T_{l,\,bulk}$ and of the vapor $T_{v,\,bubble}$);
- In a mechanical equilibrium.

For a system of constant temperature and volume, the expression of the variation of the Helmholtz free energy simplifies to the Laplace equation which holds for the mechanical equilibrium[1]:

$$P_{v,\,bubble} - P_{l,\,bulk} = \frac{2\sigma}{R} \tag{1.1}$$

The Helmholtz free energy can thus be expressed as a function of the bubble radius R. It is then shown [89] that this quantity reaches its maximal value for a given bubble radius value called "critical radius" R^{crit} corresponding to an unstable equilibrium. Contrary to any bubble embryo smaller than this critical size which will spontaneously collapse, every vapor nucleus larger than R^{crit} will grow. The critical radius value could be predicted through the Young-Laplace equation:

$$R^{crit} = \frac{2\sigma}{P_{sat}(T_{l,\,bulk}) - P_{l,\,bulk}} \tag{1.2}$$

1.1.2.2 Nucleation theory

Thermal fluctuations can make a spontaneous apparition of a vapor embryo in a superheated (metastable) liquid possible through the gathering of several vapor-like molecules. This phenomenon – which can lead to a bubble growth if the nucleus is larger than the equilibrium radius R^{crit} – is referred as "homogeneous nucleation". The temperature required to onset homogeneous nucleation can be analytically estimated [13, 99]. However, forming a vapor embryo able to grow with this process is generally related to a very low probability [28, 108] and requires much higher wall superheats than experienced in real systems[2]. In such systems, the boiling process is actually initiated by "heterogeneous nucleation", *i.e.* through the apparition of vapor nucleus in contact with foreign bodies that can be impurities in the liquid, entrapped incondensable gases or a solid surface such as a heated wall.

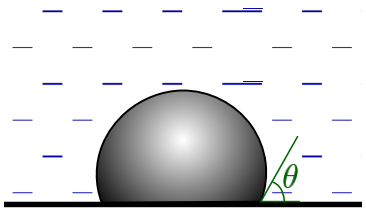

Figure 1.3 – Schematic of a bubble nucleating on a flat smooth solid surface with the related contact angle θ.

[1] In such a system, both the chemical and the thermal equilibria are assumed to be reached.

[2] Wall superheats required to onset homogeneous nucleation is typically of the order of magintude of a hundred kelvins [28, 57, 99, 108] (more than 200 K for water at atmospheric pressure for example) whereas the superheat usually encountered in experiments is of the order of magnitude of ten kelvins.

Due to the presence of a triple interface between the liquid, the vapor and the solid or particles acting as a foreign body, the bubble energy of formation – calculated analytically as in homogeneous nucleation – is reduced by a factor $\zeta(\theta)$ depending on the triple line contact angle[1] θ. In the case – depicted on Fig. 1.3 – of a bubble nucleating on an idealized (*i.e.* flat and smooth) solid surface, this function can be written as [5]:

$$\zeta(\theta) = \frac{2 + 3\cos(\theta) - \cos^3(\theta)}{4} \tag{1.3}$$

so that:

- If the liquid totally wets the surface (*i.e.* $\theta = 0\ ^\circ$), $\zeta(\theta) = 1$ and the energy of formation of a bubble nucleus is not reduced compared to the homogeneous nucleation case.
- If the liquid does not wet at all the surface, *i.e.* if $\theta = 180\ ^\circ$ (which is possible only in theory[2]), $\zeta(\theta) = 0$ and no superheat is required to initiate the apparition of a vapor embryo.

Actually, the boiling process on real surfaces is initiated with even lower superheats because of the presence of cavities which tends to reduce even further the superheat necessary to the nucleation since:

- The apparent contact angle is increased when the triple line is located inside a cavity (Fig. 1.4).

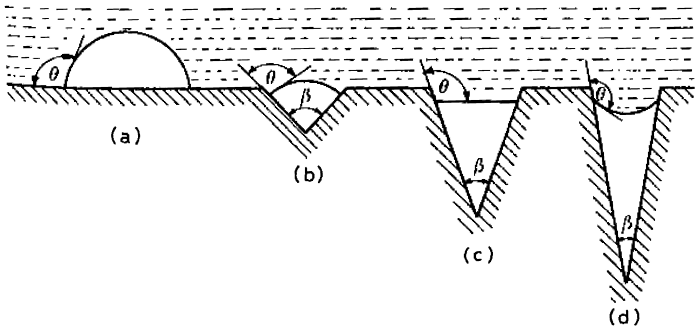

Figure 1.4 – Apparent contact angle θ in conical cavities of decreasing cavity angle β (extracted from [28]).

- The presence of cavities on raw surfaces promotes a gas or vapor entrapment during the filling of the boiling system [6]: depending on the fluid surface tension σ and of the geometry of a the considered cavity (see Fig. 1.5), the liquid is indeed able to fill it entirely or not. This mechanism tends thus to "pre-activate" some nucleation sites. The first bubbles detaching from these locations progressively evacuate the entrapped gases so that, after a while, these sites contain only vapor and remain active.

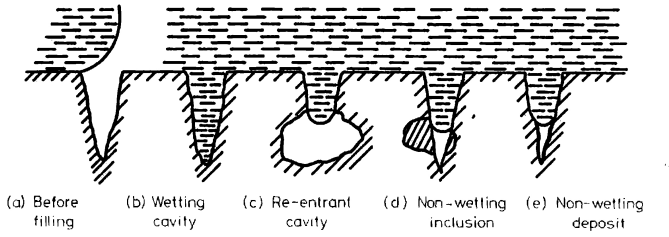

Figure 1.5 – Formation of an active nucleation site by gas or vapor entrapment in real cavities (extracted from [28]).

[1] This parameter characterizes the wettability of the fluid on the surface and therefore depends mainly on the fluid/surface pair.

[2] Contact angles are usually ranging between almost 0 ° and *ca.* 100 °.

In addition to its geometrical shape, experimental and theoretical works demonstrated that the ability of a cavity to be activated is significantly affected by its size. For instance, only cavities of a given range of radius (*i.e.* such as $r_{cav} \in [r_{cav,\,min},\, r_{cav,\,max}]$) can become active [52,56] on a raw surface with conical sites. The minimal $r_{cav,\,min}$ and maximal $r_{cav,\,max}$ sizes that enable the activation of such a cavity can be estimated analytically as a function of the thermal boundary layer thickness, of the wall superheat and of some thermophysical properties of the working fluid.

1.1.3 Bubble dynamics

1.1.3.1 Bubble growth cycle

Once a large enough vapor embryo created on a surface (when all the required conditions for it – in terms of wall imposed heat flux and temperature, fluid thermodynamic state and surface condition – are reached), the bubble will grow, depart and rise in the liquid bulk.

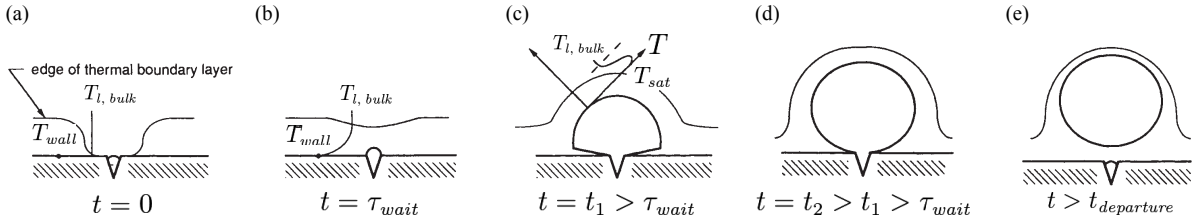

Figure 1.6 – Schematic cycle of a bubble formed at an active cavity site (adapted from [13]).

A typical bubble cycle is described in five successive steps on Fig. 1.6:

1. At $t = 0$ (Fig. 1.6a), the thermal boundary layer is broken because a previous bubble has just departed from the heated surface. As a consequence, cold liquid from the far bulk (at $T_{l,\,bulk}$) re-wets the wall and is heated by transient conduction from the surface so that the thermal boundary layer starts to grow again.

2. The thermal boundary layer keeps growing during a period of time called "waiting period" τ_{wait} during which no bubble growth takes place (Fig. 1.6b).

3. Then, the bubble begins to expand with a rather hemispherical shape (Fig. 1.6c). As the bubble grows radially, a thin liquid film – the "microlayer" – remains between it and the wall and contributes to the bubble expansion. Heat is indeed transferred from the wall to the interface across the microlayer, which results in some liquid vaporization at the bubble base. Consequently to the contact with the superheated liquid, vaporization occurs also along the rest of the liquid-vapor interface (*i.e.* in the so-called "macroregion" area). During this initial stage of bubble growth, the liquid close to the bubble edges is highly superheated so that the heat transfer across the interface is not limiting, contrary to the inertia of the liquid which tends to slow the expansion of the vapor volume: the growth is thus said "inertia-controlled".

4. After this first stage of rapid growth, the bubble expansion continues slower since the vaporization has reduced the superheat of the surrounding liquid. The bubble growth becomes therefore "heat-transfer-controlled" (or "diffusion-controlled") and the surface tension tends to give the bubble a more spherical shape (Fig. 1.6d).

5. Later (at $t = t_{departure}$, Fig. 1.6e), the bubble finally detaches from the heated wall, carrying with it a part of the thermal boundary layer. The cycle can then restart.

This classical description of a bubble growth may be discussed since – for instance – the case a bubble becoming large enough to emerge from the thermal boundary layer before its departure is not considered. Moreover, depending on the conditions under which boiling is taking place, only one of the two introduced mechanisms of growth (inertia-controlled and heat-transfer-controlled)

may be observed. Carey [13] listed some parameters which are likely to promote one or the other bubble growth regime; they are reported in Table 1.1.

Table 1.1 – Boiling conditions depending on the bubble growth regime that they are supposed to promote [13].

Parameter	**Inertia-controlled growth**	**Diffusion-controlled growth**
Wall superheat	High	Low
Imposed heat flux	High	Low
Surface condition	• Highly-polished • Only very small cavities	• Rough • Many large and moderate-sized cavities
Contact angle (corresponding wettability)	Very low (high)	Moderate (moderate)
Latent heat of vaporization	Low	High
System pressure	Low[1]	Moderate to high

Carey [13] highlighted that the combination of a high wall superheat, a low latent heat of vaporization and of a low pressure system to promote inertia-controlled bubble growth implies that this regime is more likely to occur for large Jacob number values. The Jacob number Ja is indeed a dimensionless number commonly used in phase change heat transfer to characterize the ratio of the sensible heat to the latent heat which is defined as:

$$Ja = \frac{\rho_l c_{p_l} \Delta T_{wall}}{\rho_v \Delta h_{lv}} \tag{1.4}$$

It is then not surprising that the Jacob number appears in the I_R number developed by Robinson and Judd [98] to determine if a bubble growth is mostly governed by inertia or by heat transfer diffusion. Based on a ratio of the squares of the characteristic velocities related to inertia and heat transfer, this criterion is defined according to Eq. 1.5:

$$I_R = \left(\frac{4}{27}\right)\left(\frac{\sigma}{\rho_l \alpha_l^2}\right)\frac{R^{crit}}{Ja^2} \tag{1.5}$$

According to the authors, inertia controls the bubble growth if $I_R \ll 1$ whereas diffusion is predominant if $I_R \gg 1$.

Starting from the work of Lord Rayleigh [72] who modeled the growth and collapse of an inertia-controlled spherical bubble in 1917, numerous analytical models for bubble growth were developed in the last century. Inertia-controlled bubble growth is then usually described through the Rayleigh equation [72] or its extended version [40, 93, 103]. In this case, the bubble radius is generally considered as a linear function of the time [80, 98, 112]:

$$R \sim t \tag{1.6}$$

The case of a bubble whose growth is governed by thermal diffusion was first modeled by a thermal balance at the bubble interface according to the work of Bošnjaković [11] in 1930. This approach was afterwards extended for example by Zuber [133] or Van Stralen [118]. These models generally lead to an evolution of the bubble radius proportional to the square root of the time [33, 42, 80, 93, 98, 112, 133]:

$$R \sim t^{0.5} \tag{1.7}$$

Predicting the bubble growth is actually much more complex since many parameters and processes are involved at different scales:

[1] This results generally in low vapor density and thus in a rapid volumetric growth of the bubble.

- The bubble is rarely spherical[1].
- The temperature field of the surrounding liquid is not homogeneous.
- The thermal exchanges between a bubble growing on a heated wall and its environment are of diverse nature:
  - Evaporation both in the microlayer and in the macroregion;
  - Convection between the liquid and the liquid-vapor interface in the macroregion;
  - Conduction between the heated wall and the dry area under the bubble.
- Additional effects related to convective motion occurring in the liquid may have also to be taken into account:
  - The natural convection between the activated nucleation sites;
  - The "micro-convection" induced by the expansion and rise of a bubble;
  - The "Marangoni effect" which corresponds to a liquid motion along the liquid-vapor interface induced by a surface tension gradient[2].

Numerous analytical models considering some of the cited parameters and phenomena were therefore developed. For instance, in Zuber's model [133], only the evaporation in the macroregion is considered (the microlayer evaporation is thus neglected) but the temperature field is assumed non-uniform. On the contrary, the model developed by Cooper [29] – based on the microlayer formation theory proposed by Cooper and Lloyd [32] – stands that hemispherical bubbles grow under the influence of the microlayer evaporation only[3]. On their side, Buyevich and Webbon [12] took into account the heat and mass transfer occurring both from the microlayer and the macroregion in the simplified case of a truncated spherical shaped bubble separated from the heated wall by a thin microlayer.

More recently, Dhir [37] highlighted that – because of the complex interaction between the multiple subprocesses involved in boiling at different scales – a prediction of nucleate boiling based on the analytical study of all the involved mechanisms might be not possible. The author then reviewed some results obtained in the literature with an alternative approach consisting in the complete numerical simulation of boiling. This approach appears as promising but faces specific issues. 3D-simulation remains indeed costly, while, for example:

- A proper meshing of the geometry is made difficult by the multi-scale phenomena to simulate.
- The bubble nucleation as well as the bubble interaction with the surface at the triple line, that is a physical discontinuity, needs to be well understood before it can be modeled correctly.
- Some experimental results are often required in order to validate the simulation outputs.

[1] The common use of the bubble radius R as the relevant parameter to describe the bubble growth is thus not always justified or fully satisfying. The notion of "equivalent radius" R_{eq} corresponding to the radius of a sphere of identical volume is therefore often introduced.

[2] There exist three types of Marangoni effect depending on the cause of the surface tension gradient along the interface [7]. When a temperature gradient is responsible for the surface tension gradient, one deals with the "thermal Marangoni effect" or "thermocapillary effect". In the case of mixtures or when using surfactants, a concentration difference can engender a surface tension gradient inducing a "solutal Marangoni effect". Finally, a gradient of electrical potential can lead to an "electrocapillary effect"; this might occur in a boiling process enhanced by electrohydrodynamics.

[3] This hypothesis should hold for bubbles large in comparison with the thickness of the thermal boundary layer.

1.1.3.2 Forces acting on a growing bubble

During its growth, the shape of a bubble varies with the balance of the forces acting on it. These forces are also responsible for the departure of the bubble from the heated surface: while the resultant of the forces is oriented towards the wall, the bubble remains attached and continues to grow but, as soon as the forces tending to detach the bubble become predominant, the bubble departs. The forces acting on a growing bubble are usually sorted into two groups: the so-called "static forces" which are related to the stresses applied on the motionless bubble and the "dynamic forces" which are the consequence of the bubble motion (expansion and rise). Hereafter, the most commonly invoked forces of each kind are listed and shortly described.

Four distinct static forces are generally cited:

Buoyancy force: This force corresponds to the resultant of the hydrostatic pressure forces applied on the bubble surface. It results from the vertical pressure gradient caused by gravity.

Contact pressure force: This contact pressure force is the consequence of two combined phenomena:

- As the bubble is attached to the wall and not totally immersed in the liquid, its buoyancy is actually increased[1] due to the contact area with the surface.
- The pressure applied on the contact area by the vapor bubble is higher than the pressure of the liquid so that the wall reaction on the bubble has to be considered.

One should note that this force is sometimes included as an additional term in the buoyancy force.

Surface tension force: Also known under the names of "triple line surface tension" or "triple line adhesion forces", this force represents the effect of the molecular interactions occurring between the different phases. Governed by both the liquid-vapor surface tension and the wettability of the liquid/surface pair, this force generally tends to maintain the bubble attached to the wall. It has however been shown [12,31] that, in some cases (in particular when the bubble is vertically elongated), this force can act on the bubble shape in such a way that it can promote the bubble departure from the wall.

Marangoni force: This is the force induced by a surface tension gradient which makes the liquid moving along the liquid-vapor interface. In the case of a vapor bubble growing from a heated surface facing upwards in a pure and degassed fluid without any electrical field, such a surface tension gradient can be caused only by a temperature difference[2], so that it is rather named as "thermocapillary force". The liquid flows from the base of the bubble towards its top which is cooler. This motion results in the creation of a shear viscous stress at the interface which is commonly assumed to be mostly applied on the liquid side of the interface since the liquid viscosity is generally much larger than that of the vapor.

Three dynamic forces are also usually listed:

Inertia and added mass forces: The inertia and added mass forces correspond to the reaction of the liquid to its acceleration caused by the motion of the liquid-vapor interface as the bubble expands and pushes the surrounding liquid away.

Drag force: The drag force corresponds to the viscous stress that acts opposite to the direction of the bubble rise.

Lift force: This force characterizes the influence of the wake of a preceding bubble on the next growing one: if two successive bubbles are sufficiently close to each other (*i.e.* if the waiting period τ_{wait} is small enough), the liquid flow caused by the first one acts as a rising force on the next one.

[1] In comparison with the case of a vapor bubble entirely immersed in the liquid.
[2] In this case, no concentration nor electrical potential gradient is supposed to exist.

Several analytical expressions related to all these forces can be found in the literature [19, 23, 24, 43, 65, 68, 104, 106, 107, 132]. Using bubble growth models in the momentum balance, Buyevich and Webbon [12] also obtained an enhanced determination of the dynamic forces. Yet, as highlighted by Siedel *et al.* [107], those expressions are most of the time limited by a strong assumption made on the bubble shape: bubble geometry is indeed generally idealized to a (truncated) sphere both for the analytical determination of the forces and in the growth models included in the momentum balance performed by Buyevich and Webbon [12].

Despite this limitation, all the cited studies were able to demonstrate that the relative contributions of the forces acting on a growing bubble depend on:

- The fluid and its thermophysical properties;
- The wall characteristics (material thermophysical properties as well as its geometry or roughness);
- The operating conditions of boiling (*e.g.* saturated or subcooled boiling, wall superheat and heat flux, normal or reduced gravity, pressure level);
- The time.

Conducting the analysis of momentum balance on a growing bubble whose characteristics were experimentally measured in a controlled environment, some authors [23, 24, 106, 107] were able to determine the time evolution of the contribution of each force during a bubble growth. It should however be highlighted that the results obtained with such an approach are strongly dependent on the chosen hypotheses to take into account or neglect some of the forces. The full resolution of the most general momentum balance (*i.e.* without any term *a priori* neglected) requires indeed the accurate knowledge of data which are still not experimentally accessible (such as the local rate of heat transfer or the instantaneous temperature and velocity fields). It is then commonly accepted that:

- For a bubble growing with a rather low rate of growth (which is generally the case under usual boiling conditions), the predominant forces that govern the force balance of the bubble are the buoyancy, the contact pressure and the surface tension forces.
- For a bubble growing with a relatively high rate of growth (this occurs preferentially with a high wall superheat, a high liquid subcooling degree or at low pressure), the dynamic forces (in particular the inertia) become non negligible.

The same simplification is commonly made when writing a force balance at the instant of the bubble detachment to predict the bubble departure diameter[1].

1.2 Low pressure pool boiling features

Low pressure constitutes an unconventional condition under which pool boiling can occur. Only scarce experimental studies were therefore conducted under this particular condition. However, the first few ones – mostly performed in the 1960's – reported some specific characteristics which demonstrate the challenging interest of analyzing boiling under this unusual condition. More recently, the increased need of efficient low temperature systems for electronics cooling as well as the new environmental regulations for refrigeration units and air-conditioning applications led to a renewal of interest for investigating low pressure pool boiling. The use of passive thermal management systems and of environmentally friendly fluids have indeed to be promoted in this context. As a consequence, water becomes an increasingly used refrigerant and is – for instance – the working fluid the most commonly used in sorption systems developed for air-conditioning applications. In such systems, the operating conditions in the evaporator part are characterized

[1] Refer to Ginet [43] for a detailed state-of-the-art of the usual criteria of departure and of the derivated departure diameter expressions.

by a saturation temperature of the order of 2 – 10 °C corresponding to a pressure of only a few hectopascals. The poor knowledge and understanding of the fundamental phenomena involved in boiling under such specific conditions have then made necessary new and various experimental studies on this topic. Hereafter, the already-reported features of low pressure pool boiling concerning the bubble dynamics (Section 1.2.1), the heat transfer (Section 1.2.2) and the boiling environment (Section 1.2.3) will be introduced. Finally, the difficulty to analyze and compare results from the existing literature will be discussed in Section 1.2.4.

1.2.1 Bubble dynamics observations

The bubble shape – rather hemispherical during almost all the growth – tends to prove that inertia and other dynamic effects are non negligible at low pressure. In 1966, Cole and Shulman [27] thus reported that water bubbles growing on a horizontal upward-facing plate surface at subatmospheric pressures are relatively "ellipsoidal in shape" with the longest axis in the horizontal direction. According to them, the discrepancies existing in this case between theoretical models of growth and experimental measurements bring to light the need to determine the relative importance of the dynamic effects at high Jacob numbers, a condition that can in particular be achieved at low pressure according to Carey [13] (refer to Section 1.1.3.1).

According to various experimental studies [1,4,76,77,100,102,117,119,124–126], the main characteristics of nucleate pool boiling at low pressure in terms of bubble dynamics are:

- A reduced density of active nucleation sites;
- High bubble growth rates[1], which results in large bubble volumes at departure;
- Long waiting periods between successive bubbles (then low bubble departure frequencies).

By way of illustration, for water, Van Stralen *et al.* [119] reported departure diameters up to 15.39 cm at 2.04 kPa and waiting times of the order of 10 to 100 s for bubbles whose growths lasted less than 200 ms at pressures ranging from 2.0 to 4.0 kPa.

Additional phenomena were also often mentioned:

- As illustrated on Fig. 1.7, a high-velocity liquid jet immediately following the departure of a large bubble can penetrate into its flattened base [44,81,87,100,119,122].

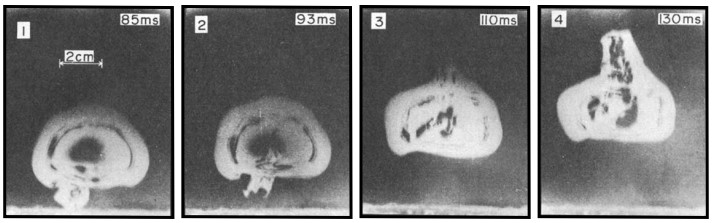

Figure 1.7 – High-velocity liquid jet penetrating into a large departed bubble (water boiling from an artificial nucleation site made on a smooth copper surface at 13.21 kPa; adapted from [119]).

- An "elongated vapor filament" [90] (Fig. 1.8a), or a "secondary vapor column" [44,100,119,122] (Fig. 1.8b) may grow between a departing bubble and the next bubble nucleating from the same site[2]. Depending on the boiling environment conditions (in particular depending on the heat flux and the subcooling degree), this secondary elongated vapor mass may reach the departed bubble prior recondensing or not. In case of contact between the departed bubble and the secondary vapor mass, the latter confers the bubble a so-called "mushroom shape" which is typical of the low pressure boiling.

[1] Bubble growth rates are so high that some authors dealt with "violent ebullition" [1] or "explosive bubbles" [125,126].

[2] This secondary vapor column may actually grow between the occurrence of the liquid jet and the nucleation of the next bubble.

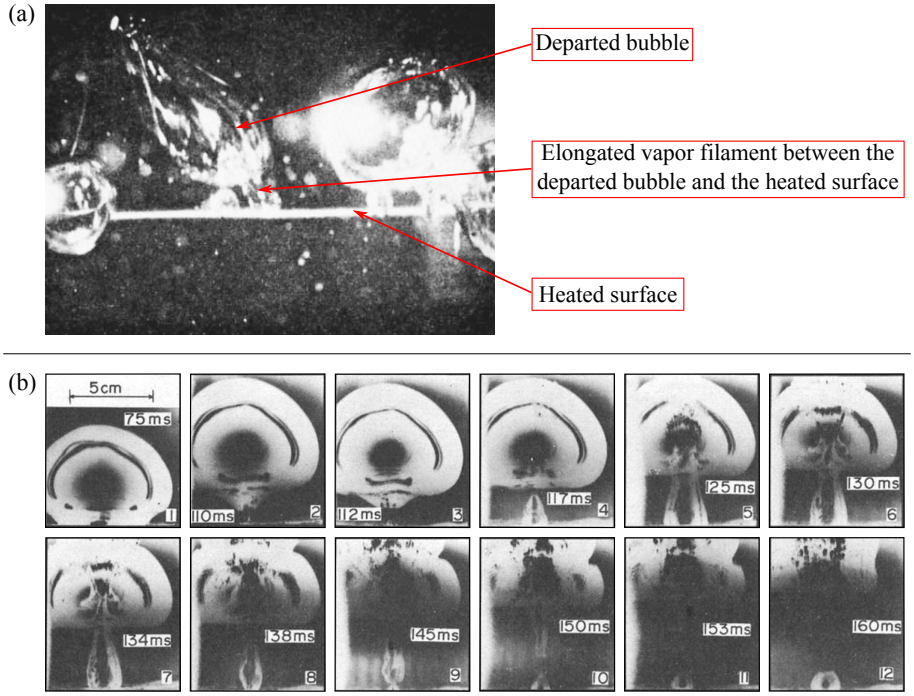

Figure 1.8 – (a) Elongated vapor filament connecting the heated surface and the departed bubble (water boiling from a nickel-chrome wire at 6.45 kPa; adapted from [90]); (b) High-velocity liquid jet followed by a vapor column (water boiling from an artificial nucleation site made on a smooth copper surface at 7.88 kPa; adapted from [119]).

Moreover, according to Labuntsov *et al.* [69] and Wu *et al.* [123], pool boiling at low pressure is known to be of an irregular and unsteady nature, especially in the very low pressure and heat flux ranges. Recently, Giraud *et al.* [46] confirmed this observation by demonstrating experimentally the existence of a new regime for boiling of water at subatmospheric pressure. From the bubble dynamics point of view, this so-called "cyclic boiling regime" is defined by the three following stages:

(A) **Waiting time:** as previously, the heat is transferred only by single phase convection (no bubble growth takes place) and the thermal boundary layer is growing by transient conduction in the vicinity of the heated wall.

(B) **Growth and departure of a large bubble:** as in nucleate boiling, a nucleation site is activated so that a bubble grows. Due to the low pressure condition, it reaches a large volume before detaching.

(C) **Bubble crisis:** many bubbles of different sizes and frequencies are created everywhere on the heated surface. The cycle can restart as soon as this nucleation crisis stops.

Pictures of this new regime in the case of water boiling at 1.2 kPa with an imposed heat flux of 12.2 $W \cdot cm^{-2}$ are shown on Fig. 1.9.

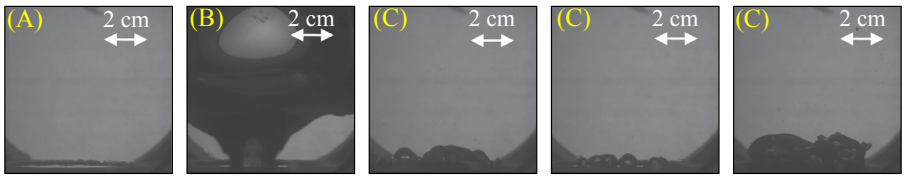

Figure 1.9 – Pictures obtained during (A) the waiting time, (B) the growth and departure of a large bubble and (C) the bubble crisis (water boiling from an artificial nucleation site made on a smooth copper surface at 1.2 kPa; adapted from [46]).

However, as emphasized by Giraud *et al.* [46], the conditions under which this cyclic boiling regime appears as well as the fundamental phenomena responsible for this behavior have still to be identified.

1.2.2 Heat transfer characteristics

Heat transfer in low pressure pool boiling is generally [1,76–78,100,102,117,119,125,126,129,131] characterized by – in comparison with more usual boiling conditions:

- A higher minimum wall superheat for a bubble nucleation from a given cavity;
- Large wall temperature fluctuations with time in the "intermittent boiling regime"[1];
- A lowered heat transfer coefficient;
- A lowered critical heat flux value.

These heat transfer characteristics can interact with each other and/or be related to the ones associated with the bubble dynamics. During the intermittent boiling regime, Van Stralen *et al.* [119] and Giraud [44] thus synchronized the heated surface temperature fluctuations to the bubble visualization and noticed that the wall temperature drops suddenly during the bubble growth whereas it increases slowly during the waiting time. As for the long duration of this waiting period, it can be explained by two phenomena, both connected to the low vapor density at low pressure[2]:

(i) **The large bubble size:** Just after a bubble detachment, cold liquid comes to re-wet the heated wall; the larger the departed bubble, the larger the involved amount of cold liquid and consequently the longer the time required to sufficiently heat it before a new bubble growth can be initiated.

(ii) **The high minimal wall superheat required to onset the nucleation at a given cavity:** A bubble growth is supposed to occur as soon as the liquid close to the wall reaches a critical superheat. A theoretical analysis can show that the lower vapor density, the larger the minimal superheat. This quantity can be indeed estimated according to the Clausius-Clapeyron equation (Eq. 1.8):

$$\Delta T \approx \frac{\Delta P T_{sat}}{\rho_v \Delta h_{lv}} \tag{1.8}$$

where the pressure difference ΔP can be evaluated through the relation for the mechanical equilibrium of a bubble (Eq. 1.1) with the bubble radius taken equal – in first approximation – to the considered cavity radius.

Most of the authors invoke the reduced density of active nucleation sites (supposed to be related to an increase of the bubble critical radius R^{crit} as the pressure is decreased) to explain the degraded heat transfer encountered at low pressure. As less cavities are active – and as a long waiting time is required for the few ones which are active, phase change is indeed not as significant in nucleate boiling at low pressure as under more conventional pressure levels. Usual correlations for heat transfer coefficient in nucleate boiling are consequently shown to be not valid for this particular condition [131]. Based on this observation, numerous studies [2–4, 17, 21, 76, 77, 88, 102, 128, 129] were performed on various enhanced surfaces in order to increase the active nucleation sites density and subsequently improve the heat transfer. Some of them also aimed at investigating the effect of the heated surface orientation (horizontal or vertical), of the confinement or of a system-like configuration within a more applied approach [18, 45, 48, 49, 79, 100].

Regarding the cyclic boiling regime, Giraud *et al.* [46] observed that, in water, it never occurs:

[1] McGillis *et al.* [77] defined this regime as a part of the isolated bubble regime such as the waiting time last longer than the bubble growth. The authors then determined a criteria to predict the transition to the "continuous boiling regime" (the regime in which the waiting time is equal or lower than the growth duration, *i.e.* the regime corresponding to both the end of the isolated bubble and the fully developed nucleate boiling regimes). They finally observed experimentally that continuous boiling can be reached as soon as a sufficiently high heat flux is imposed to maintain a large enough bubble frequency. Steady wall temperatures can then be obtained.

[2] In the case of water, the vapor density drops for instance from $\rho_v = 0.5982$ kg $\cdot$ m^{-3} at atmospheric pressure (101.4 kPa (100 °C)) to $\rho_v = 0.0656$ kg $\cdot$ m^{-3} at 9.6 kPa (45 °C), which corresponds to a variation of -89.0 %.

- At atmospheric pressure;
- At very low imposed heat flux values: this indeed leads to single phase convection;
- At sufficiently high imposed heat fluxes: this yields the continuous boiling regime.

When this regime takes place (*i.e.* in water at subatmospheric pressure for an intermediate range of imposed heat fluxes), the authors noticed the presence of similar wall temperature fluctuations as in the intermittent boiling regime (Fig. 1.10a). They conducted a parametric analysis and concluded that an increase of the imposed heat flux has no significant influence on the amplitude of the thermal variations. On the contrary, increasing the heat flux considerably affects the duration of the cycle (especially of the bubble crisis phase (C)[1]), so that the time-averaged wall temperature on the cycle time is lowered.

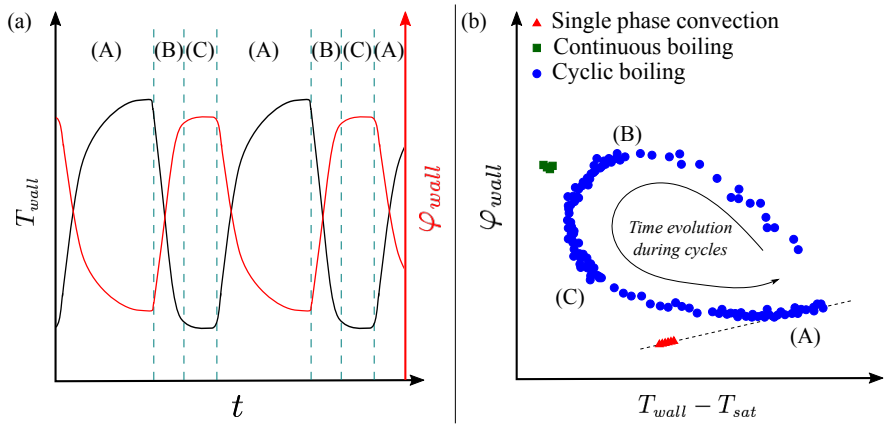

Figure 1.10 – Schematic representation of (a) the thermal fluctuations at the wall; (b) the instantaneous boiling curves during the cyclic boiling regime (and comparison with single phase convection and continuous boiling regimes; based on [46]).

Representing their experimental measurements by means of instantaneous boiling curves (illustrated on Fig. 1.10b), Giraud *et al.* [46] were able to compare visually the cyclic boiling regime with the single phase convection and continuous boiling regimes. Contrary to those two usual regimes characterized by a relatively high stability (inducing almost no scattering of the data points), measurements related to this new boiling regime display a specific cyclic scattering[2]. It appears from their parametric study that the lower the pressure, the more strongly this cyclic scattering is marked: the wall temperature fluctuations are indeed larger, and subsequently, the cycles visible on the boiling curves are of increased amplitude.

According to Giraud [44], the heater characteristics (material, geometry, size and surface finish) should also influence this cyclic regime through an effect on the amplitude and period of the thermal fluctuations. The author mentioned thus that a heater with a high thermal inertia would induce larger variations than a heater with a lower thermal inertia.

1.2.3 Remarks on the boiling environment

As first mentioned by Ponter and Haigh in 1969 [94, 95], as confirmed by Schnabel *et al.* [102] in 2008 and as again highlighted by Giraud *et al.* [45–47] in the 2010's, the height of liquid H_l over the heated surface is a parameter of major importance for the heat transfer performance in low pressure pool boiling.

[1] According to the authors, the waiting period (A) can last more than 100 s while the large bubble growth (B) is always shorter than 200 ms; at low heat fluxes, the waiting time can be more than 40 times longer than the bubble crisis (C) whereas the latter phase can – on the contrary – be longer than the waiting time at high heat fluxes.

[2] In her thesis, Giraud [44] added that the shape of the boiling curves observed in cyclic boiling tends to confirm that there may exist some analogy between cyclic boiling and transient boiling.

Giraud [44] and Giraud *et al.* [46] demonstrated indeed that – as the pressure imposed at the level of the free surface is low – the static head induced by the liquid column can be of the same order of magnitude as the system pressure, so that the static pressure cannot be neglected in the analysis as it is of common practice for higher pressures. The local pressure $P(z)$ is consequently equal to the sum of the saturation pressure P_v prevailing at the level of the free surface and of the local static head $P^{static}(z)$. It thus varies (quasi-)linearly with the local depth z in the bulk (with $z = 0$ corresponding to the free surface level). The local saturation temperature $T_{sat}(z)$ also depends on the depth, but this variation is especially significant in the very low pressure region because of the logarithmic relationship existing between the saturation temperature T_{sat} and the saturation pressure P_{sat}. Considering that the saturation state prevails at the level of the free surface ($T_v = T_{sat}(P_v) = T_{sat}(z = 0)$) and assuming that the bulk liquid is homogeneous in temperature ($T_{l,\,bulk}(z) = T_{l,\,bulk}$), one can suppose the vapor and bulk temperatures to be equal ($T_v = T_{l,\,bulk}$). The local subcooling degree $\Delta T_{sub}(z)$, defined as:

$$\Delta T_{sub}(z) = T_{sat}(z) - T_{l,\,bulk} \tag{1.9}$$

is consequently dependent on the depth too. The pressure and the subcooling degree finally cannot be considered as homogeneous around a bubble formed under low pressure conditions, which results in non-homogeneous thermophysical properties in the boiling environment.

Table 1.2 – Influence of the pressure imposed at the free surface level and of the liquid height on both the local pressure and subcooling degree in water (liquid density evaluated from REFPROP [71] database).

P_v (kPa)	T_v (°C)	H_l (cm)	$P^{static}(H_l)$ (kPa)	$P(H_l)$ (kPa)	$T_{sat}(H_l)$ (°C)	$\Delta T_{sub}(H_l)$ (K)
1.2	10	10	1.0	2.2	19.1	9.1
		20	2.0	3.2	25.1	15.1
		30	2.9	4.2	29.7	19.7
12.4	50	10	1.0	13.3	51.5	1.5
		20	1.9	14.3	53.0	2.0
		30	2.9	15.3	54.3	4.3
101.4	100	10	0.9	102.4	100.3	0.3
		20	1.9	103.3	100.5	0.5
		30	2.8	104.2	100.8	0.8

Some values illustrating the dependence of the local pressure and subcooling degree on both the liquid level H_l and the imposed pressure P_v are given in Table 1.2. From those data one can remark that the local pressure can be set by acting on the vapor saturation pressure and/or on the liquid height. However, each action yields different effects:

(i) If the vapor pressure P_v is kept constant while the liquid level H_l is increased, the local pressure as well as the subcooling degree augments.

(ii) On the contrary, if the vapor pressure P_v is increased while the liquid level H_l is kept constant, the subcooling degree decreases.

Investigating the influence of an increase of the water height on the heat transfer – at constant imposed pressure P_v, so that the local pressure at the level of the heated wall is increased – Giraud *et al.* [45] observed:

- An improvement of the heat transfer coefficient in horizontal orientation;
- A degradation of the performance in vertical orientation.

Giraud *et al.* [47] also investigated the effect of a thin layer of water on low pressure pool boiling. Two new bubble dynamics behaviors were then observed depending on the occurrence or not of a bubble bursting at the vapor-liquid-vapor interface as the growing bubble passes through the free surface. Moreover, the cyclic boiling regime was found to be less and less apparent as the liquid layer was reduced. The authors explained this result by both a less subcooled liquid and an increased difficulty for the liquid to re-wet the heated surface.

The characteristic non-homogeneity of the boiling environment at low pressure as well as its complexity is supposed to be responsible for the specific features encountered in low pressure pool boiling. For instance, the local subcooling degree that can reach relatively high values may explain the early recondensation (before departure) and/or even the quick collapse (just after the detachment from the heated wall) of bubbles obtained at low pressure. The mushroom shape of these bubbles may be due to this subcooling degree as well since this particular shape is generally reported in subcooled boiling [110]. In addition, a modified relative influence of the forces acting on a growing bubble – compared to what is commonly accepted under more conventional conditions – seems to appear[1], leading to original bubble dynamics behaviors.

Another feature of the boiling environment at low pressure is related to the particular noise which is associated with this operating condition. According to the literature review section of the article published in 1969 by Ponter and Haigh [95], boiling is indeed often accompanied by audible sounds caused by the propagation of pressure waves within the boiling liquid during the formation, growth and all the more the collapse of the vapor bubbles. The collapse of a bubble thus engenders a local pressure variation that can be the source of such pressure waves. In addition, the condensation of a bubble provoking a void in the liquid, an inrush of liquid occurs to fill this void. Sound emission can then constitute a way to dissipate the related kinetic energy. The authors explained then that acoustic studies previously conducted on boiling demonstrated a connection between variations of the sound intensity and/or its frequency spectrum and changes in boiling regimes and/or heat transfer rates. For example, in water nucleate boiling at atmospheric pressure, a reduction of the sound intensity results from a decrease of the heat flux. Ponter and Haigh finally carried out an experimental campaign with water boiling at various subatmospheric pressures from the outer surface of a stainless steel tube immersed under 61.0 cm of liquid[2]. In their experiments, they applied a supposed uniform subcooling degree (up to 60 K) to the liquid and observed that:

- Whatever the pressure or the subcooling degree, the onset of boiling can be detected by an increase of the sound intensity.
- Low pressure nucleate boiling is mainly characterized by intermittent sounds of high intensity emitted at low heat fluxes.

1.2.4 A difficult analysis of the existing literature

Although the unconventional nature of the low pressure pool boiling – which has long limited the interest of investigating this topic, the number of experimental studies reported in the literature about this phenomenon becomes to be relatively important. As for an illustration, most of them are summarized Table 1.3 (horizontal orientation) and Table 1.4 (vertical orientation). As a consequence, one could expect that a comparative analysis of the existing literature would enable the identification of more specified fundamental phenomena and of their governing processes and parameters than those described previously in this section. However, reading Tables 1.3 and 1.4 tends to demonstrate that such a synthesis may be not possible. Operating conditions are indeed generally hardly comparable from one study to the other:

Various heated surfaces and configurations: Heated surfaces used in the literature result from various combinations of types (plain or finned surfaces, wires, outer side of tubes, foam...), materials (copper, stainless steel, nickel, platinum, aluminum...), surface finishes (various roughnesses, presence or not of artificial cavities, coatings or hydrophobic spots...) and sizes. As all those surface properties are known to have a non negligible influence on the bubble nucleation and on the boiling heat transfer performance (especially at low pressure [92] since the number of potential vapor generating centers is then limited), determining one or few dominant parameter(s) explaining any difference between the reported experimental results is almost impossible.

[1] The influence of the thermal Marangoni force is for example clearly not negligible anymore when boiling in the very low pressure region with a thin layer of liquid (refer to Giraud *et al.* [47]).

[2] This height corresponds in fact to 2 ft.

Moreover, when a similar heated surface is used in several studies, the boiling configuration may differ from one to the other, so that the comparison is made difficult as well. For instance, Rullière *et al.* [100] and Giraud *et al.* [45–48] used similar surfaces to investigate the effect of the horizontal and vertical orientations as well as of the confinement.

Table 1.3 – Low pressure pool boiling experimental studies in horizontal orientation.

Study	**Fluid**	**Heated surface**	P_v **(kPa)**	H_l **(cm)**
Van Stralen [117]	Water, aqueous binary mixtures	Platinum wire	13.3 – 101.4	Unknown
Patten [90]	Water	Nickel-chromium wire	3.4 – 101.4	Unknown
Cole and Shulman [27] and Cole [26]	Water, n-pentane, methanol, carbon tetrachloride, acetone	Polished zirconium ribbon	6.7 – 101.4	Unknown
Ponter and Haigh [94, 95]	Water	Outer surface of a stainless steel tube	12.0 – 101.4	61.0
Akiyama *et al.* [1]	Water, ethanol, carbon tetrachloride	Outer surface of a stainless steel tube	5.0 – 1520.0	Unknown
Yagov *et al.* [125, 126]	Water, ethanol, NaCl aqueous solution	Nickel disks (rough or smooth with artificial cavities or addition of hydrophobic spots or screens)	3.6 – 100.0	Unknown
Stewart and Cole [109]	Water	Mirror-polished copper disk	4.9	Unknown
Van Stralen *et al.* [119, 120, 122]	Water, aqueous binary mixtures	Smooth copper disk with a centered artificial cylindrical nucleation site	2.0 – 26.7	Unknown
Labuntsov *et al.* [69]	Water, ethanol	Smooth nickel disk and outer surface of copper, nickel and stainless steel tubes	1.6 – 100.0	Unknown
Wu *et al.* [123]	Water, methanol	Rectangular copper surfaces (uncoated, nickel coated or with sintered copper screens)	6.0 – 100.0	Unknown
Tewari *et al.* [111]	Water with and without polymeric additive	Smooth and rough aluminum disks	8.0 – 100.0	Unknown
McGillis *et al.* [76]	Water	Rectangular smooth and rectangular finned copper surfaces	4.0; 9.0	Unknown
McGillis *et al.* [77]	Water	Rectangular and circular smooth copper surfaces	2.0 – 110.0	Unknown
McGillis *et al.* [78]	Water/methanol and water/2-propanol mixtures	Rectangular smooth copper surfaces	7.0 – 83.0	Unknown
Mitrovic [81]	R113	Smooth stainless steel disk with artificial cavities	37.0	Unknown
Ohue *et al.* [87]	Water	Smooth stainless steel disk	2.7	Unknown
Yagov [124]	Water, ethanol	Smooth nickel disk and outer surface of copper, nickel and stainless steel tubes	1.0 – 40.0	Unknown
Bhaumik *et al.* [8]	Water, benzene, toluene	Outer surface of stainless steel tube	20.0 – 97.4	Unknown
Pal and Joshi [88]	Water	Copper enhanced structures made of multiple layers	9.7 – 21.0	3.9
Choon *et al.* [21]	Water	Rectangular copper foam	1.8	Unknown
Schnabel *et al.* [102]	Water	Copper disks of different roughnesses or with fins	1.0; 2.0	1.0 – 2.2
Alam *et al.* [2, 3]	Water, methanol and water/methanol mixtures	Outer surface of plain and copper coated stainless steel tubes	23.0 – 97.7	Unknown
Chan *et al.* [17]	Water	Plain and finned copper disks	2.0 – 9.0	6.0
Rullière *et al.* [100]	Water	Smooth or rough copper disks with a centered artificial conical nucleation site, with or without confinement	0.9 – 4.8	12.0
Giraud *et al.* [45]	Water	Smooth copper disk with a centered artificial conical nucleation site	1.2 – 1.8	7.4 – 20.0
McNeil *et al.* [79]	Water	Tube bundle	5.0 – 85.0	80.0; 200.0
Giraud *et al.* [47]	Water	Smooth copper disk with a centered artificial conical nucleation site	1.2 – 3.0	0.3 – 20.0
Giraud *et al.* [46]	Water	Smooth copper disk with a centered artificial conical nucleation site	0.8 – 100.0	20.0
Arya *et al.* [4]	Water	Plain or nano-porous alumina structured aluminum micro wires	7.3 – 19.9	2.0 – 2.5
Zajaczkowski *et al.* [131]	Water	Copper disk	1.0 – 10.0	Unknown
Yamada *et al.* [128, 129]	Water	Copper disks with hydrophobic spots	6.8 – 101.4	12.0

Table 1.4 – Low pressure pool boiling experimental studies in vertical orientation.

Study	Fluid	Heated surface	P_v (kPa)	H_l (cm)
Giraud *et al.* [45]	Water	Smooth copper disk with a centered artificial conical nucleation site	1.2 – 1.8	7.4 – 20.0
Giraud *et al.* [48]	Water	Smooth copper disk with a centered artificial conical nucleation site, with confinement	1.2 – 5.0	15.0
Giraud *et al.* [49]	Water	Stainless steel plate, with confinement	0.8 – 16.0	5.0 – 25.0

A liquid height scarcely taken into account: As visible in Tables 1.3 and 1.4, except in the Ponter and Haigh works published in 1969 [94, 95] and in most of the investigations performed in the last ten years [4, 17, 45–49, 79, 88, 100, 102, 128, 129], the liquid height is never mentioned by the authors. The importance of this parameter on low pressure pool boiling was indeed demonstrated only recently. As the low pressure boiling environment is complex and can be totally modified by changing the value of this parameter (while keeping the same working fluid, heated surface, vapor pressure and heat flux values), the absence of this information prevents any subtle comparison or analysis of all the results available in the literature.

Different investigated fluids: Most of the reported experiments were performed with water as the working fluid. However, in order to observe the influence of the fluid thermophysical properties on low pressure pool boiling and/or within a preliminary study for a specific application (such as desalination), some other fluids – including mixtures – were tested. In these cases – as in tests conducted with pure water – only subatmospheric pressures were considered, *i.e.*, for all the authors, "low pressure" in boiling means boiling under a pressure lower than the atmospheric pressure. This simple approach, that may be valuable for a given fluid, may be not justified for another since the variations of the numerous fluid thermophysical properties involved in phase change heat transfer are then not taken into account at all along the liquid-vapor saturation curve that is specific to each individual fluid.

In the case of mixtures, the already complex boiling environment is made even more complex due to concentration gradients. A solutal Marangoni effect could consequently take place in addition to the thermocapillary effect, so that the bubble dynamics and then the heat transfer would differ even more from what is usually encountered under normal pressure conditions.

All the points discussed just above finally tend to show that defining properly what is "low pressure" in boiling and using well-defined operating conditions are necessary conditions to get a better understanding of the phenomenon and to identify its fundamental subprocesses and governing parameters.

In this chapter, the fundamental concepts regarding pool boiling were briefly introduced as a necessary background of the results produced in this thesis.

The low pressure pool boiling was then reviewed more accurately. The main features of this unconventional boiling condition that are already reported in the literature were presented:

- *A complex boiling environment;*
- *A bubble dynamics characterized by:*
  - *A long waiting time between two successive bubbles;*
  - *A very large bubble volume at departure;*
  - *The occurrence of mushroom shaped bubbles.*

- *Degraded heat transfer performances with:*
  - *Wall temperature fluctuations;*
  - *Low heat transfer coefficients that cannot be evaluated through the usual boiling correlations.*

An analysis of the existing literature finally revealed that a better understanding of the fundamental phenomena involved in low pressure pool boiling and the identification of their governing parameters require:

- *A precise definition of what "low pressure" means in pool boiling;*
- *New experimental results obtained with "well-defined" operating conditions.*

Chapter 2

Experimental setup and methods

The purpose of this chapter is to provide sufficient information about the test facility and the methods used to study experimentally the pool boiling phenomenon at low pressure. The boiling vessel and the test sample are therefore detailed in Section 2.1, the adapted procedure of use in Section 2.2 and the measurement and processing techniques which are implemented to obtain original and reliable results about low pressure boiling in Section 2.3.

2.1 Experimental setup

The test bench designed by Giraud during her thesis [44] constitutes the starting point of this work.

2.1.1 Overall view

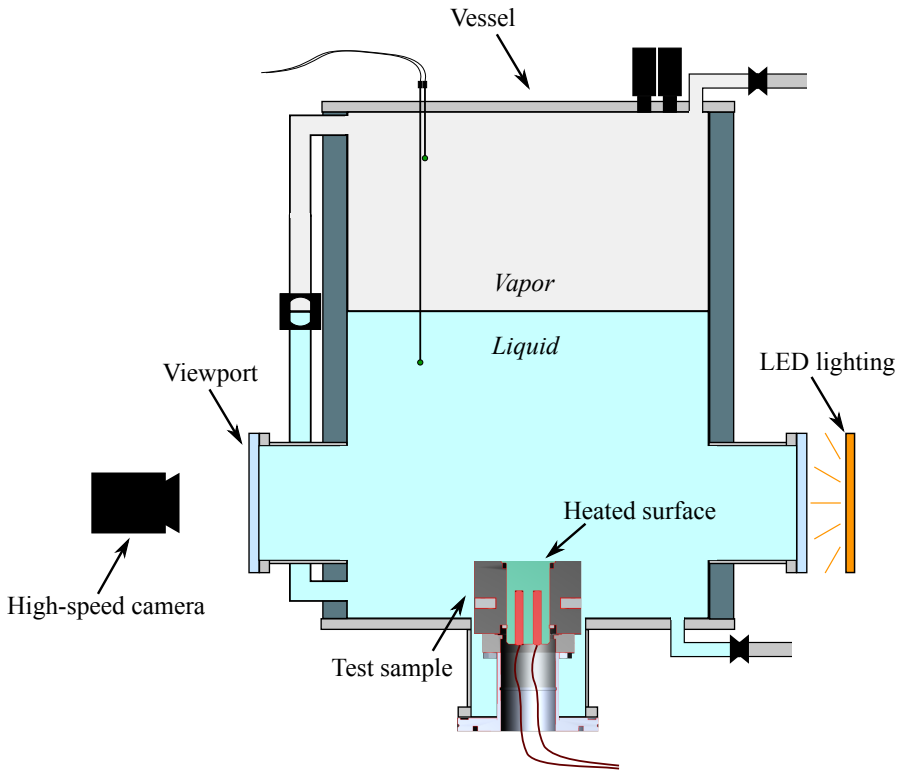

Figure 2.1 – Experimental apparatus.

The experimental facility, schematically depicted on Fig. 2.1, is mainly composed of a cylindrical vessel in which the working fluid is filled and set to the desired temperature and pressure

conditions to conduct tests. A test sample inserted at the base of the pool enables to impose an adapted heat flux to create bubble nucleation on its top surface. Four circular viewports located on the side surface of the vessel make the observation of the boiling phenomenon possible. In particular, one is used to illuminate the boiling area while a high-speed camera is placed in front of the opposite one for image recording.

2.1.2 Boiling pool

The experimental pool (Fig. 2.2) is a cylindrical stainless steel tank of 200 mm inner diameter and of 420 mm height. A 100 mm diameter borehole located at the vessel's base is used to insert the test sample (described in Section 2.1.3) into the chamber with a sufficient tightness. The copper heated surface is then horizontally centered inside the tank. Four circular viewports of the same size (100 mm diameter) are arranged on the side surface of the pool for observation, high-speed visualization and lighting of the boiling phenomenon.

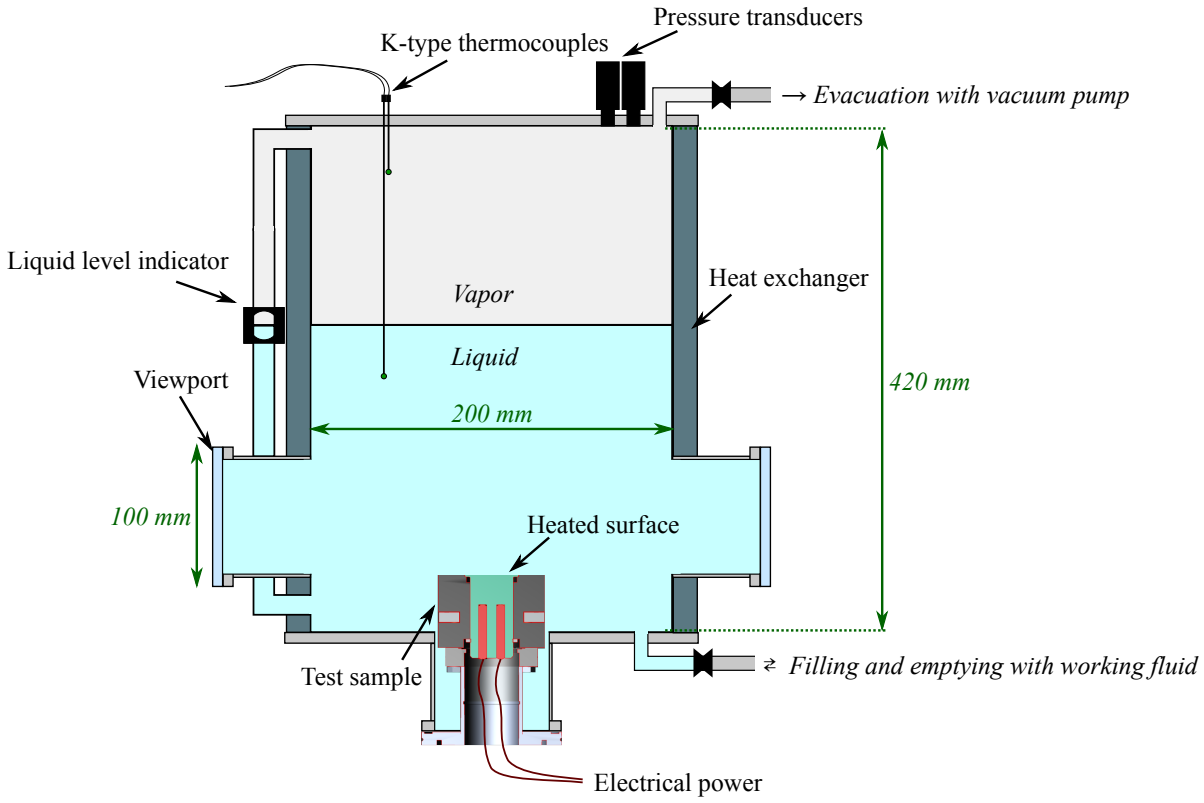

Figure 2.2 – Boiling pool.

The working fluid is filled and emptied through a valve situated at the bottom of the tank. A flexible hose connected both to the top and to the bottom of the vessel is used as a liquid level indicator. Depending on chemical resistance to the working fluid, this hose is either a flexible transparent hose made of PVC either a flexible hose made of stainless steel equipped with a small viewport. Another valve, at the top of the vessel, can be linked to a vacuum pump to evacuate gas from the chamber.

A heat exchanger, jacketed inside the pool wall and connected to a thermostatic bath, is used to set the temperature and the pressure in the chamber during the tests (which are measured with thermocouples and pressure transducers).

The whole facility is made in vacuum technology (ISO-K) to ensure a high level of tightness.

2.1.3 Test sample

2.1.3.1 Geometry of the heater

The main component of the test sample (Fig. 2.3a) is a cylindrical copper block (diameter: 40 mm, height: 78 mm) ended with a thin fin (diameter: 50 mm, thickness: 1.2 mm). Two cartridge heaters of 400 W (maximum power) each are inserted at the bottom of the copper part to impose the heat flux to the block. Two rows of four K-type thermocouples are placed along the copper cylinder to evaluate the thermal heat flux passing through it and the wall temperature.

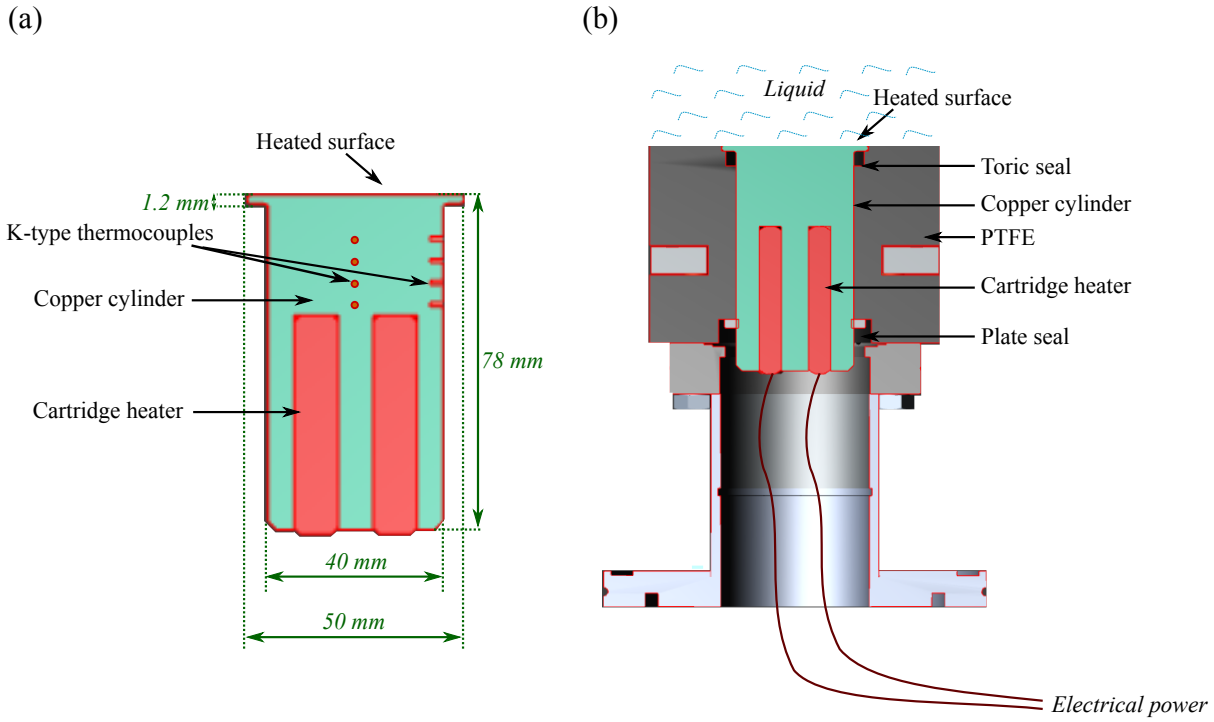

Figure 2.3 – Detail of the heater: (a) the copper block; (b) the whole test sample.

The copper block is thermally insulated with a PTFE part and the copper/PTFE block is associated with a stainless steel flange to make the connection with the vessel possible (Fig. 2.3b). The tightness of the test heater is ensured by an O-ring seal between the copper fin and the PTFE part and by a flat seal between the copper/PTFE block and the flange.

2.1.3.2 Heated surface

The heated surface corresponds to the top of the heater's fin. Its area is consequently of 19.6 cm^2. This fin is aimed at avoiding peripheral boiling and then at promoting bubble nucleation from an artificial cavity made at the center of the surface. The surface was indeed carefully prepared as follows: it was entirely mirror-polished with diamond paste and then a conical nucleation site was created with a punch at its center (Fig. 2.4). The surface's root mean square roughness S_q (lower than 0.4 µm) and the size of the cavity (110 µm diameter and 70 µm deep) were measured with a confocal microscope (refer to Appendix A.1). The outer edge of the heated surface is sealed to the PTFE insulant with glue to prevent any air leakage into the vessel.

2.1.4 Instrumentation and acquisition system

2.1.4.1 Boiling environment and thermal measurements

Operating conditions are controlled by measuring the pressure and the temperature inside the chamber. Two K-type thermocouples are indeed located in the fluid: one above the free surface (*i.e.* in the vapor phase) whereas the other one is placed at a distance of 100 mm from the

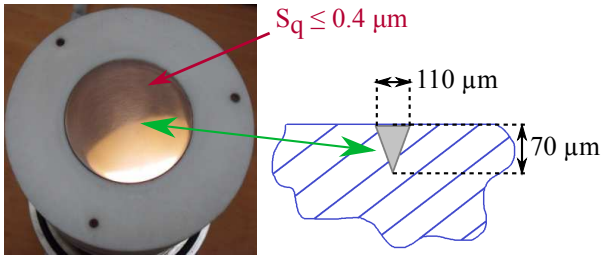

Figure 2.4 – Heated surface condition.

heated surface (*i.e.* in the liquid phase). At the top of the vessel, two pressure transducers Kobold type SEN are used to measure the vapor pressure P_v. Their working pressure ranges are 0 – 100 kPa and 0 – 16 kPa respectively and they are accurate to ± 0.25 % of their full scale range (*i.e.* ± 250 Pa and ± 40 Pa respectively).

Two rows of four K-type thermocouples are located along the copper part of the heater with an angle of 90° between them. Vertical positions of the bottom of the fin and of thermocouples are defined by the distance to the heated surface ($Z = 0$ at the top of the fin) along a vertical upward-oriented axis as shown on Fig. 2.5a. The fin thickness (Fig. 2.5b) and locations of thermocouples for *Row A* (Fig. 2.5c) and *Row B* (Fig. 2.5d) – given in Table 2.1 – were accurately determined by measuring variations of altitude along the rod with the confocal microscope.

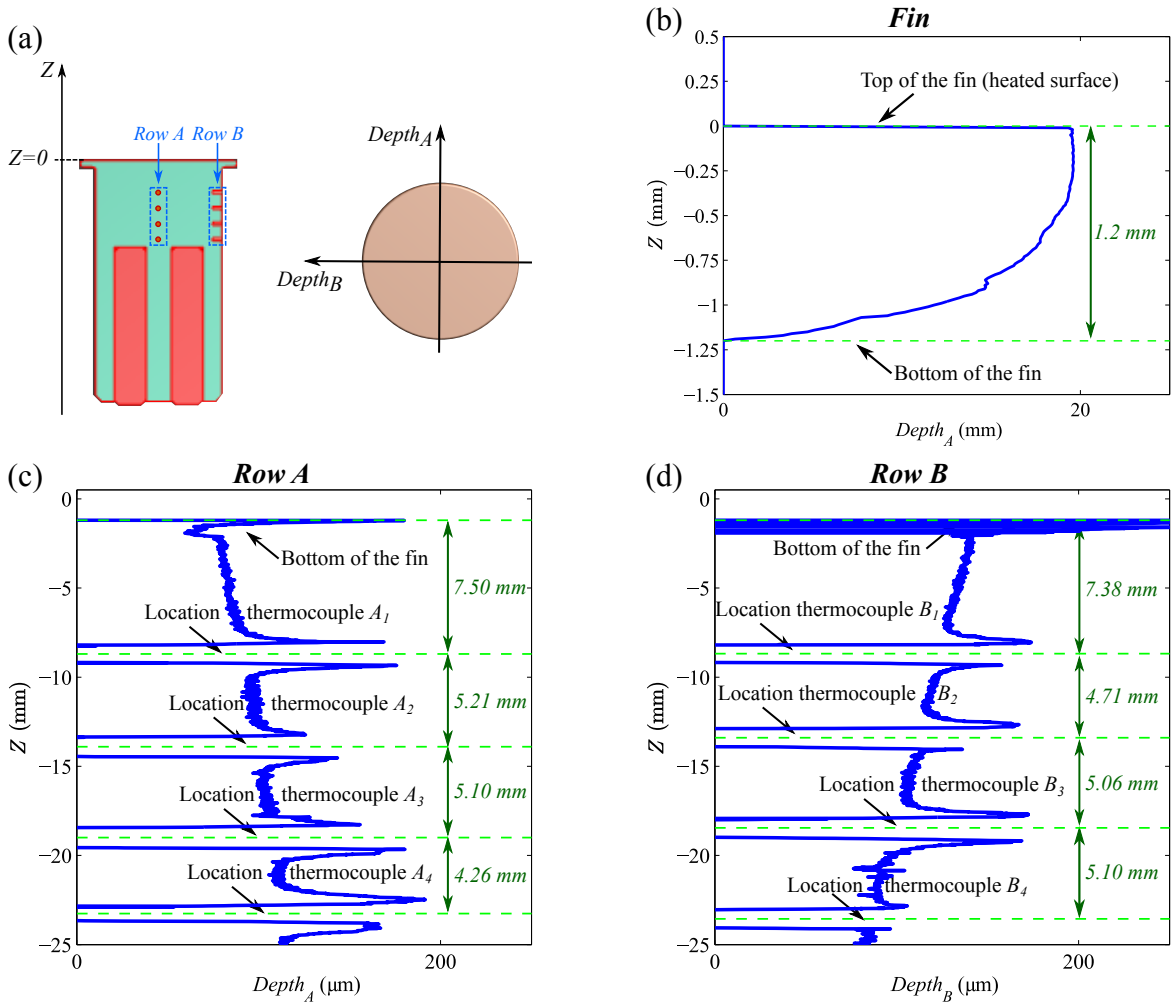

Figure 2.5 – Measurements made with the confocal microscope: (a) geometry of reference; (b) fin thickness; (c) positions of *Row A* thermocouples and (d) positions of *Row B* thermocouples.

Table 2.1 – Positions of thermocouples in the copper block for the two rows.

Row A		***Row B***	
$Z_{heated\ surface}$ (mm)	0.000	$Z_{heated\ surface}$ (mm)	0.000
$Z_{bottom\ of\ the\ fin}$ (mm)	−1.200	$Z_{bottom\ of\ the\ fin}$ (mm)	−1.200
Z_{A_1} (mm)	−8.700	Z_{B_1} (mm)	−8.575
Z_{A_2} (mm)	−13.905	Z_{B_2} (mm)	−13.285
Z_{A_3} (mm)	−19.000	Z_{B_3} (mm)	−18.345
Z_{A_4} (mm)	−23.260	Z_{B_4} (mm)	−23.445

All the cold junctions of the ten thermocouples (two in the fluid and eight in the sample) are embedded in a well-insulated compensation box in which the temperature is measured with a platinum resistance temperature detector Pt100. Measurements are then performed by a KEITHLEY 2701 acquisition unit controlled by a home-made LabVIEW program. Thermocouples were calibrated with their whole acquisition line before any experiment. They were then immersed in a thermostatic bath with a reference temperature probe (another platinum resistance thermometer Pt100) and their voltages were measured for several temperature steps between 0 °C and 100 °C to obtain their calibration curves. The uncertainty on the temperature measurements was thus estimated to ± 0.10 K.

The signals from the pressure transducers are also acquired through the KEITHLEY multimeter and the LabVIEW program. At the end of a test, all the measurements are saved in a spreadsheet file for a subsequent analysis.

As highlighted in Section 1.2.3, the liquid height H_l over the heated surface is a parameter of importance in low pressure pool boiling. This height has therefore to be estimated. This is done with an uncertainty of only ± 0.1 cm by means of a cathetometer. The vertical position H_1 of the liquid level as well as the position H_2 of the heated surface are read as illustrated on Fig. 2.6a and Fig. 2.6b respectively. The liquid height H_l is then defined as:

$$H_l = H_1 - H_2 \tag{2.1}$$

2.1.4.2 Visualization

The sample being located in the vessel, the heated surface is clearly visible through the viewports and, as a consequence, the boiling phenomenon is easy to observe. A high-speed camera (Photron Fastcam 1024 PCI, standard memory size – 2 GB) is then placed close to a viewport while a square white LED backlight device (Phlox SLLUB white led Backlight 100 × 100) illuminates the imaging area through the opposite viewport. The LED device produces a very intense and homogeneous light (luminance: 53000 $\mathrm{cd \cdot m^{-2}}$, uniformity: 98.77 %) which leads to an excellent contrast on the recorded pictures.

The high-speed camera is controlled by the Photron Fastcam Viewer (PFV) software and the following settings are chosen to record videos: the maximum image size, *i.e.* 1024 × 1024 pixels, and the highest acquisition frequency allowed with that image size, *i.e.* 1000 frames per second. Those parameters lead to the best trade-off between acquisition speed (or time resolution) and image size (or spatial resolution). However, the duration of a video file obtained with those settings is short (about 1.54 s). When necessary, experiments are carried out at a lower acquisition frequency in order to adapt the recording time to the duration of the phenomenon. As the bubble frequency can be low at low pressure (refer to Section 1.2.1), the trigger mode "END" is set for pictures acquisition: the instant when the experimenter clicks to trigger the camera (after having seen a bubble nucleating) corresponds then to the last recorded image.

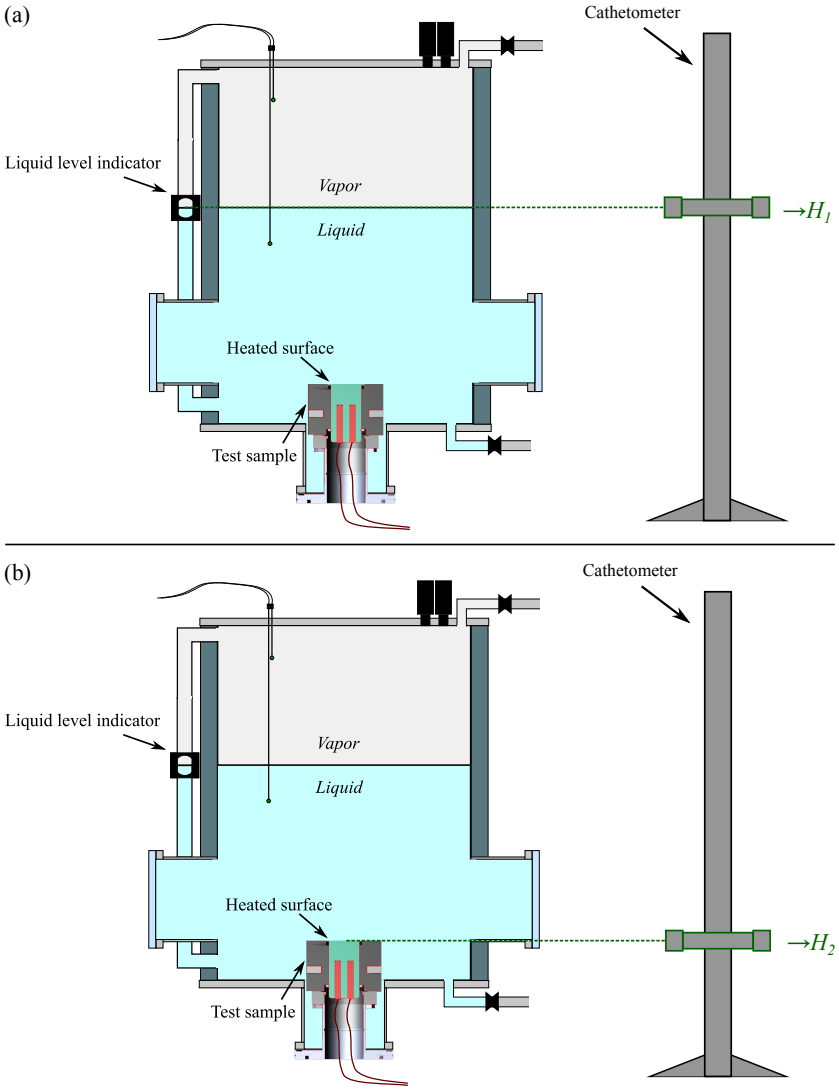

Figure 2.6 – Liquid height H_l measurement: reading of (a) the liquid level height H_1; (b) the heated surface height H_2.

2.2 Experimental procedure

2.2.1 Filling and degassing the working fluid

Once the sample assembled, it is installed into the vessel and the tank is filled with as pure as possible working fluid. The chamber is then connected to a vacuum pump to be emptied with air and non condensable gas. The fluid can thus be set to its saturation state. The pool is maintained at the vapor saturation pressure for at least two full days with periodic evacuations before starting any experiment. This step is required to ensure that the fluid is sufficiently degassed and with an appropriate liquid-vapor equilibrium which is controlled by checking if the vapor temperature T_v measured in the vapor phase corresponds to the saturation temperature of the measured vapor pressure $T_{sat}(P_v)$. After that degassing process, the liquid height H_l is measured according to the method described in Section 2.1.4 and experiments can be performed.

2.2.2 Setting the operating conditions

The desired vapor pressure is then set in the boiling pool by adjusting the temperature of the fluid that circulates in the vessel's jacket. As nucleation sites activation and deactivation as well as boiling regime transitions often induce hysteresis phenomena in boiling, it was decided to conduct experiments only by decreasing the imposed heat flux. From a practical point of

view, the electrical power imposed to the cartridge heaters is first progressively increased up to reach the highest heat flux to be tested. Then, in order to study the steady state condition, a one-hour waiting time is necessary before recording data. After acquisition, the electrical input is decreased step by step to repeat the experiment with lower imposed heat fluxes until reaching the lowest heat flux value of interest. During the whole process, the operating conditions (fluid temperature and pressure) are monitored with the LabVIEW acquisition software.

2.2.3 Acquiring measurements and images

Each test corresponds to the study of the steady state of one operating point in terms of working fluid, liquid height H_l, vapor pressure P_v and imposed heat flux φ_{input}. For each experiment, all the signals associated with the pressure transducers and with the thermocouples are collected every three seconds during the full duration of the test (*i.e.* about ten minutes). Meanwhile, several videos are recorded with the high-speed camera in order to be able to analyze the bubble dynamics.

2.3 Measurement and processing techniques

2.3.1 Heat flux and heated wall temperature determination

At any instant when the signal of the thermocouples is acquired, the heat flux φ_{meas} released to the fluid through the heated surface as well as the wall temperature T_{wall}^{exp} are estimated using the eight thermocouples located in the copper block under the following assumptions:

- Steady state conditions: all the parameters are supposed to be independent from t;
- Axisymmetric system with uniform radial heat losses through the PTFE along the rod;
- Uniform heat flux across a section of the cylinder;
- Negligible effect of the fin;
- Constant thermal conductivity λ_{Cu} of copper within the investigated range of temperature.

With the previous hypotheses, the temperature profile along the Z-axis of the heater is described as follows:

$$T(Z) = aZ^2 + bZ + c \tag{2.2}$$

where the coefficients a, b, and c can be determined by a second order polynomial datafit of the thermal measurements of a row of thermocouples. The heated surface temperature T_{wall}^{exp} and the heat flux at the surface φ_{meas} can then be deduced from it. In this case, the wall temperature is indeed given by:

$$T_{wall}^{exp} = T(Z = 0) = c \tag{2.3}$$

and with the Fourier's law applied at the heated surface level:

$$\varphi_{meas} = \varphi(Z = 0) = -\lambda_{Cu} \frac{\mathrm{d}T}{\mathrm{d}Z}\bigg|_{Z=0} \tag{2.4}$$

it is demonstrated that the identified coefficient b is directly proportional to the heat flux dissipated to the fluid by the wall:

$$\varphi_{meas} = -\lambda_{Cu}(2aZ + b)\Big|_{Z=0} = -b\lambda_{Cu} \tag{2.5}$$

Taking the second derivative of Eq. 2.2 in relation with the Fourier's law gives:

$$\frac{\mathrm{d}\varphi}{\mathrm{d}Z} = -2a\lambda_{Cu} \tag{2.6}$$

meaning that the rate of heat dissipation along the rod $\frac{d\varphi}{dZ}$ is proportional to the coefficient a.

The value of a being low, heat losses along the rod can be neglected. This is in agreement with the criterion cited by Héas [53] on the non dimensional characteristic time Δt_i of the conduction problem, defined as:

$$\Delta t_i = \frac{\alpha_{Cu} \Delta t}{d^2} \tag{2.7}$$

with α_{Cu} the copper thermal diffusivity, Δt the time step between two successive measurements and d the distance between two thermocouples. Héas' criterion stands that if Δt_i is higher than the unity ($\Delta t_i \geq 1$), a linear extrapolation of the thermal measurements is sufficient to estimate the wall temperature as well as the heat flux. As this criterion is satisfied in this work, the computation of those data is realized under that assumption. Satisfying this criterion also validates the stationary state condition hypothesis.

For each row of four thermocouples, a linear fitting of the temperature depending on the depth Z is made. The wall temperature T_{wall}^{exp} is then obtained by extending the datafit to the point $Z = 0$ while the heat flux φ_{meas} is equal to the additive inverse of the slope of this fit multiplied by the copper thermal conductivity (Fig. 2.7). As the calculation of the heated surface temperature and of the heat flux is made for *Row A* and *Row B*, the retained values for T_{wall}^{exp} and φ_{meas} are finally the average of the results obtained from the two rows[1].

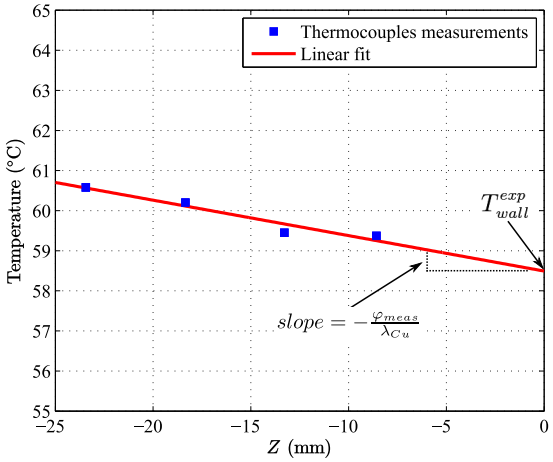

Figure 2.7 – Example of temperatures measured by a row of thermocouples of the test sample.

Concerning the uncertainties on the measured heat flux φ_{meas}, the logarithmic method applied on the Fourier's law gives:

$$\frac{\Delta \varphi_{meas}}{\varphi_{meas}} = \frac{\Delta \lambda_{Cu}}{\lambda_{Cu}} + \frac{\Delta (dT)}{dT} + \frac{\Delta (dZ)}{dZ} \tag{2.8}$$

where the error done on the copper thermal conductivity can be removed from the calculation since it has no effect on the temperature computation and is a systematic error which does not influence the differences in the observed trends on the heat flux (it results in an offset on the evaluation of this physical quantity). The uncertainties on the temperature and thermocouples positions measurements are estimated to ± 0.10 K and ± 0.4 mm respectively. Finally, the measured heat flux uncertainty is estimated to more than 50 % for low imposed heat fluxes and to 15 % for high imposed heat fluxes.

[1] For some tests, some thermocouples were found to be out of operation. In such case, only the values computed from the row with all working thermocouples were kept.

Alternatively, a Monte Carlo technique introduced by Kempers *et al.* [63] for the uncertainty estimation related to heated cylinders can be implemented. According to this method, each thermocouple measurement is assumed to be associated with both temperature and position uncertainty distributions:

- The temperature uncertainty is supposed to present a normal distribution centered on the measured value and such as the uncertainty on the temperature measurement (*i.e.* $\pm$ 0.10 K in the present case) is equal to twice the standard deviation.
- The uncertainty on the thermocouple's position is modeled by a flat distribution centered on the measured position and bounded by the difference between the radius of the hole in which the sensor is inserted and the radius of the thermocouple itself.

A set of values for the slope is then calculated by performing a large number (*e.g.* 2000) of randomized curve fits to fictive data constrained by the position and temperature uncertainty distributions at each point (as illustrated on Fig. 2.8 for the measurements displayed on Fig. 2.7). The uncertainty on the slope is then taken as twice the standard deviation of the obtained data set.

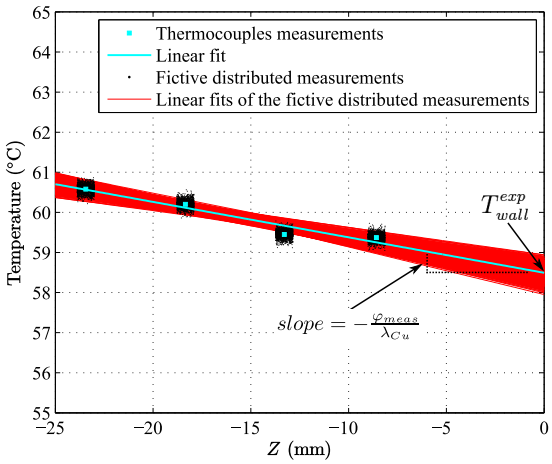

Figure 2.8 – Illustration of the uncertainty estimation through the Monte Carlo technique introduced by Kempers *et al.* [63] on the set of measurements displayed on Fig. 2.7.

When implemented on the present configuration, this Monte Carlo technique leads to an uncertainty on the measured heat flux ranging between 20 % and 25 % even for low imposed heat fluxes. This result finally means that the heat flux measurement is even more accurate than previously expected through the uncertainty estimation made with the logarithmic method.

2.3.2 Image processing

In order to reap the full benefits of the high-speed visualization, it is necessary to extract quantitative data from the video files. Therefore an adapted tool was developed to process the pictures and extract objectively and efficiently the data of interest to study the bubble dynamics. Among them, one can cite the number of bubbles recorded on an acquisition file, their volumes, growth times and frequencies for example. The large number of caught bubbles as well as the high time and space resolutions obtained during the experiments lead to such an amount of data to treat so that such a tool associated to a procedure of quality is required.

Adapted to the features of the digital pictures recorded in this work, that tool is a home-made image processing code developed under MATLAB environment. It is mainly aimed at detecting the presence of bubbles, their nucleation and detachment from the wall and at identifying their edges. Once this is done, some parameters characterizing the bubble dynamics (bubble departure frequency, instantaneous volume, *etc.*) can indeed be easily calculated. Basically, this program applies a frame-by-frame treatment based on the principle that strong gradients in gray

levels occur on the images at the interface between the two phases (liquid and vapor). However, due to some pictures features (caused by the setup and/or the boiling phenomenon), the image processing is not that simple.

In order to establish the quality of this image processing and to be able quantify the uncertainties on the bubble dynamics properties calculated with it (which are analyzed in the next chapters), a detailed description of it is given hereafter. Features of the processed pictures are listed in Section 2.3.2.1, then the algorithm is depicted in Section 2.3.2.2 before the methods to calculate some bubble dynamics parameters are explained in Section 2.3.2.3.

2.3.2.1 Pictures characteristics to be taken into account

On the grayscale images recorded, a bubble appears almost black (pixel intensity: 0) whereas the surrounding liquid appears almost white (pixel intensity: 255). This high contrast obtained with the white LED lighting is an advantage for an accurate automatic detection of the bubble interfaces. However, pictures exhibit other features (refer to Fig. 2.9) which limit this detection:

Shadow zone: As mentioned in Section 2.1.3.2, adding a glue seal at the junction between the heated surface and the PTFE insulant was necessary to reach the full air-tightness required to conduct experiments. The presence of this glue seal engenders a shadow zone just above the heated surface which results in a poor visibility of the bubble in this area and to a delay (of two or three images maximum, *i.e.* 2 or 3 ms maximum) in the detection of the bubble inception and detachment. These events of the bubble life can indeed be caught only when the bubble crosses a detection line located just over the shadow zone. This delay between the real event and the apparent (or detected) one is identical for bubble nucleation and departure and is generally small in comparison with the bubble growth time.

The presence of this glue seal hides the mirage effect which takes place in this region. Described by Cooper [30], this phenomenon occurs when light rays are refracted by passing through a medium of non constant optical index of refraction. It occurs in boiling since the temperature gradient close to the heated wall creates such a gradient of optical index. The liquid-vapor interface is then distorted which constitutes a classical source of error when observing boiling. As the shadow zone masks this effect, the mirage phenomenon is not taken into account in this work.

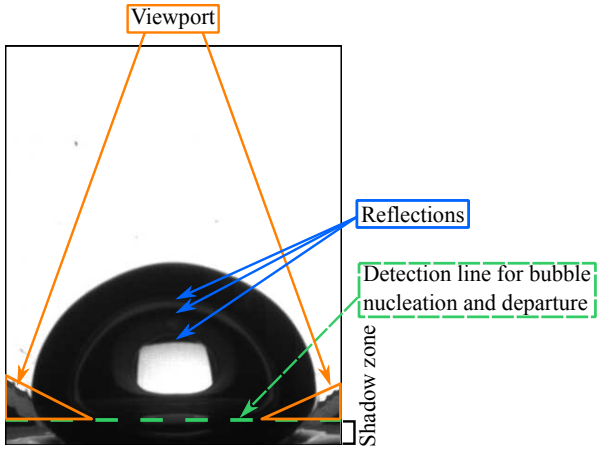

Figure 2.9 – Features of the pictures limiting the detection of bubble nucleation and departure and the localization of its edges (illustrated on an image of bubble obtained with water at $P_v = 5.6$ kPa ($T_{sat} = 35$ °C) with $H_l = 17.3$ cm and $\varphi_{input} = 2.7$ W · cm^{-2}).

Viewport's shadow: As bubbles formed in low pressure boiling are a few centimeters wide, the imaging area used for the experiments corresponds to the full size of the viewports (*i.e.* 100 mm wide). As a consequence, the shadow of the viewport used for lighting is

visible in dark gray on the recordings. This induces a poor contrast between the viewport and bubbles which makes the identification of liquid-vapor interface with the automatic algorithm difficult. However, this does not happen for the smallest bubbles recorded. Pictures are indeed always cropped to an adapted region of interest (ROI) before any further image processing to optimize the computation time while observing the whole phenomenon which has to be analyzed. Bubbles small enough not to reach the viewport's shadow are thus not impacted by this problem.

Reflections on the bubble surface: Actually several reflections occuring on the bubble's surface make the bubble appearing not only dark on a picture: for instance, its center is always light. Those reflections results thus in strong gradients in gray levels on the bubble interface that should not be chosen when looking for the real bubble edges. Selecting automatically the gradient related to the real liquid-vapor interface rather than one of those corresponding to reflections is challenging from the point of view of the computer-code.

As demonstrated hereafter (Section 2.3.2.2), solutions were found and implemented to overcome these three major difficulties.

2.3.2.2 Image processing to detect the bubbles and locate their contours

In this section, a detailed description will be given for the algorithm developed to detect when a bubble is nucleating, growing on the surface and finally departing from it and where its border is located. First the preparatory work to the computation is depicted (Section 2.3.2.2.1). The main treatment is then explained for a single picture (Sections 2.3.2.2.2 and 2.3.2.2.3), followed by the solution to the viewport problem (Section 2.3.2.2.4). Lastly, some remaining limits of the tool are recalled (Section 2.3.2.2.5).

2.3.2.2.1 Preparation of the image processing

Before any treatment under MATLAB, the video file to process is open with the high-speed camera viewer (PFV) to extract some input parameters for the image processing. This is necessary in particular to define the ROI and to determine the position of the borders between the different domains of analysis of the pictures which will be kept for the whole recording.

Definition of the ROI: The ROI is a high and wide enough rectangular window to see all the bubbles recorded on the considered video file (from nucleation to early rise and even to the beginning of recondensation in the subcooled liquid). Coordinates of two specific points are identified through PFV to define this rectangle:

- The nucleation site: its abscissa corresponds to the center of the ROI in the horizontal direction while its ordinate defines the bottom boundary of the ROI.
- The top-left point of the ROI: its abscissa delimits the ROI's width and its ordinate constitutes the top boundary of the window.

Division of the picture into domains of analysis and research: Once the picture cropped to the ROI, it is vertically divided into domains of research of the bubbles interfaces (refer to Fig. 2.10):

- Domain A: over the shadow zone induced by the glue seal, *i.e.* above the detection line;
- Domain B: corresponding to the shadow zone and subdivided into two regions:
  - Region $B1$: located at the top of domain B, this region is directly related to the presence of the glue seal itself. Bubble edges are there visible to the naked eye but hardly discernible automatically.

– Region $B2$: at the bottom of domain B, this region is associated to the shadow of the seal over the copper heated surface. Even with the eye, the bubble cannot be here distinguished from its environment.

Delimitations between those regions and domains are likened to horizontal lines whose heights are determined visually with PFV.

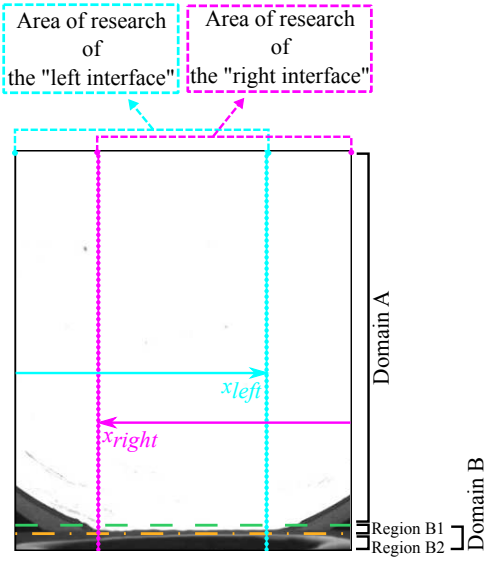

Figure 2.10 – Vertical division of a picture into domains A and B, subdivision of domain B into regions $B1$ and $B2$ and horizontal division into areas of research of the left and right interfaces (with the chosen orientation of the pixels profiles in those areas).

Horizontally, as also mentioned on Fig. 2.10, the picture is separated into two areas of research: one for the "left interface" on the left hand side of the image and the other for the "right interface" on its right hand side. Those areas cover 75 % of the left (and right respectively) hand side of the cropped picture so that they overlap each other in the middle. This arbitrary decision ensure that the bubble edges can be caught by the MATLAB program even if the bubble is not perfectly centered on the image.

Location of the viewport shadow (if applicable): If the viewport is still visible after cropping the picture according to the ROI, the locations of the concerned zones have to be given as input parameters to the algorithm in order to implement the proper way to localize the bubble interfaces. Those zones are matched to two right-angled triangles shaped regions whose right-angles are situated at the crossing point of the detection line and of the left (or right) border of the cropped image (as shown on Fig. 2.9). Their widths and heights are visually determined using PFV.

Measurement of the size of a pixel: The pixel size is evaluated by measuring a known length through the PFV software. This is required in order to estimate the bubble size or volume in real units.

2.3.2.2.2 Localization of bubbles interfaces in domain A

According to the horizontal division depicted previously, the bubble's interface – if it exists – is localized separately in the left hand side ("left interface") and in the right hand side ("right interface") of the cropped picture. For each side of domain A, the interface identification is made line of pixels by line of pixels, starting from the detection line at the bottom up to the top of the area of research. Each slice of one pixel is oriented as shown on Fig. 2.10: from left to right when working on the left hand side and from right to left when working on the right hand side. The procedure implemented to localized a bubble contour is described below for a

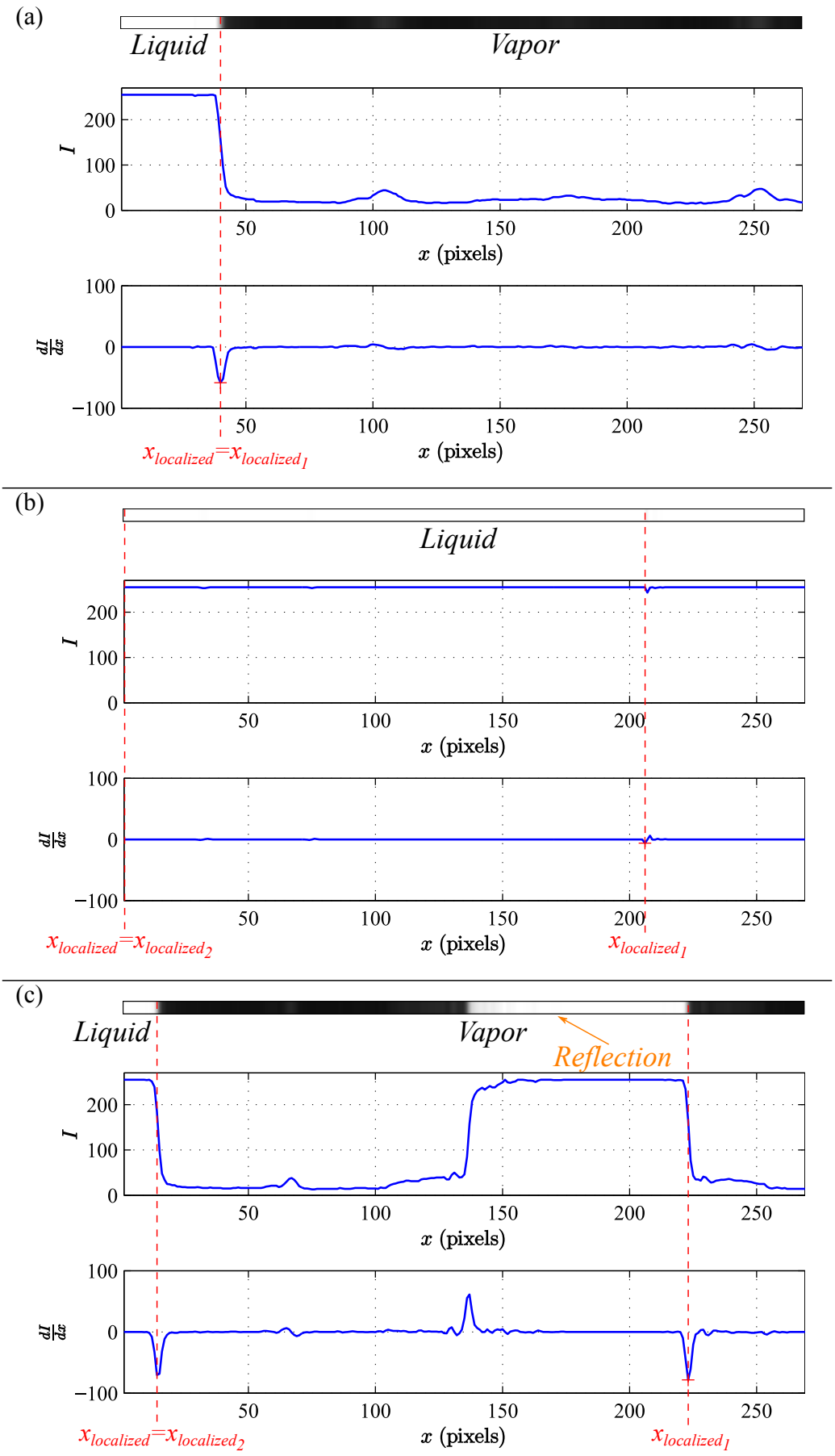

Figure 2.11 – Example of an oriented line of pixels (stretched vertically), intensity of pixels along the profile $I(x)$ and its gradient $\frac{\mathrm{d}I}{\mathrm{d}x}$ when (a) there is a bubble but no reflection effect; (b) there is only liquid and (c) there is a bubble and a reflection.

single oriented profile.

As a bubble is dark (low gray level) while the bulk liquid appears in light (high gray level) in domain A, the liquid-vapor interface is characterized by a sudden drop of intensity on the oriented profile. The bubble contour is then located by finding the minimum of the intensity gradient on the oriented profile and by taking the darkest pixel associated with that minimum. Figure 2.11a illustrates this situation.

Actually bubble interfaces should not be found on profiles where only liquid is visible (above a growing bubble or between two successive bubbles for example). An empirical criterion (EC_1, given in Eq. 2.9) on the intensity I of the pre-selected pixel (at $x_{localized}$) is therefore used to determine if this pixel is dark enough to correspond to a liquid-vapor interface or if, on the contrary, it is too light for that. In the latter case, that pixel is considered as belonging to the liquid phase, meaning that there is only liquid at the considered height (as shown on Fig. 2.11b). The interface is then arbitrarily set to $x_{localized} = 0$.

$$EC_1 : I(x_{localized}) \leq I_{max} \tag{2.9}$$

Another empirical criterion (EC_2, given in Eq. 2.10) on the mean value of pixels along the oriented profile from the side border ($x = 0$) of the image to the identified interface ($x = x_{localized}$) is defined to avoid the selection of a strong gradient in gray levels induced by a reflection. If the mean value of the pixels crossed along the profile upstream to the current position of the interface is too low, it means that quite dark pixels (*i.e.* belonging to the vapor phase) have been encountered on the profile in front of the detected interface. The current position of the contour $x_{localized}$ is then wrong since the detected interface is related to a reflection rather than to a bubble edge.

$$EC_2 : \overline{I(x \leq x_{localized})} \geq I_{min} \tag{2.10}$$

In this case, the calculation of the minimum gradient of gray level is reiterated considering then only the beginning of the oriented profile: from $x = 0$ to the current position $x_{localized}$ excluded. This operation can be done several times until the selected pixel satisfies both EC_1 and EC_2 (*i.e.* the real liquid-vapor interface is supposed to be well detected) or is found at the picture's border (*i.e.* no liquid-vapor interface is identified: there is only liquid on that profile). Figure 2.11c, shows an example where the calculation was made twice because of a strong reflection.

For a given height (a pixel slice), a last iteration of the calculation can be required both for the left and the right oriented profiles in case of inconsistency between the left and the right detected interfaces. This occurs if the "left interface" $x_{localized_{left}}$ is found on the right hand side of the "right interface" $x_{localized_{right}}$ at the scale of the full picture.

2.3.2.2.3 Localization of bubbles interfaces in domain B

To reduce the computation time, image processing is implemented in domain B only on pictures on which a bubble is growing (*i.e.* if reliable interfaces are found on the detection line).

In this case, the first step of the treatment consists in running a similar research for left and right interfaces as in domain A in region $B1$. In this restricted area of domain B, the eye is able to discriminate the bubble (almost black) from its environment (glue seal in gray). As a consequence, adapting the I_{min} value of criterion EC_2 (by lowering it) for the processing of this region can lead to the localization of some points of the bubble contour. However, seeking interfaces in region $B1$ is not as efficient as in domain A. Two cases can thus occur:

(i) Several points of the left (respectively right) interface are identified but not for all pixel slices;

(ii) Identified points of the left (respectively right) interface are too scarce and/or appear not reliable.

In situation (i), the left (respectively right) interface in the full domain B (*i.e.* the union of regions $B1$ and $B2$) is approximated through a linear fitting based on the localized points as illustrated on the left hand side of Fig. 2.12. In situation (ii), interfaces are arbitrarily approached in the full domain B by vertical lines positioned at the same abscissa as the interfaces found on the detection line (as schematically shown on the right hand side of Fig. 2.12).

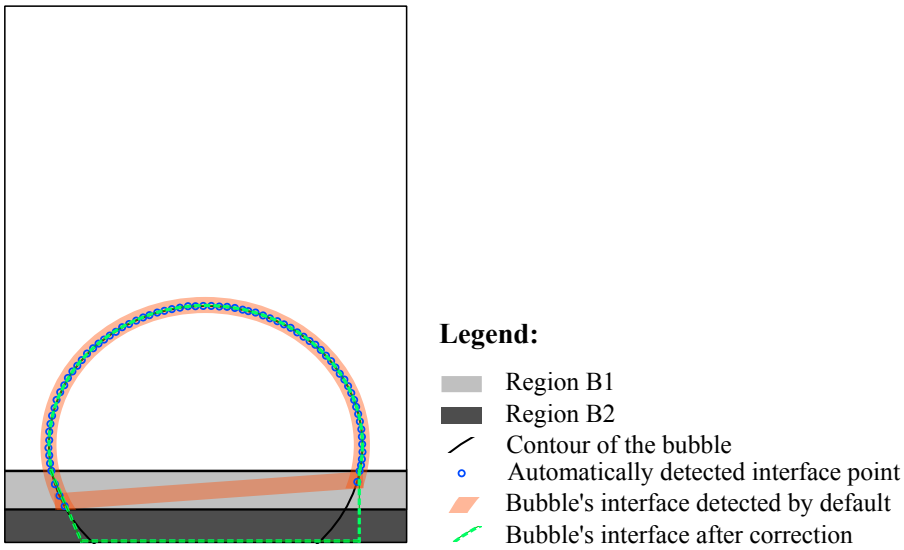

Figure 2.12 – Schematic representation of implemented solutions to the shadow zone problem: case (i) on the left hand side and case (ii) on the right hand side.

Making those approximations obviously induces errors on the identification of the bubbles edges (and hence on the volume calculation). Nevertheless, this effect is much less important than neglecting totally the presence of vapor inside the shadow zone. At the beginning of a bubble growth, most of the vapor volume is indeed included in domain B: this volume cannot be neglected and the error induced by considering vertical interface rather than following the real limits of the bubble seems acceptable. The part of the volume of vapor located in domain B decreases progressively as the bubble is growing: considering linear fittings or vertical lines instead of the real shape of the bubble in this region is then no more of major importance.

2.3.2.2.4 Specific treatment: viewport problem

The aim of the two previous sections was to explain how the bubble interface is automatically detected in both domains A and B. However, the problem related to the presence of the viewport shadow still has to be solved for some videos. On pictures where this issue arises, pixels belonging to the right-angled triangles shaped regions identified as viewport's shadow (during the preparatory work, Section 2.3.2.2.1) were beforehand changed to white. Under these conditions, the image processing algorithm depicted up to there would give the following result (refer to Fig. 2.13): starting from the top of the bubble, bubble's contour is well detected to the top of the viewport's areas, then the identified edges follow the borders of the viewport's regions (pixels belonging to a bubble being still dark whereas those belonging to the viewport are now white) and finally linear fittings (based on reliable interfaces found in $B1$) or vertical lines (aligned with the extremity of the viewport on the detection line) delimit the bubble in the shadow zone. The error induced here cannot be neglected especially considering the bubble volume. The image processing has to be improved regarding this problem.

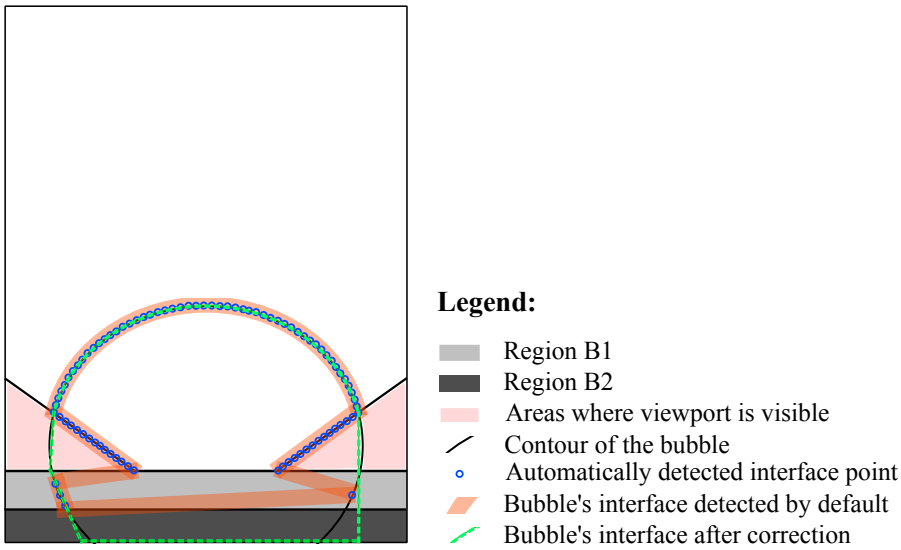

Figure 2.13 – Schematic representation of implemented solutions to the viewport problem depending on the situation encountered in domain B: case (i) on the left hand side and case (ii) on the right hand side.

The implemented solution consists in making (on both left and right hand sides of the picture) a linear fitting between the closest reliable point of the interface detected over the viewport area in domain A and the first reliable point of the interface defined in $B1$ (as illustrated on the left hand side of Fig. 2.13). If no reliable interface is found in $B1$ (situation (ii): the liquid-vapor boundary is approximated by a vertical line at the abscissa of the extremity point of the viewport on the detection line), this linear fitting is replaced by a vertical line from the last reliable point of the interface identified in domain A down to the low border of the picture (as shown on the right hand side of Fig. 2.13). This solution yields an error whose effect is much lower than when the viewport problem is omitted: the error on the bubble volume then remains tolerable.

2.3.2.2.5 Limits of the automatic detection of bubbles contours

Solutions were finally implemented to circumvent the main pictures' features which could have limited the interest of an automatic tool for identification of bubbles interfaces. However, this algorithm cannot be used when:

- There are interactions between two (or more) successive bubbles. In such case, the program treatment is performed as if there were a unique bubble.

- Several masses of vapor are visible at the same height as it often happens when a bubble collapses: these masses of vapor cannot be well defined only by the two left and right interfaces.

As a consequence, this image processing program can be used only for individual bubbles before their recondensation.

Depending on the situation, a manual identification of the bubbles contours can also be performed by – for each picture of a video file – displaying the cropped current picture, clicking on a large number of points belonging to the left interface (respectively to the right interface) and calculating a linear interpolation between successive clicked points. As shown on Fig. 2.14, automatic and manual treatments give very close results while the automatic determination of bubbles borders presents the advantages to be highly time-saving and repeatable compared to the manual identification of interfaces.

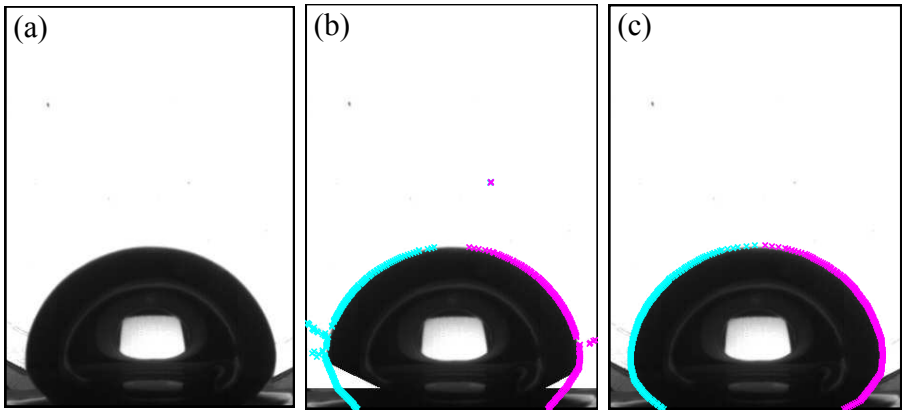

Figure 2.14 – Results of image processing (illustrated on an image of bubble obtained with water at $P_v = 9.6$ kPa ($T_{sat} = 45$ °C) with $H_l = 17.3$ cm and $\varphi_{input} = 2.7$ W · cm^{-2}): (a) original picture; (b) automatic treatment and (c) manual treatment.

2.3.2.3 Calculation of some characteristics of the bubble dynamics

Once the research of bubbles contours is done – automatically or manually – other MATLAB codes are used to quantify some bubble dynamics characteristics. Methods used for that and estimations of the associated uncertainties are given in this section. Those new calculations require the localization of the bubbles edges as input parameters: the importance of a good determination of bubbles borders is again highlighted as the first and essential step for this work.

2.3.2.3.1 Bubble growth time τ_{growth}

For a given bubble whose entire growth is recorded, the bubble growth duration corresponds simply to the time difference between the detected instants of its nucleation and its detachment:

$$\tau_{growth} = t_{departure} - t_{nucleation} \tag{2.11}$$

Due to the presence of the glue seal, the detection of those events is delayed by 2 to 3 ms, which yields an uncertainty of ± 1 to 2 ms on τ_{growth}.

2.3.2.3.2 Waiting time τ_{wait} between successive bubbles

The waiting time between two successive bubbles can be measured only when at least two bubbles are recorded on the same acquisition video file (number of bubble recorded on a video $N \geq 2$). . This property of the bubble dynamics is then evaluated between every bubble whose full growth is observed. That duration is given by the difference between the times of the next bubble nucleation and of the current bubble departure (Eq. 2.12). The uncertainty on this physical quantity is – as for the growth time – of ± 1 to 2 ms.

$$\tau_{wait} = t_{nucleation}(i+1) - t_{departure}(i) \tag{2.12}$$

2.3.2.3.3 Bubble departure frequency f

The bubble departure frequency is calculated only if at least two bubbles are entirely recorded on a video ($N \geq 2$) as well. Its value for a given recording is then obtained according to Eq. 2.13:

$$f = \frac{N}{t_{departure}(N) - t_{departure}(1)} \tag{2.13}$$

The error made on the bubble frequency is negligible since, considering the uncertainty on the instant of bubble departure of bubbles, it is evaluated to less than 4 %.

2.3.2.3.4 Instantaneous volume V

The instaneous volume V of a bubble is evaluated at each moment of its growth (*i.e.* for each picture where a growing bubble can be seen). As an image only gives a description of a bubble in two dimensions, the calculation of this volume is done by discretizing the growing bubble into slices of one-pixel height and by assuming an axial symmetry for each slice (*i.e.* each slice is considered as a cylinder). This method of calculation – which is the same as that used by Siedel *et al.* [104, 105] – presents the advantage of taking into account the whole bubble contour rather than a mathematical modeling of it (simplifying the bubble shape to a full or truncated speroid or ellipsoid) as it can be encountered in the literature (in [43] for instance). Such a mathematical simplification of bubble shape is not adapted to the present study due to the particular shapes taken by bubbles at low pressure. This method also limits the error on the volume of tilting bubbles which are not purely axisymmetric along the vertical axis.

Two sources of uncertainties can be listed on the calculated instantaneous volume:

The use of the automatic detection of the bubbles interfaces: The error induced by the use of the automatic tool itself may be estimated by comparison between the automatic and the manual treatment on few videos. Even if this method is not perfect to evaluate the effect of the MATLAB program on the calculation of bubbles volumes, at least it constitutes an attempt to take the effect of the approximations made in the shadow zone and in the viewport's areas into consideration.

A comparison between the volume $V_{automatic}$ calculated from the automatic detection of liquid-vapor interface and the volume V_{manual} obtained after a manual treatment was performed for a few videos and bubbles.

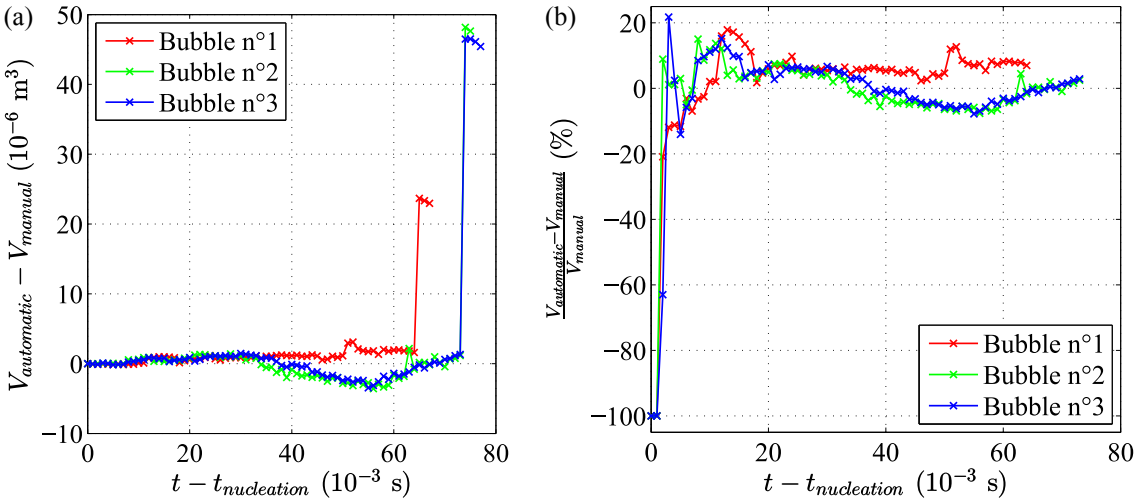

Figure 2.15 – (a) Absolute and (b) relative error between volume calculated through automatic treatment and volume estimated through manual processing (illustrated on a video file obtained with water at $P_v = 9.6$ kPa ($T_{sat} = 45$ °C) with $H_l = 17.3$ cm and $\varphi_{input} = 2.7$ W · cm^{-2}).

As shown on Fig. 2.15a, during bubble growth, the absolute error thus estimated is low (less than 3 cm^3 for bubbles that reach a maximum volume of about 50 cm^3). The sudden and significant rise of this deviation just before the bubble departure is due to the fact that, at low pressure, the bubble foot diameter decreases very quickly at those instants. This phenomenon taking place in the neighborhood of the shadow zone is not well-caught by the image processing software: the volume calculated through the automatic treatment $V_{automatic}$ overestimates then slightly the manual estimation V_{manual}.

The relative error on the volume which is defined as the ratio of the deviation between automatic and manual estimation of the volume to the volume calculated from the manual detection is displayed on Fig. 2.15b. A large underestimation of the volume by the automatic treatment occurs at the very early stages of the bubble growth due to the delay of detection in the image processing software. Later on, $V_{automatic}$ differs only from $\pm$ 12 % from the volume evaluated from the manual treatment V_{manual}. At the end of the growth, the bubble presents a very large volume, which explains that the relative error remains low whereas the deviation is maximum.

Considering the importance of the error made on the volume calculation by using the automatic detection of bubbles contours and the advantages of using it (time-save, repeatability...), we believe that this treatment is a good tool to analyze efficiently and objectively the visualization recordings.

The random error on the selection of the interface's pixel: Assuming that a liquid-vapor interface (on each side) is automatically located within an uncertainty of $\pm$ 3 pixels at each height, the error on the volume $V_{automatic}$ is equal to about 20 % at the very early stages of bubble growth (small volume of vapor) and to 5 % at the end of the growth (large volume), which seems to remain acceptable.

The experimental setup combined with its measurement and acquisition systems, the procedures of use and the methods of analysis facilitate:

- *the production of isolated bubbles from a single artificial nucleation site under controlled low vapor pressure conditions;*
- *the estimation of the wall temperature, the wall superheat and the heat flux dissipated by the heated surface to the working fluid;*
- *the visualization and the analysis of the bubble dynamics experienced in pool boiling at low pressure.*

In particular, the image processing method developed here enabled us to produce original, quantitative and reliable results on the bubble dynamics that were not available in the literature and are necessary to get a better understanding of the fundamental phenomenon of boiling under such conditions.

Chapter 3

Water boiling at subatmospheric pressures

In this chapter, results of a pool boiling test campaign conducted with water in a wide range of subatmospheric pressures are presented and discussed. The motivations of this experimental study as well as its operating conditions are given in Section 3.1 while qualitative and quantitative analyses of the experiments are carried out in Sections 3.2 and 3.3 respectively.

3.1 Introduction

3.1.1 Background and motivations

As detailed in Section 1.2, several authors reported some characteristics specific to pool boiling at low pressure [44,46,76,77,87,100,102,119,122–126,131]. Among them, as compared to normal pressure conditions, one can in particular cite:

- A long waiting time between two successive bubbles;
- A very large bubble volume at departure;
- The occurrence of mushroom shaped bubbles;
- Temperature fluctuations on the heated wall;
- A low heat transfer coefficient that cannot be evaluated through the classical correlations used in boiling.

These observations were most of the time made with water boiling at subatmospheric pressures. As a consequence, water is first selected as the fluid to be tested in the present study. In order to study only the effect of the vapor pressure P_v when it varies from the atmospheric pressure ($P_v = P_{atm}$) down to some lower values, the other parameters of influence (the liquid height H_l whose non negligible effect was demonstrated by Giraud [44] and Giraud *et al.* [46] and the imposed heat flux φ_{input}) are kept constant for the whole test campaign.

3.1.2 Operating conditions

Each experiment is related to the study of the steady state of an operating point defined by four parameters: the working fluid, the imposed heat flux φ_{input}, the vapor pressure P_v and the liquid height H_l over the heated surface. The chosen set of parameters for this test campaign is detailed hereafter.

Working fluid: As mentioned above, all the tests were carried out with pure, distilled and degassed water.

Heat flux input φ_{input}: During the whole experiment session, the imposed heat flux was set constant at the value of $\varphi_{input} = 2.7\ \mathrm{W \cdot cm^{-2}}$, so that the nucleation of bubbles would

always take place from the activated artificial nucleation site on the heated wall. A regime of isolated bubbles could then be observed.

Vapor pressure P_v range: Fifteen values of vapor pressure corresponding to increments of 5 K in saturated vapor temperature T_v from 30 °C up to 100 °C according to Table 3.1 were investigated.

Table 3.1 – Imposed vapor pressures and temperatures of water during the test campaign.

T_v (°C)	P_v (kPa)
30	4.2
35	5.6
40	7.4
45	9.6
50	12.4
55	15.8
60	20.0
65	25.1
70	31.2
75	38.6
80	47.4
85	57.9
90	70.2
95	84.6
100	101.4

The lowest tested vapor pressure ($P_v = 4.2$ kPa ($T_v = 30$ °C)) corresponds to the lowest level of pressure for which no air-leakage appears. Despite the presence of the glue seal, the tightness of the sample is indeed made possible only with a sufficient expansion of the heated copper block. In the present case, decreasing further the pressure while keeping the same imposed heat flux makes the copper part of the heater not expanded enough to avoid the penetration of air inside the vessel. As a consequence, the water is not pure anymore and the present study of water pool boiling at subatmospheric pressures cannot be performed at lower pressures.

Liquid height H_l: For all the tests, the liquid height was set constant at the arbitrary value of $H_l = 17.3$ cm.

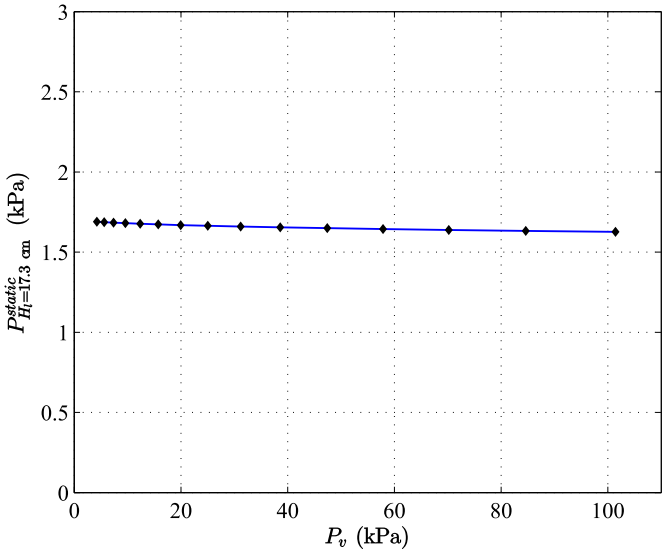

Figure 3.1 – Static head in water $P_{H_l=17.3\ \mathrm{cm}}^{static}$ depending on the vapor pressure P_v ($H_l = 17.3$ cm).

As the liquid density ρ_l is almost constant all over the investigated range of saturation

pressures, the static head induced by the column of liquid is considered as constant (refer to Fig. 3.1):

$$P^{static}_{H_l=17.3\ \text{cm}} = \rho_l(T_{l,\,bulk})gH_l \approx 1.7\ \text{kPa} \tag{3.1}$$

Assuming that the saturation conditions prevail at the liquid-vapor interface, the bulk liquid temperature $T_{l,\,bulk}$ – supposed homogeneous – is equal both to the temperature at the free surface $T_{sat}(z=0)$ and to the vapor temperature T_v. The local subcooling degree $\Delta T_{sub}(z)$ defined as:

$$\Delta T_{sub}(z) = T_{sat}(z) - T_{l,\,bulk} \tag{3.2}$$

is then given by:

$$\Delta T_{sub}(z) = T_{sat}(P_v + P^{static}(z)) - T_{l,\,bulk} = T_{sat}(P_v + \rho_l(T_{l,\,bulk})gz) - T_{l,\,bulk} \tag{3.3}$$

The local subcooling degrees are calculated (using the database REFPROP [71]) and reported on Fig. 3.2 for all the investigated vapor pressure values. According to this graph (and in agreement with Section 1.2.3), for a given liquid height H_l, the effect of the subcooling is lowered as the vapor pressure increases. At the level of the heated surface, the subcooling is indeed lower than 0.5 K for $P_v = P_{atm}$ whereas it is equal to almost 6 K for $P_v = 4.2$ kPa. Through its subcooling degree, the boiling environment is thus highly sensitive to the vapor pressure P_v especially when this parameter takes low values. As demonstrated here, this observation is valid even for a constant liquid height H_l.

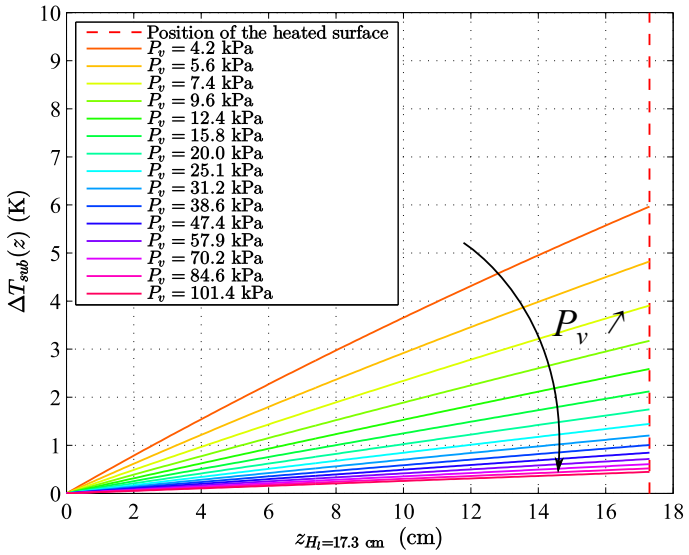

Figure 3.2 – Local subcooling ΔT_{sub} depending on the depth z in the water for the different investigated vapor pressures P_v ($H_l = 17.3$ cm).

3.2 Qualitative description of the bubble dynamics

The boiling regime observed during all the experiments is characterized by the departure of a single bubble after a waiting time which lasts longer than the bubble growth. This regime – the "intermittent boiling regime" or "isolated bubbles regime" – appears to be quite regular and steady: for a given vapor pressure P_v, bubbles appear to detach with a regular size and frequency. However, depending on the imposed vapor pressure P_v, four distinct behaviors in terms of bubble shape, size and frequency were observed and identified. They are detailed in the four following subsections (3.2.1 to 3.2.4).

3.2.1 Oblate spheroid shaped bubbles

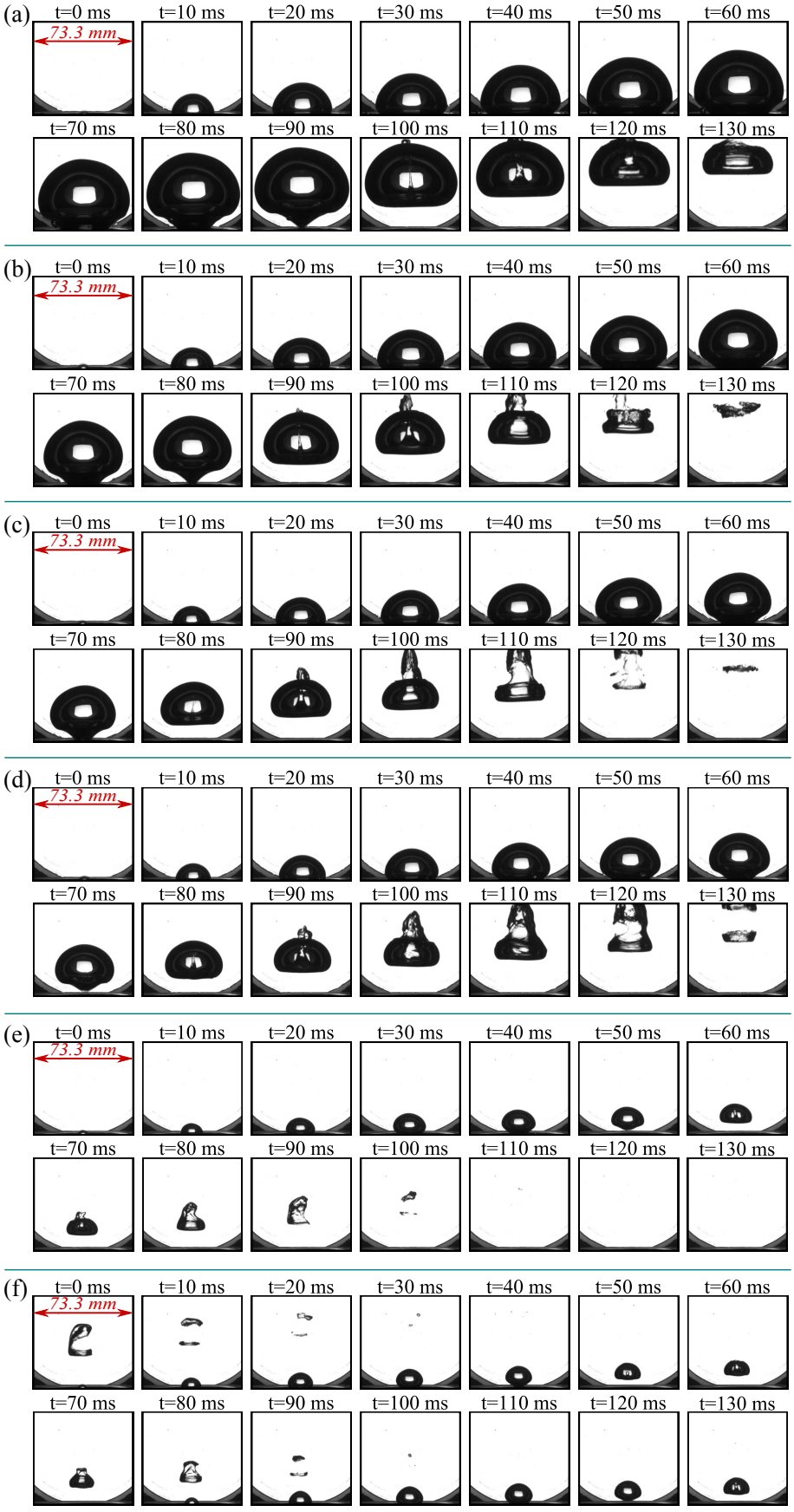

Figure 3.3 – Images of video recordings showing the time evolution of selected bubbles under the lowest investigated vapor pressures (water, $H_l = 17.3$ cm, $\varphi_{input} = 2.7$ W $\cdot$ cm^{-2}):
(a) $P_v = 4.2$ kPa ($T_v = 30$ °C); (b) $P_v = 5.6$ kPa ($T_v = 35$ °C); (c) $P_v = 7.4$ kPa ($T_v = 40$ °C); (d) $P_v = 9.6$ kPa ($T_v = 45$ °C); (e) $P_v = 12.4$ kPa ($T_v = 50$ °C); (f) $P_v = 15.8$ kPa ($T_v = 55$ °C).

As it can be seen on Fig. 3.3, the bubble dynamics of water boiling – with these particular imposed heat flux φ_{input} and liquid height H_l – can be described in the lowest range of vapor pressure (*i.e.* for 4.2 kPa $\leq P_v \leq$ 15.8 kPa (30 °C $\leq T_v \leq$ 55 °C)) by seven successive stages as follows:

1. A bubble nucleates.

2. Then, the bubble starts to grow with a hemispherical shape until it turns to an oblate spheroid shape. The bubble's top indeed starts to be flattened as the bubble is reaching a size of a few centimeters.

3. Suddenly, the bubble foot diameter decreases quickly.

4. As a consequence, the bubble departs from the wall.

5. During its early rise, a liquid jet penetrates into the volume of the detached bubble from its bottom.

6. The bubble collapses due to the subcooling of the surrounding liquid.

7. Afterwards, a long waiting time begins before the cycle starts again with the inception of a new bubble.

On the same figure, one can also observe that, as the vapor pressure P_v increases (*i.e.* from Fig. 3.3a to Fig. 3.3f), the volume V and the growth time τ_{growth} decrease significantly. The waiting time τ_{wait} also seems to be lowered (and subsequently the departure frequency f increased) as the pressure is increasing, but no direct interaction between successive bubbles occurs.

3.2.2 Mushroom shaped bubbles

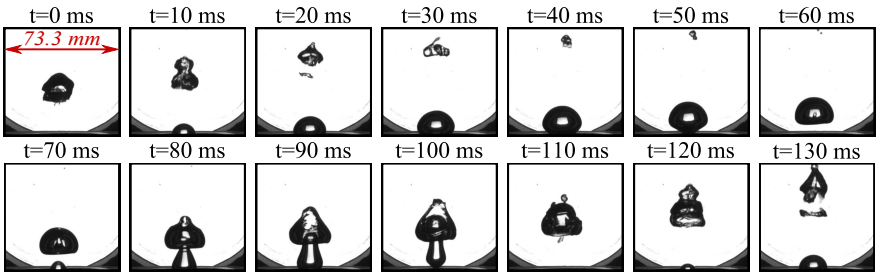

Figure 3.4 – Images of video recordings showing the time evolution of selected bubbles at $P_v = 20.0$ kPa ($T_v = 60$ °C) (water, $H_l = 17.3$ cm, $\varphi_{input} = 2.7$ W $\cdot$ cm^{-2}).

At $P_v = 20.0$ kPa ($T_v = 60$ °C), some interaction between bubbles occurs: they are indeed associated by pairs. As shown on Fig. 3.4, just after the departure of a first bubble (very similar to those observed at lower pressures), a second bubble nucleates and is sucked into the preceding bubble's wake. Because of the influence of the primary bubble's wake which sucks the secondary bubble, the latter grows faster and is more elongated in the vertical direction. The liquid jet that has penetrated into the primary bubble (as already observed in the lower pressure case) enables the secondary bubble to penetrate into the primary one without merging with it. The second bubble passes then through the first one giving to the pair of bubbles an apparent mushroom shape.

The trends reported previously concerning the variations with the vapor pressure P_v of the volume V, the growth time τ_{growth}, the waiting time τ_{wait} and consequently the departure frequency f seem to be still true for this pressure level.

3.2.3 Mushroom and column shaped bubbles

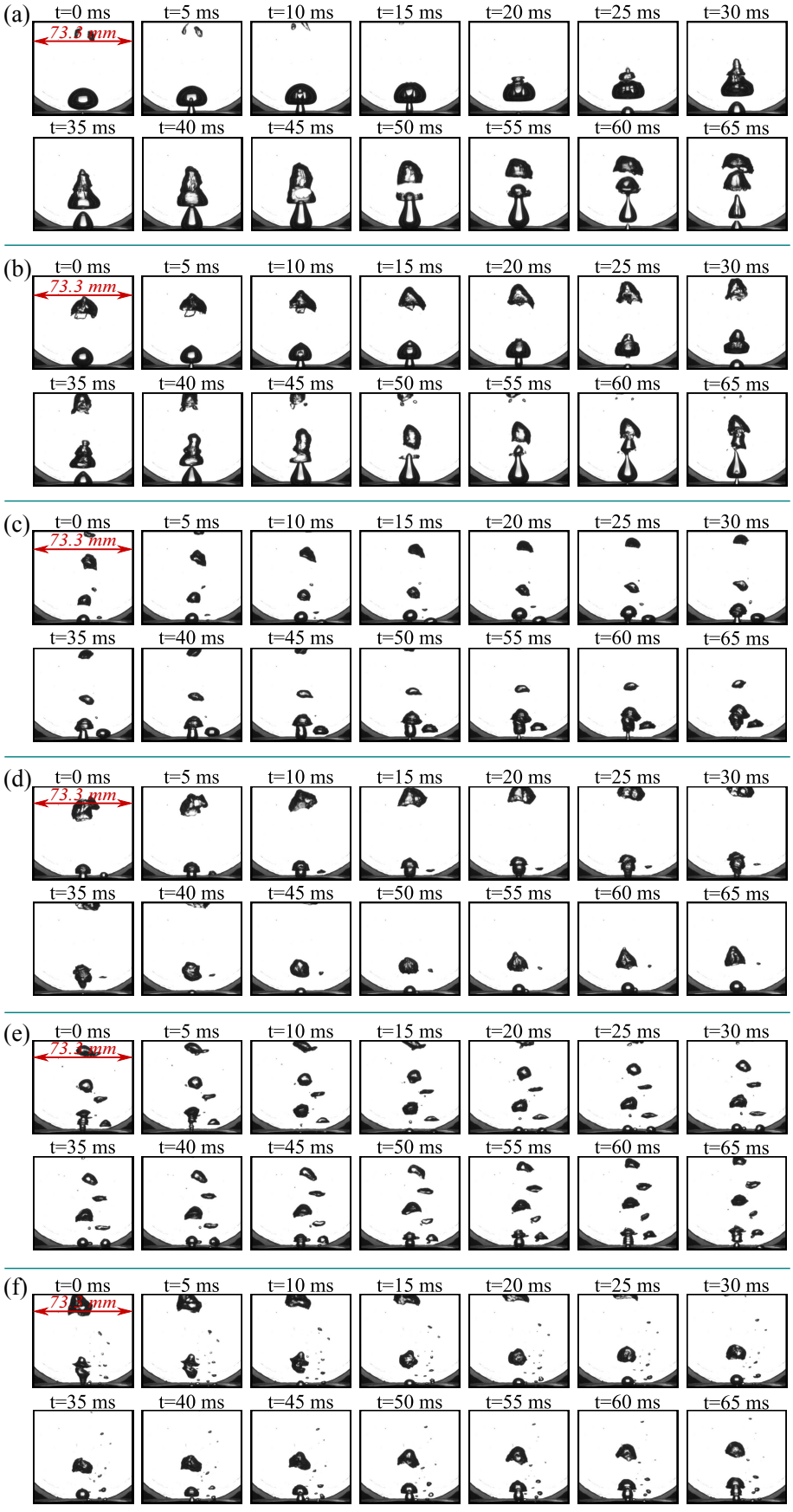

Figure 3.5 – Images of video recordings showing the time evolution of selected bubbles under the intermediate range of vapor pressure (water, $H_l = 17.3$ cm, $\varphi_{input} = 2.7$ W $\cdot$ cm^{-2}):
(a) $P_v = 25.1$ kPa ($T_v = 65$ °C); (b) $P_v = 31.2$ kPa ($T_v = 70$ °C); (c) $P_v = 38.6$ kPa ($T_v = 75$ °C); (d) $P_v = 47.4$ kPa ($T_v = 80$ °C); (e) $P_v = 57.9$ kPa ($T_v = 85$ °C); (f) $P_v = 70.2$ kPa ($T_v = 90$ °C).

In the intermediate range of pressure (*i.e.* for 25.1 kPa $\leq P_v \leq$ 70.2 kPa (65 °C $\leq T_v \leq$ 90 °C)), a transitional behavior is observed between the mushroom shaped bubbles and the individual near-spherical ones which are expected at atmospheric pressure. As shown on Fig. 3.5, a lot of interactions between bubbles are then visible: successive mushroom shaped vapor masses and/or vapor columns are indeed formed by the contact of several bubbles. As the pressure increases, the number of bubbles involved in the formation of such vapor structures seems to increase while the bubble size keeps decreasing. In addition, the bubble frequency seems to be much higher than at lower pressure and to be still rising as the pressure is increased.

One can also see on Fig. 3.5c to Fig. 3.5f that some peripheral boiling starts. This is directly linked with the fact that more and more nucleation sites can be activated as the pressure increases (since the critical radius of nucleation is then decreasing). The heated surface being mirror-polished, the artificial cavity and the (supposed smaller) cavities engendered by the addition of the glue seal are actually favorable sites for the inception of bubbles.

3.2.4 Near-spherical bubbles

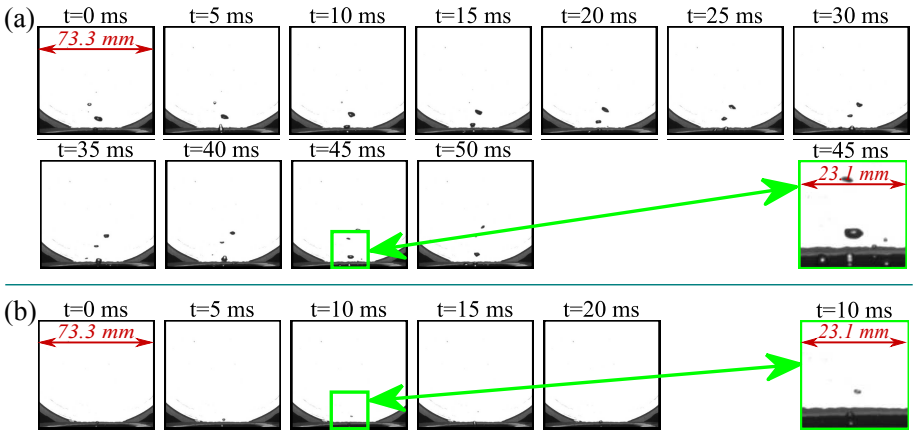

Figure 3.6 – Images of video recordings showing the time evolution of selected bubbles at (a) $P_v = 84.6$ kPa ($T_v = 95$ °C); (b) $P_v = P_{atm} = 101.4$ kPa ($T_v = 100$ °C) (water, $H_l = 17.3$ cm, $\varphi_{input} = 2.7$ W · cm^{-2}).

No more interaction between successive bubbles takes place close to atmospheric pressure (*i.e.* for 84.6 kPa $\leq P_v \leq$ 101.4 kPa $= P_{atm}$ (95 °C $\leq T_v \leq$ 100 °C)). As visible on Fig. 3.6, near-spherical bubbles are indeed separated by a very low waiting time but there is no contact between bubbles. The bubble size is still decreasing and is now of the order of a few millimeters in diameter.

3.2.5 Outcome and discussion

All the data presented in this section finally show that – for water boiling in the regime of isolated bubbles at subatmospheric pressures (with $H_l = 17.3$ cm and $\varphi_{input} = 2.7$ W · cm^{-2}) – as the vapor pressure P_v increases:

- The bubble size decreases: from a few centimeters to a few millimeters in diameter.
- The waiting time τ_{wait} decreases and subsequently the bubble departure frequency f increases.
- The bubble shape changes:
  - An oblate spheroid shape without any bubble interaction at low pressures (*i.e.* for $P_v \leq 15.8$ kPa ($T_v \leq 55$ °C));
  - A mushroom shape due to the interaction between paired bubbles at 20.0 kPa ($T_v = 60$ °C);

- A mushroom and column shape with two or more interacting bubbles in the intermediate range of pressure (25.1 kPa $\leq P_v \leq$ 70.2 kPa (65 °C $\leq T_v \leq$ 90 °C));
- A near-spherical shape without any contact between successive bubbles close to the atmospheric pressure ($P_v >$ 70.2 kPa ($T_v >$ 90 °C)).

These results are in overall agreement with the literature and especially with the observations made by Van Stralen *et al.* [119]. Some reported characteristics of the bubble dynamics are discussed hereafter.

The oblate spheroid shape: According to Madejski [73], an active bubble nucleus tends to be flattened if there is a non negligible temperature gradient in the thermal boundary layer. This result illustrates how a non homogeneous temperature field in the liquid can affect the bubble shape, even at the stage of the initial nucleus.

Contrary to the classical literature (among which [34, 36, 39, 70]), whatever the imposed vapor pressure P_v, the actual configuration do not involve a uniformly superheated liquid around the bubble. As a consequence, like in the case considered by Madejski [73], every observed bubble may have a flattened nucleus. The shape of the nucleus may have an influence on the bubble shape. Actually, this seems to be the case especially for bubbles whose departure size is not very large (in comparison with the cavity size). Close to atmospheric pressure, the near-spherical bubbles are indeed slightly flattened (Fig. 3.6) whereas the local subcooling $\Delta T_{sub}(z)$ is negligible.

As visible on Fig. 3.3 to 3.5, some bubbles present a hemispherical shape during their very early stages of growth but take afterwards an actual oblate spheroid shape. According to those figures, the concerned bubbles are:

- The bubbles recorded in the lowest range of pressure (4.2 kPa $\leq P_v \leq$ 15.8 kPa (30 °C $\leq T_v \leq$ 55 °C));
- The primary bubbles (*i.e.* the first bubble of pairs or groups of bubbles) recorded up to $P_v =$ 70.2 kPa ($T_v =$ 90 °C).

In fact, the bubble top seems to be more and more flattened as the pressure P_v is low and the local subcooling $\Delta T_{sub}(z)$ high. A local recondensation taking place at the bubble's top because of the surrounding subcooled liquid may consequently be responsible for this oblate spheroid shape.

The liquid jet: Studying experimentally the convective flow around a single bubble of water at 2.7 kPa by means of a tracer method, Ohue *et al.* [87] were able to monitor the liquid jet. They indeed observed the morphological change of the bubble in relation with the surrounding liquid flow and saw in particular the recirculating liquid that follows immediately the detachment, comes to push the bubble base upward and even penetrates into it.

Van Leeuwen [116] (cited by Van Stralen *et al.* [119]) explained this thin and high-speed liquid jet by a large depression in the detached bubble's wake that may be compared to what can occur in cavitation.

Hermans [55] described indeed such a high-velocity liquid jet created at the rear of a collapsing cavity in the case of cavitation with a translational motion while – more recently – Caupin and Herbert [16] explained that such a jet is formed as soon as a cavitation bubble loses its spherical shape.

Mitrovic developed a basic view of the bubble detachment process involving such a liquid jet in the 1970's and confirmed it by means of series of experiments conducted – over a period of about 10 years – on isolated bubbles generated from artificial cavities made on upward-facing heating surfaces for different fluids, boiling temperatures and wall superheats. Several years later, he summarized [81] his observations and illustrated them in the case of an experiment carried out with refrigerant R113 containing 1 % (mass) of oil at a

pressure of 37 kPa and a wall superheat of 39 K. Although the detachment process of a bubble is resulting from the action of several parameters (gravity, inertia, viscosity, surface tension), he focused on the effect of the surface tension which – according to him – is playing a role of major importance in the liquid jet formation through the Laplace pressure. He observed indeed that at the break-off instant, the bubble shape is very different from the equilibrium shape, which means that there is an energy excess. This excess of energy is used to make the bubble shape closer to the equilibrium shape (through a shape change which mainly takes place in the region of the former bubble neck) and can thus be related to the Laplace pressure. In the break-off region, the concave radius is very small so that the Laplace pressure is very high and the associated vapor – compressed by this pressure – is finally accelerated toward the center of the bubble[1]. For the same reasons, some liquid can be accelerated from the wall towards the bubble center. The author added that this first motion of the liquid leads to different behaviors depending on the bubble size and on the fluid thermosphyical properties. For example, this motion yields capillary waves on the bubble interface and oscillations of the bubble shape for small bubbles whereas it engenders more or less pronounced liquid jet at the base of large bubbles. As for orders of magnitude, in the specific case discussed in [81], the rear end of the bubble reached a maximum velocity of approximately 6 $\mathrm{m \cdot s^{-1}}$ just after the bubble break-off whereas the tip of liquid jet reached quickly a constant final velocity equal to about 1.65 $\mathrm{m \cdot s^{-1}}$ (higher velocity was observed during the very early stages of jet formation).

The presence of a secondary bubble: As mentioned in Section 1.2.1, the presence of a secondary bubble conferring to the pair (or group) of bubbles a mushroom shape was already reported by several authors studying water low pressure boiling.

Clark and Merte [22] (cited by Van Stralen *et al.* [119]) observed such a behavior in subcooled boiling. They attributed the rapid growth and motion of this secondary elongated bubble to the high-momentum liquid jet formed by the first bubble's wake. Van Leeuwen [116] (also cited by Van Stralen *et al.* [119]) analyzed the high-speed videos made by Van Stralen *et al.* [119]. He stated that this secondary bubble is the consequence of the local depression engendered by the liquid jet on some remaining superheated vapor trapped in the nucleation site after the detachment of the primary bubble.

The presence of a secondary bubble was reported only for vapor pressures lower than 13 kPa by Van Stralen *et al.* [119] and for vapor pressures lower than 15 kPa by Giraud [44] and Giraud *et al.* [46]. Giraud [44] explained the different values of the upper pressure limit for which a secondary bubble is visible by the fact that the liquid height H_l may be different in the two studies. She investigated indeed a liquid level equal to $H_l = 200$ mm whereas the liquid height tested by Van Stralen *et al.* [119] was not mentioned by the authors. Van Leeuwen [116] and Van Stralen *et al.* [119] noticed that the size of the contact area between the secondary bubble and the heated wall does not exceed the size $\tilde{r}$ of the dry spot left on the surface by the primary bubble. They therefore attributed the absence of a secondary bubble at higher pressures to the combined effects (as the imposed pressure increases) of:

- A decrease of the relative depression in the wake of the primary bubble;
- The diminishing radius $\tilde{r}$ of the dry area left by a departed bubble. Assuming that the radius $\tilde{r}$ of the dry area around the nucleation site is characterized by a complete local evaporation of the microlayer, Van Stralen *et al.* [121] were able to calculate this parameter. They thus highlighted that – for water – the dry spot is larger at subatmospheric pressures than at atmospheric pressure. They finally concluded that due to the small value of $\tilde{r}$, it should be difficult to keep such a dry area after the departure of a bubble in water boiling close to atmospheric pressure. A schematic description of this phenomenon is given in Table 3.2 considering a "low" subatmospheric pressure and a higher pressure just before ($t = t_{departure} - \varepsilon$) and just after

[1] The same phenomenon occurs on the vapor remaining on the wall for symmetry reasons.

$(t = t_{departure} + \varepsilon)$ the detachment of a bubble of equivalent radius R_{eq}.

Table 3.2 – Schematic interpretation of the result obtained by Van Stralen *et al.* [121] about the size variation of the dry area left on the heated wall by a departed bubble.

	"Low" subatmospheric pressure	**Close to atmospheric pressure**
$t = t_{departure} - \varepsilon$	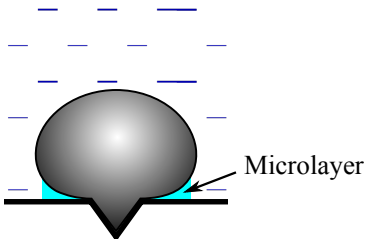	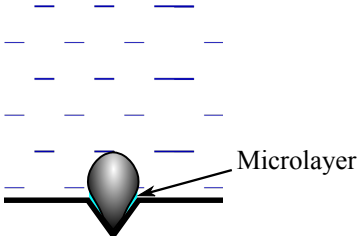
$t = t_{departure} + \varepsilon$	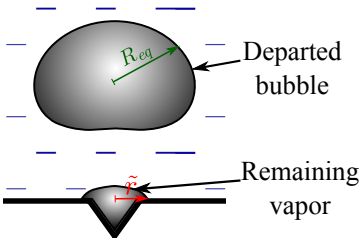	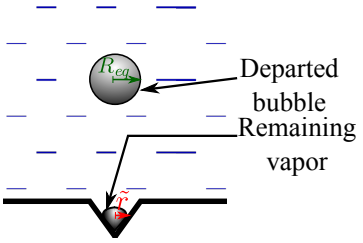

On the contrary, in the present study, a secondary bubble is observed only for vapor pressures ranging from $P_v = 20.0$ kPa ($T_v = 60$ °C) up to $P_v = 70.2$ kPa ($T_v = 90$ °C) (*i.e.* on cases associated with Fig. 3.4 and Fig. 3.5). This difference may be related to the different operating conditions imposed in the different studies (Table 3.3):

Table 3.3 – Imposed vapor pressures P_v, liquid heights H_l and heat fluxes φ_{input} depending on the study.

	Van Stralen *et al.* [119]	**Giraud *et al.* [46]**	**The present study**
P_v (kPa)	From 2.0 up to 26.7	From 0.85 up to 100.0	From 4.2 up to 101.4
H_l (cm)	Unknown	20.0	17.3
φ_{input} ($\mathrm{W \cdot cm^{-2}}$)	Unknown	From 3.1 up to 29.0	2.7

The reasons given by Van Leeuwen [116] and Van Stralen *et al.* [119] can still explain the absence of a secondary bubble for vapor pressures higher than 70.2 kPa ($P_v > 70.2$ kPa, see Fig. 3.6). On the other hand, the absence of a secondary bubble after the departure of the primary bubble and the high-velocity jet of (highly) subcooled liquid for the lowest vapor pressures ($P_v < 20.0$ kPa, refer to Fig. 3.3) may be due to the low imposed heat flux value. The value of $\varphi_{input} = 2.7$ $\mathrm{W \cdot cm^{-2}}$ may indeed be too low to retain the dry spot on the surface during the whole long waiting time that occurs at such low pressures.

3.3 Quantitative results and discussion

3.3.1 Thermal measurements

The study of the heat transfer at the heated wall is made possible through the thermocouples located inside the heater (see Section 2.1.4.1). The wall temperature T_{wall}^{exp}, wall superheat ΔT_{wall} and heat transfer coefficient h are then discussed depending on the pressure in the next sections.

3.3.1.1 Wall temperature T_{wall}

Large wall temperature fluctuations (up to 25 K according to Giraud [44]) constitute a typical characteristic of water pool boiling at subatmospheric pressures: Yavov *et al.* [125, 126], Van Stralen *et al.* [119,121], McGillis *et al.* [76,77], Giraud [44] and Giraud *et al.* [46] reported them. Making the link between the visualization of the bubble dynamics and the monitoring of the wall temperature, Van Stralen *et al.* [119] as well as Giraud [44] noticed that the increase of

the wall temperature T_{wall} slowly takes place during the waiting time whereas its sudden drop occurs during the bubble growth.

However, there are some conditions for which such thermal oscillations do not occur. McGillis *et al.* [76] reported that at heat fluxes higher than 60.0 W · cm^{-2} ($\varphi_{input} \geq 60.0$ W · cm^{-2}), the bubble departure frequency is high enough to get a stable wall temperature. According to Giraud [44], wall temperature fluctuations does not exist for imposed heat fluxes $\varphi_{input} = 27.4$ W · cm^{-2} or higher as well as for heat fluxes lower than 6.3 W · cm^{-2} ($\varphi_{input} \leq 6.3$ W · cm^{-2}). The author explains the absence of such cyclic variations at low heat fluxes by the fact that under those latter conditions the heat is mainly transferred by single phase natural convection rather than by phase change.

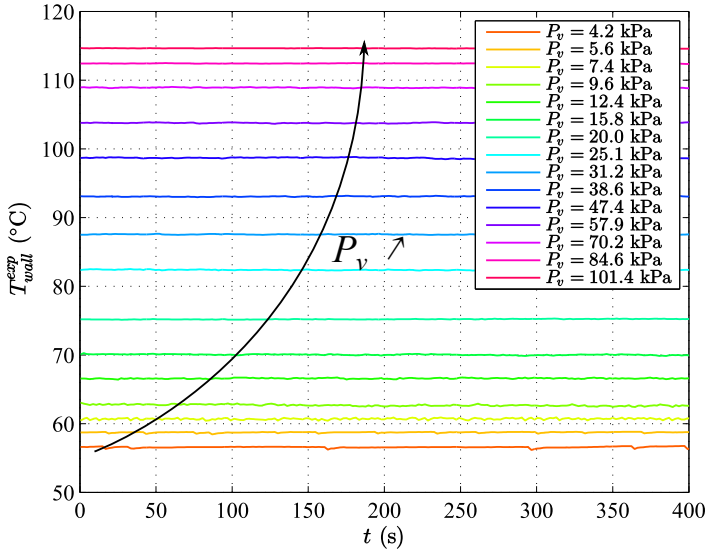

Figure 3.7 – Time evolution of the wall temperature T_{wall}^{exp} for the different investigated vapor pressures P_v (water, $H_l = 17.3$ cm, $\varphi_{input} = 2.7$ W · cm^{-2}).

In agreement with the conclusions from Giraud [44], the time evolution of the wall temperature T_{wall}^{exp} – calculated according to the method described in Section 2.3.1 and displayed on Fig. 3.7 – does not show any cyclic oscillations for the fifteen investigated vapor pressures P_v in the present study (where $\varphi_{input} = 2.7$ W · cm^{-2}).

3.3.1.2 Wall superheat ΔT_{wall}

3.3.1.2.1 Minimal wall superheat models: definition and discussion

Various models are available to determine the minimal wall superheat ΔT_{wall}^{crit} required to initiate bubble nucleation (*i.e.* to obtain a vapor nucleus larger than the critical equilibrium radius R^{crit}). Some simple ones are of analytical nature. This critical wall superheat ΔT_{wall}^{crit} is generally defined as the difference between the critical wall temperature T_{wall}^{crit} and the saturation temperature T_{sat} according to Eq. 3.4. Several relations aimed at representing this quantity are hereafter given.

$$\Delta T_{wall}^{crit} = T_{wall}^{crit} - T_{sat} \tag{3.4}$$

Combining the Clausius-Clapeyron equation:

$$\Delta P \approx \frac{\Delta T \rho_v \Delta h_{lv}}{T_{sat}} \tag{3.5}$$

and the equation of the static equilibrium of a vapor nucleus (*i.e.* the Young-Laplace equation):

$$\Delta P = \frac{2\sigma}{R^{crit}} \tag{3.6}$$

and assuming that the relation postulated by Hsu [56] between the effective cavity size r_{eff}[1] and the radius of equilibrium of a vapor nucleus R^{crit} is valid:

$$r_{eff} = 0.8R^{crit} \tag{3.7}$$

one formulation of this minimal wall superheat is [77]:

$$\Delta T_{wall}^{crit,\,1} = \frac{1.6\sigma T_{sat}}{r_{eff}\rho_v \Delta h_{lv}} \tag{3.8}$$

According to Rohsenow *et al.* [99], in the case of heterogeneous nucleation (*i.e.* when a bubble nucleates on a heated surface), the critical radius R^{crit} can be evaluated depending on the fluid thermophysical properties and on the heat flux:

$$R^{crit} = \sqrt{\frac{2\sigma T_{sat}\nu_v\lambda_l}{\varphi \Delta h_{lv}}} \tag{3.9}$$

Rohsenow *et al.* [99] then give several correlations to estimate the critical wall superheat ΔT_{wall}^{crit} depending on the case:

- If only a temperature gradient localized in the vicinity of the heated surface is considered, the critical wall superheat can be evaluated through Eq. 3.10:

$$\Delta T_{wall}^{crit,\,2} = \sqrt{\frac{8\sigma T_{sat}\nu_v\varphi}{\Delta h_{lv}\lambda_l}} \tag{3.10}$$

- If the distortion of the temperature profile that may be induced by the presence of the bubble is taken into account, assuming that the temperature in the undisturbed boundary layer that should be matched with the critical wall temperature T_{wall}^{crit} is reached at a certain distance of the surface, the following relation is proposed (Eq. 3.11):

$$\Delta T_{wall}^{crit,\,3} = \sqrt{\frac{8\sigma T_{sat}\nu_v\varphi}{\Delta h_{lv}\lambda_l}} Pr_l \tag{3.11}$$

- If the critical radius R^{crit} (calculated through Eq. 3.9) is larger than the largest cavity (radius r_{max}) present on the heated surface, the following correlation is given (Eq. 3.12):

$$\Delta T_{wall}^{crit,\,4} = \frac{2\sigma T_{sat}\nu_v}{r_{max}\Delta h_{lv}} + \frac{\varphi r_{max}}{\lambda_l} \tag{3.12}$$

The thermophysical properties have to be evaluated at the properly chosen state points to estimate the predictions of those analytical models and to compare them with experimental measurements. Those analytical models were however developed in a configuration where the subcooling of the fluid can be neglected so that care must be taken when using them in the present situation where a non negligible subcooling is induced by the static head P^{static}. As a consequence, the starting hypotheses of those models as well as the considered configuration are identified and discussed below.

All the cited critical wall superheat models were developed considering that:

[1] The effective surface cavity size r_{eff} is a constant supposed to be dependent only on the surface characteristics.

($\mathcal{H}_1$) The bulk liquid is homogeneous in temperature at $T_{l,\,bulk} = T_v$.

($\mathcal{H}_2$) Inside the boundary layer which is located above the heated surface and in which the bubble is nucleating, the liquid is superheated at a temperature $T^{crit}_{l,\,BL}$ supposed equal to the critical wall temperature T^{crit}_{wall}.

($\mathcal{H}_3$) The vapor inside the nucleating bubble is both in thermal equilibrium with the liquid of the boundary layer ($T^{crit}_{v,\,bubble} = T^{crit}_{l,\,BL}$) and in the saturation state ($P^{crit}_{v,\,bubble} = P_{sat}(T^{crit}_{v,\,bubble})$).

The two configurations – without and with subcooling respectively – are detailed and compared hereafter[1].

Configuration without subcooling: In this case (depicted on Fig. 3.8), the static head is negligible compared to the vapor pressure ($P^{static} = \rho_l(T_{l,\,bulk})gH_l \ll P_v$[2]), so that:

- The liquid bulk pressure $P_{l,\,bulk}$ is approximately equal to the vapor pressure P_v. Combined with hypothesis ($\mathcal{H}_1$), this implies that the bulk liquid is in the saturation state at $T_{l,\,bulk} = T_v$ and $P_{l,\,bulk} \approx P_v = P_{sat}(T_v)$. On the pressure-temperature diagram schematically given on Fig. 3.8b, the bulk liquid is thus located at the state point labeled $\mathcal{A}$.
- The pressure at the level of the boundary layer is also taken equal to the vapor pressure: $P_{l,\,BL} \approx P_v$. In addition to hypothesis ($\mathcal{H}_2$), this means that the liquid inside the boundary layer, even though being superheated, can be represented at the state point named $\mathcal{B}$ on the phase diagram (Fig. 3.8b).
- According to ($\mathcal{H}_3$), the vapor inside the nucleating bubble is at the state point $\mathcal{C}$ of the phase diagram (Fig. 3.8b).

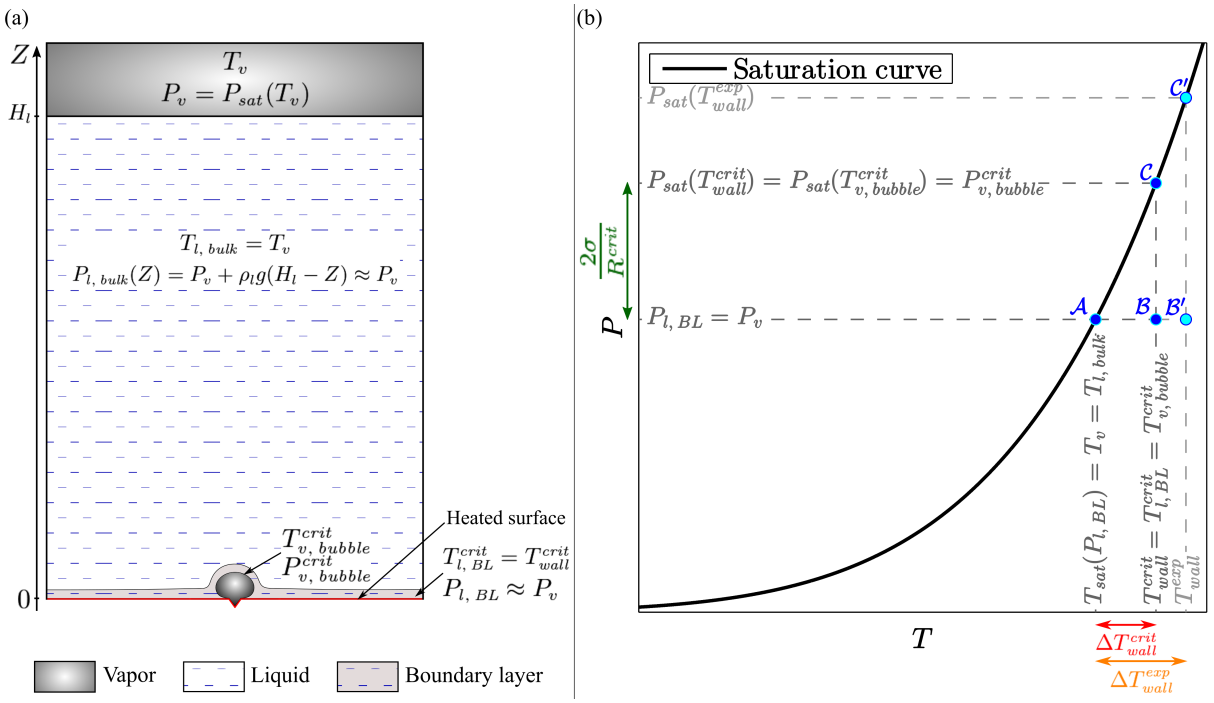

Figure 3.8 – Configuration at nucleation in absence of subcooling: (a) geometry; (b) schematic phase diagram.

[1] For the sake of readability and simplicity, the effect – mentioned and used by Rohsenow *et al.* [99] – of the curvature of the liquid-vapor interface is not reported here. This does not affect the general trends, even at low pressure.

[2] The liquid is assumed to be incompressible: its density only slightly depends on the temperature.

The critical wall superheat is then defined as:

$$\Delta T_{wall}^{crit} = T_{wall}^{crit} - \underbrace{T_{sat}(\overbrace{P_{l,\,BL}}^{P_v})}_{T_v = T_{l,\,bulk}} = T_{wall}^{crit} - T_{l,\,bulk} \tag{3.13}$$

and can be estimated through equations Eq. 3.8, Eq. 3.10, Eq. 3.11 or Eq. 3.12 where:

- T_{sat} is taken as the saturation temperature that would have the liquid in the boundary layer if it would have been in the saturation state (point $\mathcal{A}$) instead of being superheated (point $\mathcal{B}$):

$$T_{sat} = T_{sat}(P_{l,\,BL}) = T_v = T_{l,\,bulk} \tag{3.14}$$

- The properties related to the liquid phase (λ_l, Pr_l) should match the state of the superheated liquid located inside the boundary layer and therefore be evaluated at point $\mathcal{B}$:

$$\lambda_l = \lambda_l(T_{wall}^{crit},\ P_{l,\,BL} = P_v) \tag{3.15}$$

$$Pr_l = Pr_l(T_{wall}^{crit},\ P_{l,\,BL} = P_v) \tag{3.16}$$

  As the concerned properties vary more with the temperature than with the pressure, they would commonly be taken at point $\mathcal{C}$ (which is simpler since this point is at the same temperature but is on the saturation curve): $\lambda_l \approx \lambda_l(T_{wall}^{crit})$ and $Pr_l \approx Pr_l(T_{wall}^{crit})$.

- The properties related to the vapor phase (ρ_v, ν_v) should correspond to the state of the vapor of the nucleating bubble, that is point $\mathcal{C}$:

$$\rho_v = \rho_v(T_{wall}^{crit},\ P_{sat}(T_{wall}^{crit})) \tag{3.17}$$

$$\nu_v = \nu_v(T_{wall}^{crit},\ P_{sat}(T_{wall}^{crit})) \tag{3.18}$$

- The properties related to the liquid-vapor interface (σ, Δh_{lv}) should be estimated in the saturation state associated with the interface temperature, *i.e* at point $\mathcal{C}$:

$$\sigma = \sigma(T_{wall}^{crit},\ P_{sat}(T_{wall}^{crit})) \tag{3.19}$$

$$\Delta h_{lv} = \Delta h_{lv}(T_{wall}^{crit},\ P_{sat}(T_{wall}^{crit})) \tag{3.20}$$

Finally, except for T_{sat} which depends on $T_v = T_{l,\,bulk}$, all the involved properties depend from the unique unknown T_{wall}^{crit}. In fact, authors [99] assume usually that the variations of the thermophysical properties between T_{sat} and T_{wall}^{crit} are small so that they can use the critical wall superheat models with all the parameters evaluated at T_{sat} (*i.e.* at point $\mathcal{A}$).

By definition of the critical wall temperature T_{wall}^{crit}, a higher value T_{wall}^{exp} – corresponding to state points $\mathcal{B}'$ and $\mathcal{C}'$ for the superheated liquid of the boundary layer and for the vapor phase respectively – should be observed experimentally. The difference between this measured temperature and T_{sat} defines the experimental wall superheat ΔT_{wall}^{exp}:

$$\Delta T_{wall}^{exp} = T_{wall}^{exp} - \underbrace{T_{sat}(\overbrace{P_{l,\,BL}}^{P_v})}_{T_v = T_{l,\,bulk}} = T_{wall}^{exp} - T_{l,\,bulk} \tag{3.21}$$

Configuration with a subcooling induced by the static head: In this case (represented on Fig. 3.9), the static head cannot be neglected compared to the vapor pressure, so that:

- The liquid bulk pressure $P_{l,\,bulk}$ varies linearly with the depth ($z = H_l - Z$) between the vapor pressure P_v and the pressure at the wall P_{wall} defined as:

$$P_{wall} = P_v + \underbrace{\rho_l(T_{l,\,bulk})gH_l}_{P^{static}} \tag{3.22}$$

  In association with hypothesis ($\mathcal{H}_1$), this means that the bulk liquid is subcooled along the segment $\mathcal{A}_1\mathcal{A}_2$ shown on the phase diagram given on Fig. 3.9b.
- The pressure at the level of the boundary layer is in this case equal to the pressure at the heated surface level: $P_{l,\,BL} \approx P_{wall}$. Combined with hypothesis ($\mathcal{H}_2$), this implies that the liquid inside the boundary layer is at the state point named $\mathcal{B}$ on the phase diagram (Fig. 3.9b).
- According to ($\mathcal{H}_3$), the vapor inside the nucleating bubble is at the state point $\mathcal{C}$ of the phase diagram (Fig. 3.9b).

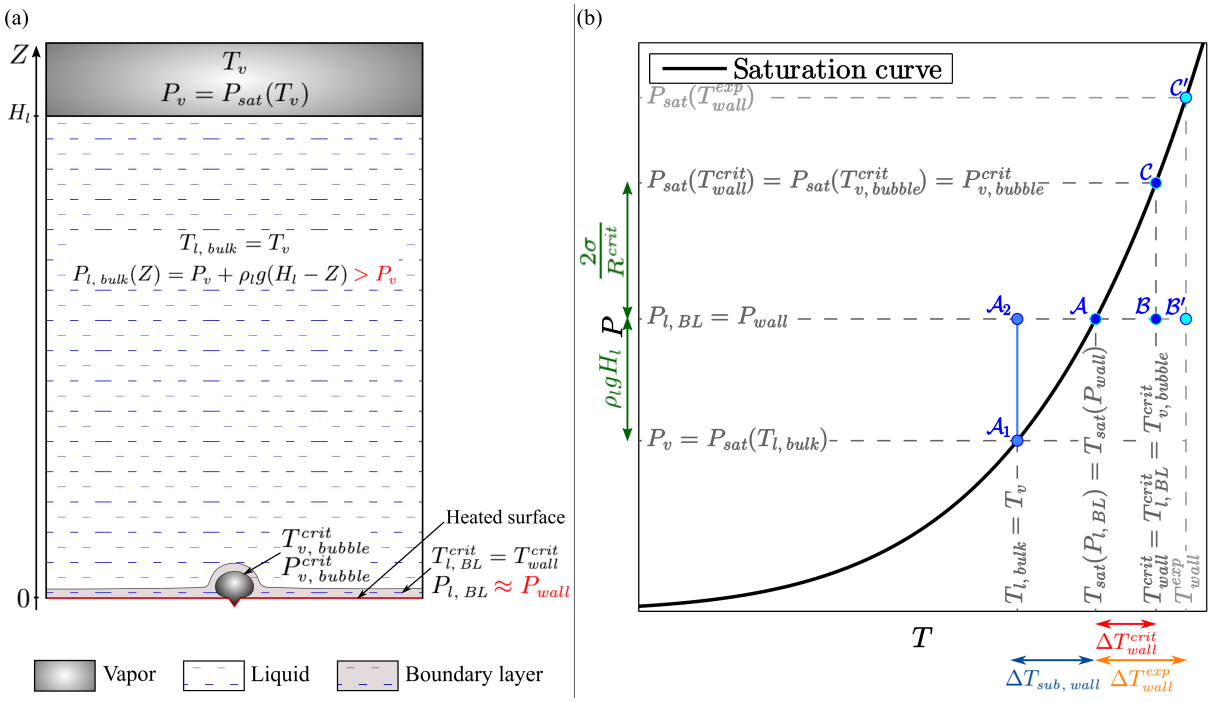

Figure 3.9 – Configuration at nucleation in presence of subcooling: (a) geometry; (b) schematic phase diagram.

The critical wall superheat is then defined as:

$$\Delta T^{crit}_{wall} = T^{crit}_{wall} - T_{sat}(\overbrace{P_{l,\,BL}}^{P_{wall}}) = T^{crit}_{wall} - T_{sat}(P_{wall}) \tag{3.23}$$

and can be estimated through equations Eq. 3.8, Eq. 3.10, Eq. 3.11 or Eq. 3.12 with:

- T_{sat} defined at state point $\mathcal{A}$:

$$T_{sat} = T_{sat}(P_{l,\,BL}) = T_{sat}(P_{wall}) \tag{3.24}$$

- The properties related to the liquid phase evaluated at state point $\mathcal{B}$:

$$\lambda_l = \lambda_l(T^{crit}_{wall},\ P_{l,\,BL} = P_{wall}) \tag{3.25}$$

$$Pr_l = Pr_l(T^{crit}_{wall},\ P_{l,\,BL} = P_{wall}) \tag{3.26}$$

- The properties related to the vapor phase and to the liquid-vapor interface evaluated at state point $\mathcal{C}$:

$$\rho_v = \rho_v(T^{crit}_{wall},\ P_{sat}(T^{crit}_{wall})) \tag{3.27}$$

$$\nu_v = \nu_v(T_{wall}^{crit},\ P_{sat}(T_{wall}^{crit})) \tag{3.28}$$

$$\sigma = \sigma(T_{wall}^{crit},\ P_{sat}(T_{wall}^{crit})) \tag{3.29}$$

$$\Delta h_{lv} = \Delta h_{lv}(T_{wall}^{crit},\ P_{sat}(T_{wall}^{crit})) \tag{3.30}$$

The critical wall temperature T_{wall}^{crit} is finally (again) the unique unknown to be determined to be able to use those analytical models of minimal wall superheat. In the present case, this is done by means of the iterative process schematically described on Fig. 3.10:

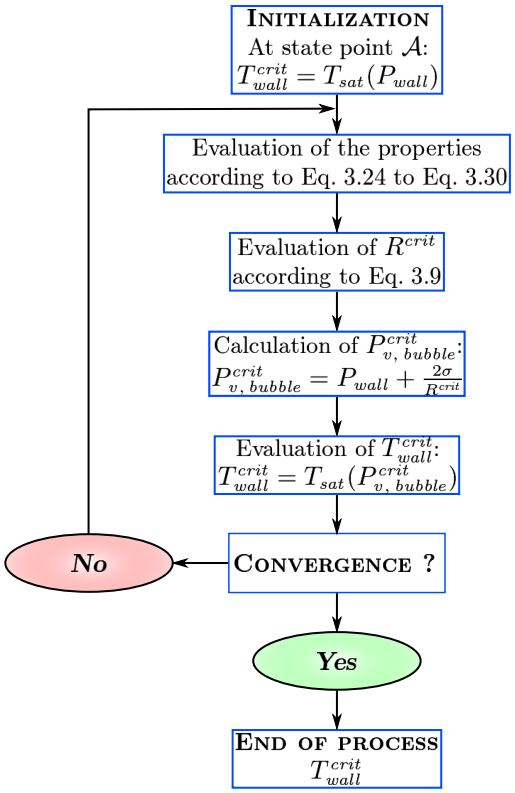

Figure 3.10 – Iterative process used for the determination of T_{wall}^{crit}.

The determination of this critical wall temperature enables the definition of another critical wall superheat $\Delta T_{wall}^{crit,\,0}$ as:

$$\Delta T_{wall}^{crit,\,0} = T_{wall}^{crit} - T_{sat}(\overbrace{P_{l,\,BL}}^{P_{wall}}) = T_{wall}^{crit} - T_{sat}(P_{wall}) \tag{3.31}$$

to be compared to the models $\Delta T_{wall}^{crit,\,1}$ (Eq. 3.8), $\Delta T_{wall}^{crit,\,2}$ (Eq. 3.10), $\Delta T_{wall}^{crit,\,3}$ (Eq. 3.11) and $\Delta T_{wall}^{crit,\,4}$ (Eq. 3.12) as well as to the experimental value $\Delta T_{wall}^{exp} = T_{wall}^{exp} - T_{sat}(P_{wall})$.

The difference between the wall temperature T_{wall} and the bulk temperature $T_{l,\,bulk} = T_v$ then corresponds to the sum of the subcooling degree at the level of the heated surface $\Delta T_{sub,\,wall}$ and of the wall superheat ΔT_{wall}. This quantity represents the superheat that exists between the heated wall and the fluid far from the heated surface (*i.e.* the rest of the system):

$$\Delta T_{wall}^{sys} = T_{wall} - T_{l,\,bulk} = \Delta T_{wall} + \Delta T_{sub,\,wall} \tag{3.32}$$

In absence of subcooling, the wall superheat ΔT_{wall} and the system wall superheat ΔT_{wall}^{sys} are obviously coinciding. Otherwise, the distinction has to be made between those two characteristics. The wall superheat ΔT_{wall} indeed characterizes the local superheat that occurs between the wall and the boundary layer and that is high enough or not to enable the nucleation of a bubble. On the contrary, the system wall superheat ΔT_{wall}^{sys} is a global characteristic parameter of the system and is the relevant parameter for the calculation of the heat transfer coefficient h observed at the wall.

3.3.1.2.2 Comparison between models and measurements

In the present case, as demonstrated on Fig. 3.2, the level of subcooling has to be considered (at least for the lowest investigated pressure levels). As a consequence, the iterative process from Fig. 3.10 was implemented for each pressure level before to evaluate the various parameters and/or thermophysical properties according to Eq. 3.24 to Eq. 3.30 with the database REFPROP [71].

The critical radius R^{crit} is then estimated according to Eq. 3.9 and compared to the radius of the largest cavity located on the heated surface. As the heated wall is mirror-polished, the largest cavity corresponds to the artificial nucleation site so that $r_{max} = r_{cav} = 55$ µm.

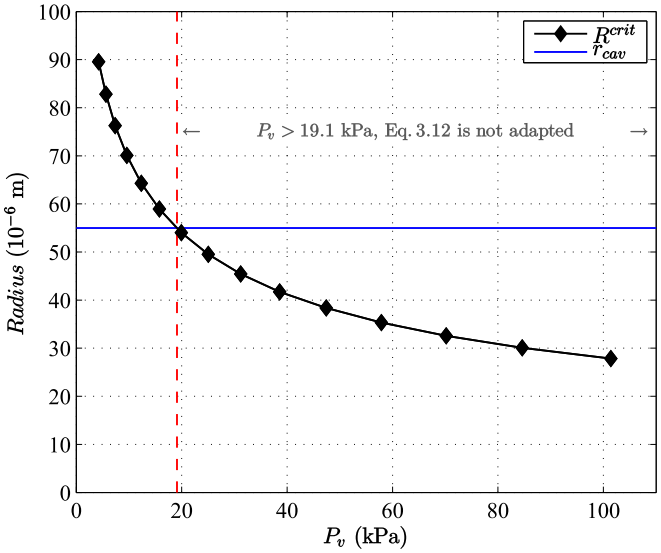

Figure 3.11 – Comparison of the critical equilibrium radius R^{crit} and the radius of the artificial nucleation site r_{cav} depending on the vapor pressure P_v.

According to Fig. 3.11, Eq. 3.12 seems to be adapted to the calculation of the minimal superheat only for vapor pressures lower than 19.1 kPa since the critical radius exceeds then the radius of the cavity ($R^{crit} > r_{cav}$).

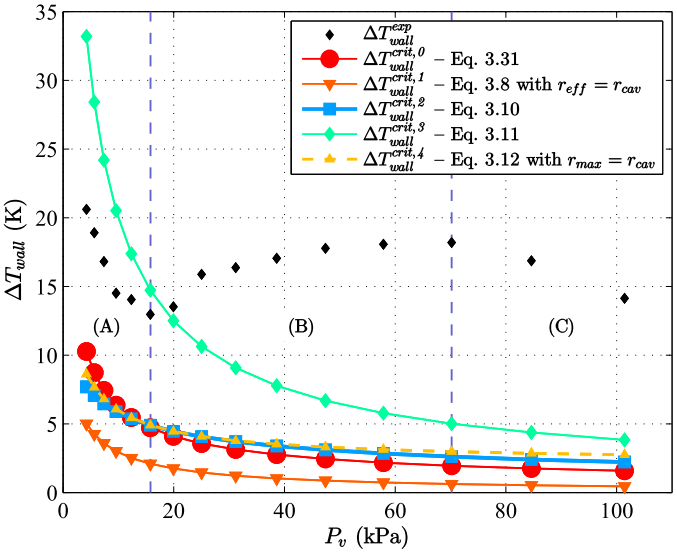

Figure 3.12 – Measured wall superheat ΔT_{wall}^{exp} vs the vapor pressure P_v and comparison with the theoretical minimal wall superheats required to activate boiling $\Delta T_{wall}^{crit,0}$, $\Delta T_{wall}^{crit,1}$, $\Delta T_{wall}^{crit,2}$, $\Delta T_{wall}^{crit,3}$ and $\Delta T_{wall}^{crit,4}$ obtained through Eq. 3.31, Eq. 3.8, Eq. 3.10, Eq. 3.11 and Eq. 3.12 respectively (water, $H_l = 17.3$ cm, $\varphi_{input} = 2.7$ W · cm^{-2}).

Critical wall superheats $\Delta T_{wall}^{crit,\,0}$, $\Delta T_{wall}^{crit,\,1}$, $\Delta T_{wall}^{crit,\,2}$, $\Delta T_{wall}^{crit,\,3}$ and $\Delta T_{wall}^{crit,\,4}$ (calculated[1] through Eq. 3.31, Eq. 3.8, Eq. 3.10, Eq. 3.11 and Eq. 3.12 respectively) are reported as a function of the vapor pressure P_v on Fig. 3.12. The measured wall temperature T_{wall}^{exp} being steady (with a minor dispersion around its mean value) for each test done at a given vapor pressure, time-averaged values are considered to evaluate the experimental[2] wall superheat ΔT_{wall}^{exp} values which are also displayed on Fig. 3.12.

Several observations can be made from this graph:

- The five curves associated with the correlations for the critical wall superheat ΔT_{wall}^{crit} present the same decreasing shape with the pressure and are relatively close to each other.
- Curves related to Eq. 3.31, Eq. 3.10 and Eq. 3.12 (*i.e.* $\Delta T_{wall}^{crit,\,0}$, $\Delta T_{wall}^{crit,\,2}$ and $\Delta T_{wall}^{crit,\,4}$) are very close to each other: they are almost superimposed even in the range of pressure where Eq. 3.12 should *a priori* be not valid because of size of the critical equilibrium radius R^{crit} (compared to the cavity size r_{cav}). Since the Prandtl number Pr_l of the liquid decreases, the curve obtained through Eq. 3.11 becomes closer to the three others as the pressure increases. The curve corresponding to the simplest model (*i.e.* related to $\Delta T_{wall}^{crit,\,1}$ and Eq. 3.8) is always slightly below the curves of the other models.
- The evolution of the measured wall superheat ΔT_{wall}^{exp} with the vapor pressure can be divided into three domains:

  (A) $\boldsymbol{P_v \leq 15.8}$ **kPa** $\boldsymbol{(T_v \leq 55}$ **°C):** In agreement with the evolution of the theoretical minimal values, the measured wall superheat decreases rapidly with the pressure. As $\Delta T_{wall}^{crit,\,0}$, $\Delta T_{wall}^{crit,\,1}$, $\Delta T_{wall}^{crit,\,2}$ and $\Delta T_{wall}^{crit,\,4}$ are smaller than the experimental values, relations given in Eq. 3.31, Eq. 3.8, Eq. 3.10 and Eq. 3.12 still seem valid in this range of pressure. On the contrary, the superheat $\Delta T_{wall}^{crit,\,3}$ calculated through Eq. 3.11 is larger than ΔT_{wall}^{exp}: this correlation may be not adapted to water boiling at such low pressure levels and heat flux.

  (B) **20.0 kPa** $\boldsymbol{\leq P_v \leq}$ **70.2 kPa (60 °C** $\boldsymbol{\leq T_v \leq}$ **90 °C):** Contrary to the decreasing evolution of the correlations, the wall superheat experimentally measured ΔT_{wall}^{exp} slowly increases with the vapor pressure P_v.

  (C) $\boldsymbol{P_v >}$ **70.2 kPa** $\boldsymbol{(T_v >}$ **90 °C):** The measured wall superheat decreases slowly as the pressure P_v increases.

Table 3.4 – Correspondence between the vapor pressure range, the observed bubble shape and the evolution of the experimental wall superheat T_{wall}^{exp} (water, $H_l = 17.3$ cm, $\varphi_{input} = 2.7$ W · cm^{-2}).

Domain	**Vapor pressure range**	**Bubble shape**	**Evolution of the wall superheat $\boldsymbol{\Delta T_{wall}^{exp}}$**
(A)	$P_v \leq 15.8$ kPa ($T_v \leq 55$ °C)	– Oblate spheroid – No bubble interaction	Rapid decrease
(B)	20.0 kPa $\leq P_v \leq$ 70.2 kPa (60 °C $\leq T_v \leq$ 90 °C)	– Mushroom or mushroom and column – Bubble interaction	Slow increase
(C)	$P_v > 70.2$ kPa ($T_v > 90$ °C)	– Near-spherical – No bubble interaction	Slow decrease

[1] As the centered artificial nucleation site is the only active cavity in this study, the effective surface cavity size r_{eff} is here taken as its radius: $r_{eff} = r_{cav} = 55$ µm.

[2] The uncertainty on the experimentally evaluated wall superheats is of ± 0.3 K and is consequently too small to be reported with error bars on Fig. 3.12.

As shown in Table 3.4, a relationship can be established between the domains (A), (B) and (C) and the vapor pressure ranges where the different bubble shapes are encountered. The slow increase of the wall superheat in domain (B) can therefore be attributed to the interaction between successive bubbles that occurs in this pressure range. More precisely, the increase of the wall superheat may be caused by the presence of the remaining dry area (on the heated wall after a bubble departure), which locally augments the wall temperature. This local increase of the wall temperature seems to be important enough to counterbalance the decrease of this parameter (and thus of the wall superheat) that is expected to occur since the bubble departure frequency increases[1].

3.3.1.3 Heat transfer coefficient h

The thermal measurements also enable the evaluation of the heat transfer coefficient h at the heated surface according to Eq. 3.33. The calculation and the related uncertainties are detailed in Appendix B.

$$h = \frac{\varphi}{\Delta T_{wall}^{sys}} \tag{3.33}$$

Whatever the vapor pressure P_v imposed during this experimental campaign, the heat transfer coefficient h is relatively low: it ranges from $h = 1000$ to $2100\ \mathrm{W \cdot m^{-2} \cdot K^{-1}}$. In agreement with the literature [102, 125, 131], this result highlights that the heat transfer is degraded at low pressure since natural convection has a larger effect than phase change. However, close to atmospheric pressure ($P_v \approx P_{atm} = 101.4$ kPa) the heat transfer coefficient could have been expected to be higher. Actually, the low surface roughness also affects the heat transfer: during the present experiments, at higher pressure, even though a few cavities were activated besides the artificial nucleation site at this imposed heat flux, the wall superheat at nucleation remained relatively high. Several authors [62, 66, 76] showed indeed that – for a given imposed heat flux – the higher the roughness of the heated wall, the higher the heat transfer coefficient. They attributed this to larger active cavity sizes (on rougher surfaces). According to this observation, it appears that – at this heat flux – the heat transfer at the wall might be more affected by the heated surface condition than by the pressure or the bubbles sizes and shapes.

Having a smooth surface with an artificial cavity is thus not neutral on the heat transfer despite the fact it is a widely used technique for the study of the bubble dynamics and – in a more general way – of the boiling phenomenon at the scale of single bubbles [82–84, 96, 105]. Actually this questions the physical meaning of the heat transfer coefficient h in such a situation. On a natural surface (*i.e.* a surface with a given roughness and no artificial site), less and less cavities are activated as the pressure decreases [44,76,77,102,131]. At low pressure, the present configuration (a smooth surface with a single active cavity) yields thus a distritution of activated nucleation sites not so different from the one occurring on a raw surface, so that the heat transfer coefficient is making sense as a classical engineering tool. The experimental values of h determined during this study for the lowest pressures are of the same order of magnitude as those given in the literature for low pressure pool boiling on natural surfaces [102, 131]. On the contrary, close to the atmospheric pressure – *i.e.* in the region where numerous nucleation sites should be active – the present surface leads to the occurrence of boiling mostly at the artificial cavity. The calculated heat transfer coefficient is then more representative of a heat transfer for single phase natural convection than for phase change.

3.3.2 Bubble dynamics

Some characteristics of the bubble dynamics can be calculated from the video recordings using the in-house image processing tool described in Section 2.3.2. The evolution of those character-

[1] One should however keep in mind that some features of the setup (in particular the ones inherent to the quality of the artificial nucleation site such as its geometry or its purity) may also disturb the analysis and thus explain some discrepancies between experimental and theoretical results and trends.

istics depend on the pressure as analyzed and discussed hereafter.

However, not all the video files were processed due to the limitations of the automatic detection of bubbles contours. As a consequence, the results presented here correspond only to the analysis of the recordings made for vapor pressures lower than 20.0 kPa ($P_v \leq 20.0$ kPa ($T_v \leq 60$ °C)):

- For $P_v \leq 15.8$ kPa ($T_v \leq 55$ °C), there is no interaction between successive bubbles (oblate spheroid bubbles) and an automatic treatment of the pictures could be implemented to localize the interfaces of the growing bubbles (Fig. 3.13a).

- At $P_v = 20.0$ kPa ($T_v = 60$ °C), successive bubbles are interacting by pairs (mushroom shaped bubbles) but the edges of individual growing bubbles can be easily identified with the naked eye. A manual treatment was then performed (Fig. 3.13b and Fig. 3.13c).

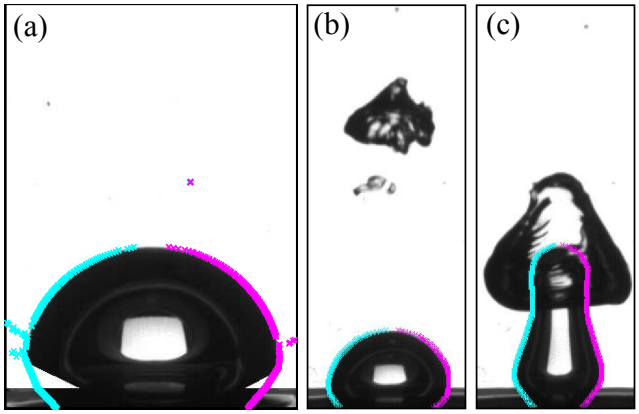

Figure 3.13 – Representative processed images after (a) an automatic treatment for a bubble of water obtained at $P_v = 9.6$ kPa ($T_{sat} = 45$ °C) or after a manual treatment for (b) a primary or (c) a secondary bubble of water obtained at $P_v = 20.0$ kPa ($T_{sat} = 60$ °C) ($H_l = 17.3$ cm and $\varphi_{input} = 2.7$ W · cm^{-2}).

- For $20.0 < P_v \leq 70.2$ kPa (60 °C $< T_v \leq 90$ °C), successive bubbles are interacting and the edges of individual growing bubbles cannot be clearly seen with the naked eye (mushroom and column shaped bubbles). The recordings were not image-processed.

- For $P_v > 70.2$ kPa ($T_v > 90$ °C), there is no bubble interaction (near-spherical bubbles) but the bubbles are small (size of a few millimeter) and depart from the wall after a very short growth time. Despite the high-speed camera acquisition frequency, only one or two pictures show(s) a bubble during its growth. In addition, it is difficult to discern such a growing bubble from the shadow zone caused by the glue seal (even with the naked eye). The recordings were not image-processed either.

3.3.2.1 Effect of the pressure on the bubble growth duration τ_{growth}

The growth duration τ_{growth} was calculated for any bubble whose entire growth had been recorded and processed (*i.e.* 102 bubbles in total) according to Eq. 2.11. Results depending on the vapor pressure P_v are displayed on Fig. 3.14[1]. As noticed in Section 3.2, the lower the pressure, the larger the bubble growth time.

[1]The uncertainty on the growth time (±1 to 2 ms) is too low to be represented with error bars on this graph.

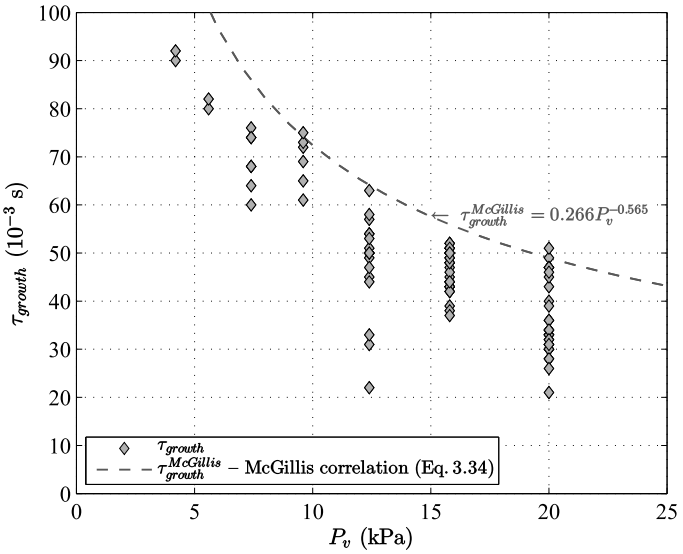

Figure 3.14 – Dependence of bubble growth duration τ_{growth} on the vapor pressure P_v (water, $H_l = 17.3$ cm, $\varphi_{input} = 2.7$ W · cm^{-2}).

Based on the experimental data obtained by Van Stralen *et al.* [119], McGillis *et al.* [77] determined an empirical correlation between the bubble growth duration and the saturated vapor pressure in water subatmospheric pressure pool boiling:

$$\tau_{growth}^{McGillis} = 0.266 P_v^{-0.565} \tag{3.34}$$

where $\tau_{growth}^{McGillis}$ is in seconds and P_v in kilopascals. This correlation is plotted on Fig. 3.14. Beyond the scattering of the experimental points caused by the random character of the boiling phenomenon, this correlation seems to over-estimate the experimental data of the present study. Although the operating conditions are different in [119] from those of the current work, it may reinforce the idea that the approach where the static head pressure P^{static} is neglected is not valid for the study of pool boiling at low pressure. As a consequence, the pressure P_{wall} at the heated surface level is now considered:

$$P_{wall} = P_v + P^{static} \tag{3.35}$$

i.e. in the present case:

$$P_{wall} = P_v + P^{static}_{H_l = 17.3 \text{ cm}} \approx P_v + 1.7 \tag{3.36}$$

where all the terms are in kilopascals.

Figure 3.15[1] then shows the experimental data depending on the pressure considering either the vapor pressure P_v or the pressure at the wall level P_{wall}. McGillis correlation is reported as well as a new one. The latter is actually a fit made on our experimental points which has the same model as the relation given by McGillis but considers the pressure at the wall P_{wall} instead of the vapor pressure P_v:

$$\tau_{growth} = 0.333 P_{wall}^{-0.708} \tag{3.37}$$

where τ_{growth} is still in seconds and P_{wall} in kilopascals.

The root mean square error (RMSE) of the new fit remains relatively high (RMSE = 7.34 ms while τ_{growth} varies from 21 ms to 92 ms in the dataset). As a consequence, it would have been interesting to test this relationship on the experimental points collected by Van Stralen *et*

[1] The uncertainty on the growth time (±1 to 2 ms) is still too low to be represented with error bars on this graph.

al. [119] to strengthen the current approach. This is yet not possible since the authors did not mention the height of liquid they used during their test campaign.

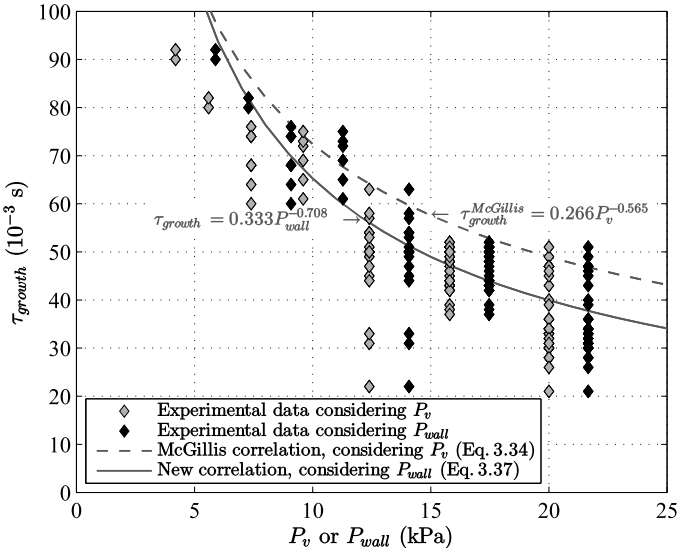

Figure 3.15 – Dependence of bubble growth duration τ_{growth} on the pressure, including or not the static head (water, $H_l = 17.3$ cm, $\varphi_{input} = 2.7$ W $\cdot$ cm^{-2}).

3.3.2.2 Dependence of the waiting time τ_{wait} on the pressure

The waiting time τ_{wait} that separates the departure of a bubble from the wall and the nucleation of a subsequent bubble was evaluated according to Eq. 2.12 each time it was possible. In other words, this characteristic parameter of the bubble dynamics was measured when at least two bubbles were recorded on the same video file ($N \geq 2$) and then between every bubble whose entire growth was observed. As it was impossible to catch two bubbles during a unique image acquisition for vapor pressure lower than 7.4 kPa ($T_v = 40$ °C) even when reducing the acquisition frequency, measurement of the waiting time was performed only for pressures ranging from $P_v = 7.4$ kPa ($T_v = 40$ °C) to $P_v = 20.0$ kPa ($T_v = 60$ °C)[1].

Results, depending on the vapor pressure P_v, are reported on Fig. 3.16[2]. In agreement with the observations made in Section 3.2, the waiting time increases significantly as the pressure decreases: it is thus equal to about 10 ms at $P_v = 20.0$ kPa ($T_v = 60$ °C) whereas it is of the order of 1000 ms at $P_v = 7.4$ kPa ($T_v = 40$ °C). The very large size of bubbles obtained at low pressure amplifies the (already intense) liquid movements caused by their departure from the wall. Those flows combined to the high subcooling of the liquid can therefore explain that a long time is required to get a new bubble subsequently to the detachment of a former one under such condition. The liquid close to the wall indeed has to be re-heated enough to trigger a new nucleation event. The evolution of the waiting time τ_{wait} with the the subcooling degree evaluated at the level of the heated wall $\Delta T_{sub,\,wall}$ can also be analyzed from Fig. 3.16. In agreement with the literature, one can then remark that the waiting time increases with the level of subcooling at the wall. In particular, a study of the effect of a uniform subcooling on bubble waiting and growth times for water boiling at atmospheric pressure on a copper surface conducted by Ibrahim and Judd [58] deserves to be considered. Investigating experimentally a subcooling degree varying from 0 K to 15 K for different values of imposed heat flux, the authors observed that the waiting period duration increases as the liquid subcooling increases until the latter reaches a value of about 6 K. Then, the waiting time decreases as the subcooling is further increased. They therefore questioned the ability of the conventional nucleation theory to predict

[1] As a reminder, at higher vapor pressures, contacts between successive bubbles make the analysis of individual growing bubbles not possible.

[2] Here again, the uncertainty on the waiting period (±1 to 2 ms) is too low to be represented with error bars on this graph.

the bubble waiting time at high degrees of subcooling. In such a case, they indeed suggested that – in addition to the one-dimensional transient conduction mechanism generally assumed – some convective mechanism may contribute to transfer heat from the heated surface to the liquid bulk, so that the waiting period can be reduced. In the present work, only an increase of the waiting time with the subcooling is observed (Fig. 3.16). This result is in agreement with Ibrahim and Judd [58] since the level of subcooling $\Delta T_{sub,\,wall}$ at the wall does not exceed 6 K for our experimental dataset.

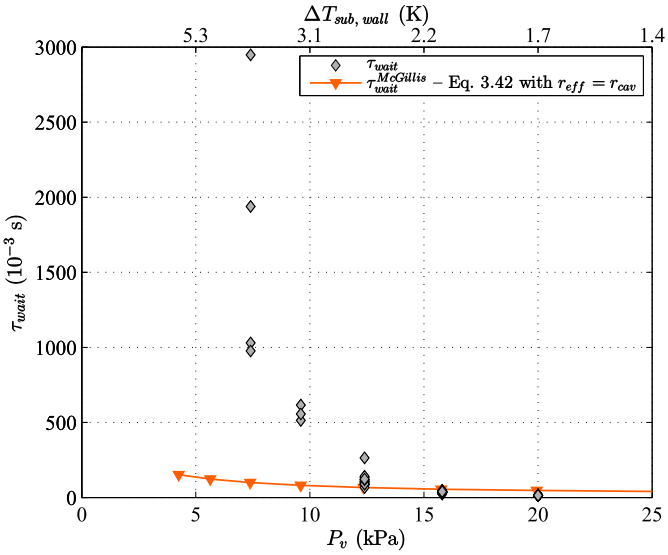

Figure 3.16 – Dependence of waiting period between successive bubbles τ_{wait} on the vapor pressure P_v and on the subcooling degree evaluated at the level of the heated wall $\Delta T_{sub,\,wall}$ (water, $H_l = 17.3$ cm, $\varphi_{input} = 2.7$ W $\cdot$ cm^{-2}).

On this graph (Fig. 3.16), each point corresponds to an actual waiting time between two successive bubbles but several points can actually be superimposed:

- At the highest considered pressures, experimental points are numerous with almost no scattering of the values: many bubbles are recorded on the same video even with a high acquisition frequency while the bubble production is repeatable and stable.
- On the contrary, at the lowest regarded pressures, bubbles recorded on a unique video become scarce even when the acquisition frequency of the camera is decreased. In addition, the waiting time values corresponding to those few bubbles are largely scattered (values varying from about 1 s to 3 s). This large scattering could be explained by the stochastic nature of the liquid flows that are engendered by the departure and collapse of a former bubble. The nucleation as well as the dynamics of a given bubble is thus strongly influenced by the history of the previous one and its consequences on the boiling environment (liquid motion in particular).

A curve corresponding to a correlation for the waiting period developed by McGillis *et al.* [77] is also displayed on Fig. 3.16. The approach implemented by McGillis *et al.* [77] to predict the waiting time that takes place between the departure of a bubble from the surface and the nucleation of a new bubble followed the subsequent stages:

Choice of the model for the determination of the temperature distribution of the fluid in the vicinity of the heated wall: As the no-slip boundary condition imposed at the solid surface reduces considerably the intensity of the convection close to the wall, the authors consider a transient conduction model to determine the local temperature field (in agreement with Han and Griffith [52]). They then refer to the solution for the temperature distribution during transient conduction of heat into a semi-infinite medium (solid or quasi-static fluid) with the boundary condition of uniform temperature and constant heat flux given by Carslaw and Jaeger [14]:

$$\Delta T_{cond}(Z,t) = \frac{2\varphi}{\lambda}\left[\left(\frac{\alpha t}{\pi}\right)^{0.5}\exp\left(\frac{-Z^2}{4\alpha t}\right) - \frac{Z}{2}\,\mathrm{erfc}\left(\frac{Z}{2(\alpha t)^{0.5}}\right)\right] \tag{3.38}$$

Choice of the boundary condition: They assume that at the end of the waiting period (*i.e.* at $t = \tau_{wait}$), the whole bubble nucleus is superheated by the critical superheat ΔT_{wall}^{crit} required to onset the nucleation. This condition is even strengthen [56] by imposing that this minimal superheat is reached at ($Z = r_{eff}$, $t = \tau_{wait}$):

$$\Delta T_{cond}(Z = r_{eff},\, t = \tau_{wait}) = \Delta T_{wall}^{crit} \tag{3.39}$$

Analytical resolution of the problem:

The authors choose to consider the minimal superheat correlation that derives both from the Clausius-Clapeyron equation and from the equation of the static equilibrium of a vapor nucleus (demonstrated in Section 3.3.1.2 and recalled below):

$$\Delta T_{wall}^{crit,\,1} = \frac{1.6\sigma T_{sat}}{r_{eff}\rho_v \Delta h_{lv}} \tag{3.40}$$

They then perform a linearization of Eq. 3.38 (valid within short times or small penetration depths):

$$\Delta T_{cond}(Z,t) \approx \frac{2\varphi}{\lambda}\left[\left(\frac{\alpha t}{\pi}\right)^{0.5} - \frac{Z}{2}\right] \tag{3.41}$$

Substituting those two quantities in Eq. 3.39, they finally obtain the following relation for τ_{wait}:

$$\tau_{wait} = \frac{\pi\lambda_l\rho_l c_{pl}}{4\varphi^2}\left[\underbrace{\frac{1.6\sigma T_{sat}}{r_{eff}\rho_v\Delta h_{lv}}}_{\Delta T_{wall}^{crit,\,1}} + \frac{r_{eff}\varphi}{\lambda_l}\right]^2 \tag{3.42}$$

Comparison to experimental data: In order to compare their predicted and experimental values of waiting time, McGillis *et al.* needed to estimate the effective surface cavity size r_{eff}. As they conducted tests on a copper surface finished with emery paper which did not present any artificial cavity, they evaluated this parameter by fitting Eq. 3.42 to the measured waiting time for a given operating point[1]. They afterwards obtained a good agreement between experimental and theoretical waiting periods over the full range of operating conditions they investigated.

The waiting period is strongly related to the configuration at the instant of nucleation since it corresponds to the time required, after the detachment of a bubble, to re-heat sufficiently the liquid contained in the boundary layer to trigger a new bubble inception event. As a consequence the correlation proposed by McGillis *et al.* [77] is here evaluated by estimating the thermophysical properties (using REFPROP [71]) in the state conditions defined in Section 3.3.1.2 in the case with subcooling. The effective cavity size r_{eff} is again taken as the radius of the artificial nucleation site r_{cav} since this site constitutes the only active cavity.

[1] One should note that this method of determination of the effective cavity size may lead to different values of r_{eff} depending on the experimental point taken as reference for the fit. In such a case, the assumption made by McGillis *et al.* [77] according to which the effective cavity size is *"a constant which is presumed to be a function of surface characteristics alone"* is no longer valid.

As visible on Fig. 3.16, there is a good agreement between this correlation and the experimental data for vapor pressures higher than 12.4 kPa ($P_v \geq 12.4$ kPa). At lower vapor pressure levels, the correlation from McGillis does not predict properly the experimental waiting time. This is most likely due to the linearization of the transient conduction model (*i.e.* of Eq. 3.38 given in Eq. 3.41). This simplification is indeed valid only for short times or small penetration depths but the measured waiting time does not reach this condition for pressures lower than 12.4 kPa since – considering mean values for each pressure level – $\tau_{wait}(P_v < 12.4 \text{ kPa}) > 0.1$ s (*i.e.* $\tau_{wait}(P_v < 12.4 \text{ kPa}) \not\ll 1$ s).

Some extensions of the approach developed by McGillis *et al.* [77] are presented and discussed in comparison with the current experimental results in Appendix C. As no satisfying agreement between this approach and our experimental data is found, a fit of our experimental measurements of τ_{wait} is performed in function of the pressure at the heated wall P_{wall} on Fig. 3.17 in a similar way as what was done in the previous section.

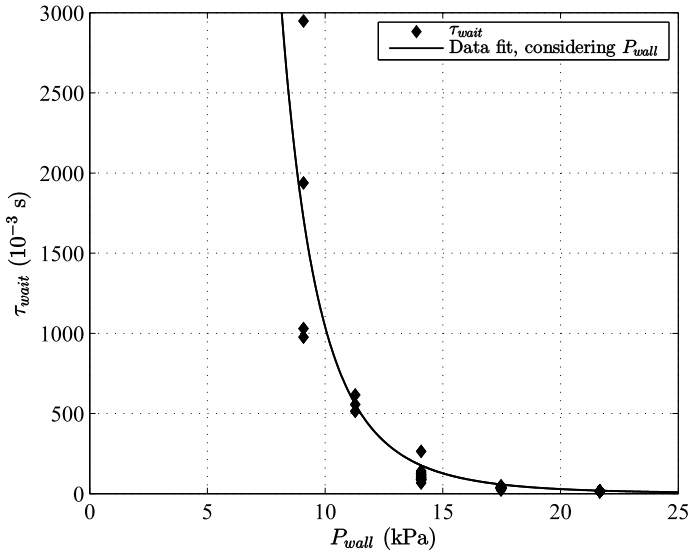

Figure 3.17 – Dependence of waiting period between successive bubbles τ_{wait} on the pressure at the heated surface level P_{wall} (water, $H_l = 17.3$ cm, $\varphi_{input} = 2.7$ W $\cdot$ cm^{-2}).

3.3.2.3 Bubble departure frequency f

The bubble departure frequency f was estimated according to Eq. 2.13 – within an uncertainty of 4 % – for the same files as for the calculation of the waiting time. Measured values are then reported on Fig. 3.18[1].

As the bubble frequency is generally defined as the inverse of the sum of the growth time and the waiting time [26, 52, 134]:

$$f = \frac{1}{\tau_{growth} + \tau_{wait}} \tag{3.43}$$

values of departure frequency obtained from experimental mean values of growth and waiting time as well as from the data fits of those two characteristics are also displayed on Fig. 3.18 for comparison. A good agreement between these three ways of evaluating the bubble departure frequency is thus noticed (in spite of the scattering observed on τ_{growth} and τ_{wait}).

Consequently to Eq. 3.43, one can conclude from the two previous sections (Sections 3.3.2.1 and 3.3.2.2) that the increase of the bubble departure frequency with the pressure is more related to the decrease of the waiting period than to the decrease of the bubble growth duration: while

[1] Several frequencies are visible for a given pressure since several videos were treated for each pressure.

the waiting time τ_{wait} is divided by 100 in the studied range of rising pressure, the growth time τ_{growth} is only divided by a factor 2.

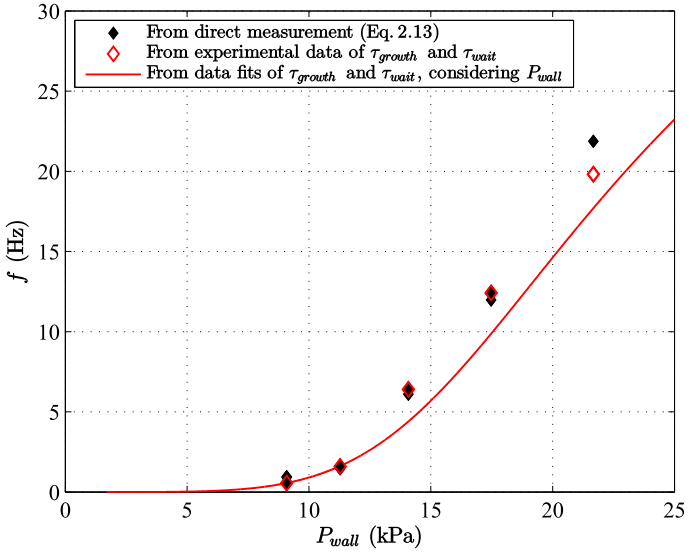

Figure 3.18 – Dependence of the bubble departure frequency f on the pressure at the heated surface level P_{wall} (water, $H_l = 17.3$ cm, $\varphi_{input} = 2.7$ W $\cdot$ cm^{-2}).

3.3.2.4 Bubble growth curves

Contrary to other studies [26, 40, 43, 70, 80, 93] where bubble growths were investigated in terms of time variations of the bubble radius/diameter (or equivalent radius/diameter, *i.e.* the radius/diameter of a sphere of the same volume), the volume V is here – as in [104, 105] – chosen as the main parameter of bubble growth since the observed bubbles clearly do not present a spherical or truncated spherical shape.

3.3.2.4.1 Dimensional growth curves

The time evolution of the instantaneous volume V can be measured and plotted for each bubble between its nucleation and departure according to the calculation method described in Section 2.3.2.3.

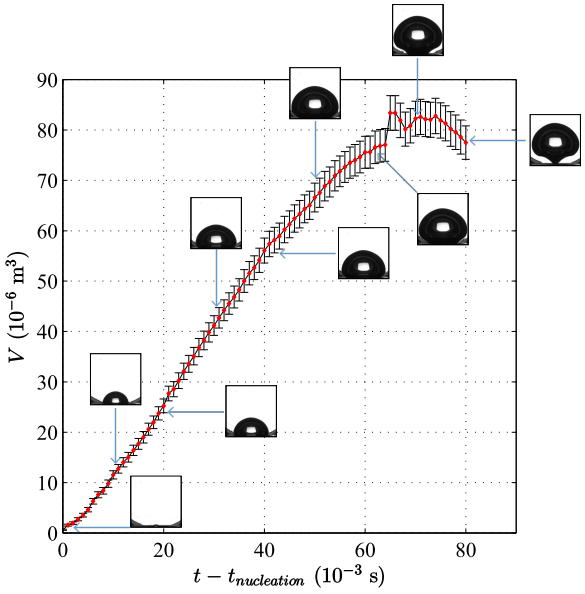

Figure 3.19 – Typical dimensional growth curve of a bubble (water, $P_v = 5.6$ kPa ($T_v = 35$ °C), $H_l = 17.3$ cm, $\varphi_{input} = 2.7$ W $\cdot$ cm^{-2}).

The growth curve of a bubble obtained for $P_v = 5.6$ kPa ($T_v = 35$ °C) is displayed on Fig. 3.19. This curve presents a small peak between $t = 60$ ms and $t = 70$ ms which is in fact caused by the limitations of the image processing program. As visible with the pictures corresponding to these two instants also shown on Fig. 3.19, the size of the dry area under the bubble (*i.e.* the size of the bubble foot) is quickly and significantly reduced during this short lapse of time. The image processing software is then limited by two simultaneous problems that occur at the bottom of the bubble: the presence of the shadow zone (due to the glue seal) and the presence of the viewport. The combination of those two issues leads to a poor detection of the liquid-vapor interfaces in this region, resulting in an overestimation of the volume during a few milliseconds. Despite this peak, one can see on Fig 3.19 that the instantaneous volume V increases almost linearly with time during a large portion of the growth. An additional result is that the volume slightly decreases just before the bubble departure: the bubble starts already to condense because of the subcooling degree of the surrounding liquid.

The error bars shown on Fig. 3.19 correspond to the uncertainty related to the random error made while selecting automatically the liquid-vapor interfaces' pixels. Considering a deviation of ±3 pixels on the detection of the bubble edges (both of left and right sides), the error is estimated to 18 % during the first stages of the bubble growth (small volume of vapor) and to 5 % at the end of the growth (large volume). This error calculation thus does not take into account the limits of the automatic image processing (shadow zone, viewport) that can also affect the measurement of the instantaneous volume V but this is not a big defect since it was demonstrated in Section 2.3.2.3 that the error made on the volume calculation through the automatic treatment remains low with respect to the other sources of error.

A similar growth curve profile was obtained for all the investigated vapor pressure levels and for all the 102 processed bubbles.

3.3.2.4.2 Non dimensional growth curves

In order to compare the bubble growth for several operating conditions, growth curves were normalized by dividing the instantaneous volume V by its maximum value V_{max} and the time by the growth duration τ_{growth} according to the following equations:

$$V^* = \frac{V}{V_{max}} \tag{3.44}$$

$$t^* = \frac{t - t_{nucleation}}{t_{departure} - t_{nucleation}} = \frac{t - t_{nucleation}}{\tau_{growth}} \tag{3.45}$$

The non dimensional growth curves of five bubbles representative of four vapor pressures ($P_v = 5.6$ kPa ($T_v = 35$ °C), $P_v = 7.4$ kPa ($T_v = 40$ °C), $P_v = 12.4$ kPa ($T_v = 50$ °C) and $P_v = 20.0$ kPa ($T_v = 60$ °C)) are plotted on Fig. 3.20[1].

Interestingly, the curves are very close to each other though the corresponding bubbles clearly present shape and size differences: the shape and the size of the bubbles seem to have no effect on the bubble growth rate. This result is particularly striking at $P_v = 20.0$ kPa ($T_v = 60$ °C) where the growth curves of the two kinds of bubbles (primary spheroidal bubble and secondary elongated bubble) are plotted and superimpose well.

[1] For the sake of readability, errors bars are not reported on Fig. 3.20. The deviation on the dimensionless volume V^* is yet supposed to be acceptable since the accuracy on the instantaneous volume V is quite good.

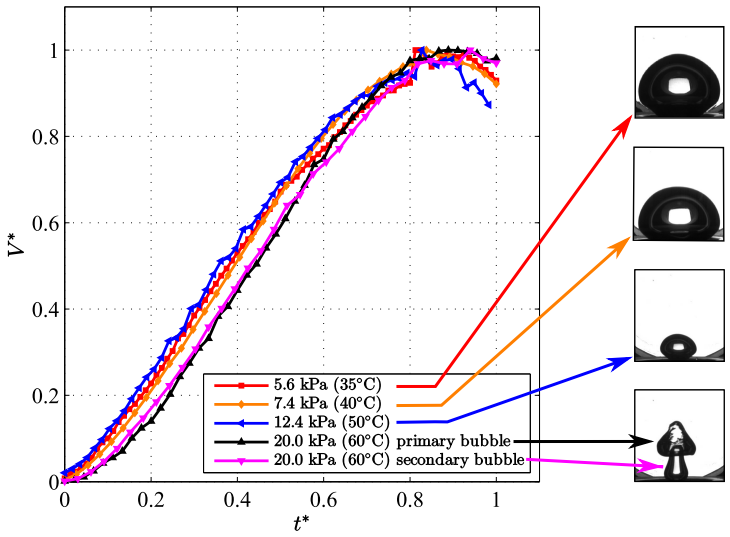

Figure 3.20 – Non dimensional growth curves of selected bubbles obtained at $P_v = 5.6$ kPa ($T_v = 35$ °C), $P_v = 7.4$ kPa ($T_v = 40$ °C), $P_v = 12.4$ kPa ($T_v = 50$ °C) and $P_v = 20.0$ kPa ($T_v = 60$ °C) (water, $H_l = 17.3$ cm, $\varphi_{input} = 2.7$ W · cm^{-2}).

Bubble growth is usually modeled by a power law of the form:

$$V^* \sim t^{*^n} \tag{3.46}$$

where n is a fitting parameter. As partly mentioned in Section 1.1.3.1:

- For a bubble growth controlled by inertia, models [80, 98, 112] generally lead to[1] $n = 3$.
- For a bubble growth governed by thermal diffusion, the classical therory [33, 42, 80, 93, 98, 112, 133] yields[2] $n = 1.5$.
- Fitting his non dimensional volume measurements obtained with pentane at atmopsheric pressure, Siedel [104] found $n = 1$ for $0 \leq t^* < 0.2$ and $n = 0.6$ for $0.2 < t^* \leq 1$.
- Studying the bubble growth rate for water and ethanol down to $P_v = 1$ kPa, Yagov [124] determined a bubble growth law[3] where $n = 2.25$ in case of high Jacob number values ($Ja \geq 600$). In such a case, he stated that the bubble growth is predominantly governed by liquid inertia but this does not mean that the thermal diffusion can be neglected. The value taken by the parameter n is indeed an intermediate one between inertia and thermal diffusion controlled bubble growth.
- Recently, Giraud [44] attempted to compare her experimental results (obtained with water at subatmospheric pressures) to the classical theory related to a bubble growth controlled by heat transfer diffusion and to the law proposed by Yagov [124]. For vapor pressure lower than 15 kPa, her data were in good agreement with Yagov's model for $t^* < 0.2$ and with the thermally controlled bubble growth law for $0.2 \leq t^* \leq 0.5$. However, none of those models was able to predict the evolution of the dimensionless volume for $t^* > 0.5$.

The entire data set from the present study (*i.e.* related to the 102 recorded and image processed bubbles) is considered and compared to the previously cited laws of growth on Fig. 3.21. According to this graph, except the linear model that could be accepted for $t^* < 0.1$, none of these models fits our experimental points. They are in particular unable to represent the inflection point visible at $t^* \approx 0.1$ nor the slow decrease of the dimensionless volume that occurs starting from $t^* \approx 0.8$.

[1] Actually, these models generally correspond a function of the (equivalent) radius of the form: $R_{(eq)} \sim t$.
[2] Actually, these models generally correspond a function of the (equivalent) radius of the form: $R_{(eq)} \sim t^{0.5}$.
[3] Yagov [124] expressed in fact a law of the form: $R_{(eq)} \sim t^{0.75}$.

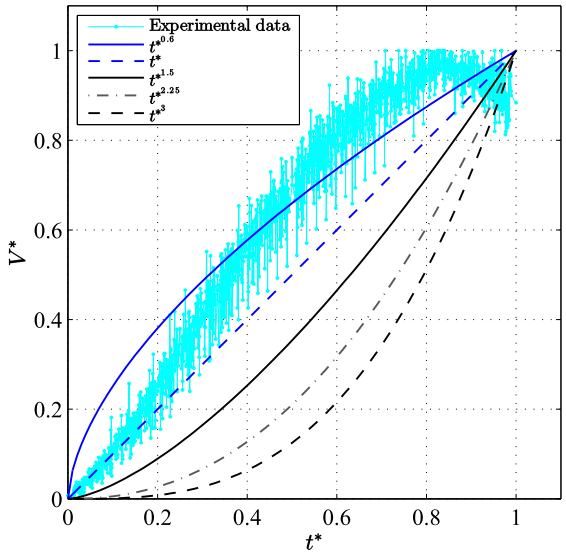

Figure 3.21 – Comparison of usual laws of growth with the experimental measurements associated with the 102 recorded and processed bubbles (water, H_l = 17.3 cm, φ_{input} = 2.7 W · cm^{-2}, 4.2 kPa ≤ P_v ≤ 20.0 kPa (30 °C ≤ T_v ≤ 60 °C)).

Similarities and differences between Giraud [44] and the present work should however be highlighted. These two test campaigns were indeed conducted with the same experimental apparatus and similar conditions:

Table 3.5 – Comparison of the operating conditions between Giraud's study [44] and the current one.

	Giraud [44]	**The present study**
Working fluid	Water	Water
P_v (kPa)	From 0.85 up to 100 kPa with a special focus on the very low pressure range (from 0.85 to 15 kPa)	From 4.2 up to 101.4
H_l (cm)	15.0 and 20.0	17.3
φ_{input} (W · cm^{-2})	From 3.1 up to 29.0	2.7

Giraud [44] observed also an inflection point in the first part of the non dimensional growth curves (at $t^* \approx 0.2$) but it was then much more visible than in the present study. In addition, she noticed that – for a liquid height of 20.0 cm – the increase of the dimensionless volume V^* was slower (and the inflection point occurring for a higher dimensionless time t^*) for vapor pressure of 15 kPa and higher ($P_v \geq$ 15 kPa) than for lower pressures: this seems not to be the case here. Giraud highlighted the beginning of the bubbles recondensation before the end of their growths: at $t^* \approx 0.7$ for the very low vapor pressures and at $t^* \approx 0.9$ for $P_v \geq$ 15 kPa. In a complementary way, according to the present study, the bubbles are found to start their recondensation at $t^* \approx 0.8$ whatever the vapor pressure. Yet, she observed a much more intense recondensation at the very low pressures (up to 80 to 90 % of the maximum volume V_{max}) than at pressures higher than 15 kPa (only about 10 % of the maximum volume V_{max}). According to Fig. 3.21, whatever the vapor pressure, only the second case (with a recondensation of only 10 % of the maximum volume V_{max} of the bubbles) is observed from the present test campaign. The local subcooling $\Delta T_{sub}(z)$ is very probably responsible for this recondensation. This characteristic parameter is however strongly related to the bulk liquid temperature $T_{l,\,bulk}$ whose homogeneity is still assumed but not confirmed (neither in Giraud's work [44] nor in the present study).

New models finally have to be found to correlate our experimental results. The ratio $\frac{\ln(V^*)}{\ln(t^*)}$ is thus plotted against the non dimensional time t^* on Fig. 3.22. As visible on this figure, this

ratio decreases linearly for $0 \leq t^* \leq 0.8$ before increasing significantly for[1] $t^* > 0.8$.

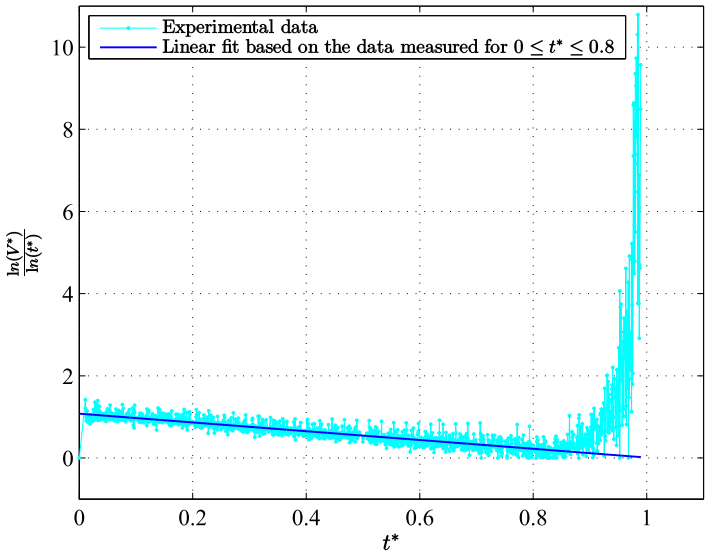

Figure 3.22 – Time evolution of the ratio $\frac{\ln(V^*)}{\ln(t^*)}$ associated with the 102 recorded and processed bubbles (water, $H_l = 17.3$ cm, $\varphi_{input} = 2.7$ W $\cdot$ cm^{-2}, 4.2 kPa $\leq P_v \leq$ 20.0 kPa (30 °C $\leq T_v \leq$ 60 °C)).

A linear fit based on the first part of the time evolution of this ratio then leads to:

$$\frac{\ln(V^*)}{\ln(t^*)} = n(t^*) = -1.069t^* + 1.079 \quad \text{for} \quad 0 \leq t^* \leq 0.8 \tag{3.47}$$

Using Eq. 3.47, the following relation is suggested for the growth law:

$$V^* = {t^*}^{n(t^*)} = {t^*}^{-1.069t^*+1.079} \quad \text{for} \quad 0 \leq t^* \leq 0.8 \tag{3.48}$$

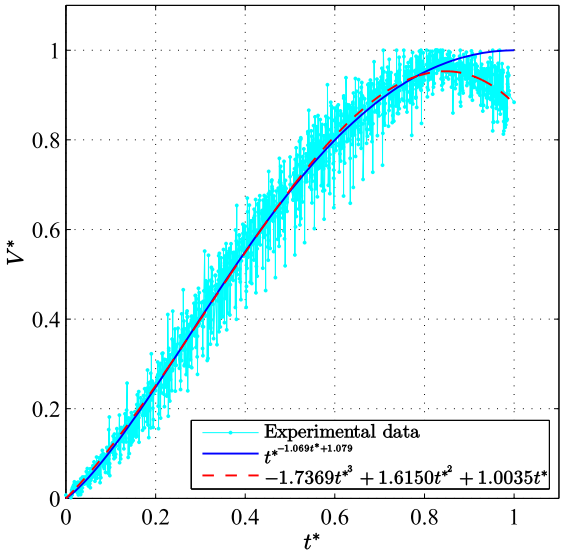

Figure 3.23 – Comparison of new models of growth with the experimental measurements associated with the 102 recorded and processed bubbles (water, $H_l = 17.3$ cm, $\varphi_{input} = 2.7$ W $\cdot$ cm^{-2}, 4.2 kPa $\leq P_v \leq$ 20.0 kPa (30 °C $\leq T_v \leq$ 60 °C)).

As shown on Fig. 3.23, this model fits well the experimental data for $0 \leq t^* \leq 0.8$. The fact that the fitting parameter n varies (and more precisely decreases) with the time is consistent with the idea of a growth law modeled by parts as described by Giraud [44] and Siedel [104]. Moreover, this parameter ranging from $n \approx 1$ down to $n \approx 0.01$, there are instants for which it

[1] In addition, points are more scattered for $t^* \approx 1$ since both $\ln(V^*)$ and $\ln(t^*)$ tend to 0.

takes the values determined by Siedel [104].

As expected because of the method used to define it, this model (Eq. 3.48) is yet unable to follow the decrease of the volume for $t^* > 0.8$. Unfortunately, other satisfying fits[1] of the ratio $\frac{\ln(V^*)}{\ln(t^*)}(t^*)$ lead to more or less pronounced oscillations of V^* in function of t^* (over the full range of t^*) which reduce the quality of the deduced model[2]. As a consequence, a simple polynomial fit of the experimental data is calculated and displayed on Fig. 3.23:

$$V^* = -1.7369{t^*}^3 + 1.6150{t^*}^2 + 1.0035t^* \quad \text{for} \quad t^* \in [0,1] \tag{3.49}$$

3.3.2.5 Maximum volume V_{max} and volume at departure $V_{departure}$

Values of maximum volume V_{max} and volume at the detachment $V_{departure}$ are reported as a function of the growth duration τ_{growth} for all the bubbles observed for a vapor pressure ranging from $P_v = 4.2$ kPa ($T_v = 30$ °C) to $P_v = 20.0$ kPa ($T_v = 60$ °C) on Fig. 3.24a and 3.24b respectively.

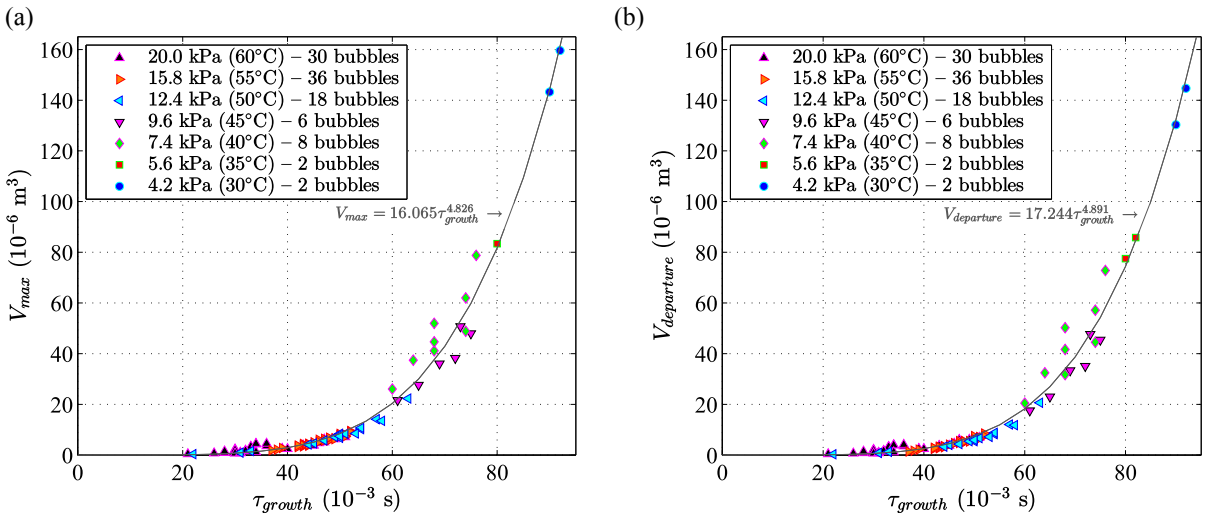

Figure 3.24 – Dependence of the bubble volume on its growth duration: (a) Maximum volume V_{max}; (b) Volume at departure $V_{departure}$ (water, $H_l = 17.3$ cm, $\varphi_{input} = 2.7$ W · cm^{-2}).

In agreement with the qualitative observations made in Section 3.2, both the growth time and the bubble volume (maximum or at departure[3]) increase significantly as the pressure decreases. Four phenomena may explain this result:

(i) **The variations of the liquid and vapor densities:** In the investigated range of saturated pressures P_v, the liquid density ρ_l of water decreases by around 1 % whereas its vapor density noticeably varies with an increase by about 330 % (see Table 3.6). As a consequence, vaporizing a given mass of liquid results in a much larger vapor volume at low pressure than at higher pressure.

(ii) **The variation of the surface tension:** Still along the investigated portion of the saturation curve of water, the surface tension σ increases by about 7 % as the pressure (and temperature) decreases (Table 3.6). According to Ginet [43] and to Siedel *et al.* [107], the contact pressure as well as the resultant of the triple line forces (also called the surface tension force) are proportional to the surface tension. The increase of the surface tension σ

[1] For instance, higher order polynomial fits or exponential fits based on the measurements for either the full range of t^* (*i.e.* $t^* \in [0,1]$) or for $t^* \in [0.8,1]$ only.

[2] The increased number of empirical coefficients also depreciates the interest of such a model.

[3] As shown previously, the maximum volume is always larger than the volume at departure since condensation starts before detachment. In average, the volume at departure corresponds indeed approximately to 90 % of the maximum volume reached by a bubble during its growth: $V_{departure} \approx 0.9V_{max}$.

as the saturation pressure decreases therefore makes the bubble detachment more difficult. This induces then longer bubble growth duration τ_{growth} and larger volume (maximum volume V_{max} or departure volume $V_{departure}$) at low pressure than at higher pressure.

Table 3.6 – Variations of liquid and vapor densities and of surface tension of water between $P_v = 4.2$ kPa ($T_v = 30$ °C) and $P_v = 20.0$ kPa ($T_v = 60$ °C).

	ρ_l $(\mathbf{kg \cdot m^{-3}})$	ρ_v $(\mathbf{kg \cdot m^{-3}})$	σ $(\mathbf{N \cdot m^{-1}})$
$P_v = 4.2$ kPa ($T_v = 30$ °C)	995.60	0.030432	0.071193
$P_v = 20.0$ kPa ($T_v = 60$ °C)	983.16	0.13048	0.066237
Variation (%)	*−1.25*	*+328.76*	*−6.96*

(iii) **The effect of the contact angle of the heated surface:** The contact angle of the wall could also have an influence on the size at detachment and on the growth time. Several studies on single bubble dynamics on hydrophobic or hydrophilic surfaces [83, 84] have indeed shown that the departure diameter tends to decrease as the contact angle decreases. However, the effect of the contact angle on the maximum or departure volume of a bubble and on the growth duration cannot be established in this study. Even if it can be inferred from Fig. 3.3 to Fig. 3.6 that the heated surface used in this study is hydrophilic, it was indeed not possible to measure properly the contact angle from our recordings because of the presence of the shadow zones due to the glue seal and to the viewport.

(iv) **Other effects:** Some other effects – poorly known nor understood for now – such as the dependence of the contact angle of a couple surface/fluid or of the liquid viscosity μ_l (and its gradient) on the pressure may also have an influence on the liquid inertia by competing the bubble expansion and thus making the bubble growth slower.

The two following relationships between a bubble growth time τ_{growth} and its volume are finally determined from our experimental points:

$$V_{max} = 16.065\tau_{growth}^{4.826} \tag{3.50}$$

$$V_{departure} = 17.244\tau_{growth}^{4.891} \tag{3.51}$$

3.3.2.6 Relationship between the bubble frequency f and its diameter at departure $D_{departure}$

Interested in the weight of the latent heat transport contribution to the heat transfer in nucleate boiling, many authors found relationships linking the bubble departure frequency f and diameter $D_{departure}$. Such relations are generally of the form:

$$f D_{departure}^{n} = C \tag{3.52}$$

where C is most of the time a constant whose dimension depends on the value of the exponent n.

- Jakob and Linke [60], Fritz and Ende [41], Perkins and Westwater [91] as well as Yamagata *et al.* [130] (all of them cited by Rallis and Jawurek [97]) determined experimentally (with different fluids and conditions) that $n = 1$ with C a constant. Zuber [134] agreed with these authors and expressed this constant C in terms of the fluid physical properties[1]:

$$C = 0.59\left[\frac{g\sigma(\rho_l - \rho_v)}{\rho_l^2}\right]^{0.25} \tag{3.53}$$

[1] As a consequence, C is a constant only at constant pressure. However, for water, the quantity defined through Eq. 3.53 decreases only of less than 5 % as the pressure increases from the triple point to the atmospheric pressure (with the thermophysical properties evaluated on the saturation curve). In this range of pressure, $C \approx 0.0937$ m $\cdot$ s^{-1}.

- Deissler [35] (cited by Rallis and Jawurek [97] and Cole [25]) first proposed n to be equal to 0.5 with $C = constant$. Cole [25] and McFadden [75] came later to the same conclusion.

- Rallis and Jawurek [97] observed that the product $fV_{departure}$ was constant whatever the imposed heat flux for water boiling at saturation from a horizontal wire. In other words, they determined $n = 3$ and $C = constant$.

- Hatton and Hall [54] (cited by Ivey [59]) observed that $n = 2$ and C is a constant which depends on the cavity diameter.

- Ivey [59] made a review of numerous studies aiming at determining the relationship between the bubble frequency and its diameter. He thus identified that, depending on the experimental results and analytic models (and their assumptions), n varies between 0.5 and 3 while C can be either a constant or a function of various parameters (thermophysical properties of fluid, gravitational acceleration and particular system parameters such as the imposed heat flux or heated surface area). He wanted then to extend the data from the literature and on small and large bubbles by performing experiments with water boiling from the outside of tubes at atmospheric and at subatmospheric pressures. He obtained different values of n depending on the major forces acting on a bubble:

  - In the hydrodynamic region: buoyancy and drag are the predominant forces acting on a bubble and n is found equal to 0.5;
  - In the transition region: buoyancy, drag and surface tension are comparable, n is equal to 0.75;
  - In the thermodynamic region: the bubble growth is governed by thermodynamic conditions and n is estimated to 2.

  He finally concluded that a single expression may not properly describe the dependence of the bubble frequency with its diameter for all bubble sizes in nucleate boiling.

- Malenkov [74] answered to Ivey [59] by demonstrating that the relationship between the bubble departure frequency and diameter can theoretically be expressed in a general way that covers the various cases cited in the literature. Some specific properties of the system must be introduced for that sake, in particular the vapor content and the bubble rise velocity that are dependent on the imposed heat flux. Malenkov however acknowledged the problem of the reliable determination of those parameters as a major limit to his solution.

To verify if a relation of the form given in Eq. 3.52 holds with the experimental data of the present study, the dependence of the inverse of the bubble departure frequency $\frac{1}{f}$ on its equivalent diameter at departure $D_{departure_{eq}}$ is reported in logarithmic scale on Fig. 3.25. On this figure, each reported point corresponds to the data taken from one recording[1] with:

- The frequency directly obtained from the image processing (through Eq. 2.13);

- The equivalent diameter at bubble departure $D_{departure_{eq}}$ defined as the diameter of the sphere whose volume is equal to the mean value of the volumes at detachment of the bubbles recorded on the video file:

$$D_{departure_{eq}} = \sqrt[3]{\frac{6}{\pi}\overline{V_{departure}}} \tag{3.54}$$

[1] Several points can then represent the same operating conditions.

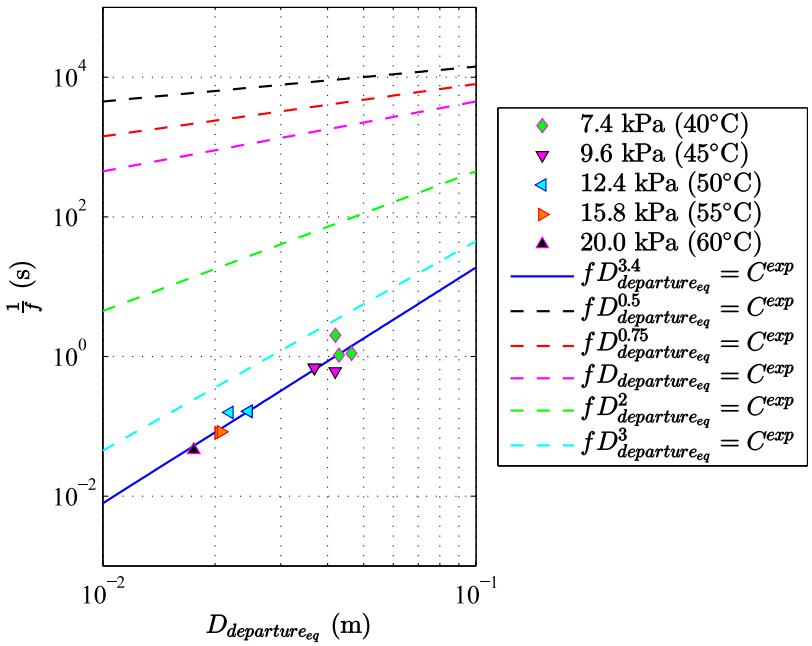

Figure 3.25 – Relationship between bubble frequency f and equivalent diameter at departure $D_{departure_{eq}}$.

As visible on this graph, experimental results can be described by the following relation:

$$fD^{3.4}_{departure_{eq}} = C^{exp} = 2.2 \times 10^{-5} \tag{3.55}$$

where C^{exp} is here in $\mathrm{m}^{3.4} \cdot \mathrm{s}^{-1}$.

As for visual comparison, the previously evoked relationships are also displayed on Fig. 3.25 with the same value taken for C. One should be aware that as this constant have a different dimension depending on the values taken by n (C is in $\mathrm{m}^{\mathrm{n}} \cdot \mathrm{s}^{-1}$), this does not have a real physical meaning. However, this enables us to compare the slopes of the curves to our experimental data, *i.e.* to compare the effect of the exponent n of Eq. 3.52. From this point of view, it appears that:

- The relation found by Rallis and Jawurek [97] with $n = 3$ is rather close to our experimental results.
- The relationships proposed by Ivey [59] are all the three far from experimental results despite this author conducted some tests with water at subatmospheric pressures to establish them.
- Such relationships linking the bubble departure frequency and diameter are actually questionable – at least in the particular case of the low pressure boiling – due to their simplicity. They are indeed most of the time obtained with the assumption that the inertia has a weak influence and/or from experiments conducted at or close to the atmospheric pressure. At low pressure, the subcooling degree makes this usual description of the physical phenomenon probably even less valid than at higher pressures.

Pool boiling of water in the regime of isolated bubbles was investigated for:

- *a large range of subatmospheric vapor pressures;*
- *a unique height of liquid H_l;*
- *a constant imposed heat flux φ_{input}.*

The influence of the pressure on the bubble dynamics was qualitatively observed for vapor pressures ranging from P_v = 4.2 kPa (T_v = 30 °C) to P_v = 101.4 kPa (T_v = 100 °C)

through the visualization made with a high-speed camera.

The effect of the pressure on the boiling phenomena was afterwards quantitatively analyzed both in terms of heat transfer (considering all the experiments) and in terms of bubble dynamics (considering only experiments for which the image processing detailed in Chapter 2 was possible, i.e. *for* $4.2\ \text{kPa} \leq P_v \leq 20.0\ \text{kPa}$ $(30\ ^\circ\text{C} \leq T_v \leq 60\ ^\circ\text{C})$*.*

- *Four different regimes of bubble dynamics were identified depending on the pressure:*
  - *Oblate spheroid shaped bubbles without any bubble interaction;*
  - *Mushroom shaped bubbles with interaction between paired bubbles;*
  - *Mushroom and column shaped bubbles with interaction between two or more successive bubbles;*
  - *Near-spherical shaped bubbles without any contact between successive bubbles.*
- *The physical meaning of the wall superheat as well as the state conditions at which the thermophysical properties involved in several wall superheat models should be evaluated were discussed in order to properly analyze the evolution (with the vapor pressure) of this parameter in presence of a subcooling degree induced by a non negligible static pressure.*
- *A correspondence between the bubble dynamics regime (more precisely the presence or the absence of bubbles interactions) and the evolution of the wall superheat with the vapor pressure was found.*
- *The strong influence of the specific implemented surface condition (low roughness and a unique artificial cavity) on the heat transfer was also highlighted, in particular close to the atmospheric pressure.*
- *Some properties of the bubble dynamics such as the growth duration, the waiting time, the bubble frequency or the instantaneous volume were measured (for a reduced range of vapor pressures) resulting especially in:*
  - *the confirmation of some characteristics of the bubble dynamics of subatmospheric water pool boiling that were already described in the literature, such as an increase of the size and of the waiting time as the pressure decreases;*
  - *the highlighting of the need to take into account the effect of the static pressure to properly conduct such analyses of pool boiling for low pressure conditions;*
  - *the establishment of an experimental law of bubble growth which raises questions about the involved mechanisms, since it differs from the classical theories that were mostly established for higher pressures;*
  - *the determination of a new relationship between the bubble frequency and the bubble size which contradicts some related results of the literature and questions about the physical meaning of such dependence and of associated models and theories.*

Chapter 4

Low pressure boiling: the concept of "mock-up fluids"

*Since – as mentioned in Chapter 1 and Chapter 3 – most of the studies on pool boiling at low pressure were carried out with water as the working fluid, it appears interesting to conduct experiments with other fluids to get a better and more general understanding of the phenomenon. The choice of the fluids (and the related operating conditions) to be tested is a key point. These new fluids should indeed be studied in a "similar state" as water at "low pressure". Otherwise, the similarities and differences observed in the behavior of the fluids may be not related to the same phenomenon (*i.e *not necessary to "low pressure pool boiling").*

This chapter is thus aimed at introducing a more general definition of "low pressure" in boiling and a series of criteria to choose mock-up fluids for water (Section 4.1). Once such a fluid selected, a test campaign with it was conducted (Section 4.2) before a comparison could be performed between the behavior of this fluid and the one of water in low pressure pool boiling (Section 4.3). This comparison was carried out with the idea of identifying some driving parameters or dimensionless numbers shared by the two fluids when they present the same behavior.

4.1 The concept of "mock-up fluids"

To make the comparison of low pressure boiling characteristics of different fluids possible, the considered fluids have to be in a "similar state" of "low pressure". As a consequence, the concepts of "low pressure" and of "similar state" have beforehand to be well defined. Like it is usual to build correlations in the fields of fluid mechanics or of thermal sciences from reasonings based on similarities (*i.e.* using mock-ups with same dimensionless numbers), a similar approach is followed in this section to propose such a new definition of "low pressure boiling" (Section 4.1.1), a methodology with a series of criteria to select mock-up fluids (Section 4.1.2) and a design of experiments adapted to the chosen fluid (Section 4.1.3).

4.1.1 A generalized definition of boiling at "low pressure"

Pool boiling at "low pressure" is commonly defined for water [46, 77, 119, 131] as boiling at pressures below the atmospheric pressure ($P_v = 101.4$ kPa, $T_v = 100$ °C). As briefly discussed in Section 1.2.4, extending the concept of "low pressure" with the same definition to other working fluids would lead to wrong interpretation of the boiling characteristics because the fluids properties would then not been taken into account.

As explained in Section 1.2.3 and as reminded in Chapter 3, Giraud *et al.* [46] demonstrated that one of the major features of the low pressure boiling is that the static head P^{static} induced by the liquid height H_l over the heated wall can be of the same order of magnitude as the vapor

pressure P_v. The static head cannot then be disregarded compared to the pressure imposed at the free surface. Considering the pressure P_{wall} at the level of the heated surface which is still defined as:

$$P_{wall} = P_v + \underbrace{\rho_l(T_{l,\,bulk})gH_l}_{P^{static}} \tag{4.1}$$

seems thus be more meaningful as the reference pressure than regarding only the vapor pressure.

Besides, in any case, boiling can only take place if the system pressure is greater than the pressure at the triple point. Consequently, an idea of a general definition of "low pressure" in pool boiling could be to have the pressure at the wall close to the triple point pressure P_t of the fluid:

$$P_{wall} \approx P_t \tag{4.2}$$

Yet,

$$P_v \geq P_t \tag{4.3}$$

so that, satisfying Eq. 4.2 means having simultaneously:

$$P_v \approx P_t \tag{4.4}$$

and

$$P^{static} = \rho_l(T_{l,\,bulk})gH_l \ll P_t \tag{4.5}$$

which is possible if the liquid density ρ_l and/or the liquid height H_l are low and/or if the triple point pressure P_t is high. This brings to a possible paradox in that sense that it was discovered previously that under low pressure, the bubbles tend to exhibit large diameters (possibly greater than 10 cm with water [44, 46, 100] for example), so that in the case of low liquid height, the bubbles are likely to emerge from the liquid (*i.e.* to cross the free surface and finally burst) – which is not comparable to pool boiling[1]. The present study of pool boiling at low pressure is therefore focused on the situation where bubbles have enough space to grow, detach and start to collapse in the liquid column in order to gain more insight into the related phenomena. Hereafter, the liquid level H_l will thus be kept relatively high even if the condition defined in Eq. 4.5 may be not satisfied.

Another way to define the "low pressure boiling" may be to observe from which low pressure value the bubble dynamics behavior deviates from the behavior usually encountered under normal or higher pressures. For instance in the case of water, referring to Section 3.2 one can see that the "low pressure" effect is visible for vapor pressures equal or lower than $P_v = 70.2$ kPa ($T_v = 90$ °C).

4.1.2 A methodology to choose mock-up fluids in "similar states"

As numerous experimental studies on low pressure boiling were conducted using water as the working fluid, water is here taken as the fluid of reference. In this section, a series of criteria is thus developed to choose a mock-up fluid to be compared with water during a low pressure boiling test campaign.

4.1.2.1 Criterion on the triple point (T_t, P_t)

In order to carry out experiments with the facility described in Chapter 2 while satisfying Eq. 4.4, the triple point pressure P_t of the mock-up fluid should not be too low so that this pressure could be reached in the boiling pool with the vacuum pump. In the same vein, the triple point pressure of the fluid should be obtained in a convenient saturation temperature range with regards to

[1] This configuration of boiling at low pressure with only a thin layer of liquid was observed by Giraud *et al.* [47] and may present some interest. However this seems too complex to study and analyze for now since simpler configuration (without interaction of the bubble with the free surface during its growth) is not sufficiently understood yet.

the limits of the cooling system of the test setup. The thermostatic bath connected to the heat exchanger jacketed inside the pool wall working with a given coolant fluid can indeed control and set the temperature of the pool only in a certain range. As the thermostatic bath available[1] for this new test campaign is limited to [0 °C, 40 °C], the triple point temperature T_t of the mock-up fluid must be in this range:

$$0\ °\text{C} \leq T_t \leq 40\ °\text{C} \tag{4.6}$$

Table 4.1 – Triple point temperature T_t and pressure P_t of different fluids [71].

Fluid	$\boldsymbol{T_t}$ **(°C)**	$\boldsymbol{P_t}$ **(kPa)**
Water	0.01	0.6117
Cyclohexane	6.32	5.2402
Benzene	5.52	4.7848
Ethanol	−114.15	7.0319×10^{-7}
Methanol	−97.54	1.8634×10^{-4}
Pentane	−129.68	7.6322×10^{-5}
Ammonia	−77.66	6.0912
Acetone	−94.65	0.0023
Toluene	−95.15	3.9393×10^{-5}

The triple point data of several fluids (including water for comparison) are listed in Table 4.1. According to this table, cyclohexane, benzene, ammonia and acetone have a sufficiently high triple point pressure P_t that can be set in the boiling pool with the vacuum pump. However, among those fluids, only cyclohexane and benzene have also a triple point temperature T_t adapted to the conditions reachable with the experimental apparatus. Considering Eq. 4.5, it is interesting to notice that these two fluids present a higher triple point pressure than water:

$$P_t \geq P_t\big|_{water} \tag{4.7}$$

4.1.2.2 Criterion on the dimensionless ratio $\frac{P_v}{P_t}$

In order to compare the mock-up fluid to water, it is desirable to conduct experiments with this fluid and with water in the same ranges of saturation temperatures:

$$T_v \approx T_v\big|_{water} \tag{4.8}$$

and pressures:

$$P_v = P_{sat}(T_v) \approx P_v\big|_{water} = P_{sat}(T_v\big|_{water}) \tag{4.9}$$

within the limits of the test bench ($T_v \in$ [0 °C, 40 °C]). Combined with Eq. 4.4 and Eq. 4.7, these conditions yields a new criterion defined as:

$$\left.\frac{P_v}{P_t}\right|_{T_v \in [0\ °\text{C},\ 40\ °\text{C}]} \lessapprox \left.\frac{P_v}{P_t}\right|_{water,\ T_v \in [0\ °\text{C},\ 40\ °\text{C}]} \tag{4.10}$$

A comparison of several fluids is performed on Fig. 4.1 considering this pressure ratio. According to this graph, the criterion given as Eq. 4.10 suggests the use of cyclohexane or benzene rather than of acetone or ammonia as the mock-up fluid for water to study low pressure boiling.

[1] The cited thermostatic bath is a LAUDA WK class WK 4600 circulation chiller working with the Kryo 30 coolant in the temperature range [0 °C, 40 °C]. The cooling power of this system is high (4.6 kW at 20 °C) which suits well to the study of low pressure boiling with the current vessel where the amount of fluid to cool is important while the pressures of interest can yield temperatures close to 0 °C. For the test campaign conducted with water up to the atmospheric pressure (*i.e* up to ($P_{v_{max}} = 101.4$ kPa, $T_{v_{max}} = 100$ °C), see Chapter 3), this thermostatic bath was temporarily substituted by a LAUDA ECO SILVER RE 1050 S recirculating chiller working with the Kryo 51 coolant in the temperature range [−50 °C, 120 °C]. The relatively low cooling power of this second chiller (0.7 kW at 20 °C) is an additional cause of the restriction of the test session of Chapter 3 to ($P_{v_{min}} = 4.2$ kPa, $T_{v_{min}} = 30$ °C).

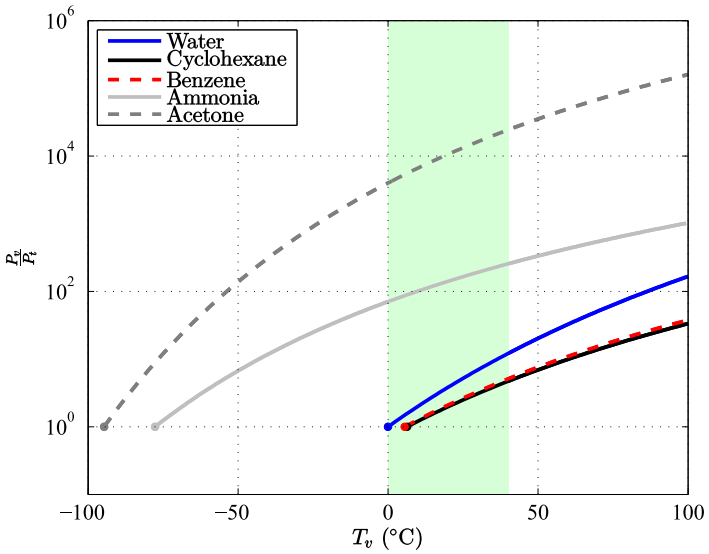

Figure 4.1 – Ratio $\frac{P_v}{P_t}$ depending on the saturation temperature T_v for different fluids [71]. – The zone colored in green corresponds to the temperature range permitted by the experimental facility.

4.1.2.3 Criterion on liquid and vapor densities ρ_l and ρ_v

As mentioned in Section 4.1.1, a low liquid density ρ_l is a desirable advantage for a suitable mock-up fluid since this is one of the conditions to satisfy Eq. 4.5. As a matter of fact, a low liquid density combined with a high triple point pressure leads to a pressure at the level of the wall P_{wall} close to that of the vapor P_v, and therefore (Eq. 4.4) close to the triple point pressure P_t.

In addition, due to the large size (few centimeters in diameter) of the bubbles observed at low pressure with water [119, 124] – sometimes larger than the viewports of the experimental setup[1] [44, 46, 100] – it would be appreciable that the selected fluid leads to bubbles slightly smaller than water:

$$V \leq V\big|_{water} \tag{4.11}$$

Considering the case in which – at a given instant – the same volume of liquid $\mathcal{V}$ is vaporized for both the mock-up fluid and water:

$$\mathcal{V} = \frac{m}{\rho_l} = \frac{m\big|_{water}}{\rho_l\big|_{water}} \tag{4.12}$$

The conservation of mass gives the following relation between the instantaneous volumes of bubbles obtained in each fluid:

$$V = \frac{\rho_l}{\rho_l\big|_{water}} \frac{\rho_v\big|_{water}}{\rho_v} V\big|_{water} \tag{4.13}$$

So that Eq. 4.11 is satisfied if:

$$\frac{\rho_l}{\rho_l\big|_{water}} \frac{\rho_v\big|_{water}}{\rho_v} \leq 1 \tag{4.14}$$

That is:

$$\frac{\rho_l}{\rho_v} \leq \frac{\rho_l\big|_{water}}{\rho_v\big|_{water}} \tag{4.15}$$

This defines thus an additional criterion to choose a mock-up fluid.

[1] As a reminder, the viewports are 10.0 cm in diameter.

Few fluids are therefore compared from this point of view on Fig. 4.2, all of them satisfy Eq. 4.15.

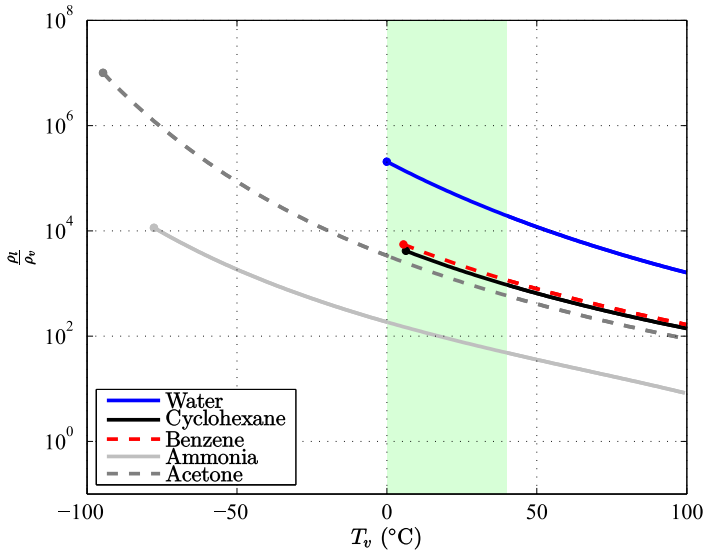

Figure 4.2 – Ratio $\frac{\rho_l}{\rho_v}$ depending on the saturation temperature T_v for different fluids [71]. – The green zone still corresponds to the temperature range permitted by the experimental facility.

4.1.2.4 Other criteria to take into account and choice of a mock-up fluid

Other criteria should be taken into account for the choice of a mock-up fluid. Among them, variations of other thermophysical properties or of some dimensionless numbers along the saturation curve could be considered in order to compare and properly explain the similarities and differences between water and another fluid in the boiling behavior at low pressure. One can think – for instance – to the surface tension σ or to the latent heat of vaporization Δh_{lv} and to the Jacob number Ja or to the I_R criterion on inertia or diffusion controlled bubble growth from Robinson and Judd [98]. However, – to the author's knowledge – such an approach of mocking up fluids has never been tried before in the field of boiling and the parameters or dimensionless numbers that govern the low pressure boiling phenomenon are not identified yet. As a first trial, it was thus decided to consider only the previously cited criteria.

Yet, from a practical point of view, chemical resistance of the different parts of the experimental setup to the fluids as well as the toxicity and the precautions of use of those fluids have absolutely to be taken into account.

Considering all the criteria cited above, cyclohexane was finally selected as the first mock-up fluid to be tested and compared with water[1].

4.1.3 Design of experiments

Previously (in Chapter 3), an experiment was related to the study of the steady state of an operating point defined by four parameters: the working fluid, the imposed heat flux φ_{input}, the vapor pressure P_v and the liquid height H_l over the heated surface. Those parameters should henceforth be rethought and properly chosen to enable a relevant comparison of experimental observations between several fluids.

Choice of the working fluids: As discussed in Section 4.1.2, tests should be carried out with pure and degassed water and cyclohexane.

[1] Considering the criteria on the triple point (Eq. 4.6 and Eq. 4.7), on the ratio $\frac{P_v}{P_t}$ (Eq. 4.10) and on the liquid and vapor densities (Eq. 4.15), benzene is very close to cyclohexane. Reading the related safety datasheets [9, 10] revealed that benzene is much more dangerous and subsequently complicated to use (due to precautions of manipulation) than cyclohexane so that the choice of the latter fluid became obvious.

Choice of the imposed heat flux φ_{input}: This parameter has to be chosen in a similar way for the two fluids. Three options were considered:

(i) Taking an arbitrary value of imposed heat flux identical for the two fluids.
This solution presents the major advantage of its simplicity of implementation. However, there would then be no guarantee that the boiling phenomena related to the two fluids would be comparable. It is indeed possible that – for similar operating conditions and with the same heat flux – one fluid is boiling in the isolated bubbles regime whereas the other one is in a regime of fully developed nucleate boiling (*i.e.* with bubbles growing from multiple activated sites) or in a natural convection regime. It would then be difficult to compare those behaviors even if they would have been obtained by setting the same imposed heat flux value.

(ii) Determining experimentally the lowest imposed heat flux which leads to a boiling regime characterized by isolated bubbles growing only – or at least mostly – from the centered artificial cavity.
This is in fact the method used for the experimental session realized with water on a wide range of subatmospheric pressures (detailed in Chapter 3). Starting from a high heat flux which yields the activation of several nucleation sites, the imposed heat flux is decreased progressively down to the lowest value which enables the nucleation of bubbles only from the artificial cavity. This value is afterwards kept for the observation and analysis of the steady state. The choice of the imposed heat flux value with this method will probably lead to one value per fluid (and possibly per operating condition). However, it will be sure that the same regime (of isolated bubbles) will be observed for the two fluids which makes the comparison of the bubble dynamics (and more generally of the boiling behavior) more meaningful than if the fluids present different regimes.

(iii) Defining theoretically an imposed heat flux value through the use of an adapted dimensionless number.
One idea could be to consider the relative contribution of the latent heat transport to the total heat transfer defined as the following ratio:

$$\varphi_{LH}^{relative} = \frac{\varphi_{LH}}{\varphi_{input}} \tag{4.16}$$

and then to choose the imposed heat flux value φ_{input} so that this relative contribution $\varphi_{LH}^{relative}$ would be the same for the two fluids. The contribution of the phase change φ_{LH} on the heat transfer must thus be properly expressed. However – as in the work of Rallis and Jawurek [97] – in addition to some fluid thermophysical properties (in particular the vapor density and thermal conductivity), the evaluation of this contribution involves some bubble dynamics parameters that can be estimated only from the analysis of the corresponding experiment. Among those parameters one can cite the number of active nucleation sites, the typical bubble departure frequency or the mean bubble volume at departure related to each active source.
Despite its obvious theoretical interest, this method cannot be used for the choice of the imposed heat flux.

Solution (ii) was finally adopted for the test campaign.

Choice of the liquid height H_l and of the vapor pressure P_v: At low pressure, the liquid height H_l has a huge influence on the static head $P_{H_l}^{static}$: depending on this parameter, the static head can become of the same order of magnitude as the vapor pressure P_v imposed at the free surface. The liquid height has consequently a non negligible effect on the pressure at the level of the heated surface P_{wall} and more generally on the local hydrostatic pressure $P(z)$.

The local subcooling degree of the liquid corresponds to the local deviation of the liquid from the saturation state. Considering that the saturation state prevails at the level of the free surface ($z = 0$, point $\mathcal{A}$ on Fig. 4.3) and assuming that the bulk liquid is homogeneous in temperature ($T_{l,\,bulk}(z) = T_{l,\,bulk} = T_v$), at a given altitude z (point $\mathcal{B}$ on Fig. 4.3), the liquid is at a pressure $P(z)$ higher than P_v but at a temperature lower than the temperature corresponding to the saturation state associated with the local pressure (point $\mathcal{B}'$ on Fig. 4.3).

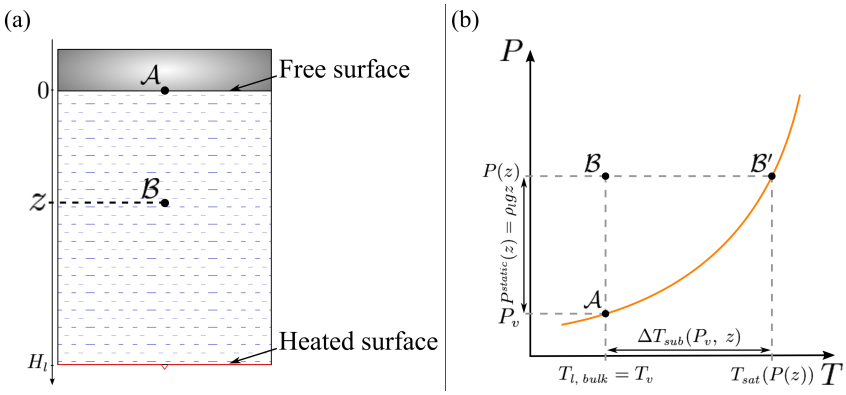

Figure 4.3 – Schematical identification of the local subcooling degree on the saturation curve: (a) geometry; (b) schematic phase diagram.

As a consequence, – for a given fluid – the local subcooling degree derives from both the pressure conditions and the vertical distance to the free surface[1]. It can be written as:

$$\Delta T_{sub}(P_v,\ z) = T_{sat}(P_v + P^{static}(z)) - T_{sat}(P_v) \tag{4.17}$$

As the subcooling degree appears actually as a parameter of major importance of the boiling environment at low pressure and thus of the related boiling phenomena, it would have been interesting to choose pairs of liquid levels ($H_l|_{cyclohexane}$, $H_l|_{water}$) and of vapor pressures ($P_v|_{cyclohexane}$, $P_v|_{water}$) so that this key parameter would be similar for the two fluids in the vicinity of the heated wall (*i.e.* in the region where bubbles should be formed):

$$\Delta T_{sub}|_{cyclohexane}(P_v|_{cyclohexane},\ z \approx H_l|_{cyclohexane}) \approx \Delta T_{sub}|_{water}(P_v|_{water},\ z \approx H_l|_{water}) \tag{4.18}$$

Or – equivalently – after the variable change[2] $Z = H_l - z$ (refer to the geometry represented on Fig. 4.4):

$$\Delta T_{sub}|_{cyclohexane}(P_v|_{cyclohexane},\ Z|_{cyclohexane} \approx 0) \approx \Delta T_{sub}|_{water}(P_v|_{water},\ Z|_{water} \approx 0) \tag{4.19}$$

[1] More precisely, it depends on both the difference of pressure existing between the local position z and the free surface position $z = 0$ (*i.e.* the local static head $P^{static}(z) = P(z) - P_v$) and the pressure P_v imposed at the free surface level. The saturation curve being not linear, depending on P_v, a given pressure difference will not induce a constant subcooling degree.

[2] In the case of different liquid levels, – contrary to the variable z (*i.e.* the altitude) – the variable Z (which corresponds also to the altitude) presents the interest of covering the same range of values ($Z \approx 0$) close to the heated surface (*i.e.* in the region where bubbles are growing).

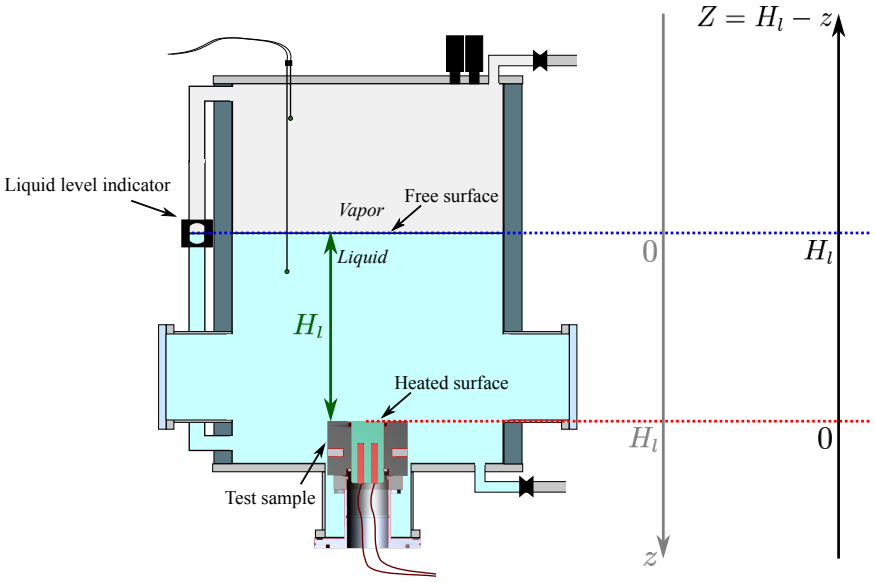

Figure 4.4 – Geometry: distinction between the vertical axes z and Z.

For a given fluid, the local static head $P^{static}(Z)$ can be expressed according to two distinct relations:

1. Through the hydrostatic law:

$$P^{static}(Z) = P(Z) - P(Z = H_l) = P(Z) - P_v = \rho_l g(H_l - Z) \tag{4.20}$$

2. Through the Clausius-Clapeyron relation[1]:

$$P^{static}(Z) = P(Z) - P_v \approx \frac{\Delta T_{sub}\rho_v \Delta h_{lv}}{T_v} \tag{4.21}$$

Equating Eq. 4.20 and Eq. 4.21 yields a direct estimation of the local subcooling degree as a function of the fluid thermophysical properties (evaluated in the saturation state at P_v), the liquid height H_l and the position Z:

$$\Delta T_{sub} \approx \frac{T_v \rho_l g}{\rho_v \Delta h_{lv}}(H_l - Z) \tag{4.22}$$

that can be rewritten as:

$$\Delta T_{sub} \approx \Psi(\text{Fluid},\ (P_v,\ T_v = T_{l,\,bulk}),\ H_l,\ Z, \rho_l(P_v,\ T_v),\ \rho_v(P_v,\ T_v),\ \Delta h_{lv}(P_v,\ T_v)) \tag{4.23}$$

The fact that Ψ depends on both the vapor pressure P_v and the liquid height H_l shows that – if the criterion of a similar local subcooling degree in the vicinity of the heated wall is retained to define the operating conditions to reach a "similar state" in different fluids – those two parameters are no longer independent. A second relation between them should then be found so that this issue could be solved analytically.

Let therefore assume that a couple of vapor pressures $(P_v|_{cyclohexane}, P_v|_{water})$ is determined and consider a given altitude $Z_0 = Z|_{cyclohexane} = Z|_{water}$ at which the subcooling degree

[1] The use of this relation is a valuable approach within the condition that the variation of the slope of the saturation curve remains small between P_v and $P(Z)$ (*i.e.* between points $\mathcal{A}$ and $\mathcal{B}'$ from Fig. 4.3), that is if those points are relatively close, *i.e.* for $z \approx 0$ or equivalently $Z \approx H_l$. This reasoning – being interesting in the domain where $Z \approx 0$ – is thus valuable within relatively small liquid levels H_l.

should be equal in both fluids:

$$\Delta T_{sub}\big|_{cyclohexane}(P_v\big|_{cyclohexane},\ Z_0) = \Delta T_{sub}\big|_{water}(P_v\big|_{water},\ Z_0) \tag{4.24}$$

That is:

$$\frac{T_v\big|_{cyclohexane}\rho_l\big|_{cyclohexane}g}{\rho_v\big|_{cyclohexane}\Delta h_{lv}\big|_{cyclohexane}}(H_l\big|_{cyclohexane}-Z_0) = \frac{T_v\big|_{water}\rho_l\big|_{water}g}{\rho_v\big|_{water}\Delta h_{lv}\big|_{water}}(H_l\big|_{water}-Z_0) \tag{4.25}$$

The two liquid heights are then linked according to Eq. 4.26:

$$H_l\big|_{cyclohexane} = (1-\xi)Z_0 + \xi H_l\big|_{water} \tag{4.26}$$

where ξ is a function of the thermophysical properties of the two fluids (depending on their own saturation state):

$$\xi((P_v, T_v)\big|_{cyclohexane}, (P_v, T_v)\big|_{water})) = \frac{T_v\big|_{water}\rho_l\big|_{water}\rho_v\big|_{cyclohexane}\Delta h_{lv}\big|_{cyclohexane}}{T_v\big|_{cyclohexane}\rho_l\big|_{cyclohexane}\rho_v\big|_{water}\Delta h_{lv}\big|_{water}} \tag{4.27}$$

For an arbitrary value of water[1] liquid height $H_l\big|_{water}$, Eq. 4.26 means that the liquid level $H_l\big|_{cyclohexane}$ for cyclohexane can be adjusted so that a same subcooling degree can be obtained in the two fluids at an arbitrarily chosen position Z_0. Yet, it is not desired to obtain the same subcooling degree only at a given position Z_0 but on a given range of altitude ($Z \in [0,\ \min(H_l\big|_{water},\ H_l\big|_{cyclohexane})]$). This is possible only if corresponding saturation states such as:

$$\xi((P_v,\ T_v)\big|_{cyclohexane},\ (P_v,\ T_v)\big|_{water})) = 1 \tag{4.28}$$

are set in the fluids[2]. With this condition, Eq. 4.26 becomes:

$$H_l\big|_{cyclohexane} = H_l\big|_{water} \tag{4.29}$$

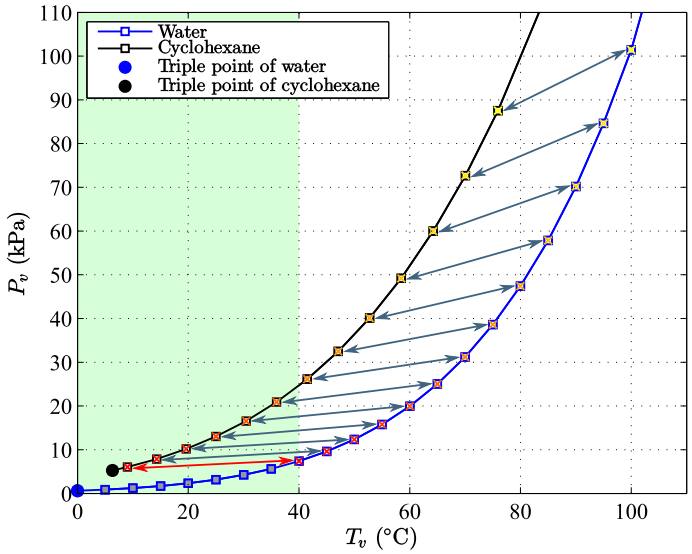

Figure 4.5 – Correspondence between saturation states of water and cyclohexane according to Eq. 4.28. – The green zone still corresponds to the temperature range permitted by the experimental facility.

An iterative process using [71] was implemented to determine – if it exists – cyclohexane

[1] Water is still taken as the reference fluid.

[2] This condition is equivalent to say that the gradient of subcooling along Z have to be identical in the two fluids (see Eq. 4.22 and 4.27).

saturation states associated with some water saturation states according to Eq. 4.28. Those corresponding points can be visualized on Fig. 4.5. The matching local subcooling degrees obtained in water and cyclohexane in the case of the conditions related to the couple of working points linked with the red arrow on Fig. 4.5 are compared on Fig. 4.6 for different liquid levels (identical for both fluids, Eq. 4.29).

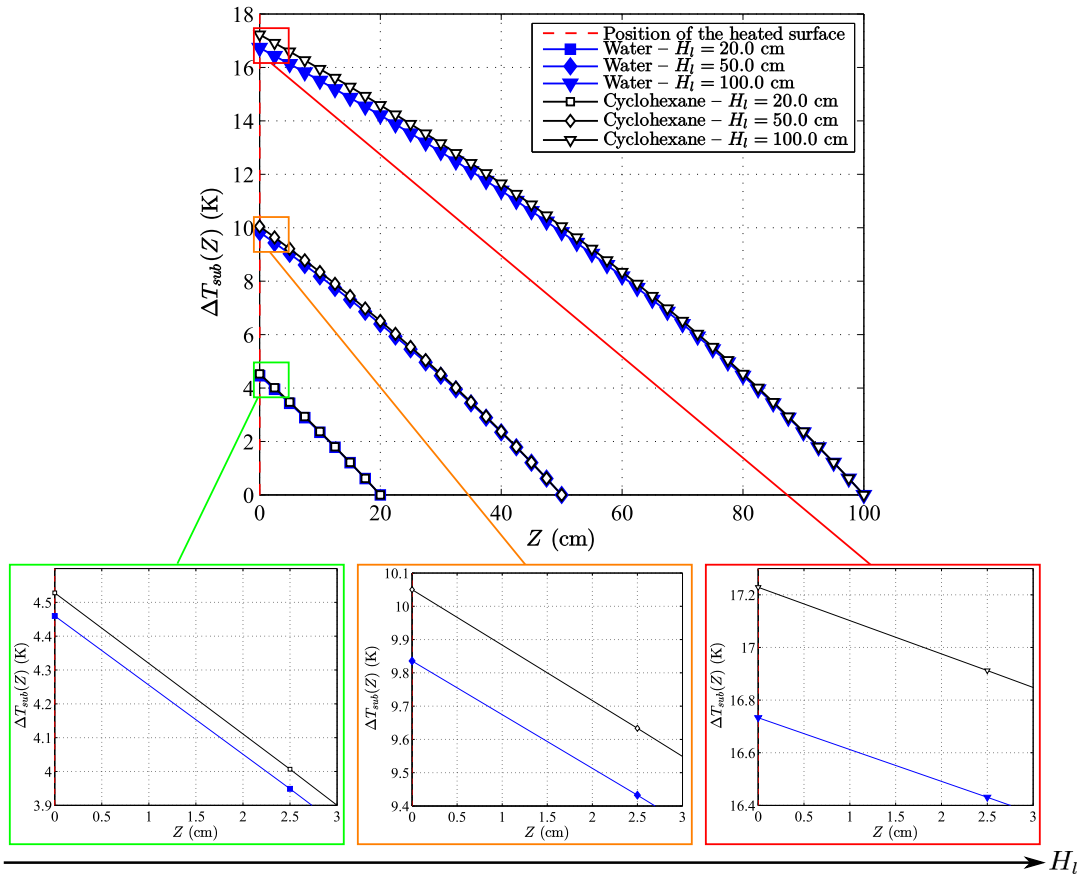

Figure 4.6 – Example of matching local subcooling obtained in water and cyclohexane and comparison depending on the liquid height – ($P_v\big|_{water}$ = 7.4 kPa, $T_v\big|_{water}$ = 40 °C), ($P_v\big|_{cyclohexane}$ = 6.0 kPa, $T_v\big|_{cyclohexane}$ = 9.0 °C).

This graph confirms that such couples of working points lead to similar local subcooling degrees in the two fluids. As expected, because of the use of the Clausius-Clapeyron relation for the determination of the working points pairs, the subcooling degree difference between the fluids increases as the distance to the heated wall decreases (*i.e.* as Z tends to zero). This deviation becomes thus greater as the liquid height H_l is increased. However, this deviation seems to remain acceptable for a relatively large range of liquid level (up to $H_l = 1$ m in the case presented on Fig. 4.6).

It appears on Fig. 4.5 that such saturation states of cyclohexane cannot be found for water at a saturation temperature strictly lower than 40 °C. Studying pool boiling of water and cyclohexane at low pressure with an identical local subcooling degree is therefore not possible with the experimental facility[1].

As a consequence, the couples of vapor pressure conditions ($P_v\big|_{cyclohexane}$, $P_v\big|_{water}$) and of liquid levels ($H_l\big|_{cyclohexane}$, $H_l\big|_{water}$) are chosen as independent parameters.

(i) The criterion on the pressure ratio $\frac{P_v}{P_t}$ (Eq. 4.10) appears finally as a good summary of the constraints imposed by both the new definition of the "low pressure boiling" and the experimental facility. The imposed values of vapor pressure P_v are subsequently

[1] As a reminder, the available thermostatic bath limits the vapor temperature T_v to the range [0 °C, 40 °C].

chosen so that the same values of the ratio $\frac{P_v}{P_t}$ are tested for the two selected working fluids:

$$\left.\frac{P_v}{P_t}\right|_{cyclohexane} = \left.\frac{P_v}{P_t}\right|_{water} \tag{4.30}$$

Vapor pressures P_v set for cyclohexane and water are thus proportional:

$$P_v\big|_{cyclohexane} = \frac{P_t\big|_{cyclohexane}}{P_t\big|_{water}} P_v\big|_{water} \approx 8.57 P_v\big|_{water} \tag{4.31}$$

(ii) Once the pairs of vapor pressure conditions chosen, it might have been of some interest to adjust the couples of liquid heights in order to obtain the same subcooling degree at the level of the heated surface (despite the gradients would be different and thus the subcooling degrees at the others levels too). However, as illustrated on Fig. 4.7 in the case where $\frac{P_v}{P_t} = 3$, this idea yields liquid levels for cyclohexane larger than the total height of the vessel.

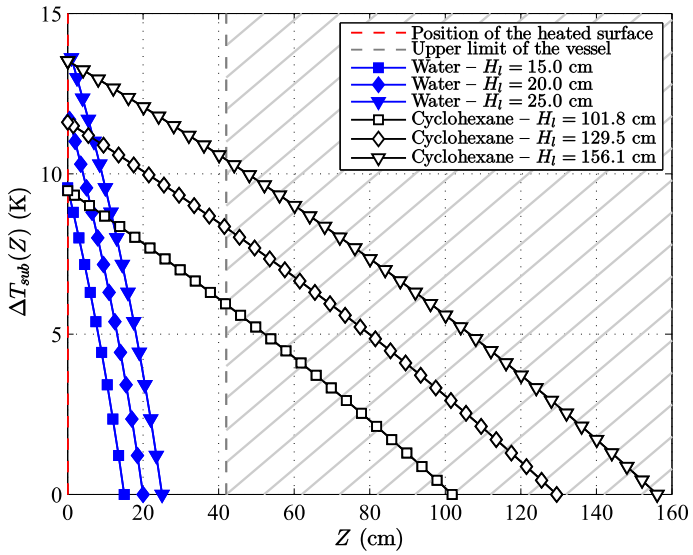

Figure 4.7 – Local subcooling degrees in water and cyclohexane with liquid heights adapted to get identical subcooling degrees at the level of the heated wall – Example at $\frac{P_v}{P_t} = 3$ ($P_v\big|_{water} = 1.8$ kPa ($T_v\big|_{water} = 15.9$ °C) and $P_v\big|_{cyclohexane} = 15.7$ kPa ($T_v\big|_{cyclohexane} = 29.3$ °C)).

Finally, because of the number of constraints that could not be solved in the time frame of this PhD work with the experimental means available, it is decided to choose arbitrary values of liquid level identical for the two fluids:

$$H_l\big|_{cyclohexane} \approx H_l\big|_{water} \tag{4.32}$$

Nevertheless, recommendations will be formulated to take into account the criteria developed in this chapter in future works.

4.2 Experiments with cyclohexane

In order to take the benefit of the concept of "mock-up fluids" described in the previous section (Section 4.1) to help identify the driving parameters leading to the specific characteristics of "low pressure pool boiling", experiments were carried out with cyclohexane. The related operating conditions are given in Section 4.2.1 while the results concerning the bubble dynamics and the heat transfer are presented in Sections 4.2.2 and 4.2.3 respectively.

4.2.1 Operating conditions

In agreement with the above discussions, the operating conditions detailed hereafter are set for the test campaign with the new fluid.

Working fluid: This experimental session is conducted with pure and degassed cyclohexane as the working fluid.

Heat flux input φ_{input}: For all the tests, the lowest imposed heat flux which enabled the observation of a regime of isolated bubbles growing from the artificial cavity was found to be equal to 2.0 $\mathrm{W \cdot cm^{-2}}$.

Vapor pressures P_v: Twelve values of vapor pressure were investigated. As shown in Table 4.2, those pressure levels are actually corresponding to twelve values of the pressure ratio $\frac{P_v}{P_t}$ covering the range of temperature reachable with the experimental facility ($T_v \in [0\ °C,\ 40\ °C]$).

Table 4.2 – Imposed pressure ratios and corresponding vapor pressures and temperatures of cyclohexane during the test campaign.

$\frac{P_v}{P_t}$	P_v (kPa)	$T_v = T_{l,\,bulk}$ (°C)
1.50	7.9	14.3
1.75	9.2	17.5
2.00	10.5	20.3
2.25	11.8	22.8
2.50	13.1	25.1
2.75	14.4	27.3
3.00	15.7	29.3
3.25	17.0	31.1
3.50	18.3	32.8
3.75	19.7	34.5
4.00	21.0	36.0
4.25	22.3	37.5

Pressure ratios lower than $\frac{P_v}{P_t} = 1.50$ were not tested. As a matter of fact, the air-tightness of the sample was not satisfied in such conditions: the glue seal alone was no longer effective enough to avoid the penetration of air inside the vessel while the very low imposed heat flux made the copper part of the heater not expanded enough to overcome the deficiency of the seal.

Liquid height H_l: For all the tests, the liquid height was set constant at the arbitrary value of $H_l = 17.8$ cm.

According to Fig. 4.8, as the liquid density ρ_l is almost constant over the investigated range of saturation pressures and temperatures, the static head induced by the column of liquid can be considered as constant:

$$P^{static}_{H_l=17.8\ \mathrm{cm}} = \rho_l(T_{l,\,bulk}) g H_l \approx 1.4\ \mathrm{kPa} \tag{4.33}$$

The local subcooling degrees $\Delta T_{sub}(z)$ are evaluated [71] and reported on Fig. 4.9 for all the investigated vapor pressure values. As already noticed for water in Section 3.1.2, the effect of the subcooling is lowered as the vapor pressure is increased since the local pressure moves away from the triple point pressure leading to a degradation of the "low pressure" conditions.

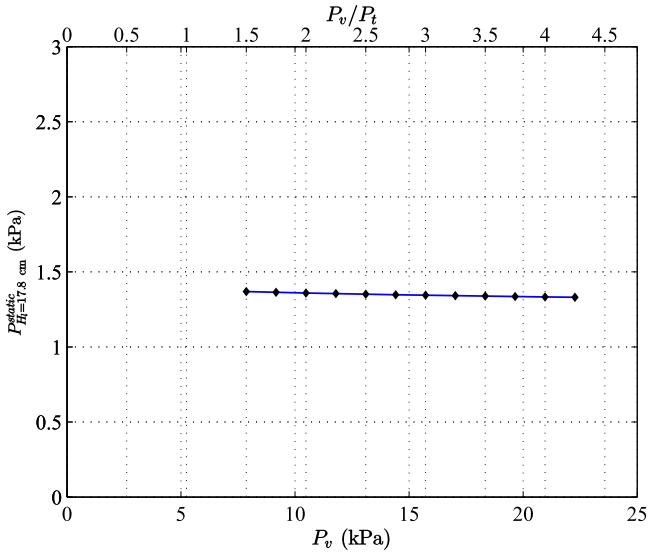

Figure 4.8 – Static head in cyclohexane $P^{static}_{H_l=17.8\ cm}$ depending on the vapor pressure P_v (bottom x-axis) and on the pressure ratio $\frac{P_v}{P_t}$ (top x-axis) ($H_l = 17.8$ cm).

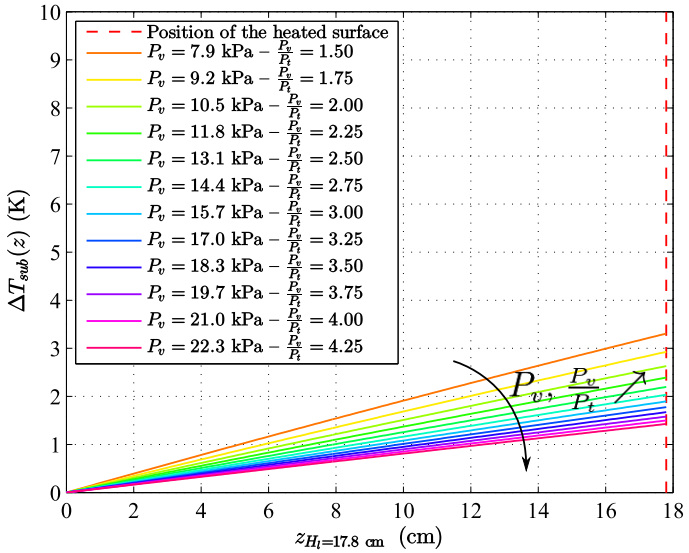

Figure 4.9 – Local subcooling ΔT_{sub} depending on the depth z in the cyclohexane for the different investigated vapor pressures P_v and pressure ratios $\frac{P_v}{P_t}$ ($H_l = 17.8$ cm).

4.2.2 Bubble dynamics

As expected when selecting the imposed heat flux, the boiling regime observed during all the experiments is the isolated bubble regime characterized by the growth and departure of single bubbles separated by a waiting time.

Contrary to what was noticed with water, this regime appears here to be not very regular or steady: for a given working point, bubbles seem to vary in size and frequency. This might be related to the wettability of cyclohexane. As a solvent commonly used in the chemical industry (in the production process of nylon for example [15]), this fluid presents a higher wettability than water[1] (*i.e.* a smaller contact angle θ), which was verified on several substrates [38]. Tong *et al.* [115] highlighted that – for highly-wetting liquids – the velocity of the liquid-vapor interface of the vapor nucleus inside the cavity changes in direction and magnitude during the bubble

[1] In the current case, the presence of the glue seal makes the measurement of the contact angle during bubble growth not possible for the two fluids. As a consequence, the actual effects induced by the higher wettability of cyclohexane compared to water on the heated surface cannot be assessed here.

embryo formation. Such a deformation of the interface leads to wide variations of the contact angle (the contact angle being low, a small distortion of the interface yields a large variation of the apparent contact angle) to which authors attributed the relatively large variations in the local wall superheat at boiling incipience reported for such fluids.

As with water, several behaviors in terms of bubble shape were observed. They are described in the following subsections.

4.2.2.1 Mushroom shaped bubbles

In the lowest range of investigated pressure, the bubble dynamics of cyclohexane boiling – with these specific liquid level H_l and imposed heat flux φ_{input} – is characterized by mushroom shaped bubbles. For 7.9 kPa $\leq P_v \leq$ 10.5 kPa (14.3 °C $\leq T_v \leq$ 20.5 °C, $1.50 \leq \frac{P_v}{P_t} \leq 2.00$), bubbles are indeed interacting by pairs. In a similar manner as in water (refer to Section 3.2.2), the departure of a primary oblate spheroid bubble is rapidly followed by a secondary elongated bubble which is sucked into the wake of the primary one and of its associated liquid jet. The pair of bubbles displays an apparent mushroom shape when the second bubble penetrates into the first one.

The case where $P_v = 7.9$ kPa ($T_v = 14.3$ °C, $\frac{P_v}{P_t} = 1.50$) – representative of the bubble dynamics behavior of cyclohexane in this range of pressure – is shown on Fig. 4.10.

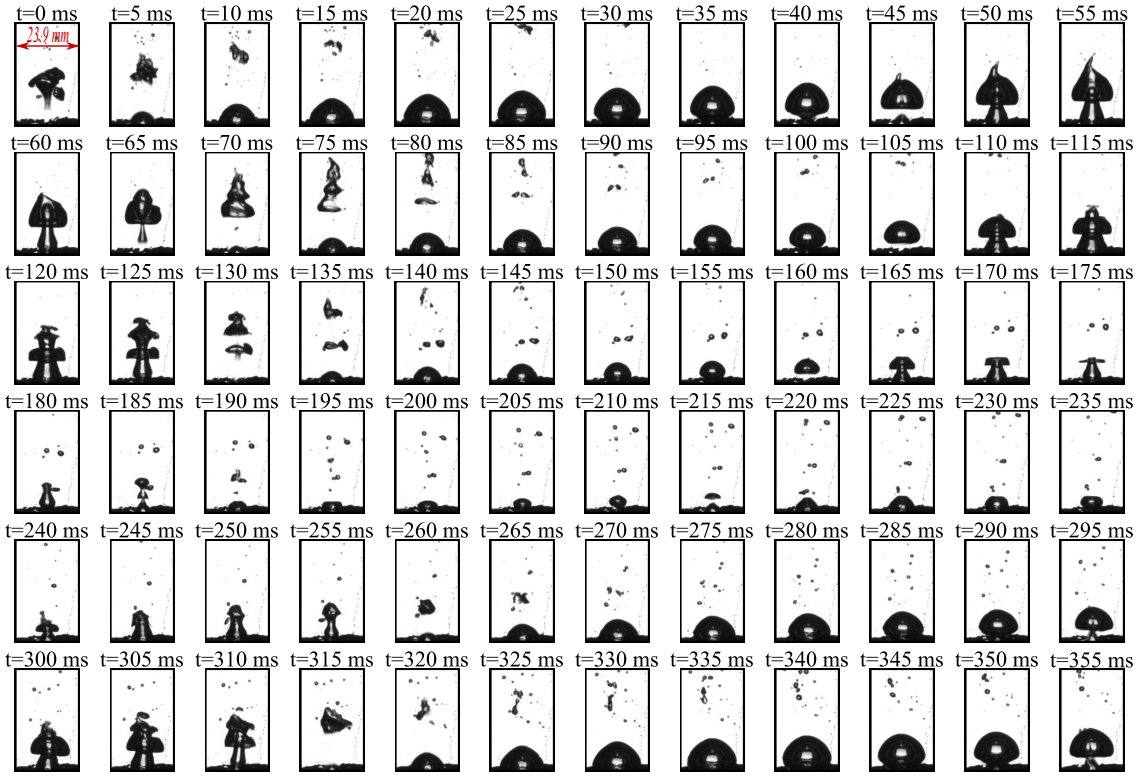

Figure 4.10 – Images of a video recording showing the time evolution of selected bubbles at $P_v = 7.9$ kPa ($T_v = 14.3$ °C, $\frac{P_v}{P_t} = 1.50$) (cyclohexane, $H_l = 17.8$ cm, $\varphi_{input} = 2.0$ W · cm^{-2}).

In this range of pressure, as illustrated on Fig. 4.10, the bubble size is varying from one pair to another: there are alternatively quite large bubbles (about 16 mm in diameter) and relatively small bubbles (about 8 mm in diameter). As explained in introduction of Section 4.2.2, this may be related to the wettability of cyclohexane which causes a poor stability of the bubble embryo leading to variations of both the contact angle and the local wall superheat from one bubble to another.

It appears here that the direct observation of the recordings does not enable the observer to conclude about any trends concerning the evolution of the bubble size, growth duration τ_{growth},

waiting time τ_{wait} or bubble departure frequency f with the pressure. Bubbles are indeed numerous on a given video and the fact they vary in size for the same operating conditions makes the direct comparison of several files difficult. However, in this case, a manual treatment of the video files was performed[1] since – as for the mushroom shaped bubbles observed in water – the contours of individual growing bubbles can be identified with the naked eye. Yet, it should be noticed that the accuracy of this image processing is here degraded compared to the situation with water because:

- The bubble frequency is clearly higher: both the growth time τ_{growth} and waiting period τ_{wait} are shorter while the absolute error on these characteristic properties is still the same ($\pm$ 1 to 2 ms) since the acquisition frequency of the camera is identical (1000 Hz).
- Bubbles are smaller while the imaging area used for the experiments still corresponds to the full size of the viewports (*i.e.* 100 mm wide): an error of a few pixels in the localization of the bubble edges leads to a larger relative error on the volume than for larger bubbles.

This quantitative analysis of the recordings confirmed that the variations of bubble growth time, waiting period or frequency of detachment with the pressure in this domain of interest (*i.e* for 7.9 kPa $\leq P_v \leq$ 10.5 kPa (14.3 °C $\leq T_v \leq$ 20.5 °C, 1.50 $\leq \frac{P_v}{P_t} \leq$ 2.00)) are small:

(i) In average, for all the three pressure levels, the growth duration τ_{growth} is almost constant and equal to about 20 ms. However, a large standard deviation (approximately 8.5 ms) is associated with this quantity. This scattering can be explained – in addition to the random character of the boiling phenomenon – by the alternation of large and small bubbles: as observed with water (refer to Section 3.3.2.5), the longer the bubble growth, the larger the bubble volume (maximum or at departure). The probability density functions (PDF) of the growth time related to each treated recording are then plotted on Fig. 4.11 to confirm this hypothesis.

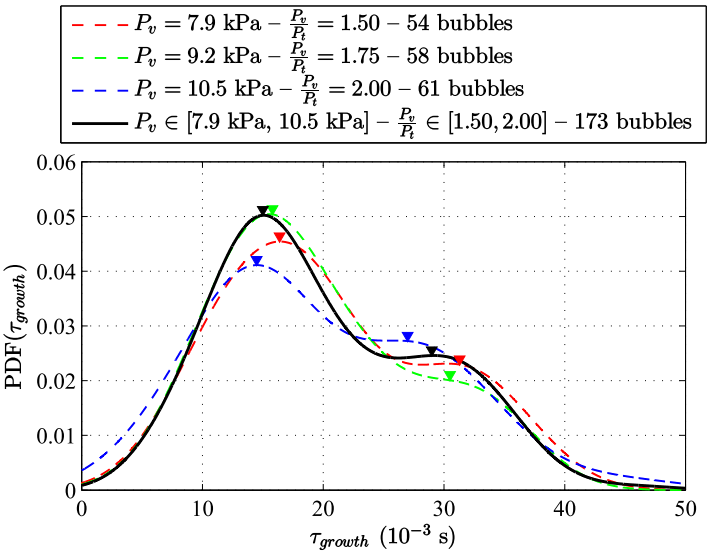

Figure 4.11 – Probability density function (PDF) of the growth duration τ_{growth} for 7.9 kPa $\leq P_v \leq$ 10.5 kPa (14.3 °C $\leq T_v \leq$ 20.5 °C, 1.50 $\leq \frac{P_v}{P_t} \leq$ 2.00) (cyclohexane, H_l = 17.8 cm, φ_{input} = 2.0 W · cm^{-2}).

For each processed file (*i.e.* for each of the three considered pressure levels), the PDF actually displays two peaks: one around τ_{growth} = 14.9 ms and a smaller one at about τ_{growth} = 29.2 ms. Those two peaks can be related to the two series of bubbles: to the

[1] Due to the number of bubbles visible on a video, the time required to process manually such a file is long (about 9 h of continuous work). Only one recording per operating condition was therefore treated. The large number of bubbles is however believed to make the extracted data representative of the behavior associated with the considered operating conditions.

group of small bubbles and to the group of the larger bubbles respectively[1]. As the pressure increases, those peaks are slightly translated to the left meaning that, statistically, the growth duration of a given bubble (small or larger) is shorter as the pressure augments[2]. This is in agreement with previous results obtained with water in Chapter 3.

(ii) The waiting time τ_{wait} which separates two successive bubbles slightly decreases when the pressure increases: its mean value varies from 6.9 ms at $P_v = 7.9$ kPa ($T_v = 14.3$ °C, $\frac{P_v}{P_t} = 1.50$) to 4.9 ms at $P_v = 10.5$ kPa ($T_v = 20.3$ °C, $\frac{P_v}{P_t} = 2.00$). Those small measured waiting times should be read with care since the associated relative uncertainty is then relatively high. According to the graph displayed on Fig. 4.12 which represents the PDF of the waiting time for the three pressure levels, in their huge majority, the waiting periods last between 0 and 10 ms. It happens yet that from time to time a waiting time lasts much longer (up to 55 ms). These outliers can be related to the random nature of boiling which is possibly reinforced by the instability of the vapor embryo caused by the high wettability of cyclohexane on the heated wall. Restricting the analysis to the data included in the major peak of the waiting time PDF yields a mean value of about 4.7 ms with a standard deviation of 1.3 ms which seems to be acceptable even though being of the same order of magnitude as the mean value.

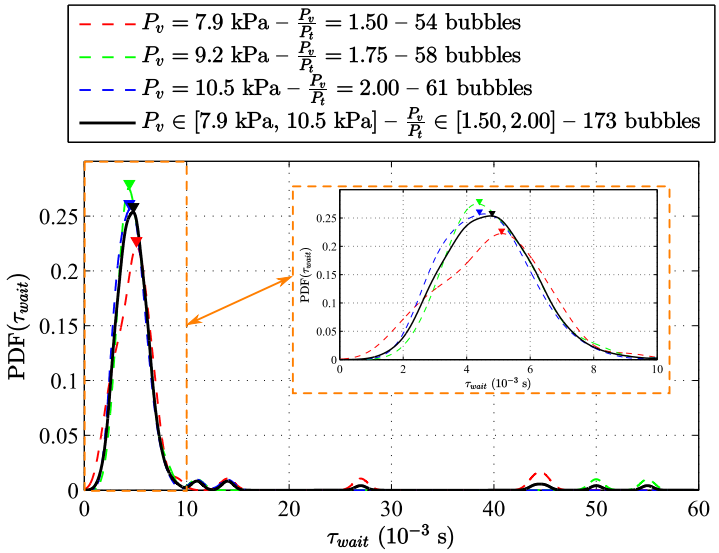

Figure 4.12 – Probability density function (PDF) of the waiting period τ_{wait} for 7.9 kPa $\leq P_v \leq$ 10.5 kPa (14.3 °C $\leq T_v \leq$ 20.5 °C, $1.50 \leq \frac{P_v}{P_t} \leq 2.00$) (cyclohexane, $H_l = 17.8$ cm, $\varphi_{input} = 2.0$ W · cm^{-2}).

(iii) The bubble departure frequency f slightly increases from 36.6 Hz up to 39.8 Hz as the vapor pressure augments. The number of bubble growths fully recorded on a file[3] changed indeed from 54 at $P_v = 7.9$ kPa ($T_v = 14.3$ °C, $\frac{P_v}{P_t} = 1.50$) to 61 at $P_v = 10.5$ kPa ($T_v = 20.3$ °C, $\frac{P_v}{P_t} = 2.00$). Consequently to (i) and (ii) and to the relationship that exists between the frequency and the growth and waiting times which is recalled as Eq. 4.34:

$$f = \frac{1}{\tau_{growth} + \tau_{wait}} \tag{4.34}$$

the increase of the bubble departure frequency with the pressure is more influenced by the evolution of the waiting period with the pressure rather than by the variation of the

[1] The fact that the second peak is smaller means that bubbles of small size are more numerous than bubbles of large size.

[2] This reduction of the growth time is however so low in the considered range of pressure that it is almost not visible on averaged values.

[3] As a reminder of Section 2.1.4.2, all the experiments were recorded with the acquisition frequency of the camera set to 1000 Hz so that all the videos last the same duration (approximately 1.54 s).

growth time.

The image processing of the recordings enabled also the quantitative analysis of the bubbles volumes.

The PDF of the bubble maximum (and at the detachment) volumes V_{max} (and $V_{departure}$) – plotted on Fig. 4.13 – confirm that for all the three considered pressures, most of the bubbles are small (with a maximum volume V_{max} lower than 0.7 cm^3). Moreover, these plots reveal that the group of larger bubbles is actually not homogeneous in size even at a given operating vapor pressure. A PDF associated to a given pressure condition presents indeed several (up to three) secondary peaks which correspond to the different greater volume values that are reached by a non negligible number of bubbles.

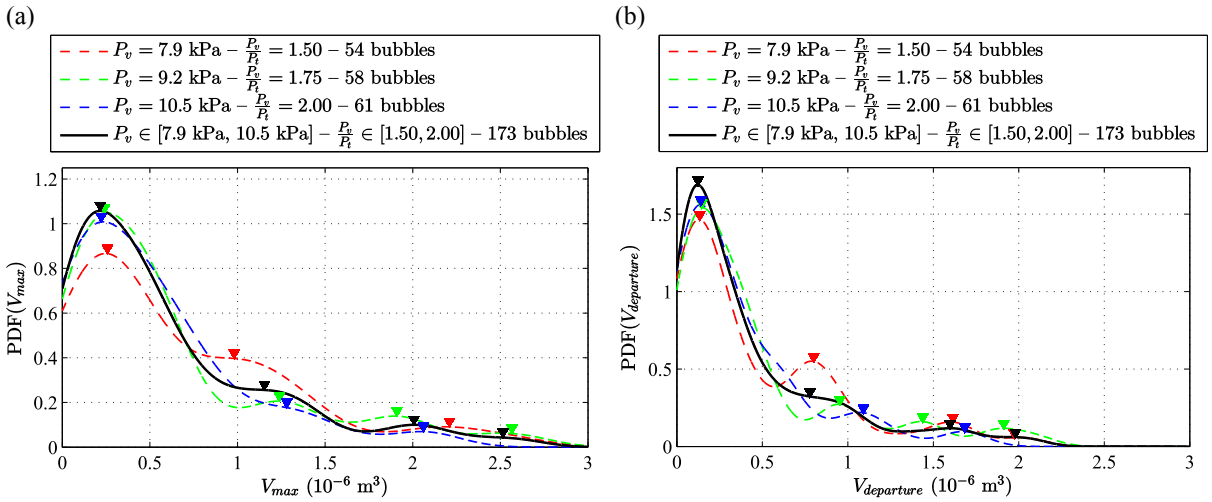

Figure 4.13 – Probability density function (PDF) of (a) the bubble maximum volume V_{max} and of (b) the volume at departure $V_{departure}$ for 7.9 kPa $\leq P_v \leq$ 10.5 kPa (14.3 °C $\leq T_v \leq$ 20.5 °C, $1.50 \leq \frac{P_v}{P_t} \leq 2.00$) (cyclohexane, $H_l = 17.8$ cm, $\varphi_{input} = 2.0$ W $\cdot$ cm^{-2}).

In a similar manner as it was done for water in Chapter 3, dimensional and non dimensional growth curves can be plotted for each recorded bubble. Hereafter, only the results concerning the dependence of the non dimensional volume V^* on the non dimensional time t^* are detailed.

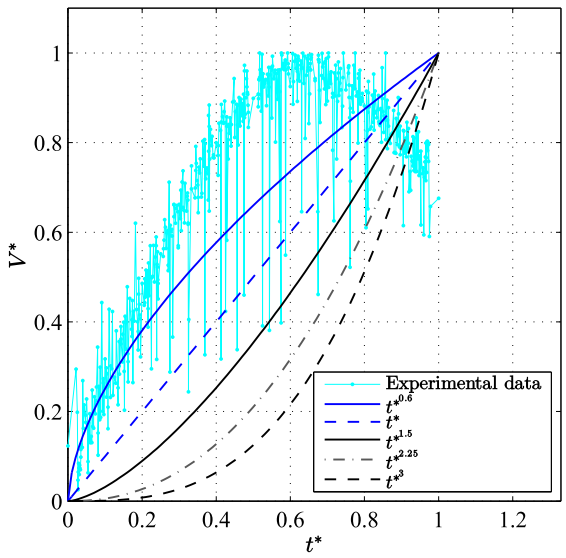

Figure 4.14 – Comparison of usual laws of growth with the experimental measurements associated with the 173 recorded and processed bubbles (cyclohexane, $H_l = 17.8$ cm, $\varphi_{input} = 2.0$ W $\cdot$ cm^{-2}, 7.9 kPa $\leq P_v \leq$ 10.5 kPa (14.3 °C $\leq T_v \leq$ 20.3 °C, $1.50 \leq \frac{P_v}{P_t} \leq 2.00$)).

On Fig. 4.14, the experimental measurements associated with the 173 recorded and processed bubbles are compared with the same usual laws of growth already listed and presented in Section 3.3.2.4.

According to this graph, the non dimensional volume V^* of cyclohexane bubbles observed under the considered conditions increases almost linearly before reaching its maximal value at $t^* \approx 0.65$. At $t^* > 0.65$, the volume decreases down to approximately 70 % of its maximal value at $t^* = 1$. One can also remark from this plot that the experimental data are relatively noisy. This may still be explained by the combination of:

- The small size of bubbles which increases the relative uncertainty on the volume evaluation;
- The scattering of the size of the bubbles associated with a given working point.

As none of the usual models fits our experimental points, the same procedure as previously is implemented to determine new models correlating the measurements. The ratio $\frac{\ln(V^*)}{\ln(t^*)}$ is thus plotted against the non dimensional time t^* on Fig. 4.15. As visible on this figure, this ratio decreases linearly for $0 \leq t^* \leq 0.65$ before increasing significantly for[1] $t^* > 0.65$.

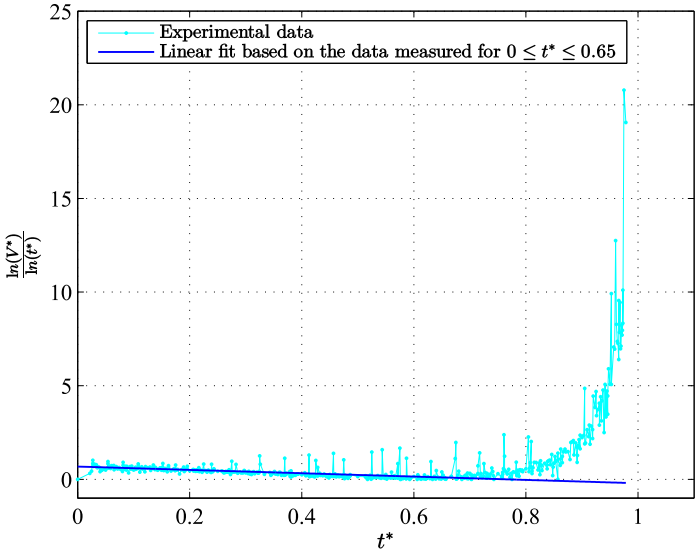

Figure 4.15 – Time evolution of the ratio $\frac{\ln(V^*)}{\ln(t^*)}$ associated with the 173 recorded and processed bubbles (cyclohexane, $H_l = 17.8$ cm, $\varphi_{input} = 2.0$ W $\cdot$ cm^{-2}, 7.9 kPa $\leq P_v \leq$ 10.5 kPa (14.3 °C $\leq T_v \leq$ 20.3 °C, $1.50 \leq \frac{P_v}{P_t} \leq 2.00$)).

A linear fit based on the first part of the time evolution of this ratio then leads to:

$$\frac{\ln(V^*)}{\ln(t^*)} = n(t^*) = -0.8915t^* + 0.6827 \quad \text{for} \quad 0 \leq t^* \leq 0.65 \tag{4.35}$$

The growth law can consequently be approached by:

$$V^* = t^{*^{n(t^*)}} = t^{*^{-0.8915t^* + 0.6827}} \quad \text{for} \quad 0 \leq t^* \leq 0.65 \tag{4.36}$$

As shown on Fig. 4.16, this model fits quite well the experimental data for $0 \leq t^* \leq 0.65$. However – as expected because of the restricted range of time t^* used to determine it – this model (Eq. 4.36) is unable to follow the decrease of the volume for $t^* > 0.65$. A simple polynomial fit of the experimental data is therefore also calculated and displayed on Fig. 4.16:

$$V^* = -0.3056t^{*^3} - 1.6422t^{*^2} + 2.6226t^* \quad \text{for} \quad t^* \in [0, 1] \tag{4.37}$$

[1] In addition, points are more scattered for $t^* \approx 1$ since both $\ln(V^*)$ and $\ln(t^*)$ tend to 0.

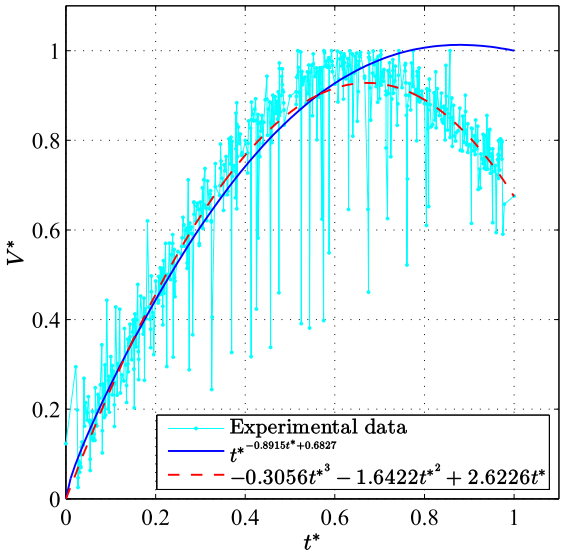

Figure 4.16 – Comparison of new models of growth with the experimental measurements associated with the 173 recorded and processed bubbles (cyclohexane, $H_l = 17.8$ cm, $\varphi_{input} = 2.0$ W $\cdot$ cm^{-2}, 7.9 kPa $\leq P_v \leq$ 10.5 kPa (14.3 °C $\leq T_v \leq$ 20.3 °C, 1.50 $\leq \frac{P_v}{P_t} \leq$ 2.00)).

4.2.2.2 Mushroom and column shaped bubbles

An alternation of pairs of bubbles displaying an apparent mushroom shape and of groups of several successive bubbles forming vapor columns characterizes the bubble dynamics associated with the pressure levels belonging to the intermediate range of investigation (*i.e.* for 11.8 kPa $\leq P_v \leq$ 15.7 kPa (22.8 °C $\leq T_v \leq$ 29.3 °C, 2.25 $\leq \frac{P_v}{P_t} \leq$ 3.00)).

A representative case of this regime – corresponding to the pressure $P_v = 11.8$ kPa ($T_v = 22.8$ °C, $\frac{P_v}{P_t} = 2.25$) – is shown on Fig. 4.17.

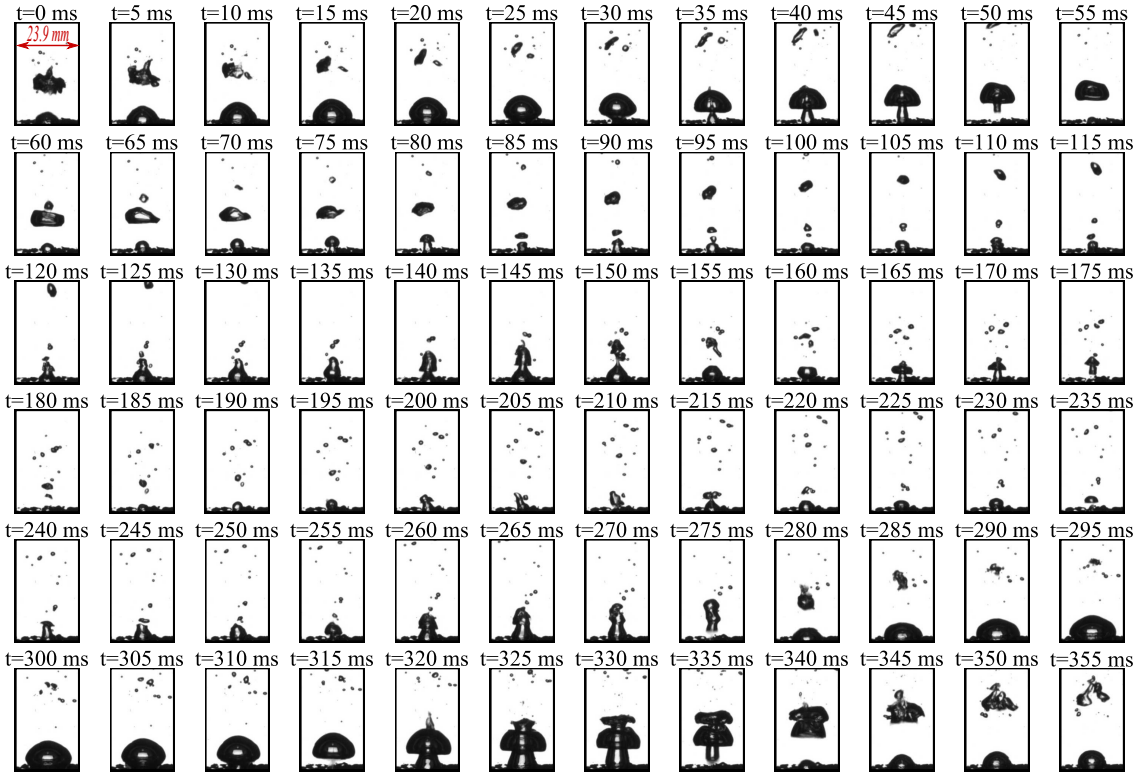

Figure 4.17 – Images of a video recording showing the time evolution of selected bubbles at $P_v = 11.8$ kPa ($T_v = 22.8$ °C, $\frac{P_v}{P_t} = 2.25$) (cyclohexane, $H_l = 17.8$ cm, $\varphi_{input} = 2.0$ W $\cdot$ cm^{-2}).

As visible on Fig. 4.17, the bubbles which form column shaped vapor masses are smaller than the bubbles which form mushroom shaped vapor masses. The bubble size still seems to decrease as the pressure is increased: for instance the diameter of the larger bubbles is of about 15 mm at $P_v = 11.8$ kPa ($T_v = 22.8$ °C, $\frac{P_v}{P_t} = 2.25$) and of approximately of 10 mm at $P_v = 15.7$ kPa ($T_v = 29.3$ °C, $\frac{P_v}{P_t} = 3.00$) whereas it was of about 16 mm at $P_v = 7.9$ kPa ($T_v = 14.3$ °C, $\frac{P_v}{P_t} = 1.50$) and of about 15.3 mm at $P_v = 10.5$ kPa ($T_v = 20.3$ °C, $\frac{P_v}{P_t} = 2.00$). The apparition of column shaped vapor masses might therefore result from the new size reduction of the smallest bubbles seen in the lower range of pressure. Such a bubble seems indeed to be so small that the depression locally induced by its detachment from the wall is too low to cause a liquid jet and to suck the subsequent bubble into its wake. Meanwhile, the number of bubbles involved in such columns of vapor seems to increase. Despite it cannot be quantified (since the numerous contacts between bubbles make the localization of individual growing bubbles edges not possible even with the naked eye), the bubble departure frequency f probably increases with the vapor pressure P_v.

4.2.2.3 Near-spherical bubbles

No more alternation of larger and smaller bubbles occurs at higher pressure (*i.e.* for 17.0 kPa $\leq P_v \leq$ 22.3 kPa (31.1 °C $\leq T_v \leq$ 37.5 °C, 3.25 $\leq \frac{P_v}{P_t} \leq$ 4.25)). In this case, bubbles are even smaller than previously, near-spherical and separated by a very short waiting time. As illustrated on Fig. 4.18 for $P_v = 17.0$ kPa ($T_v = 31.1$ °C, $\frac{P_v}{P_t} = 3.25$), successive bubbles are no more interacting despite a high detachment frequency.

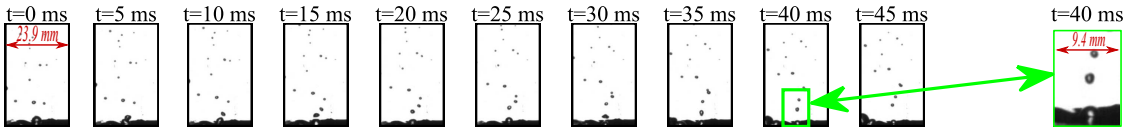

Figure 4.18 – Images of a video recording showing the time evolution of selected bubbles at $P_v = 17.0$ kPa ($T_v = 31.1$ °C, $\frac{P_v}{P_t} = 3.25$) (cyclohexane, $H_l = 17.8$ cm, $\varphi_{input} = 2.0$ W $\cdot$ cm^{-2}).

4.2.2.4 Summary

Results presented in this section finally highlight some trends concerning the bubble dynamics of cyclohexane during pool boiling in the regime of isolated bubbles at "low pressure" (with $H_l = 17.8$ cm and $\varphi_{input} = 2.0$ W $\cdot$ cm^{-2}). As the vapor pressure P_v is increased:

- The bubble size decreases: from around 15 mm (*i.e.* almost 9 times the capillary length of cyclohexane) to approximately 1.5 mm in diameter.
- The waiting time τ_{wait} decreases, yielding an increase of the bubble departure frequency f.
- The bubble shape changes:
  - An apparent mushroom shape caused by the contact between paired bubbles for 7.9 kPa $\leq P_v \leq$ 10.5 kPa (14.3 °C $\leq T_v \leq$ 20.5 °C, 1.50 $\leq \frac{P_v}{P_t} \leq$ 2.00);
  - A mushroom and column shape obtained from the interaction between two or more successive bubbles in the intermediate range of pressure (11.8 kPa $\leq P_v \leq$ 15.7 kPa (22.8 °C $\leq T_v \leq$ 29.3 °C, 2.25 $\leq \frac{P_v}{P_t} \leq$ 3.00));
  - A near-spherical shape without any contact between successive bubbles at higher pressure (17.0 kPa $\leq P_v \leq$ 22.3 kPa (31.1 °C $\leq T_v \leq$ 37.5 °C, 3.25 $\leq \frac{P_v}{P_t} \leq$ 4.25)).

Interestingly, these observations are relatively close to the ones made in Chapter 3 when studying water pool boiling at subatmospheric pressures.

4.2.3 Thermal measurements

4.2.3.1 Wall superheat ΔT_{wall}

As during the test campaign conducted with water in Chapter 3, the imposed heat flux is here so low [44] that no fluctuation is observed on the time evolution of the wall temperature T_{wall}^{exp}. However – contrary to the case of water – it was here expected to monitor some local variations of the wall temperature with time because of the alternation of small and larger bubbles which is possibly induced by the high wettability of cyclohexane (refer to the introductory paragraph of Section 4.2.2 and to [115] for details). The test sample instrumentation and its associated acquisition system make actually such an observation not possible: the acquisition frequency is too low compared to the growth time of a bubble τ_{growth}. For a given thermocouple, one measurement is indeed acquired every 3 s whereas the bubble growth duration is of the order of magnitude of only a few tens milliseconds.

Despite this huge limitation of the instrumentation, the measured values are used and time-averaged to evaluate the experimental wall superheat ΔT_{wall}^{exp} to be compared with the models of critical wall superheat $\Delta T_{wall}^{crit,\,0}$, $\Delta T_{wall}^{crit,\,1}$, $\Delta T_{wall}^{crit,\,2}$, $\Delta T_{wall}^{crit,\,3}$ and $\Delta T_{wall}^{crit,\,4}$ calculated using [71], following the method detailed in Section 3.3.1.2 in the configuration where a subcooling degree is induced by the static pressure.

First, the critical radius R^{crit} is calculated (through Eq. 3.9) and compared to the radius of the artificial nucleation site (which still constitutes the largest cavity on the heated surface, $r_{max} = r_{cav} = 55$ µm). According to Fig. 4.19, the critical superheat $\Delta T_{wall}^{crit,\,4}$ (Eq. 3.12) seems not to be adapted to the present situation since the critical radius is never exceeding the radius of the cavity. However, as this model was not so different from the others for water (refer to Fig. 3.12), this model is kept in the following comparison.

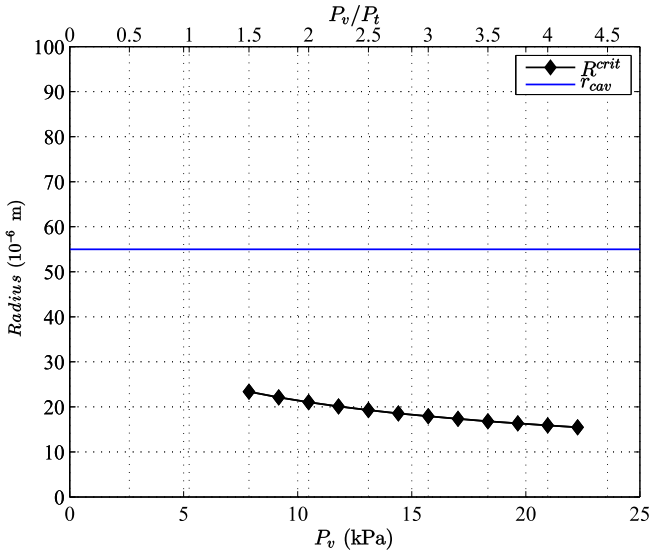

Figure 4.19 – Comparison of the critical equilibrium radius R^{crit} and the radius of the artificial nucleation site r_{cav} depending on the vapor pressure P_v and on the pressure ratio $\frac{P_v}{P_t}$.

The five critical wall superheat models as well as the experimental wall superheat are finally reported as a function of the vapor pressure P_v and of the pressure ratio $\frac{P_v}{P_t}$ on Fig. 4.20.

Contrary to what was observed with water (see Fig. 3.12), the curve corresponding to one of the five correlations for the critical wall superheat ΔT_{wall}^{crit} is clearly far from the others and from experimental values. The concerned model is $\Delta T_{wall}^{crit,\,3}$ which corresponds in fact to the model $\Delta T_{wall}^{crit,\,2}$ corrected by a factor taken equal to the Prandtl number of the liquid Pr_l. According to Kenning and Cooper [64] (cited by Rohsenow *et al.* [99] when introducing the different usual

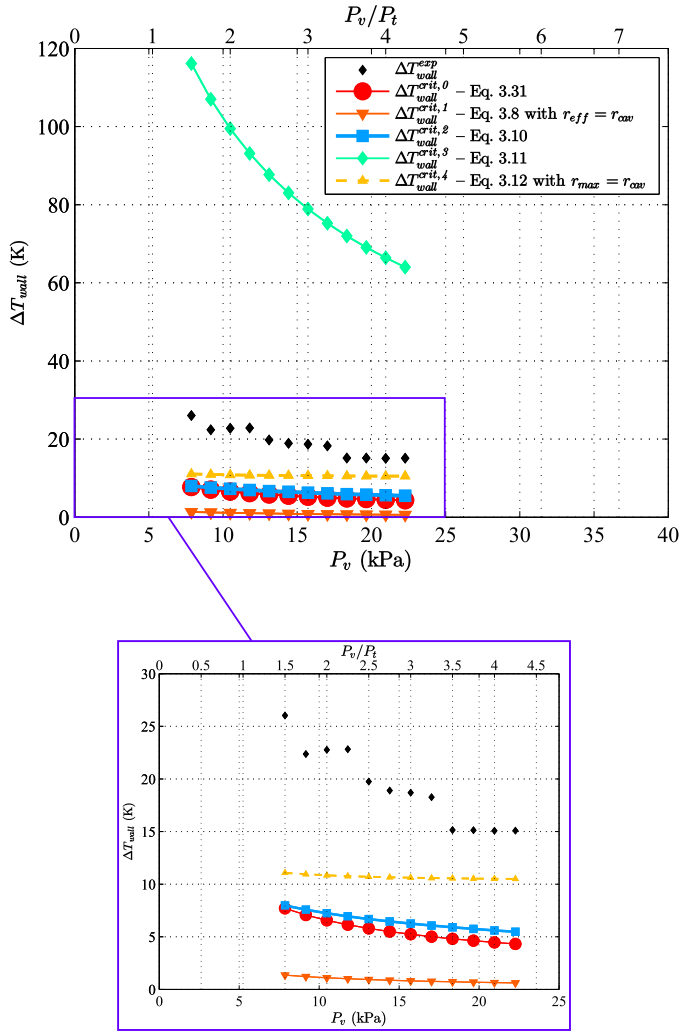

Figure 4.20 – Measured wall superheat ΔT_{wall}^{exp} vs the vapor pressure P_v and the pressure ratio $\frac{P_v}{P_t}$ and comparison with the theoretical minimal wall superheats required to activate boiling $\Delta T_{wall}^{crit,\,0}$, $\Delta T_{wall}^{crit,\,1}$, $\Delta T_{wall}^{crit,\,2}$, $\Delta T_{wall}^{crit,\,3}$ and $\Delta T_{wall}^{crit,\,4}$ obtained through Eq. 3.31, Eq. 3.8, Eq. 3.10, Eq. 3.11 and Eq. 3.12 respectively (cyclohexane, $H_l = 17.8$ cm, $\varphi_{input} = 2.0$ W $\cdot$ cm^{-2}).

models of critical wall superheat), the Prandtl number appears to play a role in the transitional situation occurring between the two limiting cases defined such as – in the layer of liquid where the bubble is nucleating:

1. The heat is essentially transferred from the wall to the fluid by single phase convection (*i.e.* the conduction process is negligible);

2. Most of the heat is transferred from the wall to the fluid by conduction (*i.e.* the convection process is negligible).

The authors justified this by the fact that the heat convection equation contains the product of the Reynolds Re and of the Prandtl Pr numbers[1]. According to Fig. 4.20, this corrected model is not adapted to the boiling of cyclohexane at such low pressures since the corresponding Prandtl number is high (decreasing from 14.6 down to 11.7 over the range of investigated working points[2]).

No specific conclusion can be made about the four other models: they only present a relatively

[1] This product defines actually the Péclet number $Pe = RePr$ which quantifies the ratio of the transfer by convection (advection) to the transfer by conduction (diffusion).

[2] In agreement with Section 3.3.1.2, these Prandtl number values are calculated for the superheated liquid at the critical wall temperature and the pressure at the level of the wall ($Pr_l = Pr_l(T_{wall}^{crit},\ P_{l,\,BL} = P_{wall})$).

flat shape which seems to be consistent with the evolution of the experimental measurements with the pressure, especially for $P_v \geq 18.3$ kPa ($T_v \geq 32.8$ °C, $\frac{P_v}{P_t} \geq 3.50$).

4.2.3.2 Heat transfer coefficient h

The heat transfer coefficient h at the heated wall is estimated as previously with reference to the system wall superheat ΔT_{wall}^{sys} (equal to the sum of the wall superheat ΔT_{wall}^{exp} and of the local subcooling degree evaluated at the level of the wall $\Delta T_{sub,\,wall}$):

$$h = \frac{\varphi}{\Delta T_{wall}^{sys}} \tag{4.38}$$

The related uncertainties are calculated as it was done for Chapter 3 in Appendix B. As the imposed heat flux φ_{input} is lowered compared to the test campaign conducted with water, the uncertainties are higher here than previously. For instance, the heat transfer coefficient is calculated within 5.8 % when considering the imposed heat flux value φ_{input} ($h_{\varphi_{input}}$) and within 60.6 % when considering the heat flux value φ_{meas} ($h_{\varphi_{meas}}$) obtained through the thermocouples measurements. As explained in Appendix B for the results given in Chapter 3, the uncertainty on the heat transfer coefficient $h_{\varphi_{input}}$ considering the imposed heat flux value φ_{input} is low but – contrary to the heat transfer coefficient $h_{\varphi_{meas}}$ considering the measured heat flux value φ_{meas}– this does not take into account the heat losses along the copper block at all. As the heat transfer coefficient $h_{\varphi_{input}}$ based on the imposed heat flux φ_{input} is always included in the uncertainty range of the heat transfer coefficient $h_{\varphi_{meas}}$ calculated from the measured heat flux φ_{meas} (Fig. 4.21), one can choose to consider either the first or the latter estimation of the heat transfer coefficient for further analysis.

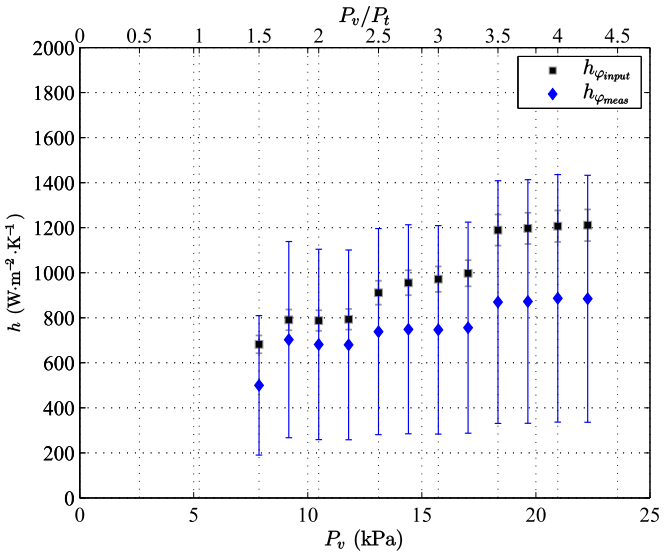

Figure 4.21 – Heat transfer coefficient based of the measured ($h_{\varphi_{meas}}$) and imposed heat flux ($h_{\varphi_{input}}$) for the different investigated vapor pressures P_v and pressure ratios $\frac{P_v}{P_t}$ (cyclohexane, $H_l = 17.8$ cm, $\varphi_{input} = 2.0$ W · cm^{-2}).

According to Fig. 4.21, during this experimental session, the heat transfer coefficient h is relatively low since it ranges from $h = 500$ to 1200 W · m^{-2} · K^{-1}. The remarks – made in Section 3.3.1.3 – which question the physical meaning of this quantity according to the current surface treatment (mirror-polished with a unique artificial cavity) still hold true with cyclohexane. One can however notice that the heat transfer coefficient is almost divided by 2 between the tests conducted with water and those carried out with cyclohexane while the same experimental apparatus – in particular the same heater and thus the same heated surface – was used. This can be explained by the combination of three facts:

- The imposed heat flux φ_{input} is slightly lowered from 2.7 W · cm^{-2} in water down to 2.0 W · cm^{-2} in cyclohexane;

- The bubbles of cyclohexane are in average much smaller than the bubbles of water while the latent heat of vaporization Δh_{lv} of cyclohexane is about five times lower than the one of water: as a consequence, despite of a higher bubble departure frequency, the amount of heat transferred by phase change may be lower in cyclohexane than in water;
- As most of the heat seems to be transferred by single phase convection (rather than by phase change), the liquid thermal conductivity λ_l may also play a role in the heat transfer coefficient difference that exists between the two fluids: this property is indeed about six times larger in water than in cyclohexane.

4.3 Comparison of the two fluids

4.3.1 Similarities and differences in terms of bubble dynamics

According to Chapter 3 and Section 4.2, the two test sessions conducted with water and cyclohexane during this work – with close liquid levels: $H_l\big|_{water} = 17.3$ cm $\approx H_l\big|_{cyclohexane} = 17.8$ cm and imposed heat flux values φ_{input} determined following an identical procedure (refer to Section 4.1.3) – exhibit similarities in terms of bubble dynamics.

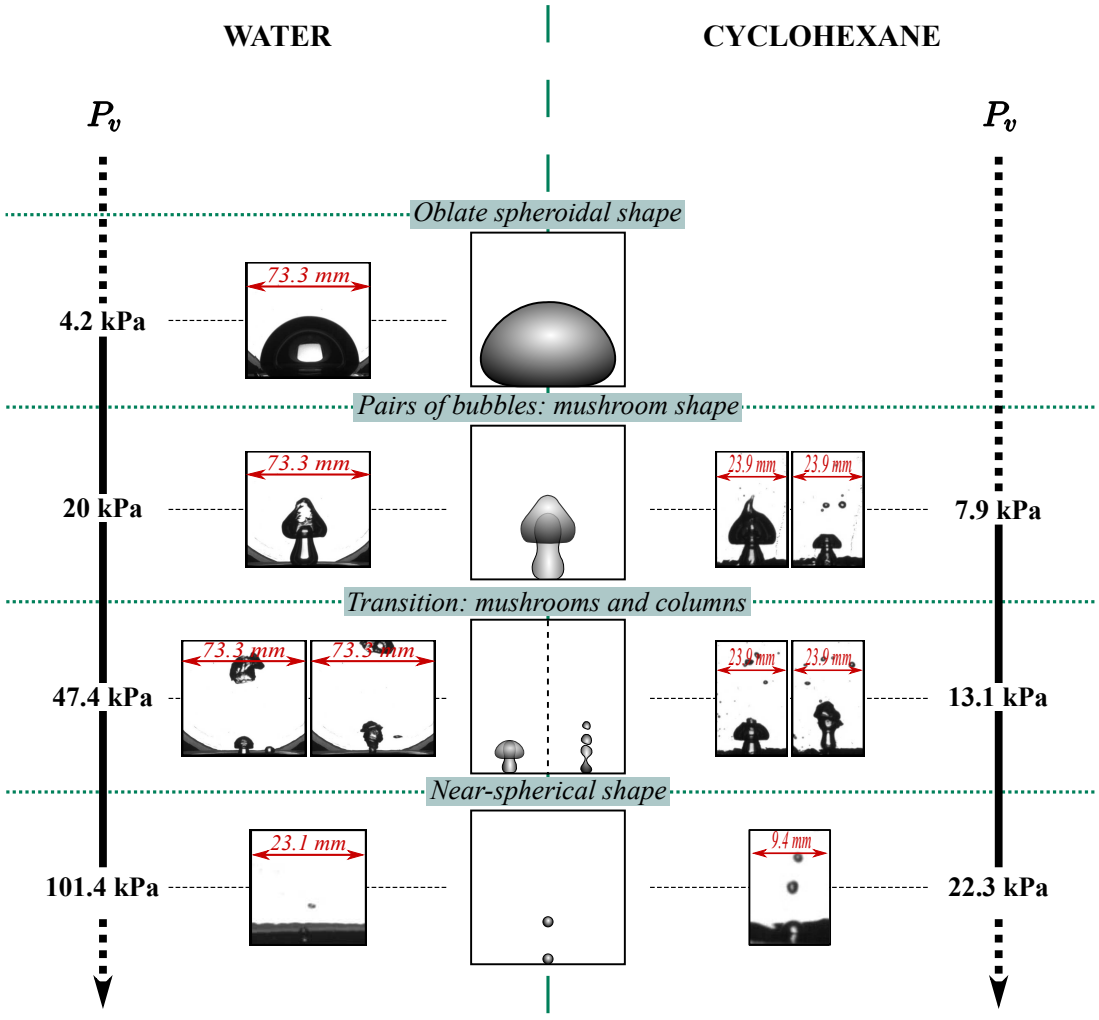

Figure 4.22 – Schematic comparison of the bubble dynamics observed in water and cyclohexane.

As schematically summarized on Fig. 4.22, three of the four behaviors identified in water are indeed also observed in cyclohexane:

- Mushroom shaped bubbles;
- Mushroom and column shaped bubbles;

- Near-spherical bubbles.

The fact that oblate spheroid shaped bubbles are not observed in cyclohexane may be related to the high wettability of this fluid on the heated surface. As illustrated in Table 4.3, in a "highly-wetting" fluid, the liquid always tends to re-wet the heated wall. The triple line is therefore still pushed towards the cavity by the liquid so that its motion on the surface during a bubble growth is small (*i.e.* the triple line tends to remain attached at the mouth of the cavity or close to it). This effect does not promote the formation of oblate spheroid shaped bubbles. On the contrary, in a "poorly-wetting" fluid, the wetting power of the liquid is small: as a bubble is growing, the triple line can move significantly away from the cavity's mouth, which may foster the apparition of bubbles of such a shape.

Table 4.3 – Schematic illustration of the possible effect of the wettability of the fluid on the bubble shape.

	"Poorly-wetting" fluid	**"Highly-wetting" fluid**
t	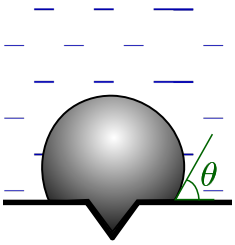	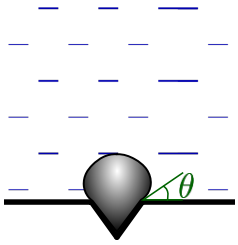
$t+\varepsilon$	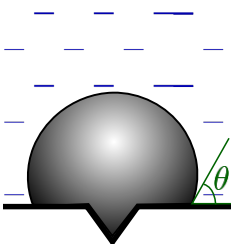	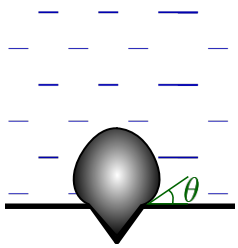

Although there exist conditions for which water and cyclohexane present a same regime of paired "mushroom shaped" bubbles, some differences in the realization of this particular pattern can be highlighted between the two fluids:

- An alternation of small and larger bubbles is visible in cyclohexane but not in water. This may be explained by the difference of wettability that exists between these two fluids (Section 4.2.2 and Tong *et al.* [115]).
- In average, bubbles are larger[1] and both the waiting and the growth times last longer[2] in water than in cyclohexane. These facts can be explained by, at once:
  - A lower liquid-vapor density ratio $\frac{\rho_l}{\rho_v}$ in cyclohexane than in water (this was actually one of the criteria of selection of cyclohexane in Section 4.1.2.3);
  - A higher contact angle (*i.e.* a lower wettability) in water than in cyclohexane: this is indeed known [61, 83, 84, 101] to slow the departure of bubbles from the surface (leading to larger sizes and longer growth periods) since it increases the downward surface tension force along the triple line.
- As shown on Fig. 4.23 where the experimental data points as well as the fits calculated for water[3] and cyclohexane – in Sections 3.3.2.4 and 4.2.2.1 respectively – are plotted, non

[1] Restricted to the measurements associated with bubbles displaying an apparent mushroom shape, the averaged maximum volume $\overline{V_{max}}$ (averaged volume at departure $\overline{V_{departure}}$ respectively) is indeed of about 2.95 cm^3 (2.82 cm^3) in water and approximately of 0.59 cm^3 (0.43 cm^3) in cyclohexane.

[2] Averaged growth duration $\overline{\tau_{growth}}$ is indeed equal to about 35.9 ms in water and to 20.0 ms in cyclohexane while the mean waiting time $\overline{\tau_{wait}}$ is of 14.7 ms in water and of 4.7 ms in cyclohexane.

[3] In fact, the models obtained for water were based on both the data associated with the oblate spheroid shaped bubbles and the mushroom shaped bubbles. As no significant difference was noticed between the experimental curves corresponding to these two behaviors, the data and models plotted on Fig. 4.23 are not restricted only to the mushroom shaped bubbles.

dimensional curves differ depending on the considered fluid. In particular:

- The maximum volume ($V^* = 1$) is reached at $t^* \approx 0.8$ in water whereas it is reached at $t^* \approx 0.65$ in cyclohexane;
- The non dimensional departure volume (at $t^* = 1$) is lower in cyclohexane than in water: $V^*_{departure}|_{cyclohexane} \approx 0.70 < V^*_{departure}|_{water} \approx 0.90$.

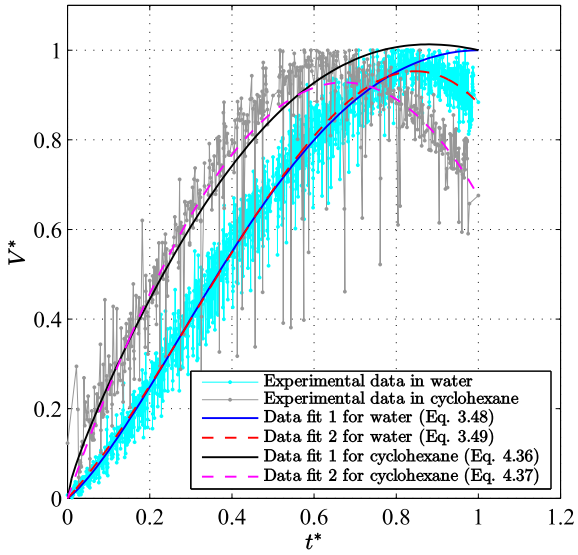

Figure 4.23 – Non dimensional growth measurements and models between water and cyclohexane.

The fact that – for experiments yielding mushroom shaped bubbles – the boiling environment where bubbles are formed and grow is more subcooled in cyclohexane than in water (refer to Fig. 4.24) may explain the more pronounced recondensation of bubbles (before their detachment from the heated surface) in the first fluid than in the latter. This higher subcooling degree combined to the higher wettability of cyclohexane might also contribute to the lower time t^* at which the maximum volume is reached. While the top of a growing bubble encounters a more subcooled liquid which fosters its recondensation, the vaporization may indeed be lowered at its base because of the small contact area of the bubble with the heated wall (*i.e.* since the microlayer is small because of the limited motion permitted to the triple line on the surface).

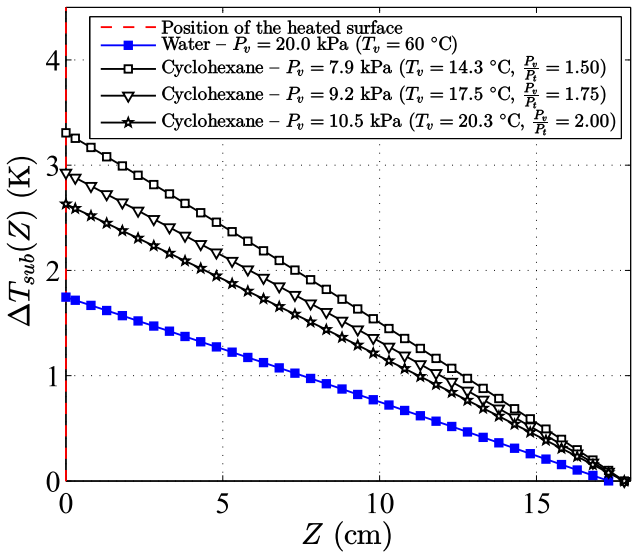

Figure 4.24 – Comparison between the local subcooling degrees $\Delta T_{sub}(Z)$ in water and cyclohexane for the experiments leading to mushroom shaped bubbles.

Using the experimental data collected by Cole and Shulman [27], Van Stralen *et al.* [119] and Han and Griffith [52] for water, n-pentane and methanol at different subatmospheric and atmospheric pressures, Kim *et al.* [67] showed that a well-chosen non-dimensionalization of the instantaneous bubble radius and growth time may lead to a kind of universal law of growth (*i.e.* independent on the bubble dynamics behavior, the working fluid and pressure level[1]). The non-dimensional characteristic radius and time the authors used were then based on a classical bubble growth model proposed by Mikic *et al.* [80] and on relationships involving several fluid thermophysical properties and the derived dimensionless Jacob number *Ja*. However, the implementation of this non-dimensionalization on our experimental data[2] related to water and cyclohexane proved to be unsuccessful.

Although similar bubble dynamics regimes were observed in water and cyclohexane, it is however clear from Fig. 4.22 that neither the vapor pressure P_v (varying from 4.2 kPa to 101.4 kPa in water and from 7.9 kPa to 22.3 kPa in cyclohexane) nor the pressure ratio $\frac{P_v}{P_t}$ (varying from 6.94 to 165.81 in water and from 1.50 to 4.25 in cyclohexane) is the governing parameter for this. An attempt to identify such driving parameters is thus presented in the following subsection (Section 4.3.2).

4.3.2 Research of driving parameters for "low pressure boiling"

4.3.2.1 Local subcooling degree ΔT_{sub}

A subcooling degree induced by the weight of the liquid column is a major characteristic of boiling at "low pressure". It was demonstrated in Section 4.1.3 that it is possible to find "corresponding saturation states" so that a same subcooling degree can be set in water and cyclohexane, it may be interesting to observe if transitions between the different bubbles dynamics behaviors occur at such corresponding points of the related saturation curves. As a reminder, those associated points are defined such as the function ξ (Eq. 4.27) is equal to the unity (Eq. 4.28) for an identical liquid height[3] in the two fluids (Eq. 4.29).

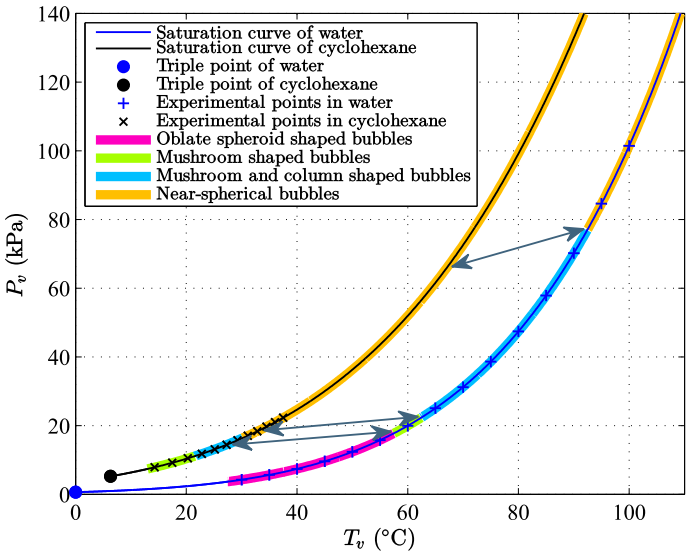

Figure 4.25 – Comparison of the transition points between bubble dynamics regimes and the associated "corresponding saturation states" in terms of local subcooling degree according to Eq. 4.28.

Saturation curves of water and cyclohexane are thus plotted on Fig. 4.25. On these curves, points experimentally tested are reported with markers while the visual distinction between the

[1] But also independent on the heated surface characteristics and liquid height since – with reference to Table 1.3 – those parameters were either different or unknown (and then supposed different) in the works of Cole and Shulman [27] and of Van Stralen *et al.* [119].

[2] For that, the equivalent radius of each bubble was derived from the instantaneous bubble volume.

[3] In the present case, the liquid heights in water and cyclohexane are not strictly equal but their difference is believed to be sufficiently small to have only a negligible influence on this analysis.

different bubble dynamics regimes is made possible with a color code. The three double-arrows also visible on this graph connect the saturation state points of transition between two successive bubble dynamics patterns in water and their associated points in cyclohexane according to Eq. 4.28. Although the subcooling degree clearly has to be taken into account at low pressure, this parameter alone does not appear to be sufficient to explain the apparition of similar boiling behaviors in the two fluids since the transition points in water do not correspond – through this criterion – to the transition points in cyclohexane.

4.3.2.2 Jacob number Ja

As mentioned in Section 1.1.3.1, the Jacob number Ja is a dimensionless number commonly used in phase change heat transfer as it characterizes the ratio of the sensible heat to the latent heat. The interest of this number seems here to be even reinforced by the large values it can reach at low pressure because of the high wall superheats and low vapor densities encountered. The Jacob number is hereafter calculated for water and cyclohexane according to Eq. 4.39:

$$Ja = \frac{\rho_l c_{p_l} \Delta T_{wall}^{sys}}{\rho_v \Delta h_{lv}} \tag{4.39}$$

so that the temperature difference considered is equal to:

$$\Delta T_{wall}^{sys} = T_{wall}^{exp} - T_{l,\,bulk} = \Delta T_{sub,\,wall} + \Delta T_{wall}^{exp} \tag{4.40}$$

and the properties related to the liquid are evaluated at $(P_v,\, T_v = T_{l,\,bulk})$ and these associated to the vapor and to the interface at $(P_{sat}(T_{wall}^{exp}),\, T_{wall}^{exp})$. The subcooling degree but also the effect of the non negligible variation of the density ratio $\frac{\rho_l}{\rho_v}$ along the saturation curve (see Fig. 4.2) are thus taken into account.

Results are reported on Fig. 4.26 as a function of the pressure ratio $\frac{P_v}{P_t}$ (in logarithmic scale for a better visualization of the data related to cyclohexane which cover only a narrow range of pressure ratio). On this graph, the same color code as previously is used to demarcate the four identified bubble dynamics regimes.

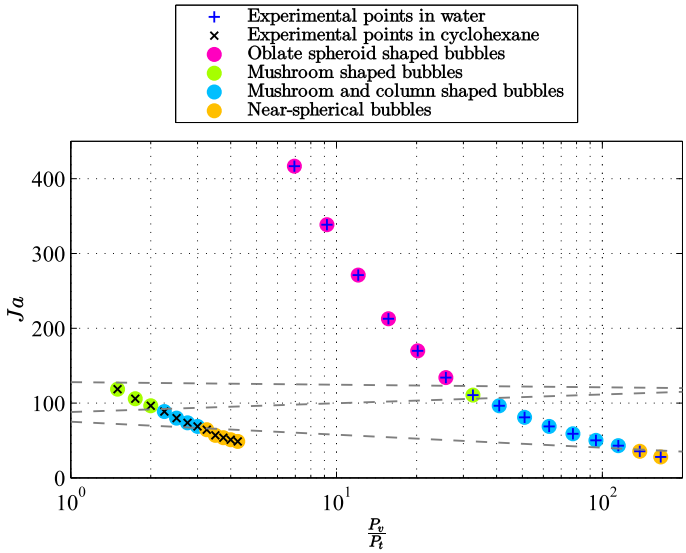

Figure 4.26 – Jacob number Ja as a function of the pressure ratio $\frac{P_v}{P_t}$ depending on the considered fluid and on the bubble dynamics behavior.

According to Fig. 4.26, a map depending on bubble dynamics pattern might be drawn according to the Jacob number. A first mapping is here attempted though more experimental data – obtained with other fluids and/or with other liquid heights (this would make vary the Jacob number even for a given fluid and a given operating pressure P_v) – are required to confirm or

refute such an approach. The four regimes (oblate spheroid shaped bubbles, mushroom shaped bubbles, mushroom and column shaped bubbles and near-spherical bubbles) could then be associated to four domains (delimited by dashed-lines on Fig. 4.26): the higher the Jacob number Ja, the more the bubble dynamics behavior deviates from the behavior usually encountered at normal or higher pressures. In addition to the lack of data to conclude about the validity of such trends, the fact that the dashed-lines plotted on the graph are not horizontal tends to show that the Jacob number cannot be the unique governing parameter of the "low pressure" boiling behaviors.

4.3.2.3 Robinson and Judd criterion I_R

At "low pressure", the bubble dynamics deviates strongly from the behavior usually seen at normal or higher pressures. In agreement with Carey [13] (see Section 1.1.3.1), Giraud [44] suggested that viscous effects and thus liquid inertia (*i.e.* dynamic forces) come into play in addition to the influence of the surface tension and buoyancy forces.

As mentioned in Section 1.1.3.1, by simulating growth of spherical bubbles in uniformly superheated infinite pools of liquid for a wide range of Jacob numbers, Robinson and Judd [98] developed a criterion to determine if a bubble expansion is mainly controlled by inertia or diffusion:

$$I_R = \left(\frac{4}{27}\right)\left(\frac{\sigma}{\rho_l \alpha_l^2}\right)\frac{R^{crit}}{Ja^2} \tag{4.41}$$

According to the authors, the bubble growth is governed by inertia if $I_R \ll 1$ whereas it is controlled by diffusion if $I_R \gg 1$.

Values of I_R reported on Fig. 4.27 are calculated through Eq. 4.41 for each experimental point with R^{crit} taken equal – in first approximation – to the radius of the artificial cavity radius: $R^{crit} = r_{cav} = 55$ µm.

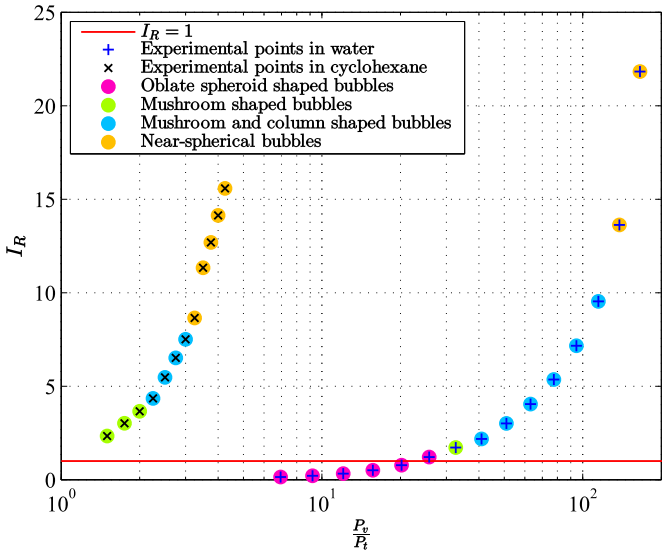

Figure 4.27 – Robinson and Judd criterion I_R as a function of the pressure ratio $\frac{P_v}{P_t}$ depending on the considered fluid and on the bubble dynamics behavior.

This graph appears actually as another way to present the dependence of water and cyclohexane regimes on the Jacob number since, for a given fluid, the involved properties (σ, ρ_l and α_l) do not vary significantly on the considered part of the saturation curve: I_R is then approximately equal to the product of a constant (of the fluid) and of the inverse of the squared Jacob number. This figure provides however an additional piece of information concerning the governing process of the growth depending on the pattern:

- Near-spherical bubbles seems clearly to be controlled by heat transfer diffusion ($I_R \gg 1$);

- Inertia tends to govern mostly the growth of oblate spheroid shaped bubbles ($I_R \leq 1$);
- Inertia and diffusion may play equivalent roles during the growth of mushroom shaped and of mushroom and column shaped bubbles since the I_R values related to those bubbles are of the order of magnitude of the unity.

These observations tend finally to confirm the idea according to which the influence on the bubble growth of inertia becomes non negligible under low pressure conditions.

As curves present an exponential-like shape on Fig. 4.27, I_R as a function of the pressure ratio is re-plotted on Fig. 4.28 in a log-log plot.

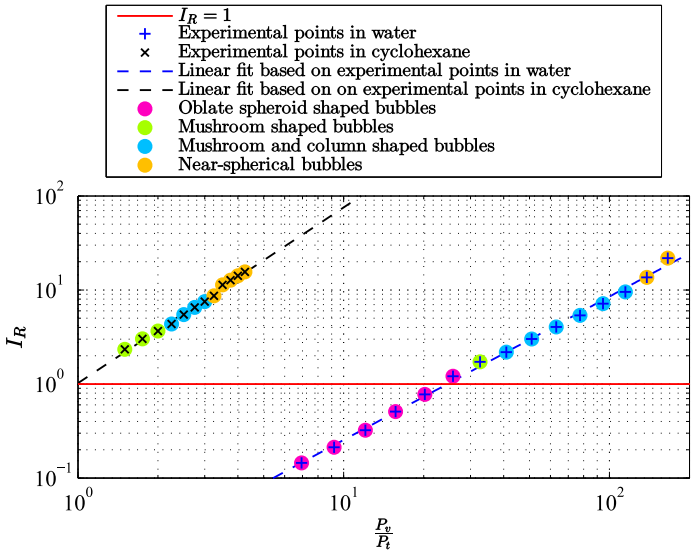

Figure 4.28 – Robinson and Judd criterion I_R as a function of the pressure ratio $\frac{P_v}{P_t}$ depending on the considered fluid and on the bubble dynamics behavior in a log-log scale.

As inferred from Fig. 4.27, in logarithmic scale, curves become linear meaning that I_R and the pressure ratio $\frac{P_v}{P_t}$ are linked according to a law of the form:

$$I_R = C\left(\frac{P_v}{P_t}\right)^n \tag{4.42}$$

Interestingly, the two curves are almost parallel so that the fits for water and cyclohexane yield relatively close values of the exponent n: $n|_{water} = 1.525$ and $n|_{cyclohexane} = 1.869$. Those results must however be considered with all the possible care since they are based on tests carried out with only two fluids (and more precisely with only one liquid height H_l per fluid for only two fluids).

Despite this approach may, to a certain extent, lack of reliability due to the limited amount of available data, it could give another indication concerning the absence of the regime of the oblate spheroid shaped bubbles in cyclohexane during this experimental work. In Section 4.3.1, one hypothesis related to the high wettability of cyclohexane was developed. Another assumption can be made from Fig. 4.28: this regime may not exist at all for this fluid under the tested conditions of liquid level and imposed heat flux. The data obtained for cyclohexane correspond indeed already to vapor pressures close to the triple point pressure which is the lower physical limit for the study of any boiling or vaporization phenomenon. The pressure range where the regime of oblate spheroid shaped bubbles could exist is therefore very narrow. In addition, the intercept[1] of the linear fit for cyclohexane plotted on Fig. 4.28 is close but slightly higher than the unity. According to the possible correspondence between the pattern of oblate spheroid

[1] This should correspond to the value of the I_R criterion at the triple point pressure.

shaped bubbles and the Robinson and Judd criterion highlighted above[1], this would mean that inertia cannot be the predominant force governing the growth of vapor bubbles in cyclohexane (*i.e.* that – within the settled liquid height and imposed heat flux – cyclohexane bubbles cannot take an oblate spheroid shape).

4.3.2.4 Concluding remarks

Collecting numerous additional experimental data is required to strengthen the analysis initiated in this section: other liquid levels and other fluids should be tested. However, some parameters seem to be unavoidable according to this first attempt to understand what is "low pressure" boiling from a general point of view. Among them, one can cite:

- The fluid wettability on the heated surface and its unknown dependence on the operating conditions among which the imposed pressure;
- The local subcooling degree induced by the weight of the liquid column;
- The Jacob number, which can also be a way to non-dimensionalize the subcooling degree;
- The inertia whose influence was highlighted here through the Robinson and Judd criterion I_R.

As inertia and dynamic forces appears to play a major role in the bubble growth at "low pressure", one can expect that both the fluid viscosity μ and the bubble velocity U (at its center of gravity or at its liquid-vapor interface) should also be taken into account in further studies.

Conducting experiments at "low pressure" with another fluid than water (under "well-defined" operating conditions) appeared as a promising track to get a better understanding of the "low pressure" pool boiling phenomenon. In this chapter, giving a more general definition of what is "low pressure" in boiling than "boiling at subatmospheric pressure in water" was therefore attempted. Several ideas were cited:

- *Boiling close to the triple point pressure: $P_{wall} = P_v + \rho_l g H_l \approx P_t$;*
- *Boiling under conditions such as the liquid height induces a non negligible local subcooling degree ΔT_{sub};*
- *Boiling at such low pressures that the bubble shape deviates from the usual shape (small size and near-spherical shape) encountered at normal or higher pressures.*

Considering simultaneously thermophysical properties of fluids and the limits of the experimental facility, cyclohexane was selected to be tested and compared with water and a design of experiments was determined.

Experiments were afterwards carried out with cyclohexane. Interestingly, three of the four bubble dynamics behaviors already identified in water (Chapter 3) were observed:

- *Mushroom shaped bubbles;*
- *Mushroom and column shaped bubbles;*
- *Near-spherical bubbles.*

Differences were quantified between the two fluids for the regime of mushroom shaped bubbles owing to the image processing tool.

Finally, a comparison of water and cyclohexane was conducted so that some driving parameters of boiling at "low pressure" could be identified. It appears from this analysis that:

[1] Bubbles of such a shape seem to be mostly controlled by inertia: $I_R \leq 1$

- *The local subcooling degree must definitely be taken into account, but it is alone not a sufficient governing parameter.*
- *The Jacob number seems to present some interest.*
- *The Robinson and Judd criterion demonstrates that inertia becomes non negligible at low pressure and may then be responsible for the deviation of bubble dynamics from higher pressures.*
- *The wettability of the fluid/wall pair also seems to have a non negligible influence.*

In the future, such an analysis certainly deserves to be continued. It however requires to collect a larger amount of experimental results. Various liquid levels and fluids should thus be tested at "low pressure". In addition, some parameters – not quantified during this work – should be estimated since they appear as to be considered. This is the case of, for instance:

- *The bubble velocity and the bubble interface velocity;*
- *The contact angle of the bubble on the heated surface depending on the fluid, vapor pressure, liquid height and imposed heat flux;*

The study of the fluid viscosity may also be of interest. At low pressure, bubbles are indeed likely to emerge from the thermal boundary layer since they reach large dimensions. As a consequence, such a bubble faces a large temperature difference between its base and its top. The encountered liquid viscosity could then be noticeably lower in the region of the bubble foot (higher temperature) than close to the bubble's top (lower temperature), because the viscosity varies relatively strongly with temperature in the vicinity of the triple point temperature. In link with the liquid inertia, this liquid viscosity variation along the bubble interface may finally result in specific bubble shape. As for a first approach, only the effect of the normal component of the fluid viscosity could be studied.

Chapter 5

An improved setup to study low pressure boiling

Previous results presented in Chapter 3 and Chapter 4 were mainly focused on the bubble dynamics at low pressure. In this chapter, some improvements are suggested, implemented and tested on the experimental facility in order to correlate the bubble dynamics with the heat transfer observed just under the bubble foot. This should help obtain a better knowledge of pool boiling at low pressure.
Section 5.1 deals with the changes made on the experimental facility, then Section 5.2 shows which issues were faced while testing the modified test bench as well as some promising preliminary results. Finally, the interest of this kind of instrumentation and acquisition system in boiling studies from a fundamental point of view is discussed in Section 5.3.

5.1 Modifications of the test bench

5.1.1 Motivations

Despite the large number of experiments conducted and despite interesting results were obtained with the setup detailed in Chapter 2, several drawbacks were identified. They are listed and described below.

A poorly known boiling environment: As demonstrated by Giraud *et al.* [46] and explained in Section 1.2.3, the boiling environment at low pressure is highly non-homogeneous. Depending on the distance z to the free surface, a non constant profile of local pressure $P(z)$, saturation temperature $T_{sat}(z)$ and subcooling $\Delta T_{sub}(z)$ settles up because of the importance of the weight of the liquid (in comparison to the vapor pressure P_v).

Presently, saturated conditions are assumed to be predominant in the vessel so that the temperature of the liquid far away from the bubbles $T_{l,\,bulk}$ is supposed homogeneous and equal to the temperature at the free surface $T_{sat}(z=0)$ and also to the saturation temperature of the vapor pressure ($T_{l,\,bulk} = T_{sat}(z=0) = T_{sat}(P_v) = T_v$). Experimentally this assumption on the bulk liquid temperature $T_{l,\,bulk}$ cannot be validated as the temperature of the liquid is measured for only one value of z. This lack had to be remedied by measuring the temperature of the bulk liquid for several heights in the improved version of the test bench.

A difficult tightness of the heater: The air-tightness is not very easy to realize with the sample described in Chapter 2 (Fig. 2.3). Adding a glue seal at the junction between the heated surface and the insulant is indeed necessary for that (inducing accordingly other problems especially for the visualization). Most of the time, a small heat flux input is also kept between experiments, during the night between two successive days of tests for example. This is done to maintain the copper expanded enough to ensure a high level

of tightness. The tightness being a critical problem for the study of pool boiling at low pressure, the design of the heater needed to be improved in this regard.

Thermal measurements inside the sample not always reliable: Several points can make the temperature measurements in the heater not fully reliable or accurate.

- Some thermocouples can be broken during the mounting procedure of the test sample to the stainless steel flange. This failure can occur even if the assembly is done with all the possible care: this issue is linked to the design of the sample itself.
- The thermal contact between the tip of the thermocouples and the copper block is ensured by a conductive silver lacquer deposit whose application is actually delicate. A good thermal contact can then be difficult to obtain.
- The estimations of the wall temperature T_{wall}^{exp} and of the heat flux φ_{meas} are actually only overall measurements of those parameters. They are indeed based on only two (even sometimes one) row(s) of four thermocouples (Section 2.1.4). In addition, holes in the copper block cannot be made deep enough to enable the insertion of the thermocouples just below the centered artificial nucleation site: the diameter of these holes being not larger than 1 mm, their depth cannot be made greater than 10 mm with conventional mechanical fabrication. As a consequence, the local effect of a growing bubble – depending on the position of the bubble on the heated surface – on the wall temperature and heat flux is difficult to observe and to quantify. This is particularly pronounced for small and centered bubbles since the thermocouples are then relatively far from the location where the nucleation and growth of bubbles take place.
- Compared to the bubble duration τ_{growth}, the acquisition frequency is low: for a given sensor, a measurement is collected every 3 s whereas the order of magnitude for a bubble growth duration at low pressure is of 100 ms maximum. It can be therefore difficult to catch the effect of the growth of a bubble on the heat transfer at the wall.
- Acquisition from the different thermocouples are made successively with a delay of about 110 ms between each which corresponds to the order of magnitude of the bubble growth duration. To minimize the error made while calculating the wall temperature or the measured heat flux, linear time-interpolations between successive measurements from the same sensor are made. The calculation of T_{wall}^{exp} and φ_{meas} is then computed using values of temperatures taken at the same instant. It would be better to have directly synchronous measurements from the different thermocouples.

All those reasons made necessary a deep modification of the test sample and of its instrumentation concerning the heat transfer monitoring.

No direct correlation between visualization and thermal measurements: The acquisition system used with the facility presented in Chapter 2 does not enable the synchronization between the high-speed camera and the thermal measurements. In fact, these two distinct aspects of the instrumentation are parts of two acquisition lines without any connection. Moreover, the ranges of acquisition frequencies possible for the visualization and for the thermal analysis are not compatible.

These four observations constituted strong motivations for a massive overhaul of the experimental facility.

5.1.2 Overall view of the improved setup

As shown on Fig. 5.1, the improved version of the setup keeps the same structure as the original one by including the same vessel, high-speed camera and lighting device. Changes concern only three elements:

1. A new thermal probe was added to measure the liquid temperature in different locations;

2. A new test sample was designed to enhance the tightness and to receive a new sensor for the thermal measurements;

3. A new acquisition system was designed and implemented in order to fit the use of the new sensors and to enable the synchronization of those acquisitions with the video recordings.

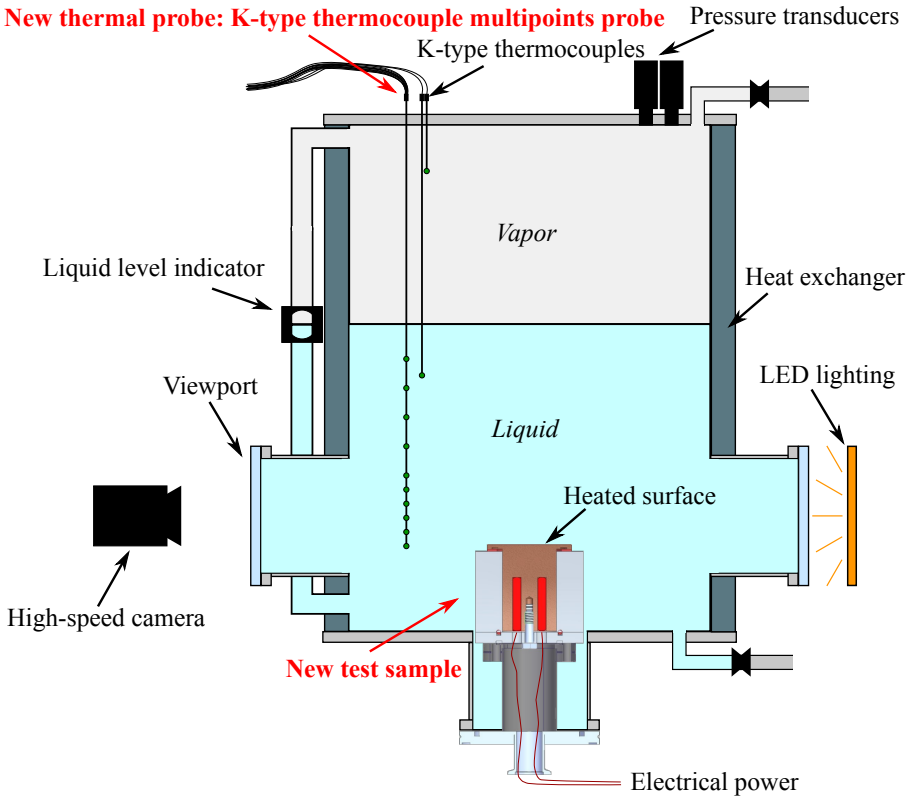

Figure 5.1 – Improved experimental apparatus.

5.1.3 A new thermal probe

In order to know the environment where bubbles are created and grow better, the bulk liquid temperature has to be measured for several heights. A new thermal sensor which consists of a 500 mm-long and 6 mm-diameter vertical multipoints probe along which the temperature is measured with ten distinct K-type thermocouples was hence added to the boiling pool.

The arrangement of the ten thermocouples (labeled from T_1 to T_{10}, starting from the probe's tip) is customized by the manufacturer (PROSENSOR) according to the diagram given in Fig. 5.2b so that they occupy the last 15 cm of the probe. The probe is settled to the chamber so as its tip (*i.e.* thermocouple T_1) is located at the same level as the heated surface. As the two other K-type thermocouples T_{vap} and T_{liq} aimed at being placed in the vapor and liquid phase respectively are not removed when adding the multipoints probe, twelve thermocouples are finally used to measure the working fluid temperature distribution. One is always located in the vapor phase (T_{vap}), while the others can be either in the liquid or in the vapor phase depending on the liquid height H_l over the heated surface. The positions (with their uncertainties) of all the twelve thermocouples in terms of distance to the heated wall (along the Z-axis[1]) are given in Table 5.1.

Horizontally, this probe is (as well as the two other thermocouples by the way) placed far enough from both the boiling area and the vessel's wall so that it can measure the bulk fluid temperature without being too much influenced by the presence of bubbles nor by the cold wall whose temperature depends on the circulation of the cooling fluid inside the vessel jacket.

[1] As a reminder: the Z-axis is oriented upward with reference ($Z = 0$) taken at the heated surface level.

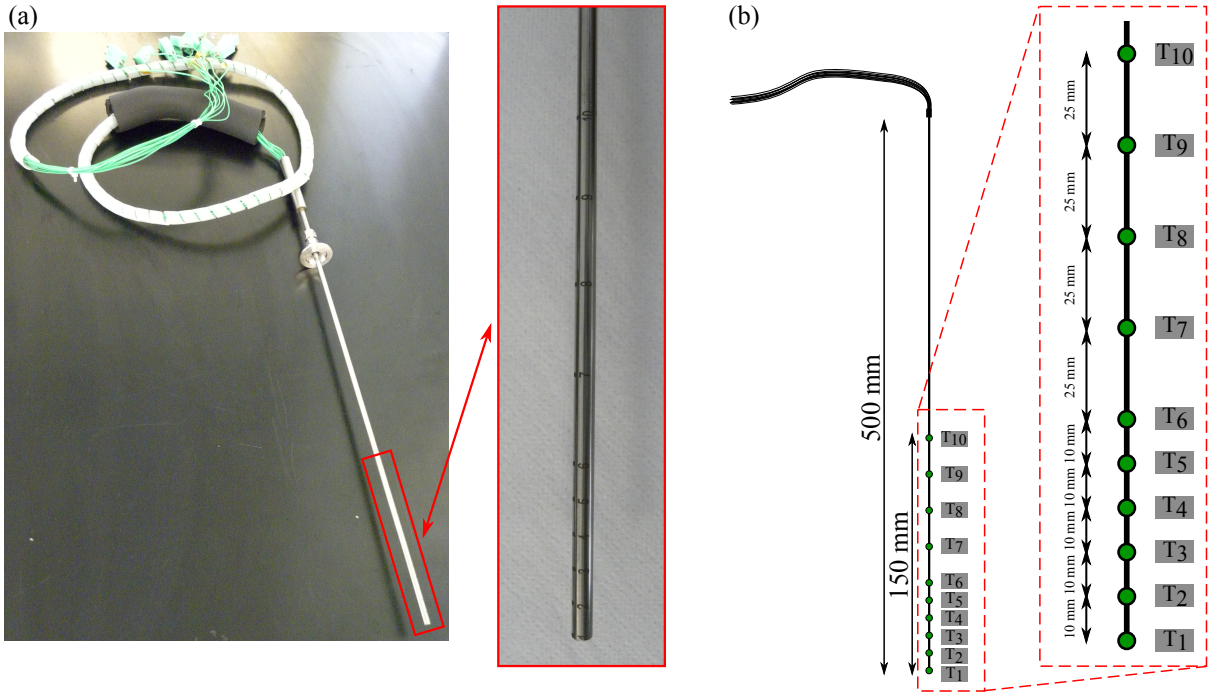

Figure 5.2 – New thermal probe: (a) Photograph; (b) Schematic diagram.

Table 5.1 – Positions of thermocouples in the fluid in terms of distance to the heated wall Z.

Thermocouple	Z **(cm)**
T_1	0.0 ± 0.1
T_2	1.0 ± 0.1
T_3	2.0 ± 0.1
T_4	3.0 ± 0.1
T_5	4.0 ± 0.1
T_6	5.0 ± 0.1
T_7	7.5 ± 0.1
T_8	10.0 ± 0.1
T_9	12.5 ± 0.1
T_{10}	15.0 ± 0.1
T_{liq}	11.3 ± 0.2
T_{vap}	32.4 ± 0.2

5.1.4 A new sample equipped with a new sensor

A new sample was designed in order to reach a higher air-tightness. This new test heater was afterwards equipped with an original sensor to improve the thermal measurements' quality. The heater's geometry is detailed in Section 5.1.4.1, followed by the description of the new sensor in Section 5.1.4.2. Consequences of the use of this new sample on the whole facility are finally exposed in Section 5.1.4.3.

5.1.4.1 Geometry of the new test heater

As it can be seen on Fig. 5.3 and similar to the previous sample, the main part of the new test heater is a copper cylinder. Two cartridge heaters (450 W maximum power) are inserted at the bottom of this cylinder to impose the heat flux to the block whereas a thin fin is machined at its top to limit peripheral boiling and to promote nucleation of bubbles on the surface. The dimensions and geometry of the copper block are different than in the previous sample. The copper cylinder is now indeed 50 mm in diameter and 80 mm high while the fin is larger (78 mm diameter instead of 50 mm). The size of the fin is increased in order to extend the surface on which boiling takes place with the aim of solving two problems observed with the previous sample:

- Some bubbles are so large that their feet are almost in contact with the boundary of the heated wall.
- The contact between the fin and the insulation part of the sample is not good enough to get a sufficient tightness.

However, enlarging the fin requires to increase its thickness to resist to mechanical stresses during machining but also when the sample is assembled. This may intensify heat losses through the fin and subsequently engender more undesired peripheral boiling. To prevent this unwanted effect, the fin is manufactured with a variable thickness (between 2.45 mm and 4 mm) within the limits of mechanical resistance as shown on Fig. 5.3).

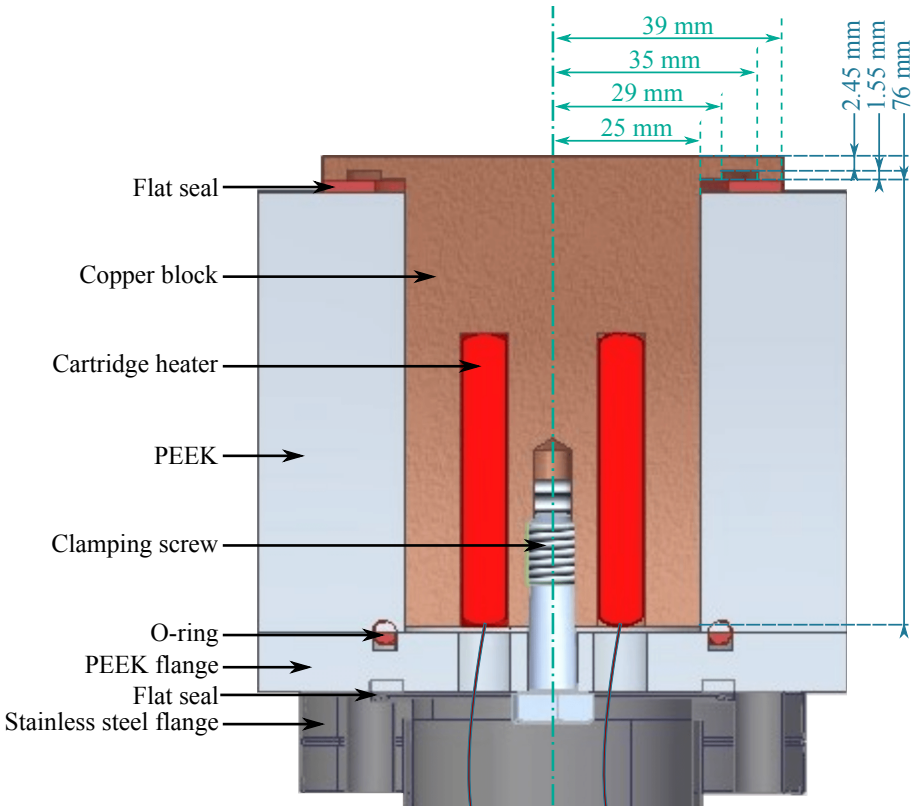

Figure 5.3 – Schematic diagram of the new test sample.

Insulation of the copper block is provided by a PEEK part and the copper/PEEK block is associated with a PEEK flange through a clamping screw to make the test heater tight. The obtained set is afterwards linked to a stainless steel flange to make the connection with the vessel possible. Seals between its different parts ensure a high tightness to the heater.

5.1.4.2 The new sensor

As bubbles show specific shapes and large size at low pressure, the bubble foot diameter is constantly varying. The local heat transfer at the wall is therefore an essential parameter to study to be able to make the link between thermal conditions, bubble dynamics and forces acting on a growing bubble under such pressure conditions. Based on the concept of the heat flux sensor used by Barthès [7], the new test sample was equipped with a thin customized heat flux transducer.

5.1.4.2.1 Principle of a heat flux sensor

The aim of using a heat flux sensor is to measure the local heat flux on a surface. In this study, the surface of interest is the heated wall on which boiling occurs and the considered heat

flux sensor uses the tangential gradient method of measurement. This method, used from few decades now [113,114], is based on the Fourier's conduction law according to which the heat flux is proportional to both the thermal conductivity and the temperature gradient. In such a heat flux transducer (also called "Théry-type heat flux sensor"), series of multiple junctions between metals having different thermoelectric powers (usually copper and constantan) are deposited on a thin insulant layer (generally made of Kapton). An asymmetry of the deposits of the two metals (illustrated on Fig. 5.4) then induces a distortion of heat flux streamlines, which engenders a tangential gradient of temperature. The presence of this temperature gradient induces afterwards a electromotive force between each terminal of each junction which is proportional to the heat flux crossing the sensor. Measuring this electromotive force and knowing the transducer sensitivity finally enable the measurement of the local heat flux crossing the sensor.

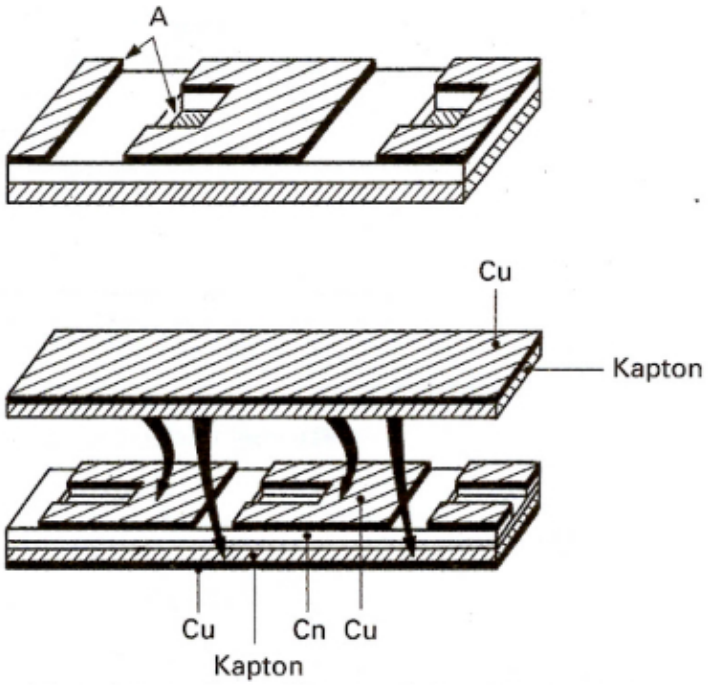

Legend:
Cu: copper
Cn: constantan
A: asymmetry due to the presence of an engraved borehole in the coppered constantan

Figure 5.4 – Cross-sectional view of a Théry-type heat flux sensor (adapted from [114]).

Details of the principle of working of that type of heat flux sensors are available – for instance – in [113, 114] and [127]. Yala-Aithammouda [127] focuses in particular on the design of the sensors sold by the company CAPTEC which produced the sensor used in this work.

5.1.4.2.2 Design of the heat flux sensor used as the heated surface

The customized heat flux sensor is aimed at being glued on the top of the heater and at being used as the heated wall. As a consequence, this sensor is circular and has the same size as the fin of the copper block (*i.e.* of 78 mm in diameter). In order to estimate the local heat flux under a (supposed) centered bubble and to follow the evolution of this variable as the bubble is growing (*i.e.* as the bubble foot is moving on the wall), the heat flux sensor is discretized into several concentrical zones of measurement. Seven areas of measurement – each one being matched to an independent heat flux sensor – are thus created inside the transducer according to the diagram shown on Fig. 5.5a. As clearly visible on Fig. 5.5b, a portion of the sensor's border is occupied by a ribbon cable containing two pins per measurement zone. Wires are soldered on those pins to take the signals out of the sensor. Fourteen wires (yellow and blue) are then associated with the seven measured heat fluxes. In addition, another pair of wires is used to measure the temperature difference ΔT which exists between the connection ribbon cable and

the center of the sensor. The temperature T_{co} on the connection cable being measured with a T-type thermocouple, the temperature T_{center} at the center of the heated wall is evaluated according to Eq. 5.1:

$$T_{center} = T_{co} + \Delta T \tag{5.1}$$

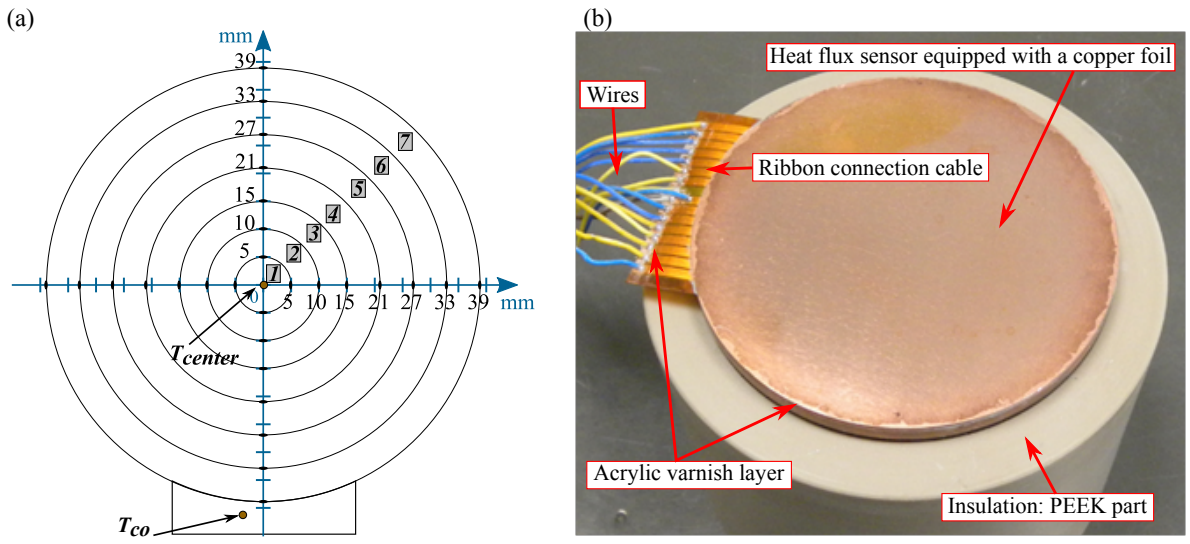

Figure 5.5 – (a) Diagram of the heat flux sensor; (b) Picture of the heat flux sensor glued on the test sample.

In addition to the customization in terms of number of zones and temperature measurement, the sensor is adapted to its peculiar conditions of use:

A heated surface structure: To be used as a heated wall, the sensor's top surface had to be prepared similarly as the heated surface of the previous experimental setup (limited roughness, creation of an artificial and centered nucleation site). For that, it had to be thick enough to allow – without any deterioration of the measuring parts – a mechanical polishing of its top surface as well as a mechanical indentation (of about 100 µm deep) at its center. This is why the copper coating usually put on the top surface of such a sensor by CAPTEC (about 0.1 mm thick) was here replaced by a copper foil of 0.3 mm. The thickness of the transducer is finally of 0.5 mm.

A liquid medium: Most of the time, heat flux transducers are used between two solid parts or between a solid part and the air. In the case of this work, it is used between a solid part and a liquid (and vapor) environment. To avoid any degradation of the sensor due to penetration of liquid inside it, its gluing on the copper block was provided by CAPTEC before the manufacturer added an additional layer of an acrylic clearcoat on the side surface of the fin. The same varnish was used on the ribbon connection cable in order to (electrically) insulate the wires welds from the working fluid but also to prevent any air from penetrating into the vessel through the small space that exists between the wires and their PTFE-sheaths.

A subatmospheric pressure environment: The sensor has to be used at low pressure. Under this condition, the air usually present inside such a sensor can induce deformations of the heated surface. To prevent this phenomenon, the transducer was filled with an epoxy resin.

5.1.4.2.3 Sensitivities of the sensor, temperature and heat fluxes determination

The sensor was calibrated properly by CAPTEC after having been glued on the copper block (the copper part shape and the glue layer have indeed an influence on the measurements that can be made with the sensor). Sensitivities of heat fluxes measurements are given for each zone in Table 5.2.

Table 5.2 – Sensitivities of the heat flux transducer depending on the zone.

Sensor	**Sensitivity** s $(\mu V \cdot (W \cdot m^{-2})^{-1})$
Zone # 1	0.50
Zone # 2	1.86
Zone # 3	3.37
Zone # 4	6.10
Zone # 5	7.70
Zone # 6	9.06
Zone # 7	7.95

Based on those sensitivities values, heat fluxes are calculated as follows:

For a given zone: The heat flux of the n^{th} zone HF_n is obtained by dividing the corresponding voltage output u_n by the associated sensitivity s_n:

$$HF_n = \frac{u_n}{s_n} \tag{5.2}$$

For an association of zones: The heat flux φ_{jk} associated with the set of zones $\# j$ to $\# k$ is simply the average of the individual heat fluxes weighted by the areas A_n of the concerned zones:

$$\varphi_{jk} = \frac{\sum_{n=j}^{k} HF_n A_n}{\sum_{n=j}^{k} A_n} \quad \text{where } j \text{ and } k \in [\![1, 7]\!] \text{ with } j \leq k \tag{5.3}$$

The overall heat flux φ_{meas} can subsequently be estimated by taking into account all the seven zones in Eq. 5.3.

Regarding the sensitivity of the temperature difference ΔT between the connection zone and the center of the heated wall, it is estimated to $s_{\Delta T} = 32\ \mu V \cdot K^{-1}$. The temperature difference is then calculated by dividing the corresponding signal output $u_{\Delta T}$ by this sensitivity:

$$\Delta T = \frac{u_{\Delta T}}{s_{\Delta T}} \tag{5.4}$$

5.1.4.2.4 Preparation of the heated surface and surface condition

As the heated wall of the first version of the experimental facility, the new heated surface is mirror-polished with diamond paste before a mechanical indentation is operated at its center to create an artificial nucleation site.

During the preparation of the surface, two critical features have to be taken into account in order not to degrade the sensor and its measurements:

- The acrylic clearcoat put on the side surface of the fin which is a little extended on the periphery of the sensor should not be removed during polishing. Otherwise, the transducer may be no more tight to the working fluid.
- The artificial nucleation site should not be deeper than the thickness of the copper foil.

The surface condition of the sensor is afterwards carefully analyzed using the confocal microscope. This analysis is required to verify that the new heated wall is comparable (in terms of roughness and cavity's size) to the heated surface of the previous test sample. The study of the surface condition is carried out in three steps:

(i) The full sensor is analyzed with a quite low spatial resolution in order to check the large-scale uniformity of the whole surface. The spatial step p is chosen to obtain a relatively good trade-off between the measurement time and the spatial resolution.

(ii) Several zones of the surface of different sizes are randomly analyzed with the microscope using an intermediate spatial step value. This is aimed at verifying – with a better spatial resolution – if the surface looks uniform or not.

(iii) A central zone is accurately (low spatial step) analyzed to evaluate the surface roughness and the size of the artificial nucleation site.

Hereafter, only the main results of this surface condition investigation are given (more details are available in Appendix A.2):

- The heated surface constituted of the heat flux sensor is homogeneous and smooth. Its root mean square roughness S_q is indeed lower than 0.4 µm which is comparable to the roughness of the heated wall of the first test sample (refer to Section 2.1.3.2).

- The artificial nucleation site is characterized in terms of position, shape and size. With a diameter of 100 µm, a depth of 110 µm, a conical shape and a centered position, this cavity is similar to the one of the first test heater.

5.1.4.3 Consequences of the use of the new test sample on the setup

As it can be inferred from Fig. 5.5b, seventeen wires (7 pairs for heat fluxes, 1 pair for temperature difference and 1 T-type thermocouple) have to be taken from the sensor to the acquisition system. Contrary to what happened with the previous test heater, these wires cannot cross through the vessel's enclosure through the bottom of the sample itself. As a consequence, a viewport which is used neither for lighting nor for video recording was changed to a home-made feedthrough. This borehole is subsequently not available anymore for any kind of visualization (naked-eyed or with a camera). In order to prevent the wires from being visible in the imaging field during experiments, they are weighted down with small stainless steel parts inside the vessel.

5.1.5 A new acquisition system

As the new instrumentation is very different from the one used with the former version of the experimental facility, a new acquisition system had to be developed. This one is aimed at:

- Acquiring all the signals from the new sensors;

- Remediating to some acquisition limits observed with the precedent version of the test setup by:

  – acquiring the signals synchronously;

  – increasing the acquisition speed;

  – enabling the synchronization between the measurements and the video recordings.

Concerning the high-speed camera, it was decided – for the sake of easier and quicker implementation – to continue to acquire the data with its own acquisition software (PFV). The camera is consequently still connected to a computer (PC_1) through an acquisition card. PFV software and the acquisition card enable the synchronization of the camera with other systems by putting the digital signals of beginning and end of video recording at disposal for such systems.

Other signals (from the thermocouples or the heat flux sensor in particular) have to be conditioned before being acquired. A customized box containing all the electronics for measurement signals conditioning was designed at the laboratory in this aim. This conditioning module includes the following elements:

The conditioning of thermocouples' signals:

- The electromotive force of each thermocouple is measured in differential voltage mode with a ground reference realized through two bias resistors (100 kΩ each) wired inside the customized module.
- All the cold junctions of the thermocouples are also embedded in this conditioner. At the nearest of the thermocouples' connections, the cold junction temperature is thus measured with two platinum resistance thermometers Pt100. The concerned area is thermally insulated to provide sufficient steady conditions in use.

The conditioning of signals related to the heat flux sensor: Similar to the signals coming from the thermocouples, the differential voltages from the heat flux sensor (associated with ΔT and with HF_1 to HF_7) are ground referenced in the conditioning box with 100 kΩ-bias resistors.

The electrical circuit associated with the pressure transducers: The pressure transducers have to be powered and deliver current signals whose values are correlated with the measured pressures. For the sake of a clearer acquisition line, the corresponding power supply is connected to the sensors through the home-made electronic module. Signals from the pressure transducers are consequently acquired at its output.

The electrical circuit related to the heating power input: The heat power input HP_{input} can be calculated by multiplying the values of the input voltage u_{input} and current i_{input} delivered by the power supply dedicated to heating:

$$HP_{input} = u_{input} i_{input} \tag{5.5}$$

u_{input} and i_{input} are deduced from two voltage signals that are also delivered by the power supply and are proportional to the input voltage and current respectively. Still for acquisition chain clarity, these signals pass through the conditioning box.

Once all the signals properly conditioned, they are acquired with an adapted National Instruments (NI) module as detailed in Table 5.3.

Table 5.3 – NI modules chosen depending on the signals to acquire.

Signal from	Quantity	Type of signal	Signal's range	NI module
Thermocouple	13[1]	Differential voltage	± 200 mV	NI 9205[2]
Pt100	2	Electrical resistance	0 – 400 Ω	NI 9217
Heat flux sensor	8[3]	Differential voltage	± 200 mV	NI 9205
Pressure transducer	2	Current	4 – 20 mA	NI 9203
Heating power supply	2	Voltage	0 – 10 V	NI 9205
High-speed camera trigger	1	Digital	TTL	PFI0 input of NI cDAQ-9178 chassis
End of video recording	1	Digital	TTL	NI 9401

[1] The thirteen thermocouples are sorted as follows: ten belonging to the PROSENSOR thermal probe (T_1 to T_{10}, K-type), two others in the fluid (T_{liq} and T_{vap}, K-type) and a last one on the ribbon cable of the heat flux sensor (T_{co}, T-type).

[2] Contrary to other standard modules (such as the NI 9214) which include a cold junction compensation, the NI 9205 module is not initially provided for temperature measurements by thermocouples (but for voltage measurements). However, to be able to acquire temperatures at the high-speed camera frequency, the decision was made to make the compensation of the signals in the conditioner before acquiring them with a NI 9205 module.

[3] The eight signals from the heat flux sensor are composed of the seven heat fluxes (HF_1 to HF_7) plus the temperature difference between the center of the sensor and its connection zone (ΔT).

The different acquisition cards are finally plugged into a NI cDAQ-9178 chassis which is connected to a second computer (PC_2) for the control, display and saving of the measurements through a home-made LabVIEW program.

A synthetic diagram representing the new acquisition system is given on Fig. 5.6.

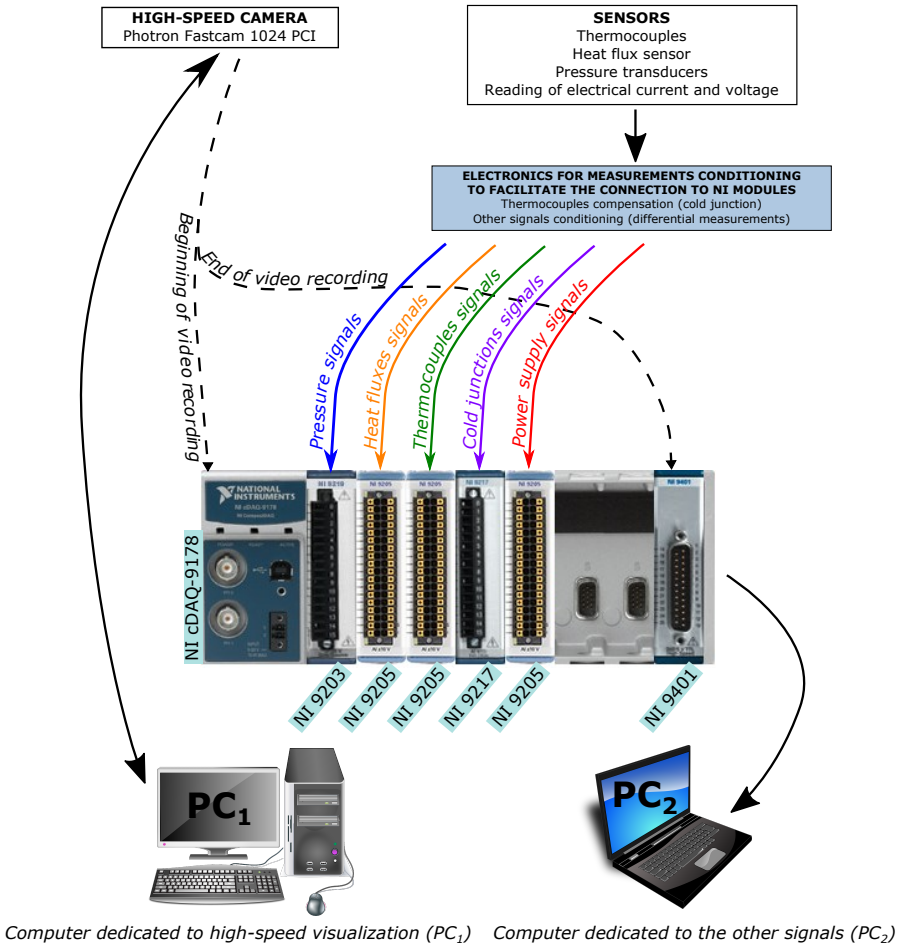

Figure 5.6 – Schematic diagram of the developed acquisition system.

As for thermocouples of the former setup, a calibration was carried out for the twelve K-type thermocouples used here with their entire acquisition line. The thermal probe as well as T_{liq} and T_{vap} thermocouples were then immersed in a stirred thermostatic bath with a reference temperature probe (a calibrated Pt100) to measure their electromotive forces for several temperatures between 0 °C and 100 °C. Their calibration curves were consequently obtained and the uncertainty on their measurements was evaluated to ± 0.15 K. This uncertainty seems acceptable in comparison with the one of the former facility's thermocouples (estimated to ± 0.10 K, see Section 2.1.4.1), especially when considering that a much quicker acquisition is now possible (up to 1000 Hz instead of about 0.33 Hz previously). The T-type thermocouple T_{co} located on the ribbon cable of the heat flux transducer was unfortunately not calibrated for practical reasons.

The heat flux sensor, already calibrated by CAPTEC, was not recalibrated. As a consequence, measurement bias that may be induced by the acquisition chain would not be corrected. However, those bias are supposed to be small and should not prevent from making – at least – a qualitative analysis of the measurements to demonstrate the added-value of using such a sensor when studying the boiling phenomenon.

A LabVIEW program was finally developed to acquire and save all the data. This one works with the high-speed camera software according to the following modes:

1. **Without synchronization:** As with the previous setup, the acquisition works as if there were two independent acquisition chains. The LabVIEW program acquires the measurements at a given frequency until the experimenter stop it while several videos of the bubble dynamics are recorded manually with the trigger mode "END".

2. **With synchronization:** In this case, the acquisition of pictures and of the other measurements are synchronized. The "START" trigger mode must then be set for the camera while acquisition frequencies set in PFV and in LabVIEW should be equal. The LabVIEW program is launched first and starts by waiting for the video recording to begin before starting the acquisition. The images recording and the measurements acquisition begin therefore at the same time (when the experimenter clicks to activate the video in PFV) and – at any instant – a picture is associated with an instantaneous measurement point for all the sensors. As the camera memory is of limited size, the video recording is limited in time. Subsequently, two ways exist to stop the acquisition:

   2.a. The measurements and the pictures recording end simultaneously.

   2.b. The measurements continue after the end of video recording until the experimenter stops the LabVIEW home-made program. In this case, the additional data are no longer correlated with images.

As the acquisition frequencies that can be accessed with the high-speed camera take only some discrete values, only six frequencies are programmed in the LabVIEW software[1]: 1000 Hz, 500 Hz, 250 Hz, 125 Hz, 60 Hz and 1 Hz. All those values but the last one (1 Hz) correspond to the frequencies that can be set for the camera with the largest image size (*i.e.* 1024×1024 pixels). Being able to acquire data at the low frequency of 1 Hz gives the possibility of monitoring the establishment of the steady state condition between two different experiments and of conducting longer[2] tests in mode 1.

5.1.6 Experimental procedure

The experimental procedure implemented with this improved facility is very close to the one used previously and described in Section 2.2. The only differences are related to the acquisition method.

Each test corresponds here to the study of the steady state of one operating point defined by the 4-tuple associating a working fluid, a liquid height H_l, a vapor pressure P_v and an imposed heating power HP_{input}. The heating energy input related to an experiment was previously cited through the value of the input heat flux φ_{input} calculated by dividing the heating power HP_{input} by the area of the cross section of the copper block (neglecting the fin). With the new heater, the influence of the presence of the fin may not be negligible anymore because of its size and thickness (refer to Section 5.1.4.1). This is why the heat flux input value φ_{input} does not characterize an experiment anymore and is substituted by the heating power HP_{input}.

Each operating point is studied successively in acquisition modes 1 and 2:

[1] A "programmed acquisition frequency in the LabVIEW software" is a frequency that can be set to measure the temperatures and heat fluxes. For each concerned frequency value, the sensitivity to the surrounding electromagnetic noise is reduced by selecting a suitable couple of sample rate (in samples per second) and of number of samples per channel (*i.e.* per signal) and by calculating the average values of the oversampled signals. These average values constitute the retained measurements and are indeed obtained at the desired frequency.

[2] The data are indeed progressively saved in a spreadsheet file (for a subsequent treatment) during the acquisition. To keep the same velocity while getting a data file of moderate size, the acquisition should not last an excessive time with regards to its frequency.

Mode 1: An acquisition frequency is chosen for signals measurements and kept during the whole test. Meanwhile, several videos of the phenomenon can be made, possibly with different frequencies in order to catch one or more bubble(s). In this case – which is very similar to the former setup procedure – the frequency set for pictures acquisition is generally higher than the frequency set for measurements, so that the time resolution for the bubble dynamics analysis can be high.

Mode 2: A same frequency is defined for the two types of acquisition. As it is more complicated to catch bubbles with the camera trigger mode "START" than with the trigger mode "END", the chosen frequency is generally taken lower in this case (mode 2) than in acquisition mode 1. The decision about the way to end the acquisition – between mode 2.a. and 2.b. – has also to be made before starting the recording.

5.2 Experimental results

Due to time spent to develop and test the new acquisition system, a limited number of experiments were conducted with the improved setup. The purpose of this section is thus to present them as well as the difficulties encountered and to show what the contributions of such an experimental facility to the understanding of low pressure boiling in a fundamental approach can be.

5.2.1 Difficulties encountered while using the improved setup

The issues that can be faced during the implementation of the setup for a new test campaign are related to three main concerns: the tightness, the presence of boiling on the periphery of the heated surface and the activation of the nucleation site. In this section, details are given on how the new test sample is (or not) affected by those problems.

Tightness: At low pressure (and in particular at subatmospheric pressure), the tightness of the vessel is essential in order to study boiling of pure and degassed fluids: no air should enter the vessel. With the previous heater, this condition was very difficult to reach (addition of a glue seal and conservation of a low heating power to keep the copper expanded). This new test sample enables to obtain a sufficient level of tightness much easier. Once the home-made feedthrough to get out the wires set and the heater assembled, only negligible leaks were indeed observed through the space existing between the wires and their PTFE-sheaths (despite the presence of the acrylic varnish).

Peripheral boiling: In order to study boiling at low pressure from a fundamental point of view, the isolated bubbles regime is chosen as the regime of interest for this work. As a consequence, peripheral bubble nucleation should be avoided. Unfortunately, despite its variable thickness (refer to Section 5.1.4.1), the fin located at the top of the new heater constitutes a place of heat losses intense enough to engender undesired peripheral boiling. In fact, during the very first tests, no bubble was created on the surface because almost all the power input was dissipated through the side surface of the fin rather than by the heated wall itself. To counter this outcome, a layer of epoxy resin was added on the lateral surface of the fin. The local insulation thus created managed to reduce the heat losses through the fin to less than 40 % of the heating power input. Even if this was not perfect, this was sufficient to stop the peripheral boiling and to obtain bubbles on the heated surface.

Nucleation site activation: To reap the full benefits of the improved setup (and especially of the concentrical multizone heat flux sensor), the artificial nucleation site made at the center of the heated wall should be activated. However, even with a high heating power, the site was impossible to activate: bubbles were nucleating from several places on the surface but never from an area corresponding to about one sixth of the surface which includes the artificial cavity. As the nucleation site is quite large (compared to other defects that exist on the heated surface) with a diameter of 100 µm and a depth of 110 µm (refer to

Section 5.1.4.2.4 and to Appendix A.2), its activation should not be so difficult to obtain. A large defect in the gluing of the heat flux sensor on the copper block in the zone where no nucleation occurs appears as the most probable reason for such a behavior by creating locally a huge thermal contact resistance. This hypothesis was confirmed after conducting the experiments which are presented hereafter.

Finally, the new test sample constitutes an improvement to get the tightness (compared to the former heater) but it is still perfectible concerning the heat losses and the thermal contact between the copper fin and the heat flux sensor in order to avoid peripheral boiling and to make the centered artificial nucleation site activated. These first tests especially highlight that a particular care must be taken during the gluing operation of the heat flux sensor on the copper block in the aim of having a good and uniform thermal contact between these two parts. Such a contact would also be a key point to reduce the heat losses.

5.2.2 Operating conditions and acquisition settings

In the following, the experimental conditions are as follows:

Working fluid: The test is conducted with pure, distilled and degassed water.

Liquid height H_l: The liquid height is arbitrarily set to $H_l = 15$ cm. Vertical distances to the free surface (along the z-axis[1]) being calculated in function of Z and H_l through Eq. 5.6, positions of thermocouples in the fluid are deduced from data given in Table 5.1 in Table 5.4.

$$z_{H_l=15\text{ cm}} = H_l - Z \tag{5.6}$$

Table 5.4 – Positions of thermocouples in the fluid in terms of distance to the free surface z when $H_l = 15$ cm.

Thermocouple	$z_{H_l=15\text{ cm}}$ (cm)
T_1	15.0 ± 0.1
T_2	14.0 ± 0.1
T_3	13.0 ± 0.1
T_4	12.0 ± 0.1
T_5	11.0 ± 0.1
T_6	10.0 ± 0.1
T_7	7.5 ± 0.1
T_8	5.0 ± 0.1
T_9	2.5 ± 0.1
T_{10}	0.0 ± 0.1 [2]
T_{liq}	3.7 ± 0.2
T_{vap}	-17.4 ± 0.2 [2]

Vapor pressure P_v: The vapor pressure is set to $P_v = 5.2$ kPa which corresponds, for water, to the saturation vapor temperature of $T_v = 33.6$ °C [71]. For this point of the saturation curve and for this liquid height, the static head $P^{static}_{H_l=15\text{ cm}}$ is not negligible in comparison with the vapor pressure P_v since it is equal to:

$$P^{static}_{H_l=15\text{ cm}} = \rho_v(T_{l,\,bulk})gH_l \approx 1.5\text{ kPa} \tag{5.7}$$

Heating power input HP_{input}: The heating power is set to $HP_{input} = 125.9$ W. This value is chosen as it is the lowest one for which a given nucleation site located on the heated wall (unfortunately not centered because of the gluing defect) is active: a bubble is regularly growing from this place.

[1] As a reminder: the z-axis is downward oriented with reference ($z = 0$) taken at the free surface level.
[2] $z \leq 0$ means the thermocouple is in the vapor phase.

Concerning the acquisition settings, this experiment is made in mode 2.a., *i.e* measurements and pictures recording are synchronized and end simultaneously. The maximum image size (1024×1024 pixels) is still selected while the frequency is chosen equal to 250 Hz. This leads to an acquisition duration of 6.15 s (with respect to the memory size of the camera) with a time step of $\Delta t = 0.004$ s between two successive recorded pictures and measurements.

5.2.3 Boiling environment

As explained in Section 5.1.1, the boiling environment is poorly defined: if the occurrence of a stratification in the fields of local pressure $P(z)$, saturation temperature $T_{sat}(z)$ and subcooling $\Delta T_{sub}(z)$ due to the importance of the static head P^{static} is known, the fact that the bulk liquid is homogeneous in temperature is still an hypothesis which needs to be validated. The addition of the new thermal probe precisely aimed at confirming or rebutting this assumption.

Figure 5.7 shows the temperatures measured in the fluid during the experiment by the twelve thermocouples whose positions are given in Table 5.4. According to this graph, the temperature in the liquid is steady and can be considered as homogeneous whatever the vertical position as all the thermocouples located in the liquid (T_1 to T_9 and T_{liq}) are included in their mutual uncertainty ranges. The assumption of a homogeneous bulk liquid temperature $T_{l,\,bulk}$ is hence corroborated.

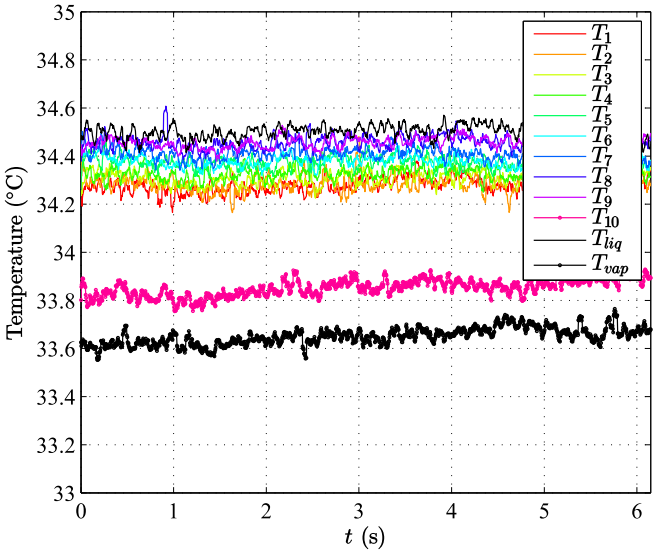

Figure 5.7 – Measured temperatures in the fluid during the experiment made with water at $P_v = 5.2$ kPa ($T_v = 33.6$ °C), with $H_l = 15$ cm and $HP_{input} = 125.9$ W.

In the present case, the bulk liquid temperature $T_{l,\,bulk}$ can be defined as the mean value of T_1 to T_9 and T_{liq}. This calculation gives $T_{l,\,bulk} = (34.38 \pm 0.15)$ °C which is higher than the imposed vapor temperature $T_v = 33.6$ °C measured by T_{vap} because the power dissipated through the heater contributes to heat up the liquid. T_{10} presents an intermediate value between $T_{vap} \approx T_v$ and $T_{l,\,bulk}$ which constitutes a particular case. Actually, this thermocouple is located at the free surface level and is thus affected both by the liquid bulk and the vapor.

As it is confirmed that the bulk liquid temperature does not change with the depth z, the local subcooling degree $\Delta T_{sub}(z)$ of the liquid which corresponds to the local deviation of the liquid from the saturation state is defined as:

$$\Delta T_{sub}(z) = T_{sat}(P(z)) - T_l(z) = T_{sat}(z) - T_{l,\,bulk} \tag{5.8}$$

and its variations are only related to variations of the local saturation temperature $T_{sat}(z)$ induced by the pressure stratification according to z.

Displayed on Fig. 5.8, the local subcooling associated with the current experiment appears as almost linear with the depth z and equal to about 4 K at the level of the heated surface. On the contrary, close to the free surface, the liquid is superheated of almost 1 K (negative subcooling value), which is in agreement with the temperature difference observed between the liquid and the vapor temperatures in the fluid.

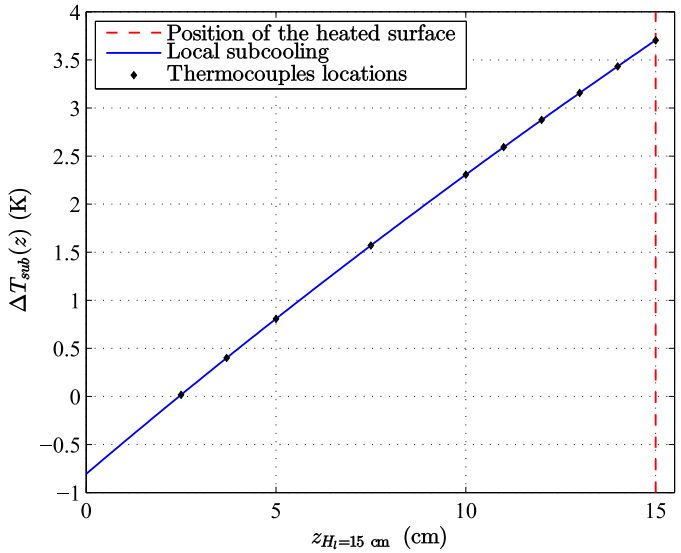

Figure 5.8 – Local subcooling ΔT_{sub} depending on the depth z in the liquid (experiment with water at $P_v = 5.2$ kPa ($T_v = 33.6$ °C), with $H_l = 15$ cm and $HP_{input} = 125.9$ W).

In low pressure pool boiling, the bulk liquid (*i.e.* the liquid far from the bubbles) is finally superheated close to the free surface and subcooled close to the heated wall level just because of the non negligible influence of the static head P^{static}. From this observation, one can easily understand how complicated the boiling environment is. The region where bubbles are growing is indeed affected simultaneously by the subcooling effect of the static head and by the superheating effect of the heater. As a consequence, the temperature – and subsequently the thermophysical properties – of the working fluid in this region is still poorly known and is probably varying along the bubble interface.

5.2.4 Study of a bubble

During the 6.15 s that lasts the present test, only one bubble nucleates on the wall. Its nucleation site is located at approximately 25.8 mm from the center of the heated surface. As schematically shown on Fig. 5.9, the bubble is thus growing from a place situated on the fifth measurement zone of the heat flux sensor and relatively close to the sixth one.

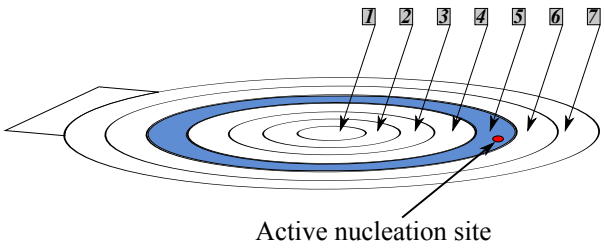

Figure 5.9 – Location of the active nucleation site.

As visible on Fig. 5.10, the bubble has an oblate spheroid shape and – as it can be inferred from its comparison with the width (86.5 mm) of the images area reported on the first picture (IMG_1) – is of a few centimeters diameter. These observations about a long waiting time τ_{wait} between successive bubbles, a large size and a specific shape of the bubble are consistent with the results obtained for water boiling in this range of subatmospheric pressures given in Chapter 3 and

also, with the literature interested in low pressure boiling which includes for example the works of Van Stralen *et al.* [119] or Yagov *et al.* [125].

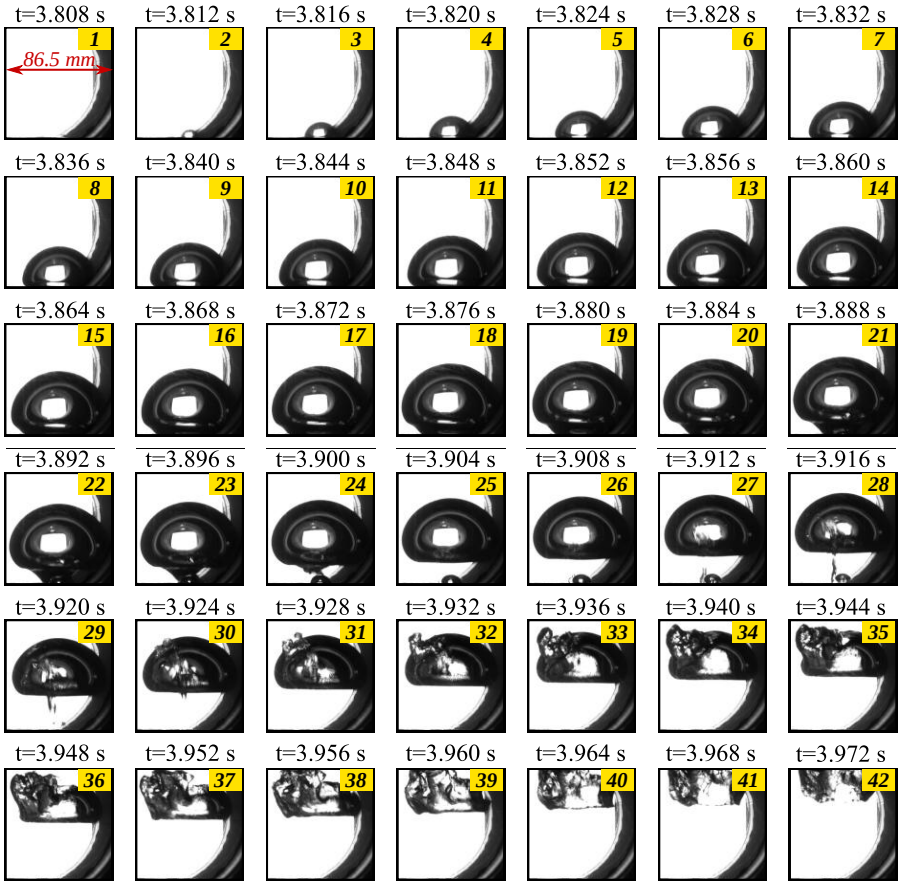

Figure 5.10 – Pictures of a bubble recorded at 250 Hz (experiment with water at $P_v = 5.2$ kPa ($T_v = 33.6$ °C), with $H_l = 15$ cm and $HP_{input} = 125.9$ W).

Unluckily, the position of the active nucleation site and the large size of the bubble do not enable the extraction of any characteristic of the bubble dynamics (such as the instantaneous volume V) from the recorded pictures. The bubble is indeed too eccentric to the center of the heated surface to be image processed, even with a manual treatment: the bubble's right hand side interface cannot be discerned from the viewport shadow (neither with the algorithm or with the naked eye). As a consequence, only a qualitative analysis of the images can be realized from Fig. 5.10. First, the bubble nucleates (between IMG_1 and IMG_2) and grows with a hemispherical shape until reaching a size of a few centimeters (to IMG_{12}). Afterwards, slowly at first and then even more quickly, the bubble foot diameter decreases which results in the departure of the bubble (between IMG_{22} and IMG_{23}). Then, a liquid jet penetrates into the volume of the detached bubble during its early rise (to IMG_{30}) before the bubble starts to collapse because of the subcooling degree of the surrounding liquid.

The heat fluxes measured from the seven zones of the heat flux sensor during the entire test are plotted on Fig. 5.11a. Before the bubble nucleation, all the seven heat fluxes are constant. Depending on the zone, different values are measured because:

- Each zone has a different area.
- The shape of the copper block (with its fin of variable thickness) affects the heat diffusion.
- Some zones are more affected by the gluing defect (suggested in Section 5.2.1 and confirmed at the end of the experiments) than others.

- The calibration used here (provided by CAPTEC) does not correct the bias effect that can be induced by the acquisition line of the sensor (refer to Section 5.1.5).

The analysis of the heat fluxes remains therefore qualitative in terms of measured values (only trends can be observed) but can still be quantitative concerning the time evolution.

To analyze heat fluxes variations during the moments when the bubble is visible (*i.e.* associated with the pictures from Fig. 5.10), a zoom on this period of time is displayed on Fig. 5.11b.

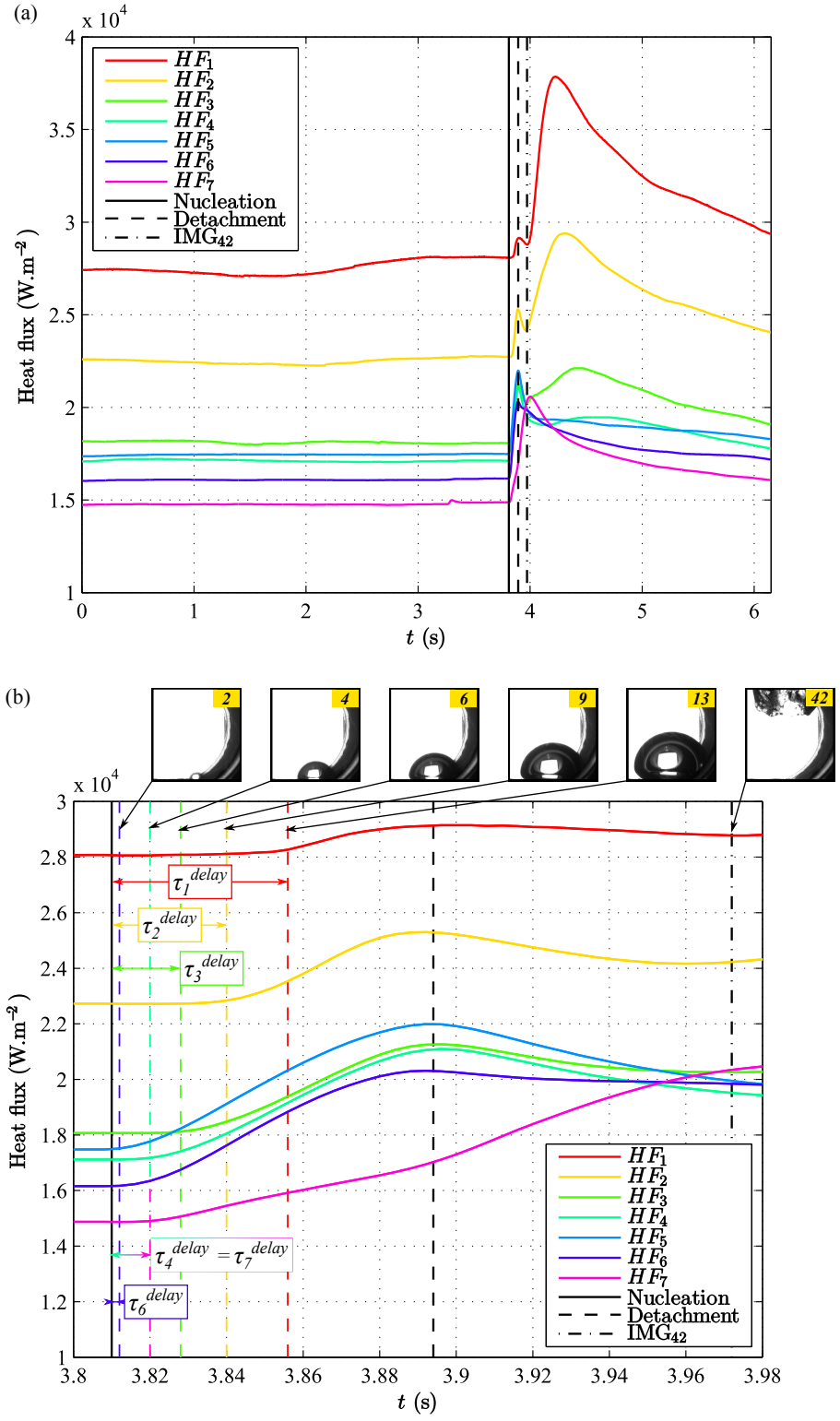

Figure 5.11 – Measured heat fluxes (a) during the whole test; (b) during the period when the bubble is visible (experiment conducted with water at $P_v = 5.2$ kPa ($T_v = 33.6$ °C), with $H_l = 15$ cm and $HP_{input} = 125.9$ W).

As soon as the bubble nucleates on *Zone* # 5, the local improvement of the heat transfer results in an increase of the local heat flux HF_5. The sensor appears very reactive and sensitive as the increase is instantaneously visible whereas the bubble is then occupying only a small part of the annular zone. These sensitivity and reactivity make the multizone heat flux sensor able to follow the motion of the triple line on the heated wall. In fact, as the bubble continues to grow and to reach the other areas of measurement, the other heat fluxes progressively start to increase too:

- At $t = 3.812$ s (IMG_2), the heat flux of the zone the closest to the nucleation site (*i.e.* *Zone* # 6) starts to rise. The delay $\tau_6^{delay} \approx 2$ ms corresponds to the time needed for the bubble to grow enough from *Zone* # 5 to *Zone* # 6.
- At $t = 3.820$ s (IMG_4), *Zones* # 4 and # 7 are simultaneously reached by the bubble. HF_4 and HF_7 start to increase with a delay $\tau_4^{delay} = \tau_7^{delay} \approx 10$ ms.
- At $t = 3.828$ s (IMG_6), *Zone* # 3 is also affected by the presence of the bubble. HF_3 augments with a delay τ_3^{delay} of about 18 ms.
- At $t = 3.840$ s (IMG_9), HF_2 increases after a delay τ_2^{delay} approximately equal to 30 ms since the bubble is then in contact with *Zone* # 2.
- At $t = 3.856$ s (IMG_{13}), the bubble reaches finally *Zone* # 1 and HF_1 rises with a delay $\tau_1^{delay} \approx 46$ ms.

Later on, the bubble foot diameter decreases. Except for *Zone* # 7 which presents a specific behavior, heat fluxes reach a maximum before they decrease as the contact line between the bubble and the surface is moving back towards the activated nucleation site. HF_1, HF_2, HF_3, HF_4, HF_6 and finally HF_5 get indeed a maximum value precisely during the very last stages of the bubble growth – between the instants $t = 3.888$ s (IMG_{21}) and $t = 3.896$ s (IMG_{23}) – and decrease afterwards. The fact that HF_7 continues to rise after the bubble detachment may be explained by the nucleation of another (smaller) bubble on this zone that can be seen on IMG_{22} to IMG_{28}.

After the bubble departure (refer to Fig. 5.11a), all the heat fluxes decrease slowly and tend to their initial value. The present acquisition is actually too short to confirm this but it would be in agreement with the long waiting time between successive bubbles usually observed at low pressure [77, 119, 125]. HF_1, HF_2 and HF_3 show large peaks between the bubble detachment and this slow decrease. Those peaks may be explained by some liquid motion and agitation, by the free surface movements induced by the departure and collapse of a such large bubble or by some convective motion and heat diffusion which could be caught by the sensor. The video recording does not help conclude on those hypotheses, but this observation is corroborated by the analysis of the time evolution of the system wall superheat ΔT_{wall}^{sys} defined as:

$$\Delta T_{wall}^{sys} = T_{wall}^{exp} - T_{l,\,bulk} = T_{center} - T_{l,\,bulk} \tag{5.9}$$

The temperature $T_{l,\,bulk}$ of the bulk liquid being constant during the experiment (Fig. 5.7), variations of the system wall superheat ΔT_{wall}^{sys} is only due to variations of the wall temperature. However, the wall temperature T_{center} and the system wall superheat ΔT_{wall}^{sys} are here not directly representative of the effect of the presence of bubble since nucleation does not take place at the center of the heated surface. As shown on Fig. 5.12, T_{center} (and consequently ΔT_{wall}^{sys}) is indeed almost non-affected by the bubble's growth and departure. On the contrary, the liquid motions greatly induce a large drop (of about 5 K) of T_{center} and of ΔT_{wall}^{sys}, which corresponds to the peaks on the local heat fluxes HF_1 to HF_3.

The peaks on HF_1 to HF_3 and the drop of T_{center} and ΔT_{wall}^{sys} are wide (they last longer than the bubble growth duration) and happen with a relatively large delay after the departure of the bubble (still in comparison with the bubble growth duration). These observations highlight that a preceding bubble has a huge and long influence on the boiling environment. Its departure

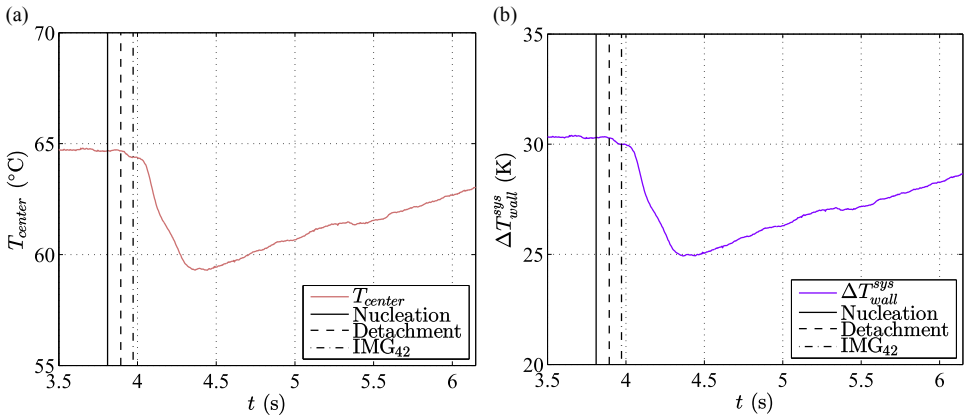

Figure 5.12 – (a) Temperature measured at the center of the heated surface T_{center}; (b) Wall superheat ΔT_{wall} (experiment conducted with water at $P_v = 5.2$ kPa ($T_v = 33.6$ °C), with $H_l = 15$ cm and $HP_{input} = 125.9$ W).

engenders some liquid and convective motion which makes – not instantaneously – the liquid close to the heated wall cooler by a few Kelvins. As a consequence, a long time is afterwards required to heat this amount of liquid up again enough to make a new nucleation possible. The motion induced by the detachment and rise of a preceding bubble is thus responsible for the long waiting time τ_{wait} between successive bubbles at low pressure. Finally, one result of this preliminary test is that the influence of what happens in the pool before the growth of a given bubble (preceding bubbles, liquid motion...) cannot be neglected when studying a single bubble. Siedel *et al.* [104, 105] came to the same conclusion when studying the bubble dynamics of saturated n-pentane boiling at atmospheric pressure from artificial cavities as they detected and quantified oscillations of growing bubbles induced by the departure of a preceding bubble.

Despite the perfectible aspects of the implementation of this improved setup (gluing defect, non centered bubble, qualitative measurement only...), this experiment demonstrates the advantages of using such sensors in a fundamental study of boiling at low pressure among which:

- The ability to investigate the bulk fluid temperature at different altitudes in order to know a bit better about the complicated boiling environment encountered at low pressure;
- The ability to follow the motion of the triple line by correlating variations of local heat fluxes with the high-speed visualization;
- The highlighting of the huge influence of the history of preceding bubbles on the boiling environment and hence on the waiting time τ_{wait} between two successive bubbles.

5.3 Conclusions

Investigating the phenomenology of boiling requires to study both the heat transfer and the bubble dynamics. As a consequence, an experimental apparatus that enables the synchronization of a visualization system with a thermal measurements system clearly appears as a good tool for such studies.

In the present work, a multizone heat flux sensor was chosen for measurements related to the heated surface to be synchronized with a high-speed camera. However, other solutions exist and are used in the literature. For instance:

> Moghaddam and Kiger [82] used a silicon membrane coated with a multi-layer benzocyclobutene film as a heated surface to study boiling of FC-72 at saturated conditions. Within and on this composite wall, numerous temperature sensors radially arranged in arrays were located around artificial cavities to measure the temperature of the heated surface beneath the bubble and to calculate the surface heat flux. With this device, the

authors managed to observe the thermal field underneath a bubble with a very high spatial resolution (spatial step of the order of few ten micrometers) and to characterize the different mechanisms of heat transfer from the surface to the bubble (microlayer, transient conduction and microconvection) and their contributions.

Chen *et al.* [20] used a laser interferometric method to observe the structure of the microlayer during a bubble cycle in nucleate water pool boiling. This enabled them to measure accurately the microlayer thickness depending on its distance the bubble inception site.

With their areas of measurement of only a few square millimeters and a spatial step of the order of the micrometer, the two cited techniques seem very accurate. However, they seem not to be adapted to the investigation of low pressure boiling. Under such condition, bubbles are indeed centimeter sized. Using such devices would then require to increase considerably their size which would even more increase their complexity. Moreover, compared to normal pressure condition, other stresses occur (tightness, higher wall superheat required to activate a nucleation site...) that need to be handled by those systems.

An instrumentation like the one described in this chapter finally constitutes a good trade-off between those cited techniques and the features of low pressure boiling. It is therefore a promising solution to get a further understanding of low pressure boiling.

In addition, due to the large bubble size at low pressure, observing the motion of the triple line and of the microlayer should be easier then than under normal pressure conditions. As a consequence, studying the phenomenology of low pressure boiling with such efficient sensors may be an interesting track to improve the knowledge and understanding of boiling in a more general manner.

Starting from observations made on the experimental facility presented in Chapter 2, some improvements were brought to the setup:

- *Original sensors were added to get a better knowledge of the boiling environment and to measure locally the heat flux underneath a growing bubble;*
- *An adapted acquisition system was developed in order to be able to synchronize the thermal measurements with the high-speed visualization.*

Experiments were conducted afterwards. In spite of some limitations mainly due to a manufacturing defect, these tests demonstrate the added-value of using such an improved setup in boiling (and especially in low pressure boiling):

- *The hypothesis of a homogeneous bulk liquid temperature is confirmed while the complexity of the boiling environment is highlighted;*
- *The motion of the triple line during the bubble growth can be characterized;*
- *The long time effect of a preceding bubble on the boiling environment is made visible.*

In the future, this work would deserve to be continued by perfecting the new facility and by conducting new experiments with various operating conditions (different fluids, liquid heights, vapor pressures and heating powers).

Conclusion and perspectives

Synthesis

Among the various conditions under which boiling can occur, low imposed pressure constitutes an unconventional condition that has gained some renewed scientific interest during the last decade because of its practical importance. In a context where new environmental regulations are settled while the need of efficient low temperature systems for electronic cooling keeps increasing, some systems may indeed require a fluid to boil at a low pressure. To date, the design of such systems – evaporators for sorption chillers or some thermosyphons for example – remains mostly empirical since these systems experience unusual boiling behaviors that cannot be predicted from the general knowledge about boiling heat transfer. The present thesis was therefore focused on low pressure pool boiling from a fundamental point of view.

First, the fundamental concepts related to pool boiling were recalled before the already-reported features of low pressure pool boiling were detailed. The low pressure bubble dynamics is thus mainly characterized by bubbles of large volume, of specific mushroom shapes and separated by a long waiting time. On the other hand, the thermal performance is known to be degraded (compared to that observed under normal or higher pressures), so that the usual boiling correlations do not apply. Significant variations of the wall temperature with time are also sometimes reported. Recently, the high degree of complexity of the low pressure boiling environment due to the non negligible influence of the static head (related to the liquid column) on the pressure and subcooling fields was also highlighted. Moreover, the diverse operating conditions used in all the previous studies (fluids, heated surfaces, orientations, liquid levels and pressure ranges) made the comparative analysis of the existing literature rather inconclusive. The need of a precise definition of "low pressure" in boiling as well as of new experimental results obtained under "well-defined" operating conditions was thus emphasized.

An experimental facility, already proven by Giraud during her thesis [44], was then used to conduct several experiments. This facility enables the production of isolated bubbles from a single artificial nucleation site under controlled pressure conditions, the high-speed visualization of these bubbles and the time-monitoring of the wall temperature, the wall superheat and the heat flux released to the working fluid through the heated surface. In addition, an image processing tool was developed in order to provide some of the quantitative and reliable data about the bubble dynamics that were necessary to get a better knowledge of boiling at low pressure.

A first test campaign was carried out with water for a large range of subatmospheric pressures. In order to observe only the influence of the imposed pressure, the other parameters of importance (namely, the liquid height and the imposed heat flux) were kept constant during all the experiments. Depending on the pressure, four regimes of bubble dynamics were then identified. The state conditions at which the thermophysical properties involved in heat transfer correlations should be evaluated were discussed and carefully defined so that the presence of the subcooling degree induced by the non negligible static pressure is taken into account. Some of the usual models of wall superheat were used with the thermophysical properties defined from

this adapted method. The results of these models were afterwards compared to the superheat measurements. For the lowest range of investigated pressures, some properties of the bubble dynamics (among which the growth duration, the waiting time, the bubble frequency or the instantaneous volume) were evaluated, yielding a general confirmation of the trends reported by previous authors. However, the establishment of a new experimental law of bubble growth raises questions about the involved mechanisms, since it differs from the classical theories that were mostly established for higher pressures.

In agreement with the main conclusions of the literature review, it appeared necessary to define more accurately what "low pressure" means in boiling. Conducting experiments with another fluid than water in this state of "low pressure" under well-identified operating conditions seemed also required to get a better insight of the phenomenon. As a consequence, the concept of mock-up fluids was developed. This led to the selection of a given fluid (namely, the cyclohexane) and to the determination of an adapted design of experiments according to the test bench abilities and to the fluid thermophysical properties. A second experimental session was then performed: three of the four bubble dynamics regimes already identified in water were observed in cyclohexane while differences between the two fluids' behaviors were noticed – sometimes quantified – and discussed. Finally, this discussion demonstrated that if the local subcooling degree is a parameter of importance in low pressure boiling, it does not constitutes a sufficient governing parameter by itself. In addition, the calculation of the Robinson and Judd criterion showed that inertia cannot be neglected in the very low pressure range, so that inertia may be considered as (partly) responsible for the deviation of the bubble dynamics from what is usually encountered at higher pressure. The influence of the wettability of the fluid/surface pair was also highlighted.

Finally, the experimental facility was modified to enable the use of original sensors. The main feature of the improved setup is to make the synchronization of the monitoring of the local thermal effect of a bubble growing on the wall with the high-speed visualization possible. Although some manufacturing defects occurred, the first results obtained with water as the working fluid display promising perspectives for a better understanding of the specific behaviors of boiling at low pressure. In particular, the motion of the triple line during the bubble growth could be followed while the long time influence of a preceding bubble on the boiling environment was brought to light.

Perspectives

All the results presented in this thesis were obtained for low pressure boiling occurring from a plain smooth surface provided with a single artificial nucleation site. Yet, as mentioned in the literature review (Chapter 1), the nature and geometry of the heated surface is known to have a significant influence on the boiling phenomenology. As a consequence, one can expect that low pressure pool boiling from heated surfaces closer to what can be encountered in real systems (such as in evaporators) will exhibit differences compared to the observations made in the present work. The effect of such system-like surfaces on low pressure pool boiling therefore deserves to be investigated. As part of a new collaboration between CETHIL (France) and Wrocław University of Science and Technology (Poland), Halon *et al.* [50, 51] performed some experiments in that goal.

Using the experimental apparatus described in Chapter 2 with a modified test heater enabling the insertion and heating of the surfaces to be tested, Halon *et al.* [50,51] conducted an experimental study under the following operating conditions:

Working fluid: pure, distilled and degassed water;

Heat flux input φ_{input}: varying from 0.25 up to 3.00 $\mathrm{W \cdot cm^{-2}}$;

Vapor pressure P_v: ranging from 0.75 to 4.00 kPa (*i.e.* corresponding to saturation temperatures ranging from 2.8 to 28.9 °C);

Liquid height H_l: varying from 0.50 to 8.62 cm.

Six samples forming complex tunneled surfaces were investigated. As visible on Fig. a, all these copper structures display a similar geometry consisting of three rows of fins located on a square base. Two types of samples must however be distinguished: the Narrow Tunnel Structures (NTS) and the Tunnel Structures (TS). The main difference between these two kinds of tunneled surfaces is the absence (in NTS) or the presence (in TS) of bridges between the fins belonging to a given row, so that the liquid can or cannot flow between the channels. In addition, some of the samples are covered with a thin (0.1 mm thick) perforated copper foil which creates subsurface tunnels.

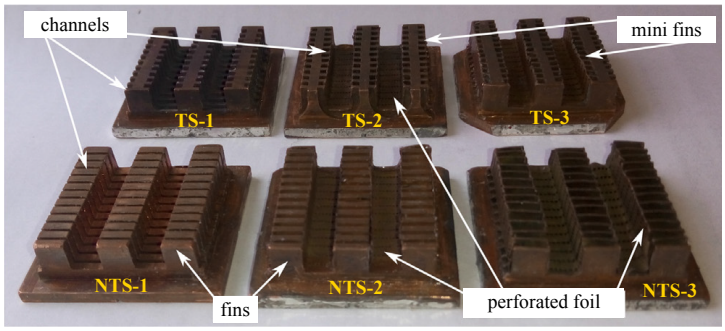

Figure a – Picture of the six enhanced structures (adapted from [51]).

Such structures are supposed to improve the thermal performances of low pressure boiling (compared to the plain surface case) as a consequence of their complex shapes that, at once:

- Increase the heat exchange surface's area;
- Increase the active nucleation sites density;
- Improve the fluid circulation and the feeding of the active nucleation sites.

In order to analyze the influence of the pitch and width of the tunnels on the heat transfer, those geometrical parameters vary from one sample to another according to the data displayed on Fig. b.

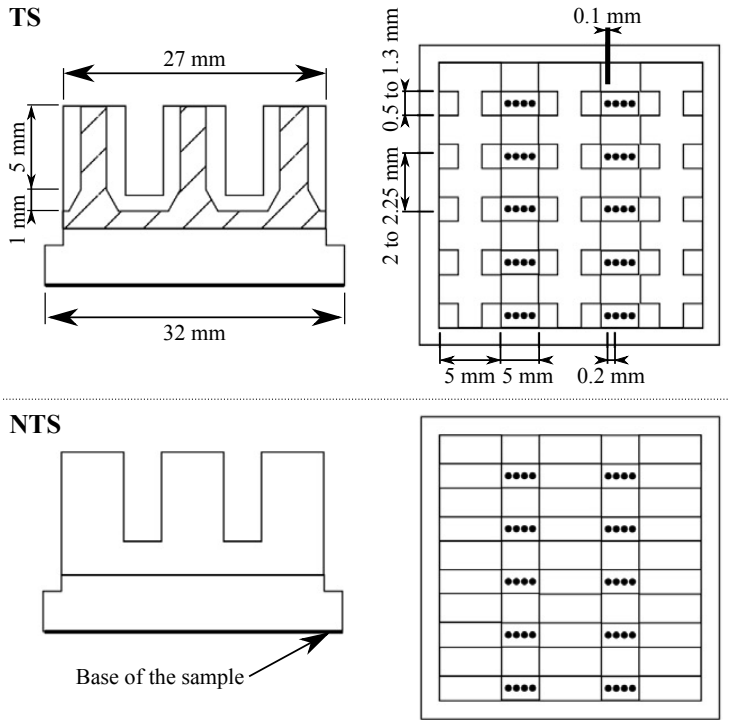

Figure b – Sketch of the samples (adapted from [51]).

Depending on the liquid level, different behaviors were reported:

- At $H_l = 0.50$ cm, the free surface level was corresponding to the top of the fins. Bubbles were therefore growing above it, engendering double vapor-liquid-vapor interface that finally bursted or collapsed.
- At $H_l = 2.87$ cm, intermittent boiling occurred. Natural convection took place between the growths of large mushroom shaped bubbles (*i.e.* during waiting periods). These large bubbles were generally formed at the periphery of the sample (*i.e.* at the junction between the sample and its assembly with the rest of the heater) and were thus fed in vapor by tunnels. As in the case shown on Fig. c, the departure of such peripheral bubbles occasionally triggered a secondary boiling phase from the horizontal tunnels. In such a case, this secondary boiling phase is characterized by a high departure frequency and intense bubble coalescence.

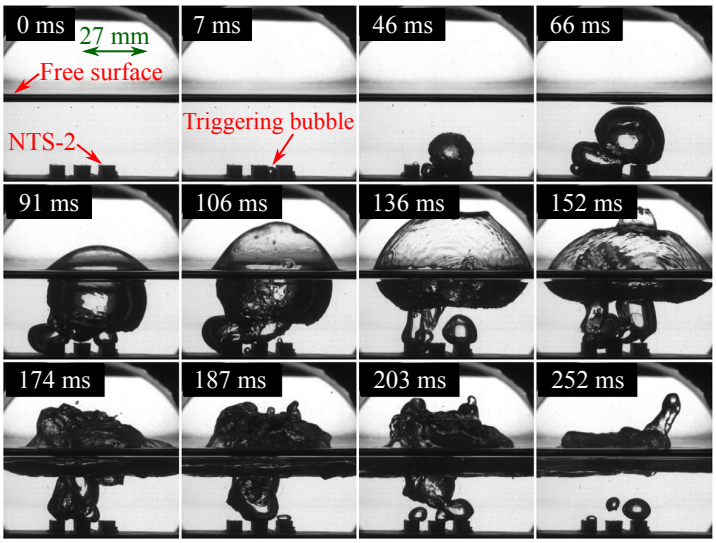

Figure c – Example of visualization of boiling from NTS-2 at $P_v = 2.0$ kPa ($T_v = 17.5$ °C) (water, $H_l = 2.87$ cm, $\varphi_{input} \geq 1.0$ W · cm^{-2}; adapted from [50]).

- At $H_l = 8.62$ cm, most of the bubbles were reaching large volumes but usually collapsed while remaining attached to the heated surface. The few bubbles that were able to depart from the sample were actually small.

Halon *et al.* [50, 51] finally confirmed that the introduction of enhanced tunnel and/or narrow tunnel structures is able to reduce the negative effect of the low pressure condition on the boiling heat transfer coefficient (with respect to the plain surface). This appeared to be especially the case in presence of the perforated foil.

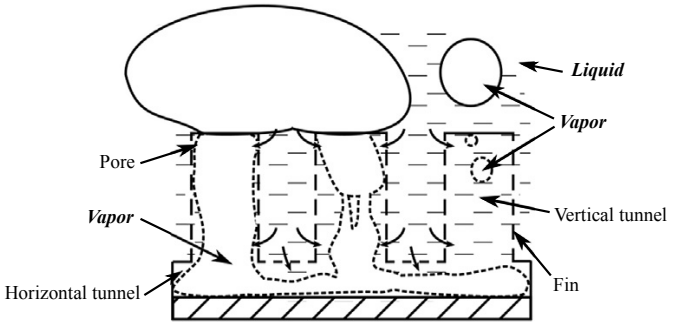

Figure d – Schematic diagram of the boiling mechanism inside the NTS (adapted from [50]).

According to them, this improvement can be attributed to the mechanism schematically represented on Fig. d. The pumping action of the growing and departing bubbles from the fins' ends

contributes to suck the liquid into the tunnels through the holes made in the foil, evaporation of the liquid then takes place in the tunnels, so that the generation and motion of bubbles can continue. With regards to the plain surface configuration, this feeding mechanism is consequently supposed to improve the boiling heat transfer (*i.e.* to reduce the low pressure influence) owing to two simultaneous effects: the reduction of the wall superheat and the increase of the boiling process stability.

The few pieces of information exposed just above emphasize the need to perform additional low pressure boiling experimental studies on system-like heated surfaces with a fundamental approach before implementing them in real systems. The boiling phenomenology can indeed be totally changed by the heated surface geometry. However, the involved processes may rapidly become too complicated to achieve the analysis – especially when using complex surfaces such as TS or NTS. In that context, a rather precise understanding of the low pressure boiling phenomenon in simpler configurations (like from horizontal upward-facing plain surfaces) remains finally a key point.

Several actions that should be given priority for future works are therefore suggested hereafter. In the continuity of this thesis, all of them are aimed at getting a better knowledge and understanding of low pressure pool boiling at the bubble scale.

- As it was demonstrated that a particular attention should be paid to the wettability (both to its influence on low pressure boiling and to its dependence on the operating conditions), and as this property – characterized by the contact angle θ – is related to the surface/fluid pair, two complementary parametric studies could be undertaken:
  - For a given surface/fluid pair: the dependence of the apparent contact angle θ of a growing bubble on the heat flux, the liquid level and more particularly on the vapor pressure should be investigated[1]. Variations of this parameter with operating conditions may indeed explain some of the observed changes in the bubble dynamics behaviors.
  - For a given set of operating conditions (*i.e.* imposed heat flux, liquid height and vapor pressure): changing the fluid and/or the heated surface may enable to identify some of the driving parameters related to wettability and to get a better understanding of the nucleation process in low pressure boiling. Heaters made of different materials, with different roughnesses and presenting or not one or several artificial cavities of various sizes and shapes could for example be tested with a few fluids.
- Based on the results obtained during this thesis, the study of the isolated bubble regime deserves to be taken forward in order to:
  - Measure and take into consideration the bubble's velocity whose importance has been brought to light when the non negligible effect of inertia on the bubble growth at low pressure was confirmed.
  - Establish the interest of the concept of "mock-up fluids" and reap all the benefits of it. New and numerous experimental data are then required so that the mapping of the bubble dynamics behaviors according to the parameters governing low pressure boiling could be refined. Experiments should therefore be conducted at various pressure levels with several fluids and/or liquid heights such as a "similar state of low pressure" could always be reached and observed. In particular, setting conditions which lead to an identical subcooling degree in different fluids seems to present some interest for purpose of fluids' behaviors comparison since this makes the analysis free from the influence of differences in this boiling environment property from one fluid to another.

[1] In addition, it should be highlighted that, for a given growing bubble obtained under a given set of conditions, monitoring the time-evolution of the contact angle is also of interest for the evaluation of some of the forces acting on the bubble (in particular of the surface tension force).

  - Improve the knowledge and understanding of the link that exists between the bubble dynamics and the boiling heat transfer through the use of the modified version of the experimental facility. A first step aiming at characterizing properly the new heater (provided with the multizone heat flux sensor and connected with the new acquisition system) would beforehand be required. The sensitivies of measurement provided by CAPTEC have indeed to be adjusted due to the effect of the in-house acquisition line that was implemented. In the same vein, the response times associated with all the measurement zones can be cited – for instance – as critical parameters to be known for the quantitative exploitation of the heat flux sensor outputs. Afterwards, the synchronization of the multizone heat flux sensor with the camera would make possible the high-speed monitoring of the triple line motion and of its consequences on the local heat transfer during a bubble growth. A study of the evolution of the microlayer geometry (size, shape and thickness) in relation with the heat transfer rate in this region may therefore be carried out (this would require to reduce the imaging area to the bubble foot zone in order to increase the spatial resolution). The amount of heat transferred from the wall to the fluid by evaporation of the microlayer might thus be estimated. Finally, the evaluation of the relative contribution of the microlayer evaporation to the total heat transfer could indicate if this subprocess is of major importance or not in low pressure pool boiling (depending on the working fluid and on the other operating conditions).

- In the future, the effect of the heated surface orientation and inclination may also deserve to be studied since real systems would certainly impose different configurations of use than the basic horizontal upward-facing situation.

A long-term goal of all these perspectives could be to identify the parameters governing the fundamental phenomena involved in low pressure pool boiling and in its subprocesses, so that the predominant forces acting on a growing bubble could be properly estimated and an adapted bubble growth model developed.

Appendix A

Surface condition of heated surfaces

A.1 The original heated surface

A.1.1 Introduction

As the heated surface described in Chapter 2 was already used and characterized by Giraud [44], only few rough measurements were performed with the confocal microscope in order to verify that the surface condition and the artificial nucleation site had not changed too much with time.

Three (randomly chosen) squared-zones 5 mm wide were thus investigated according to the diagram given as Fig. A.1. Whatever the considered zone, the spatial step p – defined as the distance between two points for which the altitude $\tilde{z}$ is measured – was chosen identical for the both directions of the horizontal plane (along the $\tilde{x}$ and $\tilde{y}$-axes) and equal to $p = 10$ µm. All the areas being of the same size and explored with the same spatial step, all the measurements lasted the same duration *i.e.* about 1 h.

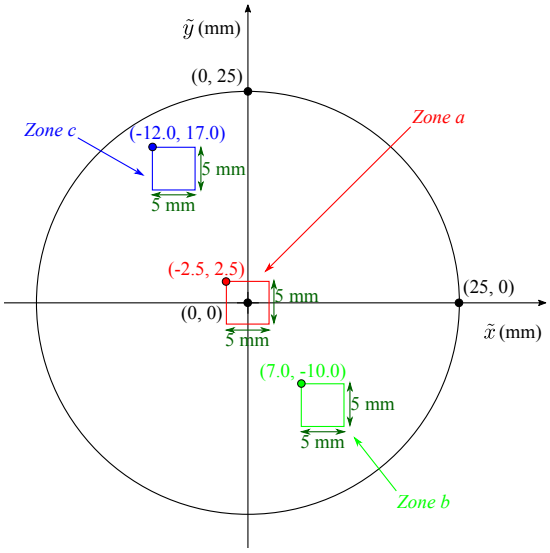

Figure A.1 – Diagram of the heated surface with locations of the three zones tested with the microscope ($p = 10$ µm).

A.1.2 Surface analysis

Zone a – analysis of a central zone

The measurements made with the confocal microscope on *Zone a* are displayed on Fig. A.2. The local elevation of the copper around the cavity caused by the mechanical indentation is clearly visible on Fig. A.2a. Actually this elevation creates large reflections that impedes the

observation of the shape and depth of the nucleation site. Despite this issue, the diameter of the nucleation site is estimated to 110 µm which corresponds to the size evaluated by Giraud [44]. As a consequence, the nucleation site is assumed unchanged, *i.e.* it is still conical and 70 µm deep. According to Fig A.2b, the rest of the surface appears to be very smooth.

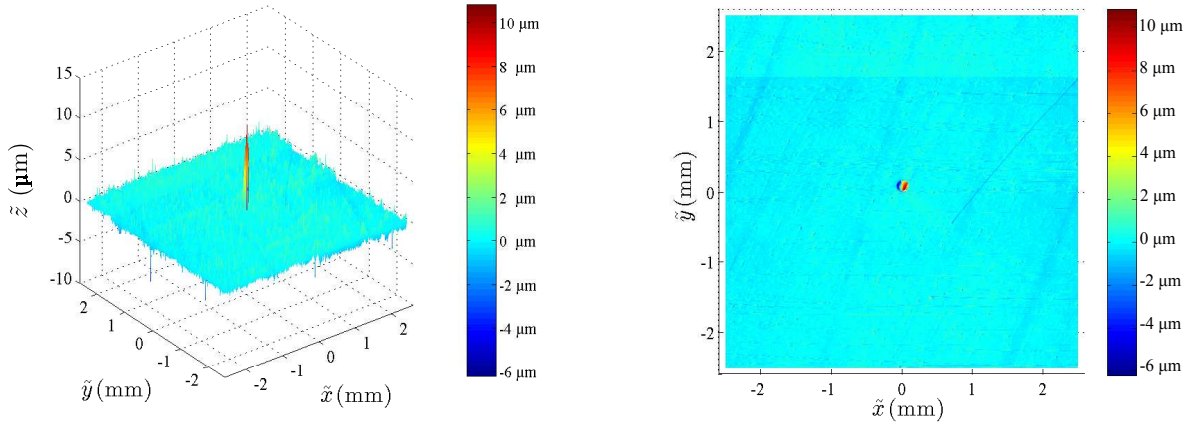

(a) 3D-view. (b) Top-view.

Figure A.2 – Visualizations of the *Zone a* obtained with the confocal microscope ($p = 10$ µm).

Zones b and c – analysis of non-centered zones

According to Fig. A.3 and A.4, the heated surface seems to be uniformly smooth. The spatial resolution of the measurement being high enough to be representative, the root mean square roughness S_q can be evaluated through the usual relation given as Eq A.1:

$$S_q = \sqrt{\frac{1}{M_{\tilde{x}} M_{\tilde{y}}} \sum_{k=0}^{M_{\tilde{x}}-1} \sum_{l=0}^{M_{\tilde{y}}-1} [\tilde{z}(\tilde{x}_k,\, \tilde{y}_l) - \tilde{\mu}]^2} \tag{A.1}$$

where $M_{\tilde{x}}$ and $M_{\tilde{y}}$ are the numbers of points for which the altitude is measured along respectively the $\tilde{x}$ and $\tilde{y}$-axis while $\tilde{\mu}$ is equal to the mean value of the altitude $\tilde{z}$ on the considered area.

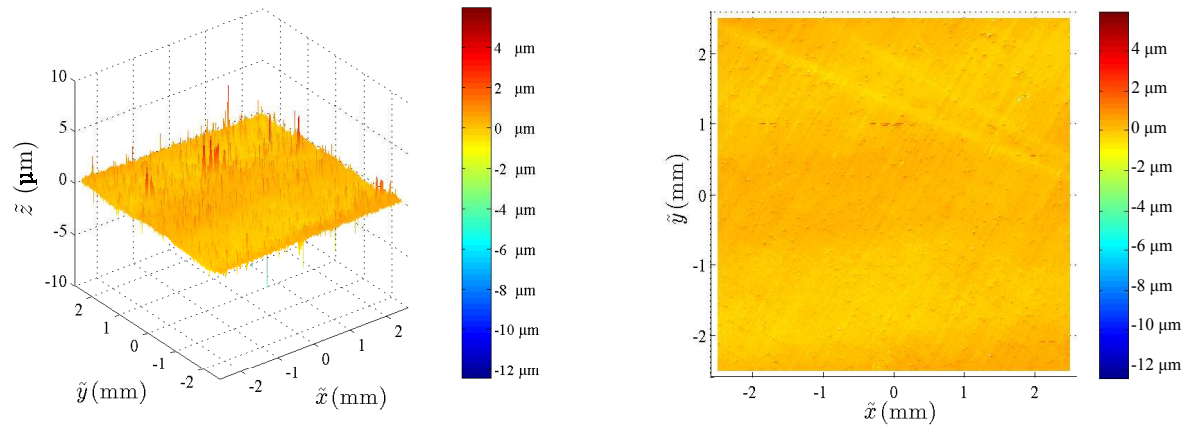

(a) 3D-view. (b) Top-view.

Figure A.3 – Visualizations of *Zone b* obtained with the confocal microscope ($p = 10$ µm).

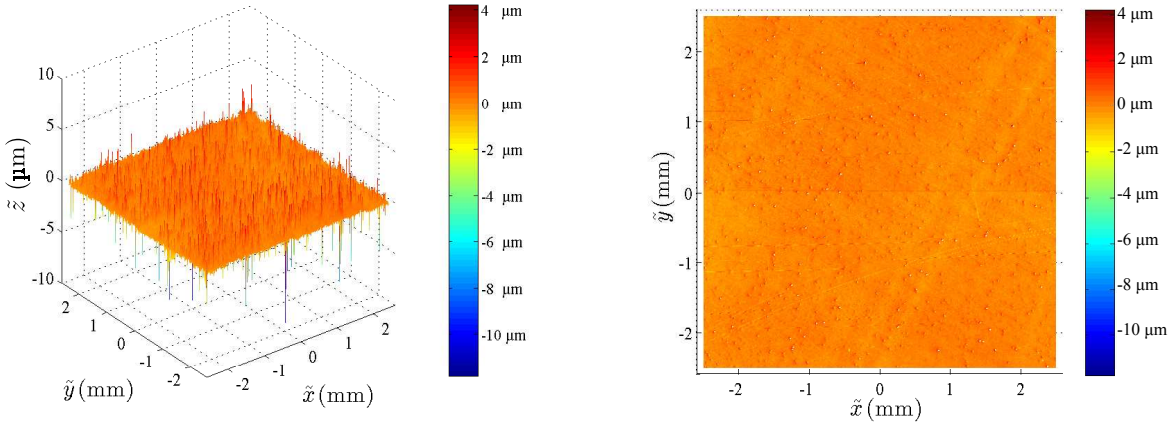

(a) 3D-view.

(b) Top-view.

Figure A.4 – Visualizations of *Zone c* obtained with the confocal microscope ($p = 10$ µm).

Averaging the results of the calculations performed on *Zone b* and *c* respectively yields a surface roughness of $S_q = 0.32$ µm. This value is in agreement with the one given by Giraud [44] ($S_q < 0.4$ µm).

A.1.3 Conclusion

According to the measurements made with the confocal microscope, the heated surface condition and the geometry of the artificial nucleation site are still close to the one used by Giraud [44].

A.2 The heat flux sensor used as a heated surface

A.2.1 Introduction

As mentioned in Chapter 5, the surface condition of the sensor was also carefully analyzed using the confocal microscope in order to verify that it was comparable to the one of the heated wall of the previous test sample. This was done by following the three following stages:

i) The full sensor was analyzed with a quite low spatial resolution in order to check the large-scale uniformity of the whole surface. The spatial step p was chosen to obtain a relatively good trade-off between the measurement time and the spatial resolution.

ii) Several zones of the surface of different sizes were randomly analyzed with the microscope using an intermediate spatial step value. This was aiming at verifying – with a better spatial resolution – if the surface looked uniform or not.

iii) A central zone was accurately (low spatial step) analyzed to evaluate the surface roughness and the size of the artificial nucleation site.

Similar to what was done for the heated surface from the first version of the sample, the spatial step p is the same for the two directions of the horizontal plane of the microscope (*i.e.* along the $\tilde{x}$ and $\tilde{y}$-axes).

A.2.2 Surface analysis

Stage i) – analysis of the whole sensor

The entire surface was observed with the spatial step set to $p = 35$ µm which led to a measurement duration of 12 h because of the large size of the sensor.

As shown on Fig. A.5, there is no major defect on the surface: except for some isolated points close to the edges, the vertical distance between the highest and the lowest points can be estimated as smaller than 50 µm, which is negligible compared to the surface's size.

However, the surface's roughness cannot be calculated from this measurement because of the low spatial resolution which makes this computation not representative.

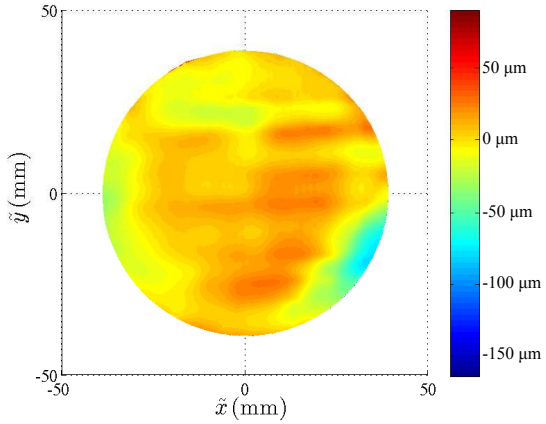

Figure A.5 – Visualization of the whole surface with the confocal microscope ($p = 35$ µm).

Stage ii) – analysis of several random zones

At this step, three zones (labeled *Zone a*, *b* and *c* respectively) were randomly chosen to be analyzed with an intermediate spatial resolution: $p = 20$ µm. This spatial step is still too large to enable the calculation of a fully reliable roughness of the surface from those measurements. The three zones are located as illustrated on Fig. A.6.

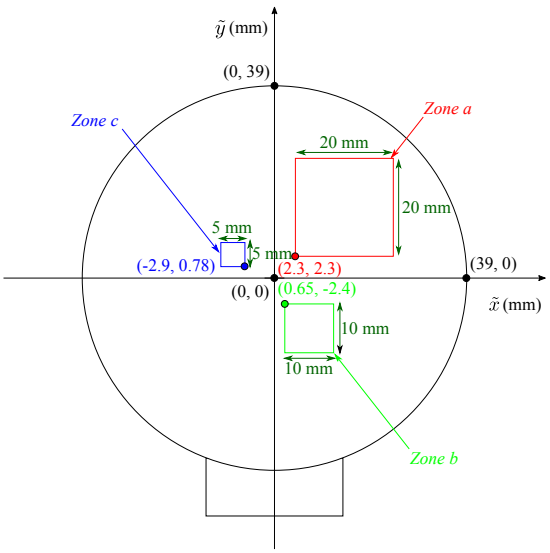

Figure A.6 – Diagram of the heat flux sensor with locations of the three zones tested with the microscope ($p = 20$ µm).

The measurement time depending on the size of the investigated areas (and of the chosen spatial resolution), microscope measurements lasted about 3 h 30 min for *Zone a*, 1 h for *Zone b* and only 16 min for *Zone c*.

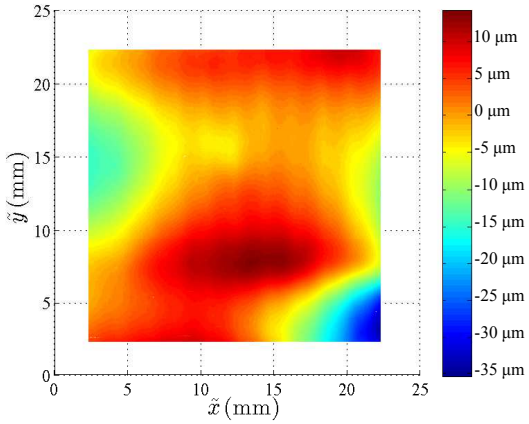

(a) *Zone a.*

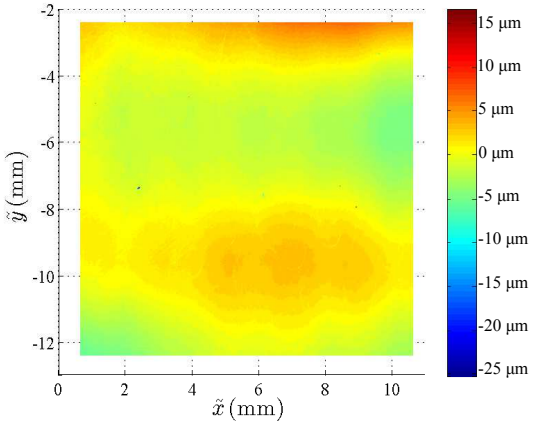

(b) *Zone b.*

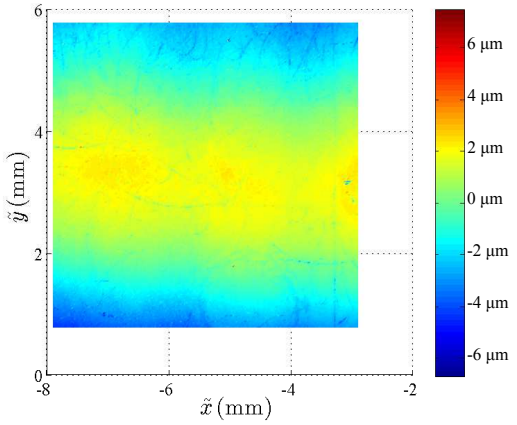

(c) *Zone c.*

Figure A.7 – Visualization of the three zones made with the microscope ($p = 20$ µm).

Visualizations of those measurements are given on Fig. A.7. From that figure, one can again conclude that the surface is relatively uniform: variations of altitude are very small (smaller than 5 µm), especially when looking at *Zone b* and *c* (refer to Fig. A.7b and A.7c). Vertical lines are nevertheless visible on *Zone a* (Fig. A.7a). Actually, they correspond to small grooves made on the bottom face of the copper foil to ensure a good working of the sensor (by contributing to the creation of the asymmetry between copper and constantan, refer to Section 5.1.4.2.1) as well as a satisfying gluing between the foil and the rest of the sensor. However, the difference of

height between the ridges and the valleys is still of only a few micrometers which is comparable to variations in the other investigated zones.

Stage iii) – analysis of a small centered zone

Finally, a small centered zone ($\tilde{x},\ \tilde{y} \in [-0.75\text{ mm}\,;0.75\text{ mm}]$) was investigated with a very high resolution ($p = 1$ µm). This measurement lasted then 2 h 30 min.

The acquired data were treated afterwards in two distinct phases aiming at:

1. Locating the nucleation site and measuring its size;
2. Estimating the surface roughness.

In phase 1, all the visualization was used while in phase 2 only a part of it was used in order to avoid any disturbance of the roughness estimation due to the presence of the artificial cavity (which is supposed to be the largest defect of the full surface).

Phase 1

The mechanical indentation made to create the artificial nucleation site also induced a local elevation of the copper around the cavity itself as it can be seen on Fig. A.8a. Except this, the cavity is very clean with a very circular opening and an almost conical shape. The nucleation site thus machined is 110 µm deep with a diameter of 100 µm.

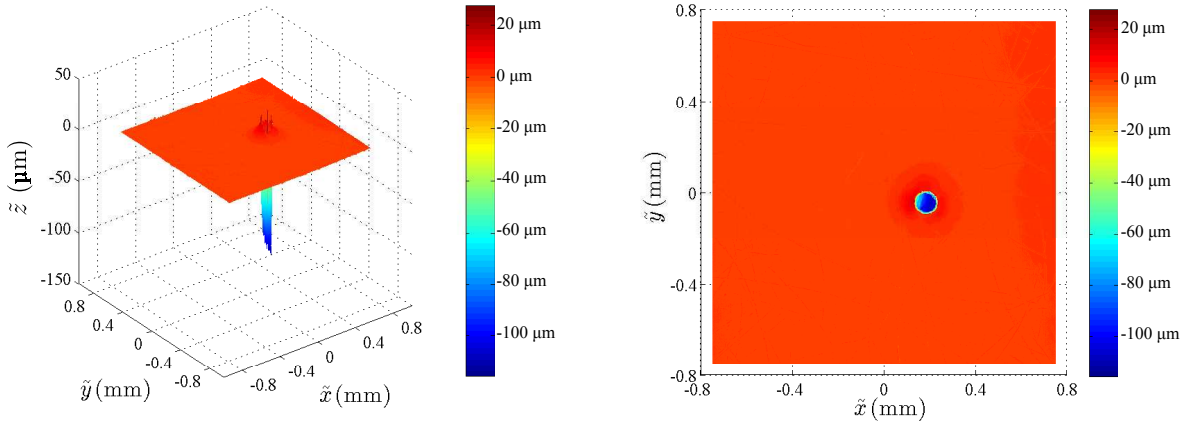

(a) 3D-view.

(b) Top-view.

Figure A.8 – Visualizations of the centrered zone obtained with the microscope ($p = 1$ µm).

Figure A.8b reveals that the artificial cavity is not perfectly centered on the heated wall: its center is in fact located at the position ($\tilde{x} = 0.184$ mm, $\tilde{y} = 0.045$ mm) instead of the expected location ($\tilde{x} = 0$, $\tilde{y} = 0$).

Phase 2

To estimate the surface roughness, only the bottom-left quarter of the centered zone is investigated. The nucleation site is thus excluded from the calculation.

As visible on Fig. A.9b, there are only few small stripes on the surface. Equation A.1 applied on the area displayed on Fig. A.9 leads to the following result: $S_q = 0.28$ µm.

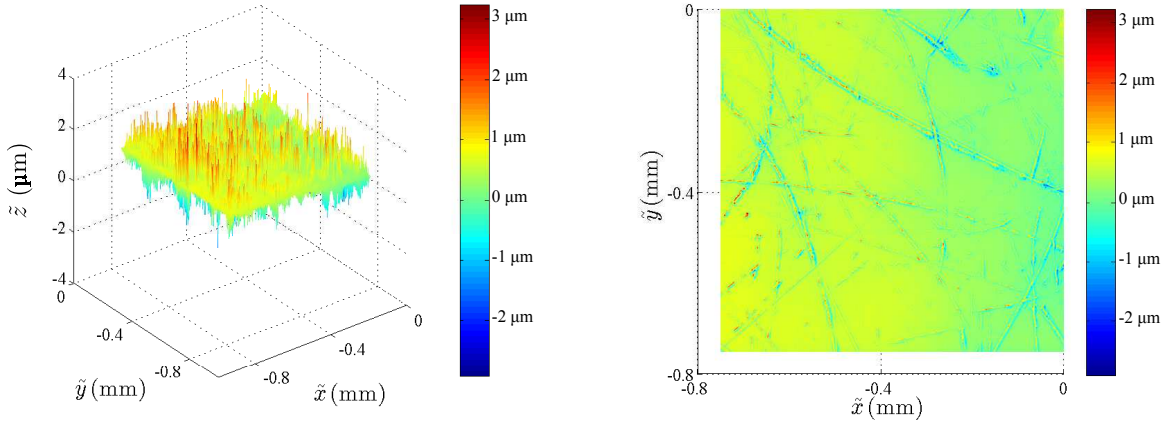

(a) 3D-view.

(b) Top-view.

Figure A.9 – Visualizations of the bottom-left quarter of the centrered zone obtained with the confocal microscope ($p = 1$ µm).

A.2.3 Conclusion

According to the measurements made with the confocal microscope and presented in this appendix, the heated surface constituted of the heat flux sensor is homogeneous and relatively smooth. Its roughness being equal to $S_q = 0.28$ µm, it is lower than 0.4 µm which is comparable to the roughness of the heated wall of the first test sample (refer to Section A.1).

The artificial nucleation site is also characterized in terms of position, shape and size. With a diameter of 100 µm, a depth of 110 µm, a conical shape and a centered position, the geometry of the cavity is similar to the one of the first test heater's nucleation site.

Appendix B

Calculation of the heat transfer coefficient and associated uncertainties

Case of the test campaign conducted with water (Chapter 3)

The heat transfer coefficient h at the heated surface can be calculated from the measurements of the system wall superheat ΔT_{wall}^{sys} according to the following relation:

$$h = \frac{\varphi}{\Delta T_{wall}^{sys}} \tag{B.1}$$

In the present appendix, the accuracy of the heat flux φ determination during the experimental session presented in Chapter 3 is discussed before the corresponding heat transfer coefficient is evaluated with its own uncertainty.

B.1 Discussion on the heat flux φ

During all the test campaign whose results are presented in Chapter 3, the imposed heat flux was set constant. As – whatever the imposed vapor pressure P_v – almost no temperature fluctuation was observed (refer to Section 3.3.1.1), it is expected that the measured heat flux φ_{meas} does not depend on time (*i.e.* that there is no heat storage in the heater or in the wall).

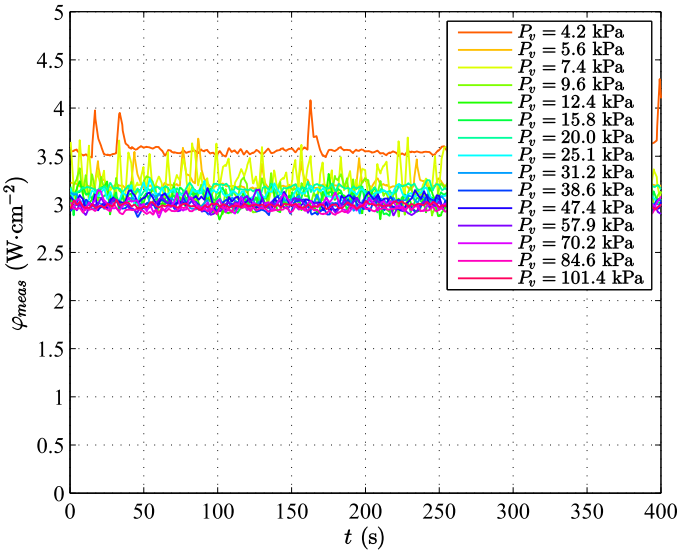

Figure B.1 – Time evolution of the measured heat flux φ_{meas} for the different investigated vapor pressures (water, $H_l = 17.3$ cm, $\varphi_{input} = 2.7$ W $\cdot$ cm^{-2}).

According to Fig. B.1, despite the small noise linked to their calculation method (through the derivative of a linear fit as explained in Section 2.3.1), measured values of heat flux are constant with time for all the investigated pressures. It appears yet that the measured values overestimate the input value. As this is not consistent even if there is no heat loss (since there is no storage of heat), the question of the uncertainties on the heat flux arises.

Uncertainty on the imposed heat flux φ_{input}: The imposed heat flux φ_{input} is evaluated through Eq. B.2:

$$\varphi_{input} = \frac{u_{input} i_{input}}{A} \tag{B.2}$$

where u_{input} and i_{input} are the voltage and current delivered by the power supply (in Volts and Amperes respectively) while A (in square meters) is the area of the cross section of the copper block (the influence of the fin is not considered).

The uncertainty on this parameter is therefore obtained through:

$$\frac{\Delta\varphi_{input}}{\varphi_{input}} = \frac{\Delta u_{input}}{u_{input}} + \frac{\Delta i_{input}}{i_{input}} + \frac{\Delta A}{A} \tag{B.3}$$

In the present case, with the uncertainties on the voltage, the current and the diameter of the cross section of the copper block estimated to ± 0.1 V, ± 0.01 A and ± 0.5 mm respectively, the calculation of the error on the imposed heat flux leads to:

$$\frac{\Delta\varphi_{input}}{\varphi_{input}} = 4.1\ \% \tag{B.4}$$

Uncertainty on the measured heat flux φ_{meas}: The measured heat flux is obtained according to the method detailed in Section 2.3.1. The uncertainty on it is evaluated through Eq. 2.8 where the error on the thermal conductivity of copper can be neglected, so that the relation becomes:

$$\frac{\Delta\varphi_{meas}}{\varphi_{meas}} = \frac{\Delta(dT)}{dT} + \frac{\Delta(dZ)}{dZ} \tag{B.5}$$

At the present low heat flux, the uncertainty calculation (with errors of ± 0.1 K and ± 0.4 mm on temperature and position of thermocouples in the heater) gives:

$$\frac{\Delta\varphi_{meas}}{\varphi_{meas}} = 45.0\ \% \tag{B.6}$$

At such low heat flux, the measured values through the rows of thermocouples inside the heater are then much less accurate than the evaluation of the imposed heat flux through the knowledge of the power input[1]. As no variation with time is observed in this study, imposed heat flux φ_{input} can be considered for further analyses (calculation of the heat transfer coefficient for instance). Otherwise, only instantaneous measurements φ_{meas} should be considered in spite of their high uncertainty. For the same reason, only time-averaged values are regarded hereafter.

As visible on Fig. B.2, the imposed heat flux value is always included in the uncertainty range of the measured heat flux. The difference between the two quantities varies with the pressure: the associated relative error (with the imposed value as reference) is indeed about 19.0 % at low pressure ($P_v \leq 20.0$ kPa) whereas it is about 11.6 % at higher pressures ($P_v > 20.0$ kPa).

[1] One should however be aware that the heat losses that can occur along the copper cylinder are not considered at all in the evaluation of the imposed heat flux through the knowledge of the power input nor of its uncertainty. They may yet be considered with the temperature measurements since the thermocouples are located close to the wall.

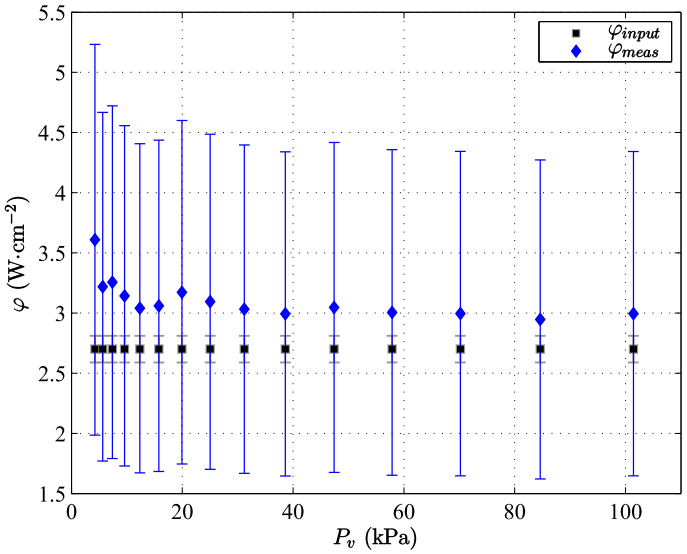

Figure B.2 – Measured heat flux φ_{meas} and imposed heat flux φ_{input} for the different investigated vapor pressures (water, $H_l = 17.3$ cm, $\varphi_{input} = 2.7$ W $\cdot$ cm^{-2}).

B.2 Calculation of the heat transfer coefficient *h*

The heat transfer coefficient h can finally be evaluated through Eq. B.1 where the considered value for heat flux φ is either the imposed heat flux value φ_{input} ($h_{\varphi_{input}}$) or the measured heat flux value φ_{meas} ($h_{\varphi_{meas}}$).

Depending on the case, the uncertainty on the heat transfer coefficient is given by:

$$\frac{\Delta h_{\varphi_{input}}}{h_{\varphi_{input}}} = \frac{\Delta \varphi_{input}}{\varphi_{input}} + \frac{\Delta(\Delta T_{wall}^{sys})}{\Delta T_{wall}^{sys}} \tag{B.7}$$

or

$$\frac{\Delta h_{\varphi_{meas}}}{h_{\varphi_{meas}}} = \frac{\Delta \varphi_{meas}}{\varphi_{meas}} + \frac{\Delta(\Delta T_{wall}^{sys})}{\Delta T_{wall}^{sys}} \tag{B.8}$$

With an uncertainty of $\pm$ 0.3 K on the wall superheat ΔT_{wall}^{sys}, Eq. B.7 and Eq. B.8 lead to:

$$\frac{\Delta h_{\varphi_{input}}}{h_{\varphi_{input}}} = 5.7\ \% \tag{B.9}$$

and

$$\frac{\Delta h_{\varphi_{meas}}}{h_{\varphi_{meas}}} = 46.6\ \% \tag{B.10}$$

The variations of the heat transfer coefficient h with the vapor pressure P_v – visible on Fig. B.3 – are mostly caused by the wall superheat ΔT_{wall}^{sys} dependence on this parameter (see Fig. 3.12).

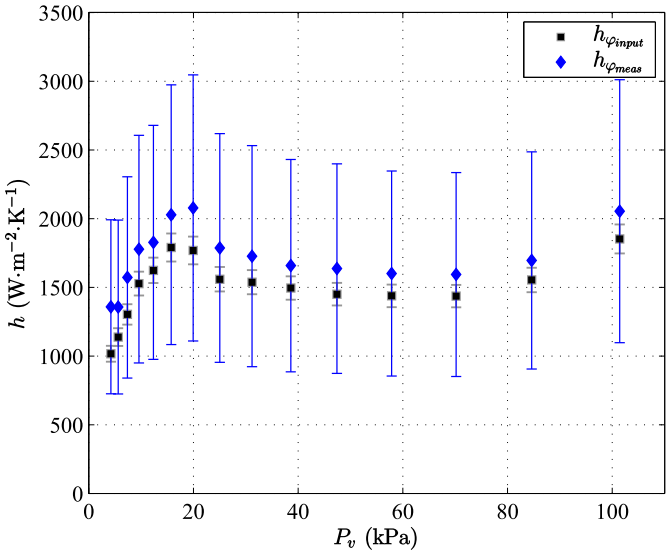

Figure B.3 – Heat transfer coefficient based on the measured ($h_{\varphi_{meas}}$) and imposed heat flux ($h_{\varphi_{input}}$) for the different investigated vapor pressures (water, $H_l = 17.3$ cm, $\varphi_{input} = 2.7$ W $\cdot$ cm^{-2}).

Whatever the vapor pressure P_v imposed during this experimental campaign, the heat transfer coefficient h is low and ranges from $h = 1000$ to 2100 W $\cdot$ m^{-2} $\cdot$ K^{-1}. This is in agreement with the literature since, at low pressure, heat is mainly transferred by natural convection rather than by phase change. However, close to the atmospheric pressure ($P_v \approx P_{atm} = 101.4$ kPa) the heat transfer coefficient could have been expected to be higher. This is related to the influence of the low heated surface roughness on the heat transfer: only a few cavities are activated at this imposed heat flux resulting in a high wall superheat at nucleation.

Appendix C

Waiting time: extension of McGillis *et al.* [77] approach and discussion

C.1 The original approach

As explained in Chapter 3, McGillis *et al.* [77] developed a correlation for the waiting time that separates the departure of a bubble from the surface and the nucleation of a new bubble. For that, they considered – in agreement with Han and Griffith [52] – a transient conduction model to determine the temperature distribution of the fluid in the vicinity of the heated surface. This appears as a valuable approach since the no-slip boundary condition at the solid surface makes there the convection intensity negligible. The authors then refered to a solution[2] of the form given by Carslaw and Jaeger [14]:

$$\Delta T_{cond}(Z,t) = \frac{2\varphi}{\lambda}\left[\left(\frac{\alpha t}{\pi}\right)^{0.5}\exp\left(\frac{-Z^2}{4\alpha t}\right) - \frac{Z}{2}\,\mathrm{erfc}\left(\frac{Z}{2(\alpha t)^{0.5}}\right)\right] \tag{C.1}$$

They assumed then that at $t = \tau_{wait}$ the entire bubble nucleus is at a temperature equal to or higher than the superheat temperature needed to initiate the nucleation. This condition is even reinforced (according to Hsu [56]) by requiring that the minimal superheat is reached for ($Z = r_{eff}$, $t = \tau_{wait}$). As they consider the critical superheat defined according to Eq. 3.8, they finally take the following boundary condition:

$$\Delta T_{cond}(Z = r_{eff},\, t = \tau_{wait}) = \Delta T_{wall}^{crit,\,1} \tag{C.2}$$

Using a linearized form of Eq. C.1 to solve Eq. C.2 in terms of waiting time, McGillis *et al.* [77] obtained finally the following relation:

$$\tau_{wait} = \frac{\pi\lambda_l\rho_l c_{p_l}}{4\varphi^2}\left[\underbrace{\frac{1.6\sigma T_{sat}}{r_{eff}\rho_v\Delta h_{lv}}}_{\Delta T_{wall}^{crit,\,1}} + \frac{r_{eff}\varphi}{\lambda_l}\right]^2 \tag{C.3}$$

C.2 Extension of the approach

As mentioned in Section C.1, McGillis *et al.* [77] choose to establish their correlation with the model of critical wall superheat ΔT_{wall}^{crit} based on the Clausius-Clapeyron and static equilibrium of a vapor nucleus equations. Their approach can then be extended by considering other models of critical superheat:

[2] According to Carslaw and Jaeger [14], Eq. C.1 corresponds actually to the general solution for the temperature distribution during transient conduction of heat into a semi-infinite medium (solid or quasi-static fluid) with the boundary condition of uniform temperature and constant heat flux.

$$\tau_{wait} = \frac{\pi \lambda_l \rho_l c_{p_l}}{4 \varphi_{input}^2} \left[\Delta T_{wall}^{crit} + \frac{r_{eff} \varphi_{input}}{\lambda_l} \right]^2 \tag{C.4}$$

On Fig. C.1, a comparison between our experimental results and the evaluation of Eq. C.4 considering the five wall superheat models detailed in Section 3.3.1.2 ($\Delta T_{wall}^{crit,\,0}$, $\Delta T_{wall}^{crit,\,1}$, $\Delta T_{wall}^{crit,\,2}$, $\Delta T_{wall}^{crit,\,3}$ and $\Delta T_{wall}^{crit,\,4}$) and an effective surface cavity size equal to the radius of the artificial nucleation site ($r_{eff} = r_{cav}$) is performed. A last comparison is also conducted by injecting the experimental values of wall superheat ΔT_{wall}^{exp} in the McGillis correlation (still with the effective surface cavity size taken equal to the radius of the artificial nucleation site).

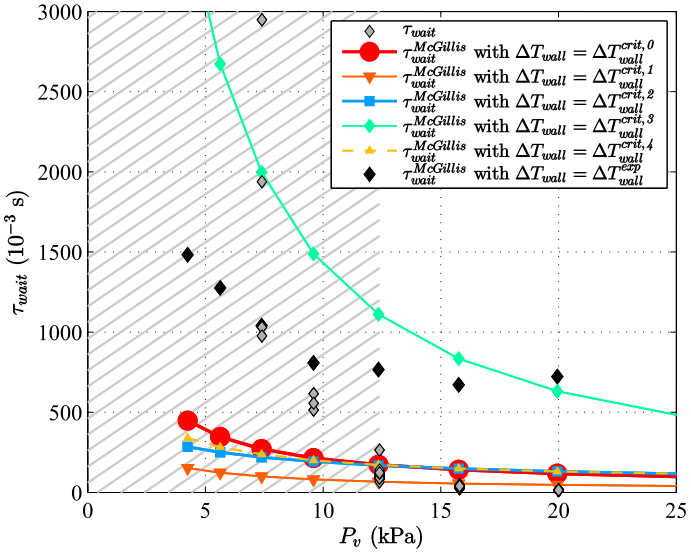

Figure C.1 – Dependence of the waiting period between successive bubbles τ_{wait} on the vapor pressure P_v and comparison with McGillis correlation depending on the model considered for minimal wall superheat ΔT_{wall}^{crit} as well as with this correlation where the experimental wall superheat ΔT_{wall}^{exp} is considered (water, $H_l = 17.3$ cm, $\varphi_{input} = 2.7$ W $\cdot$ cm^{-2}). – The shaded domain corresponds to the domain of pressure where the linearization for the correlation is not valid according to the measured waiting time values.

As visible on Fig. C.1, whatever the considered wall superheat (different models or even experimental values), the correlation established by McGillis *et al.* [77] does not corresponds to our experimental measurements of the waiting time with a good agreement. At the lowest pressures ($P_v < 12.4$ kPa), this can still be explained by the linearization performed on the transient conduction model which is not valid there (since the waiting period is then not short). At higher pressures, the simplest model of critical wall superheat (*i.e.* the one originally used by McGillis *et al.* which is based on the static equilibrium of a vapor nucleus and on the Clausius-Clapeyron equation) yields the best agreement.

Consequently to this short study, the approach developed by McGillis *et al.* in [77] is not extended further in Chapter 3 and a fit of our experimental data is simply performed depending on the pressure at the heated surface level P_{wall}.

List of references

[1] Akiyama, M., Tachibana, F., and Ogawa, N. Effect of pressure on bubble growth in pool boiling. *Bulletin of the Japan Society of Mechanical Engineers*, 12 (1969), 1121–1128. [Cited on pages 13, 15, and 19]

[2] Alam, M. S., and Agarwal, V. K. Pool boiling of liquids & their mixtures on enhanced surfaces at sub-atmospheric pressures. In *Proceedings of International Conference on Chemical & Process Engineering* (Rome, Italy, 2009). [Cited on pages 15 and 19]

[3] Alam, M. S., Prasad, L., Gupta, S. C., and Agarwal, V. K. Enhanced boiling of saturated water on copper coated heating tubes. *Chemical Engineering and Processing: Process Intensification*, 47 (2008), 159–167. [Cited on pages 15 and 19]

[4] Arya, M., Khandekar, S., Pratap, D., and Ramakrishna, S. A. Pool boiling of water on nano-structured micro wires at sub-atmospheric conditions. *Heat and Mass Transfer*, 52 (2016), 1725–1737. [Cited on pages 13, 15, 19, and 20]

[5] Bankoff, S. G. Ebullition from solid surfaces in the absence of a pre-existing gaseous phase. *Transactions of the American Society of Mechanical Engineers*, 79 (1957), 735–740. [Cited on page 7]

[6] Bankoff, S. G. Entrapment of gas in the spreading of a liquid over a rough surface. *American Institute of Chemical Engineers Journal*, 4 (1958), 24–26. [Cited on page 7]

[7] Barthès, M. *Ébullition sur site isolé : étude experimentale de la dynamique de croissance d'une bulle et des transferts associés*. PhD thesis, Université de Provence – Aix-Marseille I, 2005. [Cited on pages 10 and 115]

[8] Bhaumik, S., Agarwal, V. K., and Gupta, S. C. A generalized correlation of nucleate pool boiling of liquids. *Indian Journal of Chemical Technology*, 11 (2004), 719–725. [Cited on page 19]

[9] Bonnard, N., Falcy, M., Fastier, A., and Jargot, D. Base de données Fiches toxicologiques – Cyclohexane - Fiche toxicologique n°17. `http://www.inrs.fr/publications/bdd/fichetox/fiche.html?refINRS=FICHETOX_17`, 2010. [Cited on page 83]

[10] Bonnard, N., Falcy, M., Jargot, D., and Pasquier, E. Base de données Fiches toxicologiques – Benzène - Fiche toxicologique n°49. `http://www.inrs.fr/publications/bdd/fichetox/fiche.html?refINRS=FICHETOX_49`, 2011. [Cited on page 83]

[11] Bošnjaković, F. Verdampfung und Flüssigkeitsüberhitzung. *Technische Mechanik und Thermodynamik*, 1 (1930), 358–362. [Cited on page 9]

[12] Buyevich, Y. A., and Webbon, B. W. Dynamics of vapour bubbles in nucleate boiling. *International Journal of Heat and Mass Transfer*, 39 (1996), 2409–2426. [Cited on pages 10, 11, and 12]

[13] Carey, V. P. *Liquid-vapor phase-change phenomena*, 2nd ed. CRC Press, Taylor & Francis Group, 1992. [Cited on pages xxi, xxvii, 6, 8, 9, 13, and 107]

[14] Carslaw, H. S., and Jaeger, J. C. *Conduction of heat in solids*, 2nd ed. Clarendon Press – Oxford University Press, 1959. [Cited on pages 65 and 151]

[15] Castellan, A., Bart, J. C. J., and Cavallaro, S. Industrial production and use of adipic acid. *Catalysis Today*, 9 (1991), 237–254. [Cited on page 91]

[16] Caupin, F., and Herbert, E. Cavitation in water: a review. *Comptes Rendus Physique*, 7 (2006), 1000–1017. [Cited on page 50]

[17] Chan, M. A., Yap, C. R., and Ng, K. C. Pool boiling heat transfer of water on finned surfaces at near vacuum pressures. *Journal of Heat Transfer*, 132 (2010), 031501–1–6. [Cited on pages 15, 19, and 20]

[18] Chang, S. W., Lo, D. C., Chiang, K. F., and Lin, C. Y. Sub-atmospheric boiling heat transfer and thermal performance of two-phase loop thermosyphon. *Experimental Thermal and Fluid Science*, 39 (2012), 134–147. [Cited on page 15]

[19] Chen, Y., Groll, M., Mertz, R., and Kulenovic, R. Study of forces acting on a growing bubble from smooth and enhanced tubes. *International Journal of Heat and Technology*, 20 (2002), 31–39. [Cited on page 12]

[20] Chen, Z., Haginiwa, A., and Utaka, Y. Detailed structure of microlayer in nucleate pool boiling for water measured by laser interferometric method. *International Journal of Heat and Mass Transfer*, 108 (2017), 1285–1291. [Cited on page 131]

[21] Choon, N. K., Chakraborty, A., Aye, S. M., and Xiaolin, W. New pool boiling data for water with copper-foam metal at sub-atmospheric pressures: Experiments and correlation. *Applied Thermal Engineering*, 26 (2006), 1286–1290. [Cited on pages 15 and 19]

[22] Clark, J. A., and Merte, H. Private communication with Van Stralen, 1973. [Cited on page 51]

[23] Cochran, T. H., and Aydelott, J. C. Effects of subcooling and gravity level on boiling in the discrete bubble region. Tech. Rep. NASA-TN-D-3449 (1966), National Aeronautics and Space Administration. Lewis Research Center, Cleveland, Ohio, USA. [Cited on page 12]

[24] Cochran, T. H., Aydelott, J. C., and Spuckler, C. M. Experimental investigation of nucleate boiling bubble dynamics in normal and zero gravities. Tech. Rep. NASA-TN-D-4301 (1968), National Aeronautics and Space Administration. Lewis Research Center, Cleveland, Ohio, USA. [Cited on page 12]

[25] Cole, R. A photographic study of pool boiling in the region of the critical heat flux. *American Institute of Chemical Engineers Journal*, 6 (1960), 533–538. [Cited on page 75]

[26] Cole, R. Bubble frequencies and departure volumes at subatmospheric pressures. *American Institute of Chemical Engineers Journal*, 13 (1967), 779–783. [Cited on pages 19, 67, and 68]

[27] Cole, R., and Shulman, H. L. Bubble growth rates at high Jakob numbers. *International Journal of Heat and Mass Transfer*, 9 (1966), 1377–1390. [Cited on pages 13, 19, and 105]

[28] Collier, J. G., and Thome, J. R. *Convective boiling and condensation*, 3rd ed. Oxford University Press, 1994. [Cited on pages xxi, 6, and 7]

[29] Cooper, M. G. The microlayer and bubble growth in nucleate pool boiling. *International Journal of Heat and Mass Transfer*, 12 (1969), 915–933. [Cited on page 10]

[30] Cooper, M. G. The 'mirage' in boiling. *International Journal of Heat and Mass Transfer*, 26 (1983), 1088–1090. [Cited on page 32]

[31] Cooper, M. G., Judd, A. M., and pike, R. A. Shape and departure of single bubbles growing at a wall. In *Proceedings of the 6th International Heat Transfer Conference* (Toronto, Canada, 1978). [Cited on page 11]

[32] Cooper, M. G., and Lloyd, A. J. P. The microlayer in nucleate pool boiling. *International Journal of Heat and Mass Transfer*, 12 (1969), 895–913. [Cited on page 10]

[33] Cooper, M. G., and Merry, J. M. D. A general expression for the rate of evaporation of a layer of liquid on a solid body. *International Journal of Heat and Mass Transfer*, 16 (1973), 1811–1815. [Cited on pages 9 and 70]

[34] Darby, R. The dynamics of vapour bubbles in nucleate boiling. *Chemical Engineering Science*, 19 (1964), 39–49. [Cited on page 50]

[35] Deissler, R. G. In *Proceedings of the Columbia University Heat Transfer Symposium* (New York, New York, USA, 1954). [Cited on page 75]

[36] Dergarabedian, P. Observations on bubble growths in various superheated liquids. *Journal of Fluid Mechanics*, 9 (1960), 39–48. [Cited on page 50]

[37] Dhir, V. K. Mechanistic prediction of nucleate boiling heat transfer – achievable or a hopeless task? *Journal of Heat Transfer*, 128 (2006), 1–12. [Cited on page 10]

[38] Ethington, E. F. Interfacial contact angle measurements of water, mercury, and 20 organic liquids on quartz, calcite, biotite, and Ca-montmorillonite substrates. Tech. Rep. USGS-OFR-90-409 (1990), United States Department of the Interior Geological Survey. [Cited on page 91]

[39] Florschuetz, L. W., Henry, C. L., and Khan, A. R. Growth rates of free vapor bubbles in liquids at uniform superheats under normal and zero gravity conditions. *International Journal of Heat and Mass Transfer*, 12 (1969), 1465–1489. [Cited on page 50]

[40] Forster, H. K., and Zuber, N. Dynamics of vapor bubbles and boiling heat transfer. *American Institute of Chemical Engineers Journal*, 1 (1955), 531–535. [Cited on pages 9 and 68]

[41] Fritz, W., and Ende, W. Über den Verdampfungsvorgang nach kinematographischen Aufnahmen an Dampfblasen. *Zeitschrift für Physik*, 37 (1936), 391–401. [Cited on page 74]

[42] Fyodorov, M. V., and Klimenko, V. V. Vapour bubble growth in boiling under quasi- stationary heat transfer conditions on a heating wall. *International Journal of Heat and Mass Transfer*, 32 (1989), 227–242. [Cited on pages 9 and 70]

[43] Ginet, N. *Analyse des mécanismes contrôlant la croissance et l'ascension d'une bulle isolée en ébullition nucléée.* PhD thesis, Institut National des Sciences Appliquées de Lyon, 1999. [Cited on pages 12, 40, 68, and 73]

[44] Giraud, F. *Vaporization of water at subatmospheric pressure: fundamentals of boiling phenomena and path towards the design of compact evaporators for sorption chillers.* PhD thesis, Institut National des Sciences Appliquées de Lyon, 2015. [Cited on pages xxvii, 13, 15, 16, 17, 23, 43, 51, 52, 53, 61, 70, 71, 72, 80, 82, 99, 107, 133, 139, 140, and 141]

[45] Giraud, F., Rullière, R., Toublanc, C., Clausse, M., and Bonjour, J. Experimental study of water pool boiling at very low pressure on a vertical or horizontal heated surface. In *Proceedings of the 4th IIR Conference on Thermophysical Properties and Transfer Processes of Refrigerants* (Delft, The Netherlands, 2013). [Cited on pages 15, 16, 17, 19, and 20]

[46] Giraud, F., Rullière, R., Toublanc, C., Clausse, M., and Bonjour, J. Experimental evidence of a new regime for boiling of water at subatmospheric pressure. *Experimental Thermal and Fluid Science*, 60 (2015), 45–53. [Cited on pages xxi, 14, 15, 16, 17, 19, 20, 43, 51, 52, 79, 80, 82, and 111]

[47] Giraud, F., Rullière, R., Toublanc, C., Clausse, M., and Bonjour, J. Preliminary experimental investigation on water boiling phenomena in a liquid layer at subatmospheric pressure. In *Proceedings of the 24th International Congress of Refrigeration* (Yokohama, Japan, 2015). [Cited on pages 16, 17, 18, 19, 20, and 80]

[48] Giraud, F., Rullière, R., Toublanc, C., Clausse, M., and Bonjour, J. Subatmospheric pressure boiling on a single nucleation site in narrow vertical spaces. *International Journal of Heat and Fluid Flow*, 58 (2016), 1–10. [Cited on pages 15, 19, and 20]

[49] Giraud, F., Toublanc, C., Rullière, R., Bonjour, J., and Clausse, M. Experimental study of water vaporization occurring inside a channel of a smooth plate-type heat exchanger at subatmospheric pressure. *Applied Thermal Engineering*, 106 (2016), 180–191. [Cited on pages 15 and 20]

[50] Halon, T., Zajaczkowski, B., Michaie, S., Rullière, R., and Bonjour, J. Experimental study of low pressure pool boiling of water from narrow tunnel surfaces. *International Journal of Thermal Sciences*, 121 (2017), 348–357. [Cited on pages xxv, 134, and 136]

[51] Halon, T., Zajaczkowski, B., Michaie, S., Rullière, R., and Bonjour, J. Enhanced tunneled surfaces for water pool boiling heat transfer under low pressure. *International Journal of Heat and Mass Transfer*, 116 (2018), 93–103. [Cited on pages xxv, 134, 135, and 136]

[52] Han, C. Y., and Griffith, P. The mechanism of heat transfer in nucleate pool boiling – Part I: Bubble initiation, growth and departure. *International Journal of Heat and Mass Transfer*, 8 (1965), 887–904. [Cited on pages 8, 65, 67, 105, and 151]

[53] Héas, S. *Étude expérimentale des transferts thermiques en ébullition libre et régime transitoire*. PhD thesis, Institut National des Sciences Appliquées de Lyon, 2001. [Cited on page 30]

[54] Hatton, A. P., and Hall, I. S. Photographic study of boiling on prepared surfaces. In *Proceedings of the 3rd International Heat Transfer Conference* (Chicago, Illinois, USA, 1966). [Cited on page 75]

[55] Hermans, W. A. H. J. *On the instability of a translating gas bubble under the influence of a pressure step*. PhD thesis, Eindhoven University of Technology, 1973. [Cited on page 50]

[56] Hsu, Y. Y. On the size range of active nucleation cavities on a heating surface. *Journal of Heat Transfer*, 84 (1962), 207–213. [Cited on pages 8, 54, 66, and 151]

[57] Hu, H. Y., Peterson, G. P., Peng, X. F., and Wang, B. X. Interphase fluctuation propagation and superposition model for boiling nucleation. *International Journal of Heat and Mass Transfer*, 41 (1998), 3483–3489. [Cited on page 6]

[58] Ibrahim, E. A., and Judd, R. L. An experimental investigation of the effect of subcooling on bubble growth and waiting time in nucleate boiling. *Journal of Heat Transfer*, 107 (1985), 168–174. [Cited on pages 64 and 65]

[59] Ivey, H. J. Relationships between bubble frequency, departure diameter and rise velocity in nucleate boiling. *International Journal of Heat and Mass Transfer*, 10 (1967), 1023–1040. [Cited on pages 75 and 76]

[60] Jakob, M., and Linke, W. Der Wärmeübergang von einer waagerechten Platte an siedendes Wasser. *Forschung im Ingenieurwesen*, 4 (1933), 75–81. [Cited on page 74]

[61] Jo, H., Kim, S., Kim, H., Kim, J., and Kim, M. H. Nucleate boiling performance on nano/microstructures with different wetting surfaces. *Nanoscale Research Letters*, 7 (2012), 242.1–9. [Cited on page 103]

[62] Jones, B. J., McHale, J. P., and Garimella, S. V. The influence of surface roughness on nucleate pool boiling heat transfer. *Journal of Heat Transfer*, 131 (2009), 121009.1–14. [Cited on page 61]

[63] Kempers, R., Kolodner, P., Lyons, A., and Robinson, A. J. A high-precision apparatus for the characterization of thermal interface materials. *Review of Scientific Instruments*, 80 (2009), 095111.1–11. [Cited on pages xxi and 31]

[64] Kenning, D. B. R., and Cooper, M. G. Flow patterns near nuclei and the initiation of boiling during forced convection heat transfer. In *Proceedings of the Institution of Mechanical Engineers, Conference Proceedings* (London, United Kingdom, 1965). [Cited on page 99]

[65] Keshock, E. G., and Siegel, R. Forces acting on bubbles in nucleate boiling under normal and reduced gravity conditions. Tech. Rep. NASA-TN-D-2299 (1964), National Aeronautics and Space Administration. Lewis Research Center, Cleveland, Ohio, USA. [Cited on page 12]

[66] Khan, N., Pinjala, D., and Toh, K. C. Pool boiling heat transfer enhancement by surface modification/micro-structures for electronics cooling: a review. In *Proceedings of the 6th Electronics Packaging Technology Conference* (Singapore, Singapore, 2004). [Cited on page 61]

[67] Kim, J., Huh, C., and Kim, M. H. On the growth behavior of bubbles during saturated nucleate pool boiling at sub-atmospheric pressure. *International Journal of Heat and Mass Transfer*, 50 (2007), 3695–3699. [Cited on page 105]

[68] Klausner, J. F., Mei, R., Bernhard, D. M., and Zeng, L. Z. Vapor bubble departure in forced convection boiling. *International Journal of Heat and Mass Transfer*, 36 (1993), 651–662. [Cited on page 12]

[69] Labuntsov, D. A., Yagov, V. V., and Gorodov, A. K. Critical heat fluxes in boiling at low pressure region. In *Proceedings of the 6th International Heat Transfer Conference* (Toronto, Canada, 1978). [Cited on pages 14 and 19]

[70] Lee, H. S., and Merte, H. Spherical vapor bubble growth in uniformly superheated liquids. *International Journal of Heat and Mass Transfer*, 39 (1996), 2427–2447. [Cited on pages 50 and 68]

[71] Lemmon, E. W., Huber, M. L., and McLinden, M. O. NIST Standard Reference Database 23: Reference Fluid Thermodynamic and Transport Properties-REFPROP, Version 9.1, National Institute of Standards and Technology. `https://www.nist.gov/srd/refprop`, 2013. [Cited on pages xxiii, xxvii, 17, 45, 59, 66, 81, 82, 83, 87, 90, 99, and 124]

[72] Lord Rayleigh. On the pressure developed in a liquid during the collapse of a spherical cavity. *The London, Edinburgh, and Dublin Philosophical Magazine and Journal of Science*, 34 (1917), 94–98. [Cited on page 9]

[73] Madejski, J. Activation of nucleation cavities on a heating surface with temperature gradient in superheated liquid. *International Journal of Heat and Mass Transfer*, 9 (1966), 295–300. [Cited on page 50]

[74] Malenkov, I. G. Detachment frequency as a function of size for vapor bubbles. *Journal of Engineering Physics*, 20 (1971), 704–708. [Cited on page 75]

[75] McFadden, P. W., and Grassmann, P. The relation between bubble frequency and diameter during nucleate pool boiling. *International Journal of Heat and Mass Transfer*, 5 (1962), 169–173. [Cited on page 75]

[76] McGillis, W. R., Carey, V. P., Fitch, J. S., and Hamburgen, W. R. Pool boiling enhancement techniques for water at low pressure. In *Proceedings of the 7th Annual IEEE Semiconductor Thermal Measurement and Management Symposium* (Phoenix, Arizona, USA, 1991). [Cited on pages 13, 15, 19, 43, 52, 53, and 61]

[77] McGillis, W. R., Fitch, J. S., Hamburgen, W. R., and Carey, V. P. Pool boiling on small heat dissipating elements in water at subatmospheric pressures. In *ASME National Heat Transfer Conference* (Minneapolis, Minnesota, USA, 1991). [Cited on pages xvi, 13, 15, 19, 43, 52, 54, 61, 63, 65, 66, 67, 79, 129, 151, and 152]

[78] McGillis, W. R., Fitch, J. S., Hamburgen, W. R., and Carey, V. P. Boiling binary mixtures at subatmospheric pressures. In *Proceedings of the 3rd InterSociety Conference on Thermal Phenomena in Electronic Systems* (Austin, Texas, USA, 1992). [Cited on pages 15 and 19]

[79] McNeil, D. A., Burnside, B. M., Rylatt, D. I., Elsaye, E. A., and Baker, S. Shell-side boiling of water at sub-atmospheric pressures. *International Journal of Heat and Mass Transfer*, 85 (2015), 488–504. [Cited on pages 15, 19, and 20]

[80] Mikic, B. B., Rohsenow, W. M., and Griffith, P. On bubble growth rates. *International Journal of Heat and Mass Transfer*, 13 (1970), 657–666. [Cited on pages 9, 68, 70, and 105]

[81] Mitrovic, J. Formation of a liquid jet after detachment of a vapour bubble. *International Journal of Heat and Mass Transfer*, 40 (1997), 4309–4317. [Cited on pages 13, 19, 50, and 51]

[82] Moghaddam, S., and Kiger, K. Physical mechanisms of heat transfer during single bubble nucleate boiling of FC-72 under saturation conditions – I. Experimental investigation. *International Journal of Heat and Mass Transfer*, 52 (2009), 1284–1294. [Cited on pages 61 and 130]

[83] Nam, Y., Aktinol, E., Dhir, V. K., and Ju, Y. S. Single bubble dynamics on a superhydrophilic surface with artificial nucleation sites. *International Journal of Heat and Mass Transfer*, 54 (2011), 1572–1577. [Cited on pages 61, 74, and 103]

[84] Nam, Y., Wu, J., Warrier, G., and Ju, Y. S. Experimental and numerical study of single bubble dynamics on a hydrophobic surface. *Journal of Heat Transfer*, 131 (2009), 121004.1–7. [Cited on pages 61, 74, and 103]

[85] Nukiyama, S. Maximum and minimum values of heat transmitted from metal to boiling water under atmospheric pressure. *Journal of the Japan Society of Mechanical Engineers*, 37 (1934), 367–374. [Cited on pages 3 and 158]

[86] Nukiyama, S. The maximum and minimum values of the heat Q transmitted from metal to boiling water under atmospheric pressure. *International Journal of Heat and Mass Transfer*, 9 (1966), 1419–1433. *Translation of [85].* [Cited on page 3]

[87] Ohue, H., Yang, W. J., and Kawashima, G. Convective flow around a single bubble during growth and departure. In *Proceedings of the 11th International Conference on Thermal Engineering and Thermogrammetry* (Budapest, Hungary, 1999). [Cited on pages 13, 19, 43, and 50]

[88] Pal, A., and Joshi, Y. Boiling at sub-atmospheric conditions with enhanced structures. In *Proceedings of the 10th InterSociety Conference on Thermal Phenomena in Electronic Systems* (San Diego, California, USA, 2006). [Cited on pages 15, 19, and 20]

[89] Papon, P., and Leblond, J. *Thermodynamique des états de la matière*, 1st ed. Hermann, 1990. [Cited on page 6]

[90] Patten, T. D. Some characteristics of nucleate boiling of water at sub-atmospheric pressures. In *Proceedings of the Institution of Mechanical Engineers, Conference Proceedings* (London, United Kingdom, 1963). [Cited on pages xxi, 13, 14, and 19]

[91] Perkins, A. S., and Westwater, J. M. Measurements of bubbles formed in boiling methanol. *American Institute of Chemical Engineers Journal*, 2 (1956), 471–476. [Cited on page 74]

[92] Pioro, I. L., Rohsenow, W., and Doerffer, S. S. Nucleate pool-boiling heat transfer. I: review of parametric effects of boiling surface. *International Journal of Heat and Mass Transfer*, 47 (2004), 5033–5044. [Cited on page 18]

[93] Plesset, M. S., and Zwick, S. A. The growth of vapor bubbles in superheated liquids. *Journal of Applied Physics*, 25 (1954), 493–500. [Cited on pages 9, 68, and 70]

[94] Ponter, A. B., and Haigh, C. P. The boiling crisis in saturated and subcooled pool boiling at reduced pressures. *International Journal of Heat and Mass Transfer*, 12 (1969), 429–437. [Cited on pages 16, 19, and 20]

[95] Ponter, A. B., and Haigh, C. P. Sound emission and heat transfer in low pressure pool boiling. *International Journal of Heat and Mass Transfer*, 12 (1969), 413–428. [Cited on pages 16, 18, 19, and 20]

[96] Qiu, D. M., and Dhir, V. K. Single-bubble dynamics during pool boiling under low gravity conditions. *Journal of Thermophysics and Heat Transfer*, 16 (2002), 336–345. [Cited on page 61]

[97] Rallis, C. J., and Jawurek, H. H. Latent heat transport in saturated nucleate boiling. *International Journal of Heat and Mass Transfer*, 7 (1964), 1051–1068. [Cited on pages 74, 75, 76, and 84]

[98] Robinson, A. J., and Judd, R. L. The dynamics of spherical bubble growth. *International Journal of Heat and Mass Transfer*, 47 (2004), 5101–5113. [Cited on pages 9, 70, 83, and 107]

[99] Rohsenow, W. M., Hartnett, J. P., Cho, Y. I., et al. *Handbook of heat transfer*, 3rd ed. McGraw-Hill New York, 1998. [Cited on pages 6, 54, 55, 56, and 99]

[100] Rullière, R., Siedel, B., and Haberschill, P. Experimental evaluation of bubble growth of water at very low pressure. In *Proceedings of the ECI 8th International Conference on Boiling and Condensation Heat Transfer* (Lausanne, Switzerland, 2012). [Cited on pages 13, 15, 19, 20, 43, 80, and 82]

[101] Sarker, D., Franz, R., Ding, W., and Hampel, U. Single bubble dynamics during subcooled nucleate boiling on a vertical heater surface: An experimental analysis of the effects of surface characteristics. *International Journal of Heat and Mass Transfer*, 109 (2017), 907–921. [Cited on page 103]

[102] Schnabel, L., Scherr, C., and Weber, C. Water as refrigerant – Experimental evaluation of boiling characteristics at low temperatures and pressures. In *Proceedings of International Sorption Heat Pump Conference* (Seoul, Korea, 2008). [Cited on pages 13, 15, 16, 19, 20, 43, and 61]

[103] Scriven, L. E. On the dynamics of phase growth. *Chemical Engineering Science*, 10 (1959), 1–13. [Cited on page 9]

[104] Siedel, S. *Bubble dynamics and boiling heat transfer: a study in the absence and in the presence of electric fields.* PhD thesis, Institut National des Sciences Appliquées de Lyon, 2012. [Cited on pages 12, 40, 68, 70, 72, 73, and 130]

[105] Siedel, S., Cioulachtjian, S., and Bonjour, J. Experimental analysis of bubble growth, departure and interactions during pool boiling on artificial nucleation sites. *Experimental Thermal and Fluid Science*, 32 (2008), 1504–1511. [Cited on pages 40, 61, 68, and 130]

[106] Siedel, S., Cioulachtjian, S., Robinson, A. J., and Bonjour, J. Experimental determination of the forces acting on a bubble during boiling on a single nucleation site. In *Proceedings of the ECI 8$^{\text{th}}$ International Conference on Boiling and Condensation Heat Transfer* (Lausanne, Switzerland, 2012). [Cited on page 12]

[107] Siedel, S., Cioulachtjian, S., Robinson, A. J., and Bonjour, J. Integral momentum balance on a growing bubble. *Physics of Fluids*, 25 (2013), 123301.1–22. [Cited on pages 12 and 73]

[108] Simpson, H. C., and Walls, A. S. A study of nucleation phenomena in transient pool boiling. In *Proceedings of the Institution of Mechanical Engineers, Conference Proceedings* (London, United Kingdom, 1965). [Cited on page 6]

[109] Stewart, J. K., and Cole, R. Bubble growth rates during nucleate boiling at high Jakob numbers. *International Journal of Heat and Mass Transfer*, 15 (1972), 655–664. [Cited on page 19]

[110] Tang, J., Yan, C., and Sun, L. A study visualizing the collapse of vapor bubbles in a subcooled pool. *International Journal of Heat and Mass Transfer*, 88 (2015), 597–608. [Cited on page 18]

[111] Tewari, P. K., Verma, R. K., Ramani, M. P. S., and Mahajan, S. P. Effect of surface roughness & polymeric additive on nucleate pool boiling at subatmospheric pressures. *International Communications in Heat and Mass Transfer*, 13 (1986), 503–514. [Cited on page 19]

[112] Theofanous, T., and Patel, P. D. Universal relations for bubble growth. *International Journal of Heat and Mass Transfer*, 19 (1976), 425–429. [Cited on pages 9 and 70]

[113] Thery, P., and Pauquet, J. Thermoelectric properties of thin electroplated foils. Application to the measurement of heat fluxes. *Journal of Physics E: Scientific Instruments*, 13 (1980), 323–327. [Cited on page 116]

[114] Thureau, P. *Fluxmètres thermiques.* Techniques Ingénieur, 1996. [Cited on pages xxiv and 116]

[115] Tong, W., Bar-Cohen, A., Simon, T. W., and You, S. M. Contact angle effects on boiling incipience of highly-wetting liquids. *International Journal of Heat and Mass Transfer*, 33 (1990), 91–103. [Cited on pages 91, 99, and 103]

[116] Van Leeuwen, H. J. W. Private communication with Van Stralen, 1973. [Cited on pages 50, 51, and 52]

[117] Van Stralen, S. J. D. Heat transfer to boiling binary liquid mixtures at atmospheric and subatmospheric pressures. *Chemical Engineering Science*, 5 (1956), 290–296. [Cited on pages 13, 15, and 19]

[118] Van Stralen, S. J. D. The growth rate of vapour bubbles in superheated pure liquids and binary mixtures: Part I: Theory. *International Journal of Heat and Mass Transfer*, 11 (1968), 1467–1489. [Cited on page 9]

[119] Van Stralen, S. J. D., Cole, R., Sluyter, W. M., and Sohal, M. S. Bubble growth rates in nucleate boiling of water at subatmospheric pressures. *International Journal of Heat and Mass Transfer*, 18 (1975), 655–669. [Cited on pages xxi, 13, 14, 15, 19, 43, 50, 51, 52, 63, 64, 79, 82, 105, 127, and 129]

[120] Van Stralen, S. J. D., Sluyter, W. M., and Cole, R. Bubble growth rates in nucleate boiling of aqueous binary systems at subatmospheric pressures. *International Journal of Heat and Mass Transfer*, 19 (1976), 931–941. [Cited on page 19]

[121] Van Stralen, S. J. D., Sohal, M. S., Cole, R., and Sluyter, W. M. Bubble growth rates in pure and binary systems: combined effect of relaxation and evaporation microlayers. *International Journal of Heat and Mass Transfer*, 18 (1975), 453–467. [Cited on pages xxvii, 51, and 52]

[122] Van Stralen, S. J. D., Zijl, W., and De Vries, D. A. The behaviour of vapour bubbles during growth at subatmospheric pressures. *Chemical Engineering Science*, 32 (1977), 1189–1195. [Cited on pages 13, 19, and 43]

[123] Wu, W. G., Ma, T. Z., and Li, H. Q. Experimental study of critical heat flux in pool boiling at low pressures. In *Proceedings of the 7th International Heat Transfer Conference* (Munich, Germany, 1982). [Cited on pages 14, 19, and 43]

[124] Yagov, V. V. Bubble growth rate at pool boiling in wide range of reduced pressures. In *Proceedings of the 5th World Conference on Experimental Heat Transfer, Fluid Mechanics and Thermodynamics* (Thessaloniki, Greece, 2001). [Cited on pages 13, 19, 43, 70, and 82]

[125] Yagov, V. V., Gorodov, A. K., and Labuntsov, D. A. Experimental study of heat transfer in the boiling of liquids at low pressures under conditions of free motion. *Journal of Engineering Physics*, 18 (1970), 421–425. [Cited on pages 13, 15, 19, 43, 52, 61, 127, and 129]

[126] Yagov, V. V., and Labuntsov, D. A. Intensification of heat transfer and stabilization of the boiling process in the very low pressure region. *Journal of Engineering Physics*, 20 (1971), 693–698. [Cited on pages 13, 15, 19, 43, and 52]

[127] Yala-Aithammouda, M. *Étude et réalisation de microcapteurs de flux thermique en technologie silicium*. PhD thesis, Université des Sciences et Technologies de Lille – Lille I, 2007. [Cited on page 116]

[128] Yamada, M., Shen, B., Hidaka, S., Kohno, M., Takata, Y., and Takahashi, K. Heat transfer enhancement of sub-atmospheric pool boiling with biphilic surfaces. In *Proceedings of the 9th World Conference on Experimental Heat Transfer, Fluid Mechanics and Thermodynamics* (Iguazu Falls, Brazil, 2017). [Cited on pages 15, 19, and 20]

[129] Yamada, M., Shen, B., Imamura, T., Hidaka, S., Kohno, M., Takahashi, K., and Takata, Y. Enhancement of boiling heat transfer under sub-atmospheric pressures using biphilic surfaces. *International Journal of Heat and Mass Transfer*, 115 (2017), 753–762. [Cited on pages 15, 19, and 20]

[130] Yamagata, K., Hirano, F., Nishikawa, K., and Matsuoka, H. Nucleate boiling of water on the horizontal heating surface. *Memoirs of the Faculty of Engineering, Kyushu University*, 15 (1955), 99–163. [Cited on page 74]

[131] Zajaczkowski, B., Halon, T., and Krolicki, Z. Experimental verification of heat transfer coefficient for nucleate boiling at sub-atmospheric pressure and small heat fluxes. *Heat and Mass Transfer*, 52 (2016), 205–215. [Cited on pages 15, 19, 43, 61, and 79]

[132] Zeng, L. Z., Klausner, J. F., and Mei, R. A unified model for the prediction of bubble detachment diameters in boiling systems – l. Pool boiling. *International Journal of Heat and Mass Transfer*, 36 (1993), 2261–2270. [Cited on page 12]

[133] Zuber, N. The dynamics of vapor bubbles in nonuniform temperature fields. *International Journal of Heat and Mass Transfer*, 2 (1961), 83–98. [Cited on pages 9, 10, and 70]

[134] Zuber, N. Nucleate boiling. The region of isolated bubbles and the similarity with natural convection. *International Journal of Heat and Mass Transfer*, 6 (1963), 53–78. [Cited on pages 67 and 74]

FOLIO ADMINISTRATIF

THÈSE DE L'UNIVERSITÉ DE LYON OPÉRÉE AU SEIN DE L'INSA LYON

NOM : MICHAÏE

DATE de SOUTENANCE : 04/05/2018

Prénom : Sandra

TITRE : Experimental study of the fundamental phenomena involved in pool boiling at low pressure
(Étude expérimentale des phénomènes fondamentaux de l'ébullition en vase à basse pression)

NATURE : Doctorat

Numéro d'ordre : 2018LYSEI040

École doctorale : MEGA (Mécanique, Énergétique, Génie Civil, Acoustique)

Spécialité : Thermique et Énergétique

RÉSUMÉ :

L'ébullition est un mode de transfert de chaleur intervenant dans de nombreux systèmes thermiques ou énergétiques en raison de son efficacité. Dans certains systèmes – par exemple les évaporateurs des machines frigorifiques à sorption ou certains thermosiphons – l'ébullition se produit sous de faibles pressions. Dans ces conditions, la pression statique induite par la colonne de liquide au-dessus de la surface où les bulles de vapeur se forment n'est pas négligeable devant la pression de saturation prévalant au niveau de la surface libre, la pression locale dans le liquide étant alors la somme de la pression de saturation et de la pression statique. Dès lors, la pression et le sous-refroidissement induit par la pression ne peuvent plus être considérés comme homogènes autour des bulles, ce qui conduit à des inhomogénéités des propriétés thermophysiques dans le fluide. En conséquence, les influences relatives des différentes forces s'exerçant sur une bulle lors de sa croissance ne sont plus les mêmes que dans des conditions de pressions normales ou hautes, ce qui implique une dynamique de bulles différente : la taille, la forme ou encore la fréquence des bulles sont modifiées. Les transferts thermiques sont également affectés par ces conditions particulières.

Afin d'observer l'influence de la pression sur l'ébullition en vase d'un point de vue fondamental, ce travail s'est restreint à l'étude expérimentale de l'ébullition en site unique en régime de bulles isolées. L'eau a d'abord été testée à flux imposé et hauteur de liquide constants pour une large gamme de pressions subatmosphériques. En termes de dynamique de bulles, quatre comportements ont alors pu être identifiés grâce à la visualisation par caméra rapide. Pour certains de ces régimes, l'emploi d'un outil de traitement d'images adapté – développé dans le cadre de cette thèse – a alors permis la quantification de plusieurs paramètres de la dynamique (temps de croissance, fréquence de détachement, volume instantané, *etc.*) à partir de l'exploitation des séquences vidéo enregistrées. Afin de généraliser le concept d'ébullition en vase à « basse pression » et de mieux en appréhender les phénomènes fondamentaux, de nouveaux essais ont été réalisés avec un second fluide, le cyclohexane, choisi en respectant des critères de similitude thermodynamique vis-à-vis de l'eau bouillant à des pressions inférieures à la pression atmosphérique. L'étude comparative des comportements des deux fluides a permis d'identifier un certain nombre de paramètres responsables des phénomènes spécifiques de l'ébullition à basse pression.

Au-delà de ces résultats, le dispositif expérimental a été amélioré afin de lui conférer de nouvelles fonctionnalités. Il s'agit notamment d'effectuer la mesure rapide de la densité de flux transférée localement sous la bulle au cours de sa croissance, de rendre ces mesures thermiques synchrones avec l'acquisition par caméra rapide et enfin d'étudier l'ébullition à basse pression sur des surfaces structurées (agencement de tunnels perforés). Les résultats obtenus ouvrent des perspectives encourageantes pour mieux analyser les comportements spécifiques de l'ébullition à basse pression afin de pouvoir les exploiter dans des applications pratiques.

MOTS-CLÉS : Ébullition en vase, basse pression, essais expérimentaux, visualisation, dynamique de bulles, comparaison de fluides, similitude thermodynamique.

Laboratoire de recherche : CETHIL

Directeur de thèse : BONJOUR Jocelyn

Président de jury : DI MARCO Paolo

Composition du jury : BARTHÈS Magali ; BONJOUR Jocelyn ; DI MARCO Paolo ; ROBINSON Anthony J. ; RULLIÈRE Romuald ; TADRIST Lounès ; ZAJACZKOWSKI Bartosz.